MECHATRONIC DESIGN OF MICRO AUTONOMOUS UNDERWATER VEHICLES FOR CONFINED SPACES

A Dissertation
Presented to
The Academic Faculty

By

Ali A. AlSaibie

In Partial Fulfillment
of the Requirements for the Degree
Doctor of Philosophy in the
George W. Woodruff School of Mechanical Engineering

Georgia Institute of Technology

December 2018

MECHATRONIC DESIGN OF MICRO AUTONOMOUS UNDERWATER VEHICLES FOR CONFINED SPACES

Approved by:

Dr. William Singhose, Advisor
School of Mechanical Engineering
Georgia Institute of Technology

Dr. Kamal Youcef-Toumi
School of Mechanical Engineering
Massachusetts Institute of Technology

Dr. Eric Johnson
School of Aerospace Engineering
Georgia Institute of Technology

Dr. Aldo Ferri
School of Mechanical Science
Georgia Institute of Technology

Dr. Jonathan Rogers
School of Mechanical Engineering
Georgia Institute of Technology

Date Approved: November 2, 2018

Let me say quite categorically that there is no such thing as a fuzzy concept... We do talk about fuzzy things but they are not scientific concepts. Some people in the past have discovered certain interesting things, formulated their findings in a non-fuzzy way, and therefore we have progressed in science.

Rudolf E. Kalman

(May 19, 1930 - July 2, 2016)

I dedicate this dissertation to my family. To my father Ameen, my mother Mona, my wife and love Kholood, and my little princess Jenna. Thank you for everything.

ACKNOWLEDGEMENTS

I would like to express my deepest appreciation to my committee chair, Professor William Singhose, for his support and patience throughout my journey in graduate school. And for giving me the room and encouragement to learn and gain a rich, broad and fun experience of which I am extremely proud of. I would like to thank Professor Charles Ume, for the opportunity to support teaching the subject of Mechatronics.

I would like to thank my committee member, Professor Kamal Youcef-Toumi for the hospitality I received in his research lab, and for the guidance I received in this work. And special thanks to You Wu.

I would also like to thank my committee members, Professor Eric Johnson, Dr. Aldo Ferri and Dr. Jonathan Rogers.

I would like to thank my colleagues, Arto Kivila, and CJ Adams for their support. And special thanks to Jonah Burgin for the effort he put in to help me perform some of the experiments.

A special thanks goes to all the contributors to the open-source community, I hope I can one day pay back the benefit I received by what they generously provide, however priceless it is.

I would like to thank my home country Kuwait, and specifically Kuwait University, for the generous scholarship opportunity to attain my Ph.D.

And last but not least, a warm thank you to my dear wife Kholood, for standing by me throughout my graduate studies, half the world away from her family.

TABLE OF CONTENTS

LIST OF TABLES

LIST OF FIGURES

SUMMARY

In utility piping and fluid transportation pipelines, it is often desired to have a robotic device that can navigate the complex structure to carry inspection to maintain the integrity of these infrastructures. In this work, an attempt to design an untethered micro autonomous underwater vehicle, μAUV, is conducted. The mechanical, electrical, control and perception system are developed through a proposed model-based mechatronic design approach. Key design tools are validated including the measurement of hydrodynamic drag and thruster performance, a visual dynamic software-in-the-loop simulation is developed that incorporates the validated vehicle model, a model-based quaternion error attitude controller is implemented and a structure light perception system and method is proposed.

CHAPTER 1

INTRODUCTION

1.1 Motivation

With the advent of improved computing, sensing, and prototyping technologies it is becoming easier to develop robots with improved mobility, smaller scale, and increased autonomy. Opportunities exist to use such robots in new environments and in new ways. Autonomous Unmanned Vehicles in particular have received great interest in recent years, specially multi-rotors. An interesting subset are autonomous underwater vehicles that are developed for use in military, inspection, installation, photography and scientific exploration.

This thesis explores an area rarely addressed within autonomous underwater vehicles, which is the use of such systems in confined spaces and in close proximity to other structures, where the dynamic behavior changes in complex ways requiring a more reliable perception system, an adaptive controller and an agile dynamic response. The specific use case considered in this work, is in the navigation of a robot within a network of water pipelines.

Considering all of the various pipeline infrastructures in the world, be it gas, oil, or water, there have been major improvements in the inspection technologies available. However, there remains a large percentage of facilities that current technologies cannot address, with one major challenge being the ability for tools to access and perform the inspection.

And given the increasing pressure to maintain higher levels of equipment integrity, and the fact that millions of miles of pipelines will only grow older, outliving their

design life where more frequent inspection is required to extend their operations, there is an important need to develop new inspection techniques, and not just the transducers that perform the inspection measurements, but as importantly the locomotion methods that deliver them to the inspection spot. The technologies required to address the gaps in pipeline inspection vary and may require custom solutions, depending on the use case.

Currently, there is limited autonomy available on pipe and pipeline inspection tools. Introducing a higher level of autonomy and intelligence to inspection tools will allow for a larger degree of flexibility in reaching complex parts of the piping network, in minimizing critical service interruptions where tools can be deployed and "live" inside the infrastructure, in optimized inspections where the system performs decisions in real-time as to where to perform higher resolution inspection, without resorting to off-line analysis and redeployment.

Consider the case where an extended network of pipelines are inspected, a standard inspection tool will likely be passively propelled through the network, performing scans at a certain resolution. The data is then analyzed off-line and it is determined that few anomalies require higher resolution inspections, so deployment is needed. A system with the ability to flexibly maneuver within the network and which can perform high level decisions on where to perform higher resolution inspections can significantly optimize the inspection process.

The motivating vision behind this work is the expectation that integrated autonomous inspection systems are to exist in the future, across infrastructure facilities, and the work performed in this thesis is focused on exploring the feasibility of having a maneuverable autonomous underwater vehicle that can serve to be part of this integrated inspection system.

More specifically, the purpose of this thesis is to develop an autonomous mobile

robot platform that can navigate, untethered, in a confined underwater environment, and to develop a design framework that can be used to replicate said design and enable its functional optimization. The design approach used is a mechatronic design approach, where different components of the system are designed coherently and in parallel. The designed system is divided into three parts: A. The electromechanical system which, as the name suggests, encompasses the mechanical design, electrical, electronics and optics. B. The perception system, and C. The control system design.

In pursuing this project we hope to advance the feasibility of using a maneuverable robot in confined environments, and in doing so understand the limitations and opportunities that come with such a system.

1.2 Related Work

1.2.1 Pipe and Pipeline Inspection Technologies

Existing pipe and pipeline inspection technologies, commercial or research oriented, can be classified into two main categories, internal and external. Internal inspection can be divided into tethered and untethered tools. External inspection can be performed manually by a technician passing the inspection tool over the structure. High level inspection and surveillance of pipelines is being increasingly performed via unmanned aerial vehicles. Robotic locomotion mechanisms carrying the inspection tool for external inspection generally use a crawling locomotion mechanism. Crawling locomotion can be further subdivided into snake locomotion, inchworm locomotion such as those developed in [1], [2] and [3] or wheeled locomotion as in [4] and [5]. External inspection technologies, aside from aerial high level scanning, are limited in their use and reach. They are generally reserved for short sections of exposed pipelines and for facility piping.

Internal inspection tools, on the other hand, have witnessed more interest both commercially and within the research community. Internal inspection tools make it possible to inspect buried and or subsea pipelines, or insulated piping. Untethered internal inspection tools can be used in pressurized and isolated pipe systems, and can travel long distances. The most widely used commercial tool in pipeline inspection is called a "smart pig" or "ILI" (In-line Inspection) tool, as in [6]. Such tools are untethered, and are designed to create a seal around the circumference inducing a pressure build up upstream that propellers the tool forward, as illustrated in Figure 1.1.

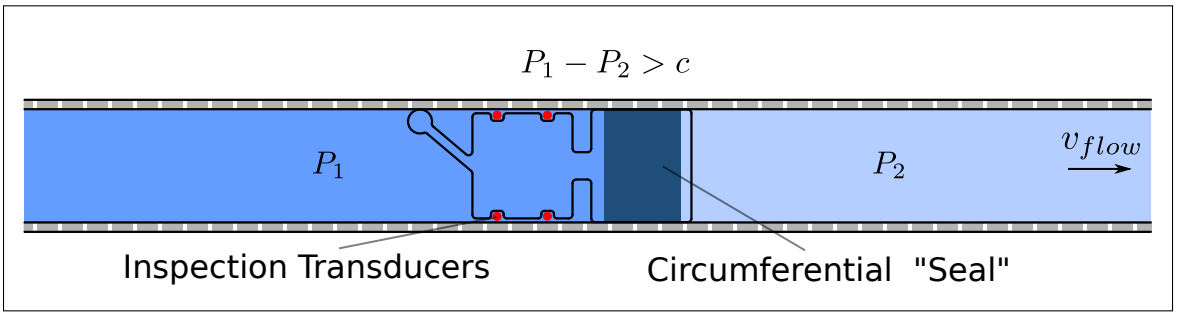

Figure 1.1: In-Line Inspection Tool "Smart Pig"

While "smart pigs" have been successful commercially, they have limitations, and it is estimated that 60% of gas pipelines in North America for example are "unpiggable" [7], that is, they are not suitable for deploying a "smart pig". The case for water piping would likely be similar, since these water pipe networks are not traditionally equipped with similar in-line inspection deployment and retrieval channels.

Some of the limitations with in-line inspection tools include: flowrate/pressure, variable diameter pipelines, internal obstruction, branches and non-ferrous material. Furthermore, such tools are not used on facility piping. Researchers have developed a number of different internal locomotion mechanisms. Hu [8] developed an untethered system by which a propeller converts rotation induced by the pipe fluid flow, into a reciprocating motion. Many other researchers have developed a variety of in-

ternal tethered crawler type locomotion. Yoon, Roh, Choi and others [9], [10], [11] developed inspection robots with wheeled locomotion. Qiao [12] and Takahashi [13] developed an inchworm type robot. While, Trebun [14], Kuwada [15] and Suzumori [16] used snake locomotion.

In this work, we would like to use a self-propelled, untethered micro underwater vehicle to navigate the pipe systems. Our work is an extension of the work done by Wu [17] and in collaboration with Massachusetts Institute of Technology's Mechatronics Research Lab (MIT MRL). The focus of this work is not on the inspection aspect of the technologies but on locomotion, the method by which the inspection tool is carried.

1.2.2 Underwater Robots

Development of unmanned underwater vehicles, also termed remotely operated vehicles (ROV), goes back decades. Beginning in the 1960s, they were first developed to conduct dangerous and important work, such as bomb recovery. The oil and gas industry adopted their use in the 1970's with the development of off-shore structures [18]. ROVs are built for high stability, maneuverability, and are usually equipped with manipulator arms of various sizes and for various purposes [19]. Other attachments include cameras and sensors for monitoring and exploration activities. Pluto, shown in Figure 1.2 is a remotely operated underwater vehicle used in underwater mine identification and destruction.

Another class of underwater vehicle is the underwater glider [21], which is designed to sink controllably, gliding toward the target. It then floats back to the surface and repeats the motion with a high degree of energy efficiency and autonomy. Such underwater vehicles have been used to gather oceanic data, monitor oil spills, and they have been tested for military use.

There are very few existing underwater robot designs that are on the same scale

Figure 1.2: Remotely Operated Underwater Vehicle - Pluto [20]

considered in this thesis. Bhattacharyya [22] developed a football sized underwater robot that employs 6 micro pumps to propel the robot. Bio-inspired underwater water robots inspired by fish, octopus, and others [23], have been investigated. We will consider "small" or "micro" underwater robots to be those that can be carried with one hand.

1.2.3 Underwater Perception

Suitable perception sensors and methods, would allow the robot to localize its position, determine its position and orientation with respect to its surrounding and detect obstacles ahead.

Acoustic

Sonar is, by far, the most widely used perception technique in underwater vehicles. Sound waves have the ability to travel long distances underwater. However, sound waves at, and around, the sonic wave range have low bandwidth.

Vision

Vision systems are increasingly being deployed in underwater applications for the purposes of perceptions. Camera sensors continuously improve in speed and ac-

curacy. These improvements are accompanied by improved on-board computing power.

In [24], a monocular vision camera was used to estimate the pose relative to an elliptical dock. In [25], a monocular vision camera was used to estimate the location of circular features underwater. In [26], 3D scanning was performed underwater using a stereo monocular vision by taking refraction into account.

Within confined spaces, such as pipelines and pipes, vision systems have been used to detect obstacles, bends, and tees [27]. One of the main areas investigated in this thesis is the ability to achieve sufficiently accurate pose estimation in order to navigate the robot within the pipe network, or other structured confined space with minimal to no collisions.

1.2.4 Control

In the area of remotely operated vehicles, or underwater robots, there is a robust body of literature dealing with modeling and control, [19]. However, the challenges posed by controlling an underwater robot in a confined space are unsolved and the author is not aware of work attempting to provide 4-D, or above, dynamic control of a robot in such environments.

Zeng et al.[28] surveyed the existing path planning algorithms used in autonomous underwater navigation. Most of the planning algorithms are used for long to medium range navigation. For our application, a more near field planning algorithm is required in order to navigate within a network of pipes.

1.3 Technical Approach and Outline

The dynamics of underwater vehicles will be presented first, and this will allow for analytically integrating the subcomponents of the mechatronic system. The mechanical design variables will influence and determine the dynamic performance,

in exchange governing the characteristics of the controller and the performance of the perception system. Further optimizations of the design will also be founded on the analytical dynamic model of the system. The mechatronic design methodology will then be presented along with developed design architecture and physical design realizations.

Methods to determine and derive the model parameters will then be discussed and key empirical methods will be validated. A visual-dynamic software-in-the-loop simulation is developed and presented that incorporates the real dynamics of the vehicle. Then a proposed pose estimation method through perception is presented, and finally an attitude and rate control systems are implemented in the simulation and on the physical realized design and are presented.

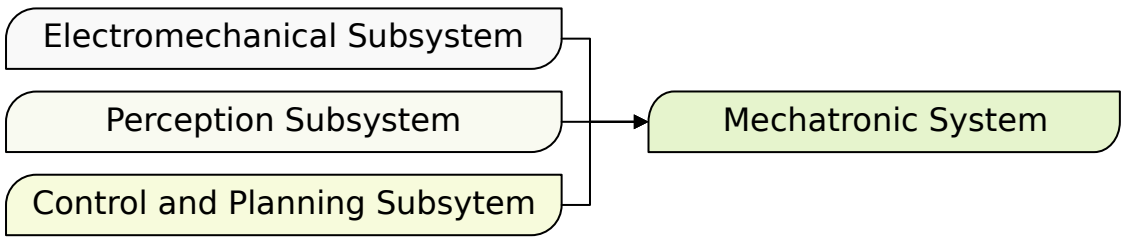

Figure 1.3: Mechatronic Design Subsystems

1.4 Thesis Contribution

As part of this research, a mechatronic design methodology for a class of underwater vehicles is developed. A functioning design realization is produced. An experimentally validated method for computing the hydrodynamic damping and the thruster dynamics is achieved. A visual dynamic software-in-the-loop simulation environment is developed, implementing the validated dynamic model. A structured light pose estimation perception system is proposed, and a model-based attitude rate controller and quaternion-based attitude controller are implemented.

CHAPTER 2

UNDERWATER VEHICLE MODEL

In this chapter the underwater vehicle dynamics for a completely submerged vehicle in a homogenous liquid, is presented.

Underwater vehicle models have been studied previously by a number of researchers including [29], [19] and others.The model presented here is for reference. Details of how the model parameters are calculated is given in Chapter 5. A design variables parametrized model will be given in the next chapter.

2.1 Notations

Bold capital letters denote transformation operator or a matrix. For transformation operators the leading subscript denotes the origin frame, and the lagging superscript denotes the target frame. ${}^{I}\boldsymbol{R}_{B}$ for instance, denotes the transformation matrix from frame B to from I. ${}^{I}\boldsymbol{q}_{B}$ denotes the orientation of frame B in frame I expressed in quaternion notations. Bold lower case letters denote vectors. $\mathbb{R}$, $\mathbb{H}$ and $\mathbb{C}^{n}$ denote the real numbers space, Hilbert space and n-continuous number space respectively. The lagging superscript denoting the reference frame on a vector is dropped unless it is used to express the vector in a frame different than the vector's parent frame.

Table ?? below summarizes the notation used in the domain of the vehicle dynamic model and control, unless otherwise noted. Quaternion math and notations will be explained further in Chapter 6

Table 2.1: Notation Summary

Notation Symbol	Description
${}^{I}\boldsymbol{x} = {}^{I}\boldsymbol{R}_{B}\,{}^{B}\boldsymbol{x}$	Vector $\boldsymbol{x}$ rotated by the rotation operator $\boldsymbol{R}$ from frame B to frame I
$\mathbb{R}$, $\mathbb{H}$, $\mathbb{C}$	Real Numbers Space, Hilbert Space, Continuously Differentiable Space
$\boldsymbol{x}$, $\boldsymbol{v}$, $\boldsymbol{\eta} \in \mathbb{R}^n$	n-dimensional real vector
x_B, y_B, z_B	Principal coordinate vectors in frame B
${}^{I}\boldsymbol{q}_{B} \in \mathbb{H}$	Frame B orientation w.r.t. to frame I expressed in quaternion notation
${}^{I}\boldsymbol{x} = {}^{I}\boldsymbol{q}_{B}^{-1} \otimes {}^{B}\boldsymbol{x} \otimes {}^{I}\boldsymbol{q}_{B}$	Vector $\boldsymbol{x}$ rotated by the quaternion rotation operator ${}^{I}\boldsymbol{q}_{B}$ from frame B to frame I

Used in expressing the dynamic model and controller

2.2 Pose Representation

In marine systems the position and orientation; together referred to as the pose, of the vehicle are represented by the six parameters shown on Figure 2.1, common convention places the x axis along the surge direction, y along the sway, and z along the heave. Euler angles are used to express the attitude of the vehicle in an North-East-Down (NED) frame. The rotation sequence followed is a Tait-Bryan Z-Y-X extrinsic sequence. That is, attitude is represented by the yaw-pitch-roll sequence.

Let $\boldsymbol{p} \in \mathbb{R}^6$ denote the pose of the vehicle in the inertial frame while $\boldsymbol{\eta} \in \mathbb{R}^6$ denotes the pose in the body-fixed frame. The body-fixed pose vector $\boldsymbol{\eta}$ does not have a visual representation, but its derivate, the velocity vector is composed of the linear and angular body-fixed velocities, expressed as

$$\boldsymbol{v} \in \mathbb{R}^6 = \begin{bmatrix} \boldsymbol{v_1} \\ \boldsymbol{v_2} \end{bmatrix} = \begin{bmatrix} \dot{x} & \dot{y} & \dot{z} & \dot{\phi} & \dot{\theta} & \dot{\psi} \end{bmatrix}^T \tag{2.1}$$

The body-fixed velocity vector $\boldsymbol{v}$, is useful in expressing the dynamics of the vehicle. The inertial-frame pose vector $\boldsymbol{p}$, is useful in representing the kinematics of the vehicle; its position and attitude.

$$\boldsymbol{p} \in \mathbb{R}^6 = \begin{bmatrix} \boldsymbol{p}_1 \\ \boldsymbol{p}_2 \end{bmatrix} = \begin{bmatrix} p_x & p_y & p_z & \phi & \theta & \psi \end{bmatrix}^T \tag{2.2}$$

It follows that the derivative of inertial-frame pose vector, $\dot{\boldsymbol{p}}$ represents the linear and angular velocities with respect to the inertial frame.

$$\dot{\boldsymbol{p}} \in \mathbb{R}^6 = \begin{bmatrix} \dot{\boldsymbol{p}}_1 \\ \dot{\boldsymbol{p}}_2 \end{bmatrix} = \begin{bmatrix} \dot{p_x} & \dot{p_y} & \dot{p_z} & {}^I\dot{\phi} & {}^I\dot{\theta} & {}^I\dot{\psi} \end{bmatrix}^T \tag{2.3}$$

To transform between the body-fixed velocity vector $\boldsymbol{v}$ and the inertial-frame velocity vector $\dot{\boldsymbol{p}}$ we define the transformation matrix ${}^I\boldsymbol{T}_B \in \mathbb{R}^{6\times6}$, such that $\dot{\boldsymbol{p}} = {}^I\boldsymbol{T}_B\boldsymbol{v}$

$${}^I\boldsymbol{T}_B = \begin{bmatrix} {}^I\boldsymbol{R}_B(\boldsymbol{p}) & \boldsymbol{0} \\ \boldsymbol{0} & {}^I\boldsymbol{J}_B(\boldsymbol{p}) \end{bmatrix} \text{ , } {}^I\boldsymbol{R}_B(\boldsymbol{p}) \in \mathbb{R}^{3\times3} \text{ , } {}^I\boldsymbol{J}_B(\boldsymbol{p}) \in \mathbb{R}^{3\times3} \tag{2.4}$$

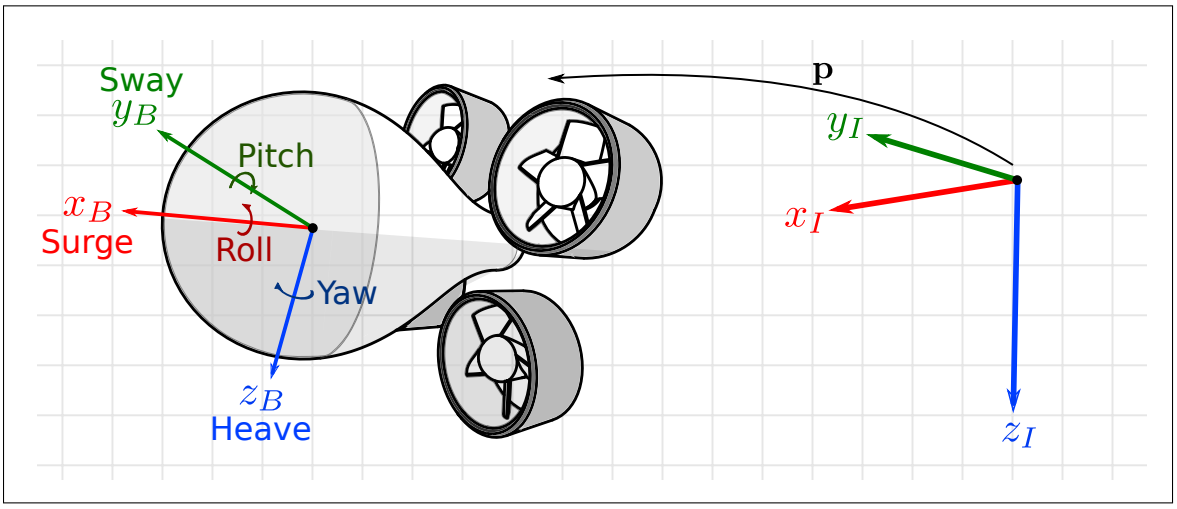

Figure 2.1: Underwater Vehicles Motion Convention

In Chapter 6, further discussion of quaternion attitude representations and frame transformations will be discussed. The above is sufficient for presenting the basics of underwater vehicle dynamics.

2.3 Dynamics

From [29], the general form of an underwater vehicle's dynamic model in matrix form, expressed in the body-fixed frame is given by

$$\tilde{\boldsymbol{M}}(\dot{\boldsymbol{v}}) + \tilde{\boldsymbol{C}}(\boldsymbol{v}) + \boldsymbol{D}(\boldsymbol{v}) + \boldsymbol{G}({}^{I}\boldsymbol{R}_{B}) = \boldsymbol{\tau}\ ,\ \forall \boldsymbol{v} \in \mathbb{R}^{6} \tag{2.5}$$

Where $\tilde{\boldsymbol{M}}(\dot{\boldsymbol{v}})$ is the lumped inertial term, $\tilde{\boldsymbol{C}}(\boldsymbol{v})$ is the lumped coriolis term, $\tilde{\boldsymbol{D}}(\boldsymbol{v})$ is the damping effects term, $\boldsymbol{G}({}^{I}\boldsymbol{R}_{B})$ is the restoring forces term, and $\boldsymbol{\tau}$ represents the external forces acting on the underwater vehicle, by either the environment or on-board actuators. In the following, a description of the different terms of the dynamic model will be given.

2.3.1 Inertial Term: $\tilde{\boldsymbol{M}}(\dot{\boldsymbol{v}})$

The inertial term expresses the resistance of the vehicle to the change in its linear velocity and angular velocity due to its mass and mass moment of inertia respectively. The lumped mass includes both the vehicle's own rigid-body mass, and what is termed "the added mass", which expresses the virtual fluid mass surrounding the underwater vehicle's body that resists the acceleration of the vehicle. It is not a constant physical volume of mass, but rather a virtual one that moves out of phase with the rigid-body motion. This term is often negligible for vehicles moving in-air, but is significant for underwater vehicles.

Assuming the relationship between the vehicle's acceleration and mass is linear, the inertial term can then be divided into a rigid-body and added mass term, expressed as:

$$\tilde{\boldsymbol{M}}(\dot{\boldsymbol{v}}) \in \mathbb{R}^{6\times 6} = (\boldsymbol{M}_{RB} + \boldsymbol{M}_{A})\dot{\boldsymbol{v}} \tag{2.6}$$

Defining the skew symmetric operator matrix $[a]_\times \in \mathbb{R}^{3\times3}$ as

$$[a]_\times = \begin{bmatrix} 0 & -a_3 & a_2 \\ a_3 & 0 & -a_1 \\ -a_2 & a_1 & 0 \end{bmatrix} \tag{2.7}$$

The rigid body mass matrix term, $\boldsymbol{M}_{RB}$ is a constant positive definite matrix that can be expressed as

$$\boldsymbol{M}_{RB} > \boldsymbol{0} \ \in \mathbb{R}^{6\times6} = \begin{bmatrix} m\boldsymbol{I} & -m[\vec{\boldsymbol{r}}_{B/C}]_\times \\ m[\vec{\boldsymbol{r}}_{B/C}]_\times & \boldsymbol{I}_O \end{bmatrix} \tag{2.8}$$

In (2.8), $\vec{\boldsymbol{r}}_{B/C}$ is the vector from the body-frame origin to the Center of Mass, CoM , and $\boldsymbol{I}_O \in \mathbb{R}^{3\times3}$ is the inertia tensor matrix. For simplicity, the body-frame origin and the CoM can be set coincident reducing the off-diagonal terms in $\boldsymbol{M}_{RB}$ to zero. The added mass matrix $\boldsymbol{M}_A$ is not necessarily positive definite in all cases. For certain motion frequencies and bodies near the surface the added mass term may have negative terms [29]. For a completely submerged body of liquid operating in open water and at low velocities, the added mass term is proven to be positive definite [30].

The added mass matrix, $\boldsymbol{M}_A$ can be assumed to be a constant matrix for a rigid and fully submerged volume in open water. It is primarily a property of the surface geometry and the fluid density. For a simple spheroid for example the added mass matrix can be approximated as a diagonal matrix:

$$\boldsymbol{M}_A \in \mathbb{R}^{6\times6} = -diag(X_{\dot{v}_x}, Y_{\dot{v}_y}, Z_{\dot{v}_z}, K_{\dot{v}_\phi}, M_{\dot{v}_\theta}, N_{\dot{v}_\psi}) \tag{2.9}$$

The diagonal terms in $\boldsymbol{M}_A$ are the coefficients derived from the kinetic energy to forces and moments relationship.

2.3.2 Coriolis and Centripetal Term: $\tilde{\boldsymbol{C}}(\boldsymbol{v})$

The lumped Coriolis-Centripetal effects term is, similar to the Mass Matrix, composed of two parts, the coriolis-centripetal effects from the rigid body mass and that of the added mass. The lumped term is often expressed as a coriolis-centripetal matrix $\boldsymbol{C}(v)$ that is linear in the velocity times the vehicle's velocity. The coriolis-centripetal matrix can then be divided in to a rigid-body term and added mass term:

$$\tilde{\boldsymbol{C}}(\boldsymbol{v}) = \boldsymbol{C}(\boldsymbol{v})\boldsymbol{v} = (\boldsymbol{C}_{RB}(\boldsymbol{v}) + \boldsymbol{C}_{A}(\boldsymbol{v}))\boldsymbol{v} \tag{2.10}$$

The Coriolis-Centripetal Matrix can be parametrized such that it is skew-symmetric, if the vehicle body is moving through an ideal fluid:

$$\boldsymbol{C}(\boldsymbol{v}) = -\boldsymbol{C}^{T}(\boldsymbol{v}), \quad \forall \boldsymbol{v} \in \mathbb{R}^{6} \tag{2.11}$$

With a symmetric positive definite mass matrix $\boldsymbol{M}$, the kinetic energy of the system can be expressed as $T = -\frac{1}{2}\boldsymbol{v}^{T}\boldsymbol{M}\boldsymbol{v}$. A Langrangian derivation [31] can prove that a valid parameterization of the coriolis-centripetal matrix exists, and is expressed as

$$\boldsymbol{C}(\boldsymbol{v}) = \begin{bmatrix} \boldsymbol{0} & -[\boldsymbol{M}_{11}\boldsymbol{v}_1 + \boldsymbol{M}_{12}\boldsymbol{v}_2]_{\times} \\ -[\boldsymbol{M}_{11}\boldsymbol{v}_1 + \boldsymbol{M}_{12}\boldsymbol{v}_2]_{\times} & -[\boldsymbol{M}_{21}\boldsymbol{v}_1 + \boldsymbol{M}_{22}\boldsymbol{v}_2]_{\times} \end{bmatrix} \tag{2.12}$$

where

$$\boldsymbol{M} = \begin{bmatrix} \boldsymbol{M}_{11} & \boldsymbol{M}_{12} \\ \boldsymbol{M}_{21} & \boldsymbol{M}_{22} \end{bmatrix} \tag{2.13}$$

and

$$\boldsymbol{v} = \begin{bmatrix} \boldsymbol{v}_1 \\ \boldsymbol{v}_2 \end{bmatrix} \tag{2.14}$$

2.3.3 Damping Term: $\boldsymbol{D}(\boldsymbol{v})$

The damping term represents the dissipative or damping effects caused by potential damping; damping due to forced oscillation by wave excitation, skin friction, wave drift damping, damping due to vortex shedding; also known as fluid drag forces, and lift forces. Ignoring wave effects for vehicles moving underwater, the dissipative effects are assumed to be caused only by drag (damping due to vortex shedding) and lift forces. In a simplified form, for a vehicle that is symmetric across the three planes and motion is assumed to be uncoupled, The damping term can be set as a block diagonal.

$$\boldsymbol{D}(\boldsymbol{v}) = \boldsymbol{D}_{Drag}(\boldsymbol{v}) + \boldsymbol{D}_{Lift}(\boldsymbol{v}) = \begin{bmatrix} \boldsymbol{D}_{11}(\boldsymbol{v}) & \boldsymbol{0} \\ \boldsymbol{0} & \boldsymbol{D}_{22}(\boldsymbol{v}) \end{bmatrix} \tag{2.15}$$

The resulting damping affects are nonlinear and in reality coupled in motion even between translational and rotational terms. It is difficult to estimate a hydrodynamic damping model explicitly, but experimental and computational methods exist to estimate these parameters. This will be d later in Chapter 5. Nevertheless, the diagonal terms contribute the most in each respective motion direction.

2.3.4 Hydrostatic Effects: $\boldsymbol{G}({}^{I}\boldsymbol{R}_{B})$

Gravitational and buoyancy forces act on the vehicle in opposite directions, the resultant force is referred to in marine systems as "restoring forces". The combination of the difference between the weight and buoyancy force, the attitude of the vehicle, and the geometric relationship between the center of mass (CoM) and center of buoyancy (CoB) determine the restoring forces $\boldsymbol{G}$ acting on the vehicle.

$$\boldsymbol{G}({}^{I}\boldsymbol{R}_{B}) = -\begin{bmatrix} {}^{I}\boldsymbol{R}_{B}^{-1}(W-B) \\ [\vec{\boldsymbol{r}}_{gc}]_{\times}{}^{I}\boldsymbol{R}_{B}^{-1}W - [\vec{\boldsymbol{r}}_{bc}]_{\times}{}^{I}\boldsymbol{R}_{B}^{-1}B \end{bmatrix} \tag{2.16}$$

Expanding (2.16) gives

$$\boldsymbol{G}^T({}^I\boldsymbol{R}_B) = \begin{bmatrix} (W-B)sin(\theta) \\ -(W-B)cos(\theta)sin(\phi) \\ -(W-B)cos(\theta)sin(\phi) \\ -(y_gW - y_bB)cos(\theta)cos(\phi) & + & (z_gW - z_bB)cos(\theta)sin(\phi) \\ (z_gW - z_bB)sin(\theta) & + & (x_gW - x_bB)cos(\theta)cos(\phi) \\ -(x_gW - x_bB)cos(\theta)sin(\phi) & - & (y_gW - y_bB)sin(\theta) \end{bmatrix} \tag{2.17}$$

For a neutrally buoyant vehicle, where $W = B$, the restoring forces become a function of the vehicle's geometry, more specifically, the geometric relationship between its CoM and CoB, $\vec{\boldsymbol{r}}_{bg}$. The restoring forces vector then reduces to

$$\boldsymbol{G}^T({}^I\boldsymbol{R}_B) = mg \begin{bmatrix} 0 \\ 0 \\ 0 \\ -(y_g - y_b)cos(\theta)cos(\phi) & + & (z_g - z_b)cos(\theta)sin(\phi) \\ (z_g - z_b)sin(\theta) & + & (x_g - x_b)cos(\theta)cos(\phi) \\ -(x_g - x_b)cos(\theta)sin(\phi) & - & (y_g - y_b)sin(\theta) \end{bmatrix} \tag{2.18}$$

This property will become useful when designing the vehicle to produce a desired steady state attitude for the vehicle.

2.3.5 External Forces and Moments: $\boldsymbol{\tau}$

Environmental forces and moments acting on underwater vehicles include current and wave forces and moments. For underwater vehicles operating in open steady water and below the surface, we can neglect these environmental forces and set them as external disturbances. Actuation forces and moments depend on the actuation method used and the control surfaces present. For underwater vehicles propelled via rotary thrusters the external forces and moments vector can be defined as

$$\boldsymbol{\tau} = \begin{bmatrix} \sum T_i \\ \sum T_i \times r + \sum Q_i \end{bmatrix} \tag{2.19}$$

T_i are thrust forces generated by the thrusters and Q_i are moment torques generated by the rotation of the thruster impellers. The external forces and moments vector $\boldsymbol{\tau}$ can be linearized if we assume a quadratic relationship between the thrust and moment torques of the thrusters such that

$$T = k_T \omega |\omega|, \quad k_T \in \mathbb{R}^+ \tag{2.20}$$

$$Q = k_Q \omega |\omega|, \quad k_Q \in \mathbb{R}^+ \tag{2.21}$$

where k_T and k_M are the thruster's thrust and torque constants respectively. With that, the external forces and moments vector becomes

$$\boldsymbol{\tau} = \boldsymbol{B}\boldsymbol{\omega}|\boldsymbol{\omega}|, \qquad \boldsymbol{B} \in \mathbb{R}^{6\times n}, \boldsymbol{\omega} \in \mathbb{R}^n \tag{2.22}$$

Figure 2.2 shows an example of a fully actuated underwater vehicle in translation and over-actuated in rotation. The matrix $\boldsymbol{B}$ is termed the thruster allocation ma-

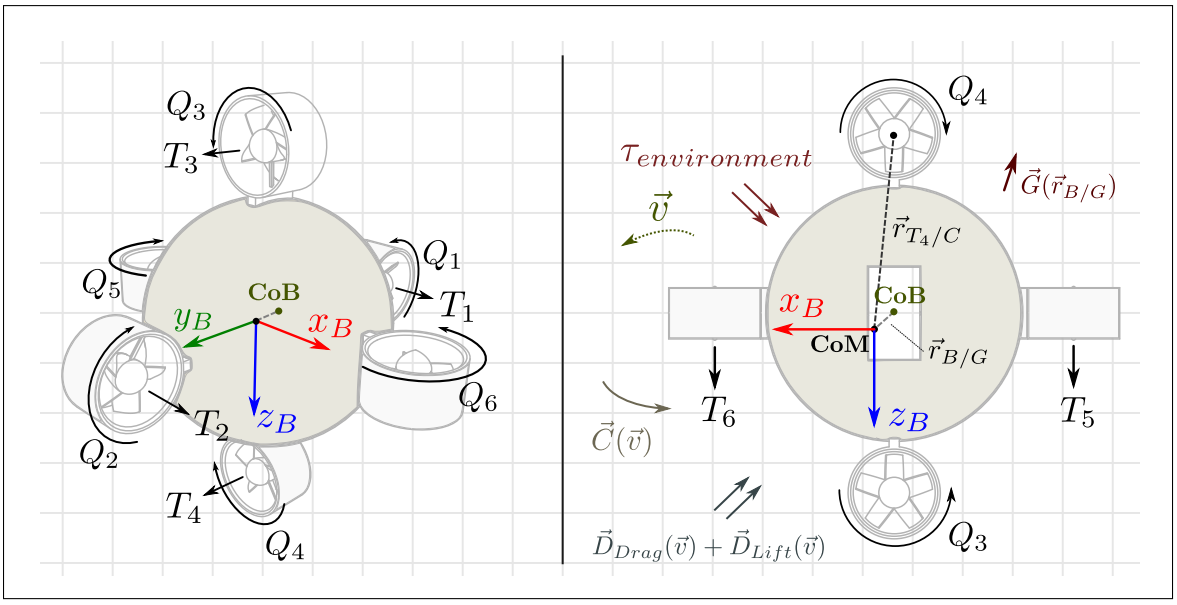

Figure 2.2: Example of a Fully Actuated Underwater Vehicle

trix. For the configuration in the figure, the allocation matrix would be defined as

$$\boldsymbol{\tau} = \begin{bmatrix} k_{T_1} & k_{T_2} & 0 & 0 & 0 & 0 \\ 0 & 0 & k_{T_3} & k_{T_4} & 0 & 0 \\ 0 & 0 & 0 & 0 & k_{T_5} & k_{T_6} \\ k_{Q_1} & -k_{Q_2} & k_{T_3}(\vec{r}_{T_3} \cdot z) & -k_{T_4}(\vec{r}_{T_4} \cdot z) & 0 & 0 \\ 0 & 0 & k_{Q_3} & -k_{Q_4} & k_{T_5}(\vec{r}_{T_5} \cdot x) & -k_{T_6}(\vec{r}_{T_6} \cdot x) \\ k_{T_1}(\vec{r}_{T_1} \cdot y) & -k_{T_2}(\vec{r}_{T_2} \cdot y) & 0 & 0 & k_{Q_{z1}} & -k_{Q_{z2}} \end{bmatrix} \boldsymbol{\omega}|\boldsymbol{\omega}| \quad (2.23)$$

This notation follows that for a positive thruster speed, thrust will be positive with respect to the principal coordinates. The orientation of a thruster's propeller and its positive rotation direction determines the torque direction. The sign of the torque is carried in the allocation matrix based on the arrangement of the propeller.

If we don not have any assumptions about relationship between speed and thrust/torque, we can generalize the thruster allocation matrix as

$$\boldsymbol{\tau} = \hat{\boldsymbol{B}}\, \boldsymbol{f}(\boldsymbol{\omega}) = \begin{bmatrix} \hat{\boldsymbol{B}}_{11} & \boldsymbol{0}_{12} \\ \hat{\boldsymbol{B}}_{21} & \hat{\boldsymbol{B}}_{22} \end{bmatrix} \begin{bmatrix} \boldsymbol{T}(\boldsymbol{\omega}) \\ \boldsymbol{Q}(\boldsymbol{\omega}) \end{bmatrix}, \ \hat{\boldsymbol{B}} \in \mathbb{R}^{6 \times 2n}, \ \boldsymbol{f}(\boldsymbol{\omega}) \in \mathbb{R}^{2n \times 1} \quad (2.24)$$

Where $\hat{\boldsymbol{B}}$ includes the thruster mapping matrix, mapping the thruster actions to onto the vehicle, and n is the number of thrusters installed. This form is useful when implementing a complex parameterized thruster model as will be discussed in Chapter 5.

The basic underwater vehicle dynamic model has been presented. In the next chapter we will develop the design methodology for the μAUVand parameterize the dynamic model with respect to the design variables.

CHAPTER 3

DESIGN METHODOLOGY

In this chapter, a review of the design space with respect to the operating space of the system is presented. The underwater vehicle dynamic model is parameterized in terms of the mechatronic design variables, to facilitate a better understanding of their contribution to the performance of the system, and to setup a framework for a goal-driven design optimization.
The mechatronic design methodology will also be proposed, this will serve to provide an overview of the design activities carried out as part of this research and to serve as a reference for developing similar systems.

3.1 Design Space

There are two design spaces that intersect in this work, the design space of underwater vehicles and the design space of pipe inspection locomotions. Within the sphere of underwater vehicles, there is a limited amount of vehicles designed for relatively small confined and shallow spaces. The majority of underwater vehicles have been designed for relatively large open-water and often deep environments, targeting sea exploration, mapping, military and facility operations such as in the oil and gas industry.

Within the pipe and pipeline inspection ecosystem, there is a variety of locomotion mechanisms available either commercially or as research platforms. However, existing locomotion technologies still do not meet the full demand of the operating environments, the limitations to existing technologies include for instance: flow-rate restrictions, accessibility into and out of the pipe, variable diameter pipes, pipes

with protruding or the high cost associated with using certain commercial technologies. [7]

Figure 3.1 classifies the existing locomotion mechanisms used in pipe inspection. They are grouped as external and internal mechanisms. External mechanisms are normally limited to localized inspection, with the exception of area surveillance. Internal inspection tools are predominantly in use for longer range, that is if the facility is equipped to handle the deployment of internal inspection tools, into the pipe or pipeline infrastructure. Highlighted on the figure is class of internal, untethered and self-propelled pipe inspection locomotion mechanism. We believe that this subspace is under-explored, due primarily to technological limitations that had previously existed before, but are being overcome.

In this work, we are concerned with developing a novel locomotion platform for pipe inspection and or mapping, that is intended to carry specific transducers, such as ultrasonic sensors, or even use the on-board vision sensor for inspection purposes. Micro Autonomous Underwater Vehicles are a candidate for this subclass of locomotion mechanisms, and we will explore their applicability in this context.

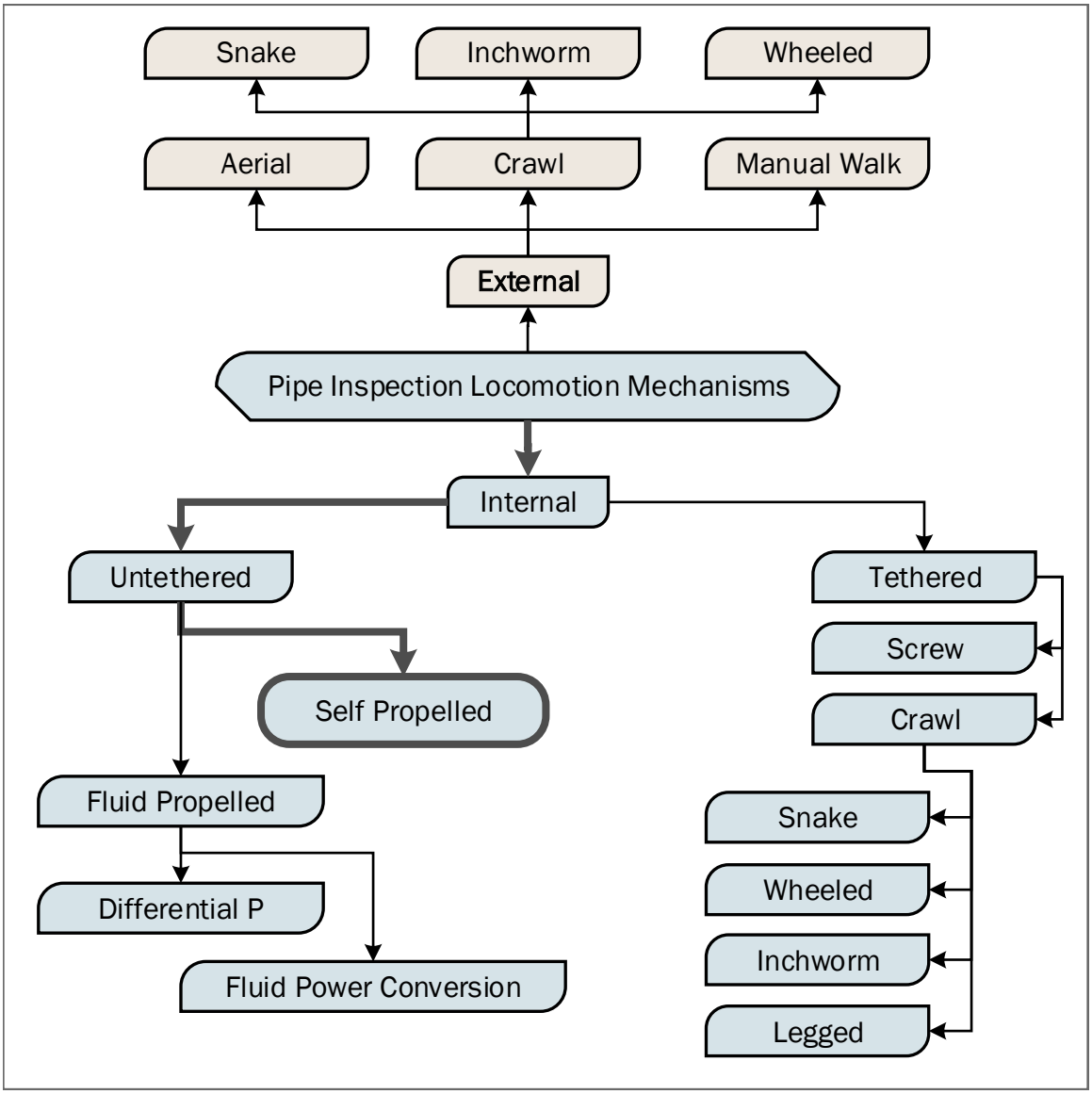

Figure 3.1: Locomotion Classification for pipe and pipeline inspection systems

3.2 Parameterized μAUV Dynamic Model

From the underwater vehicle dynamic model we would like to map the relationship between design variables and the model parameters. This mapping will inform our process for framing the design requirements and specifications, for producing a design realization and for allowing for a practical optimization framework.

Given the general form of the underwater vehicle dynamics in the body-fixed frame

$$\tilde{\boldsymbol{M}}(\dot{\boldsymbol{v}}) + \tilde{\boldsymbol{C}}(\boldsymbol{v}) + \boldsymbol{D}(\boldsymbol{v}) + \boldsymbol{G}({}^{I}\boldsymbol{R}_{B}) = \boldsymbol{\tau}\ ,\ \forall \boldsymbol{v} \in \mathbb{R}^{6} \tag{3.1}$$

with,

$$\boldsymbol{v} = \begin{bmatrix} \boldsymbol{v}_1 \\ \boldsymbol{v}_2 \end{bmatrix} \tag{3.2}$$

Each of the model parameters can be mapped to specific design variables.

3.2.1 Inertia Matrix

$\boldsymbol{M}$ represents both the rigid-body mass of the vehicle and the added mass. While the rigid-body mass matrix is a function of the mass and mass distribution, the added mass term is a function of the vehicle's volume, surface geometry and fluid density.

$$\boldsymbol{M} \in \mathbb{R}^{6\times 6} = \boldsymbol{M}_{RB} + \boldsymbol{M}_{A} = f(m, g, I_o) + f(\bar{V}, \bar{L}, \rho) \tag{3.3}$$

3.2.2 Coriolis-Centripetal Matrix

Similar to the inertia matrix, the coriolis-centripetal matrix $\boldsymbol{C}(\boldsymbol{v})$ is the sum of the rigid body's effects in addition to the effects from the added mass. The added mass coriolis matrix is a function of the body mass, surface geometry, volume and veloc-

ity of the vehicle.

$$\boldsymbol{C} \in \mathbb{R}^{6\times6} = \boldsymbol{C}_{RB}(v) + \boldsymbol{C}_{A}(v) = f(m, g, I_o, \boldsymbol{v}) + f(\bar{m}, \bar{V}, \bar{L}, \rho, \boldsymbol{v}) \tag{3.4}$$

3.2.3 Damping Matrix

For fully submerged underwater vehicles the two dominant hydrodynamic forces are due to skin friction and vortex shedding, $\boldsymbol{D}(\boldsymbol{v}) = \boldsymbol{D}_S(\boldsymbol{v}) + \boldsymbol{D}_M(\boldsymbol{v})$.

The damping effect is nonlinear and coupled, but assuming the vehicle is performing non-coupled motion, which is true if the vehicle is in pure surge for example. And assuming it has three planes of symmetry, has sub-critical flow, and 3rd order and higher terms are ignored, then we can assume damping to have a diagonal structure. The contribution from vortex shedding can be computed by knowing the drag and lift coefficient of the vehicle.

$$F_{drag} = 0.5\rho v^2 A C_d(R_n) \tag{3.5}$$

$$F_{lift} = 0.5\rho v^2 A C_l(R_n, \alpha) \tag{3.6}$$

where α is the angle of attack, v is the forward velocity of the vehicle, R_n is the Reynolds number, and A is the equivalent cross-sectional frontal area of the vehicle. C_d, and C_l are the lift and drag coefficients respectively. Damping is a function of the vehicle's surface geometry, volume, liquid density, Reynolds number, speed and skin friction.

$$\boldsymbol{D}(\boldsymbol{v}) \in \mathbf{R}^{6x6} = f(\bar{L}, \bar{V}, \rho, Re, v, f_s) \tag{3.7}$$

3.2.4 Restoring Forces: Gravity and Buoyancy

Restoring forces are due to gravity and buoyancy, which is a function of volume. The resultant restoring force is a function of the difference between them, and a function of the distance between the center of Mass CoM to Center of Buoyancy CoB.

$$G({}^{I}\boldsymbol{R}_{B}) \in \mathbb{R}^{6} = f(m, V, \vec{r}_{G/B}) \tag{3.8}$$

For a neturally buoyant vehicle, the restoring forces are only a function of the distance between CoB and CoM.

$$G({}^{I}\boldsymbol{R}_{B}) \in \mathbb{R}^{6} = f(\vec{r}_{G/B}) \,,\, \forall W = B \tag{3.9}$$

3.2.5 External Forces

Using thrusters to drive the vehicle and assuming a quadratic thruster model. The external force from the thrusters can be expressed as

$$\tau \in \mathbb{R}^{6} = \boldsymbol{B} \left|\boldsymbol{\omega}\right| \boldsymbol{\omega} \tag{3.10}$$

The thruster matrix is composed of the thrust and torque coefficients. The coefficients for a ducted thruster propeller are a function of the propellers geometric profile, their blade pitch angle, diameter, advance speed of the thrusters, fluid density, duct geometry and thruster placements. The rotation speed range is a function of the motors, which have their own mechanical and electrical power characteristics.

$$\boldsymbol{B} \in \mathbb{R}^{6\times 6} = f(\alpha, N, D, v_{a}, \rho, \vec{r}_{T}) \tag{3.11}$$

The range of thruster motor speeds is governed by the motors voltage V, current draw I, resistance R, electro-mechanical force E, motor load Q and operating temperature T.

$$[\boldsymbol{\omega}_{min}, \boldsymbol{\omega}_{max}] \longleftrightarrow f(V_m, I_m, E_m, R_m, T_m, Q_m) \tag{3.12}$$

3.2.6 Dynamic Performance

Assessing the performance of the μAUVis both a quantitative and subjective matter, but for our application we will be interested in measuring the vehicle's range, speed, peak-efficiency cruising speed, dynamic agility and controller tracking error. These performance measures; however, are a function or a byproduct of the vehicle's dynamic model and the controller.

3.2.7 Controller

Assuming we have a well validated model and identified parameters, we can apply a model-based rate controller of the form

$$\tau_{sp} = \underbrace{\mathbf{M}\dot{\boldsymbol{v}}_r + \boldsymbol{C}(\boldsymbol{v}_r)\boldsymbol{v}_r + \boldsymbol{D}(\boldsymbol{v}_r)\boldsymbol{v}_r + G(\mathbf{R}_B^I)}_{\text{Feedforward Term}} \quad + \quad \underbrace{\mathbf{J}^T(q)\tilde{e}}_{\text{Feedback Term}} \tag{3.13}$$

Ideally, with the absence of external disturbances, the largest contributor to the control effort is the feedforward, or compensation, term, which is directly composed of the dynamic parameters of the vehicle computed at the reference velocity $\boldsymbol{v}_r$. Minimizing the compensation terms will minimize the actuator effort, and increasing the certainty in the dynamic parameters, and the precision and reliability of the vehicle sensors, will increase the stability of the vehicle under feedback control.

The significance of each term will be based on the desired performance profile of the μAUV. For instance, the penalty for carrying a larger body mass and consequently a larger volume may not be significant if the vehicle operates at low steady

state speeds. But if agile motion is desired, then the inertia effect becomes significant in comparison. This is a trivial trade-off, but it is useful as an approach in developing a framework for design optimization.

Table 3.1 summarizes the parameterized dynamic model terms and the associated design variables. The table provides a bird's eye view of the key design variables that affect the outcome of the design. In this work we will investigate the relationships between the design variables and model parameters and provide either an analytical or validated empirical techniques for mapping these relationships.

Table 3.1: Summary of Parameterized μAUV Model

Model Term	**Parametrized Function**
Inertia: $\boldsymbol{M}(\dot{\boldsymbol{v}})$	$f(m, g, I_o, \bar{V}, \bar{L})$
Coriolis: $\boldsymbol{C}(\boldsymbol{v})$	$f(m, g, I_o, \boldsymbol{v}) + f(\bar{m}, \bar{V}, \bar{L}, \rho, \boldsymbol{v})$
Damping: $\boldsymbol{D}(\boldsymbol{v})$	$f(\bar{L}, \bar{V}, \rho, Re, v, f_s)$
Restoring Forces: $\boldsymbol{G}$	$f(m, V, \vec{r}_{G/B})$
Thruster Matrix: $\boldsymbol{B}$	$f(\alpha, N, D, v_a, \rho)$
Thruster Speed: $\boldsymbol{\omega}$	$f(V_m, I_m, E_m, R_m, T_m, Q_m)$

Motor Design Variables	
I_m	Current Rating
E_m	Electromech. Power
R_m	Resistance
T_m	Operating Temperature
Q_m	Load
V_m	Supply Voltage
C	Battery Capacity

Design Variables	
m	Mass
g	Gravity
I_o	Tensor
$\boldsymbol{v}$	Velocity
V	Volume
Re	Reynold's Number
ρ	Fluid Density
$\vec{r}_{G/B}$	CoM to CoB vector
α	Propeller Blade Pitch
N	No. Propeller Blades
D	Propeller Diameter
v_a	Advance Velocity
$\bar{L}$	Surface Length
$\vec{r}_T$	Thruster Placement

3.3 Requirements, Specifications & Design Constraints

The basic functional requirements for μAUV design are summarized in Table 3.2. They form the qualitative list of design targets. The implementation environment

selected is a network of $6in$ PVC water pipes. The produced design architecture should also be scalable to $4in$ pipe diameter, a common size for water piping networks.

Table 3.2: Summary of Functional Requirements

Item	**Requirement**	**Primary Design Area**
1	Traverse through a complex pipe network with minimal collision	Control
2	Fit into a $6in$ pipe network	Electromechanical
3	Travel the range of a standard pipe network segment	Electromechanical
4	Navigate autonomously to a target and return to base	Perception / Mapping
5	The μAUV should be untethered	Electromechanical
6	The μAUV design should be manufactureable at low cost	Electromechanical
7	The μAUV should be rechargeable, preferably without breaking the seal	Electromechanical
8	The μAUV should be controllable at close proximity and should communicate data wirelessly	Electromechanical
9	The μAUV should be able to localize itself within the pipe	Perception / Mapping
10	The μAUV design architecture should be scalable to smaller pipe diameter targets	Electromechanical
11	The μAUV design architecture should be scalable to smaller pipe diameter targets	Electromechanical

Table 3.3 lists the key design specifications, which are quantitative measures of the μAUVdesign. While this work does not intend to produce a final industrial grade design, this list of specifications should serve as a reference for benchmarking the μAUVfunctional performance. Numerous secondary design specifications exist, but are not the subject of this work.

Table 3.3: Summary of Primary Design Specifications

Item	Primary Specification	Units
1	Travel Range	m
2	Nominal Travel Speed	m/s
3	Maximum Speed	m/s
4	Axial Positional Tracking Error	$\pm m$
5	Radial Positional Tracking Error	$\langle \pm r\,,\, \pm \beta \rangle$
6	Attitude Tracking Error	$\langle \pm rad,\, \pm rad,\, \pm rad \rangle$
7	Mechanical Seal Strength / Operating Depth	mH_2O
8	Impact Strength	m/s^2
9	Volumetric Geometry	$\langle L_x\,,\, L_y\,,\, L_z \rangle$
10	Total Mass	kg
11	Mass Distribution	$\langle kg\,m^2,\, kg\,m^2,\, kg\,m^2 \rangle$
12	Manual Control In-Water Range	m
13	Data Transmission Rate	bps
14	Data Transmission In-Water Range	m
15	Maximum Current Draw	A
16	Idle Current Draw	A

A number of constraints limit the possible range of geometries and architectural configurations. The constraints can be divided into geometrical constraints and parts availability constraints. Geometrical constraints include limitations on battery dimensions, motor dimensions or vehicle total volume. Parts availability constraints are specific tp each design case. For our design realization, for instance, the choice of battery geometrical form, or motor geometry and characteristics are limited. The design constraints are summarized in Table 3.4

Table 3.4: Summary of Design Constraints

Item	**Constraint**	**Unit**	**Type**
1	Electronics Dimensions	$\langle L, W, D \rangle : \langle m, m, m \rangle$	Geometric
2	Battery Mass	kg	Geometric
3	Battery Dimensions	$\langle L, W, D \rangle : \langle m, m, m \rangle$	Parts Availablity
4	Battery Capacity	mAh	Geometric / Parts Availablity
5	Battery Nominal Voltage	$Volts$	Parts Availability
6	Battery Current Draw	A	Parts Availability
7	Motor Dimensions	$\langle r, l \rangle : \langle m, m \rangle$	Parts Availability
8	Motor Characteristics	$\langle w, Q, I \rangle$	Parts Availability
9	Optics Dimensions	$\langle m, m, m \rangle$	Geometric
10	Vehicle Maximum Dimensions	$\langle m, m, m \rangle$	Geometric

3.4 Design Methodology

Another goal of this research is to assess the feasibility of designing such system, another goal is to present a practical and validated design method for improving the existing design and developing similar scale underwater vehicles in general. This section also gives an overview of the structure for the remainder of the thesis.

The design methodology is presented in Figure 3.2. An exploratory design prototype is first developed to serve as a learning tool and a preliminary feasibility validation test, for both the prototyping methods and the platform itself. This step provides invaluable insight for the design steps that follow. Next, and with insight from the exploratory design, the vehicle model and its parameterized relationship, a nominal design is then conceived and prototyped.
A key step in the design process to identify the model parameters and solving the mapping relationship between the design variables and the parameterized model.

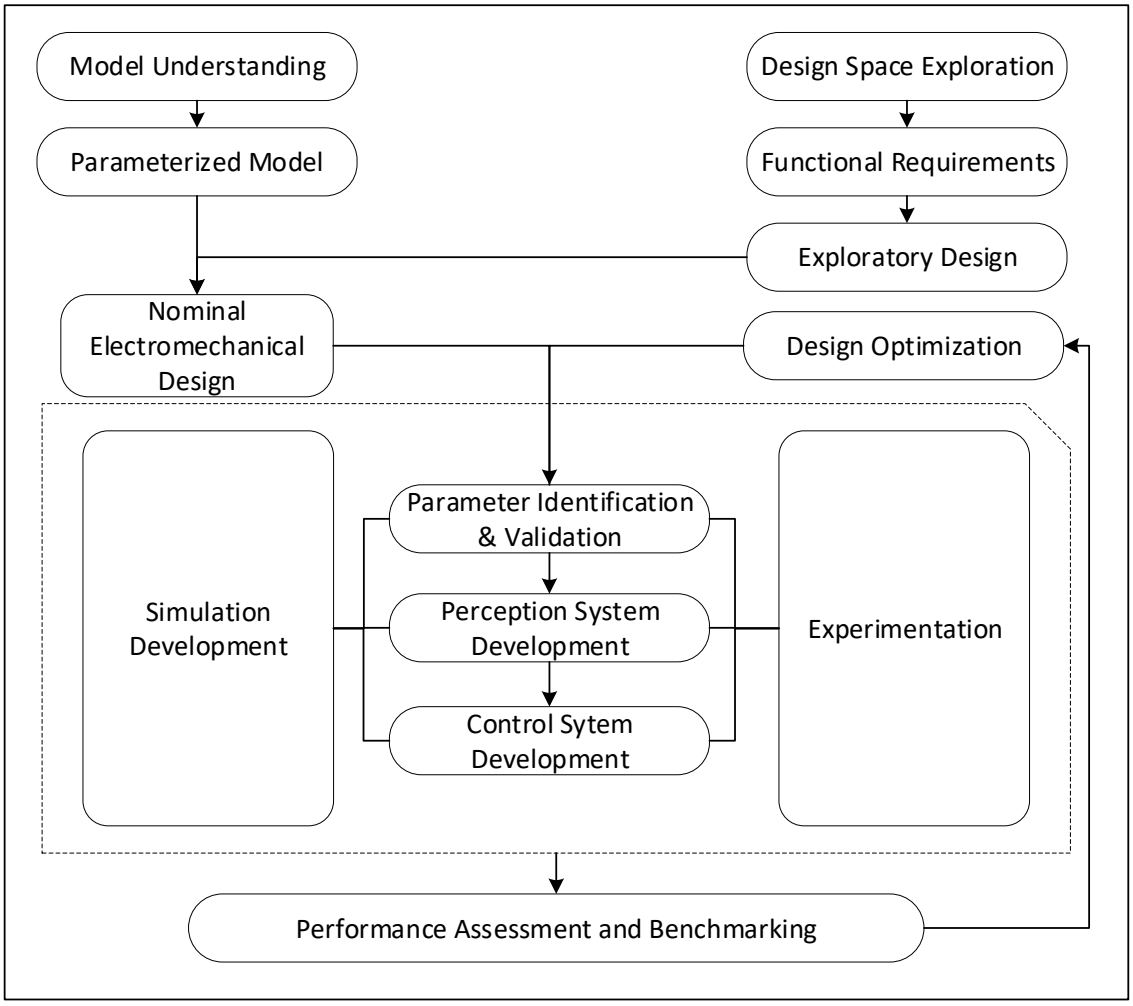

Figure 3.2: Mechatronic Design Process

While some of the model parameters are derived through analytical methods, others, like the hydrodynamic drag and thruster characteristics, rely on empirical methods to accurately produce them. We use a computational approach to derive these terms and conduct experiments to validate the results.

The validated dynamic model is then used to develop a comprehensive visual-dynamic simulation environment. The dynamic model serves as a powerful tool to develop a software in the loop controller that can be directly transferred onto the physical controller, behaving identically to its simulation counterpart. This is especially useful for underwater vehicles where the cost of access to the controller for reprogram-

ming and tuning is high. Output from the simulation can then be used to benchmark and test the performance of the vehicle against desired design specifications.

With the realized nominal design and its architecture, the parameter identification tools, and the simulation environment, a complete set of tools and methods shall be available for producing and optimizing the μAUVand other underwater vehicles of similar architecture.

In reality, actual design and prototyping activities were carried out in a more parallel manner than outline here. Available tools, fabrication methods, and mechatronic technologies change and present new opportunities as the research progresses, but the methodological relationship between the design steps remain valid and are reflective of the proposed, and undertaken, mechatronic design process.

CHAPTER 4

ELECTROMECHANICAL DESIGN

This chapter documents the design architecture produced for the μAUVand presents a number of realized electromechanical designs. The first design is an exploratory design that helped understand practical challenges in constructing the μAUV. Following that, a general design architecture for the μAUVdesign is presented. A number of design considerations are discussed in that respect, and then a realized design based on the proposed architecture is produced, and termed a nominal design. The nominal design is used as the basis for further model analysis, simulation and controller development.

4.1 Exploratory Design

In order to understand the practical challenges of constructing a micro underwater vehicle μAUV, an exploratory design based on a prior concept was produced. The exploratory design is based on a design realized by [32], where a spheroidal shell was used with two internally placed impellers as shown on Figure 4.1. The impellers were driven by outboard motors, that were designed and fabricated in-house.

This specific design targeted a $4in$ pipe network. It was only capable of 3DOF motion, that is surge, yaw and roll. It had very limited space for additional internal components. This design was adopted and scaled to target $6in$ pipes, also giving more freedom in the choice of internal components and actuators, which can then be scaled down as matter of engineering realization.

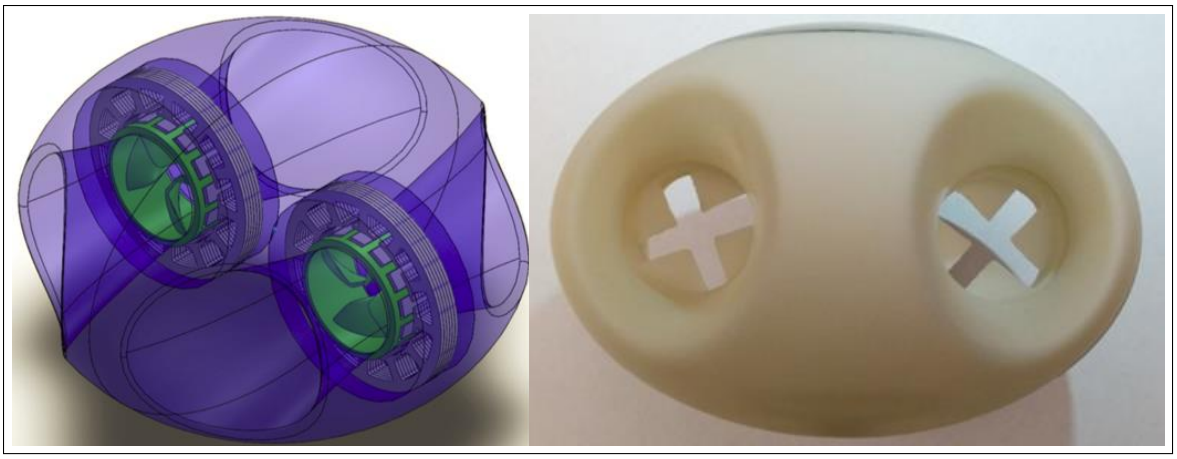

Figure 4.1: Prior Design of a 3DOF μAUVwith Outboard Motors [32]

Two variations of the exploratory design are shown on Figures 4.2 and 4.3. The spheroidal shape and impeller channel profiles in this design concept were chosen with the goal of conceptually minimizing hydrodynamic drag. In design revision A, a complex form of an optical port was intended, one that preserves the spheroidal surface continuity, but manufacturing techniques were not conveniently available to produce an optically clear version, so in revision B the port was segmented into three flat sections.

Internally, a lip-seal was used over the impeller in revision A, but with the lip-seal it was not possible to have both a proper seal and friction resistance that is low enough for the propellers to rotate. In revision B, the drive system included an additional gear was added with a low diameter shaft passing through a precision journal bearing. The journal bearing serves as the rotating seal interface. Further engineering details of the exploratory design are included in appendix A

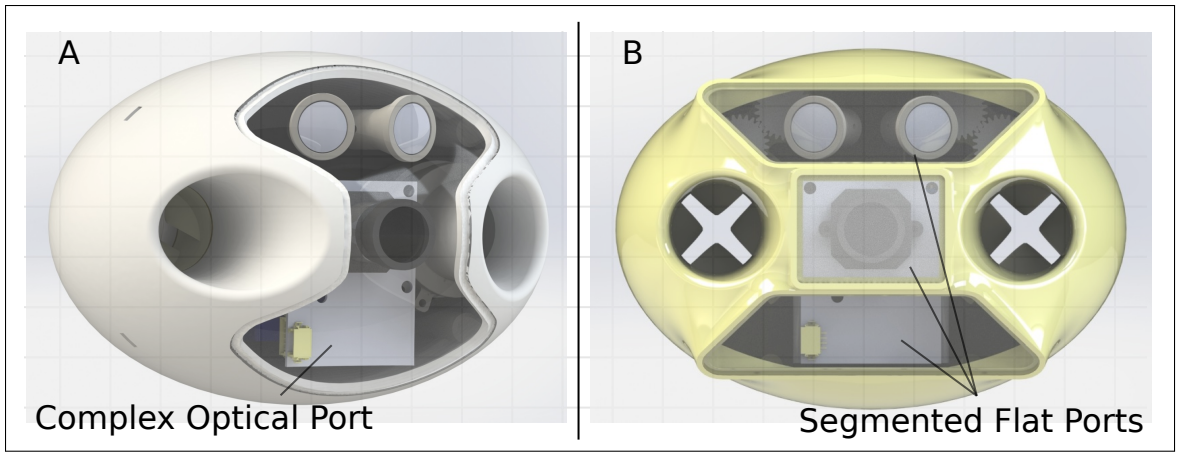

Figure 4.2: Exploratory Design Realizations - External View

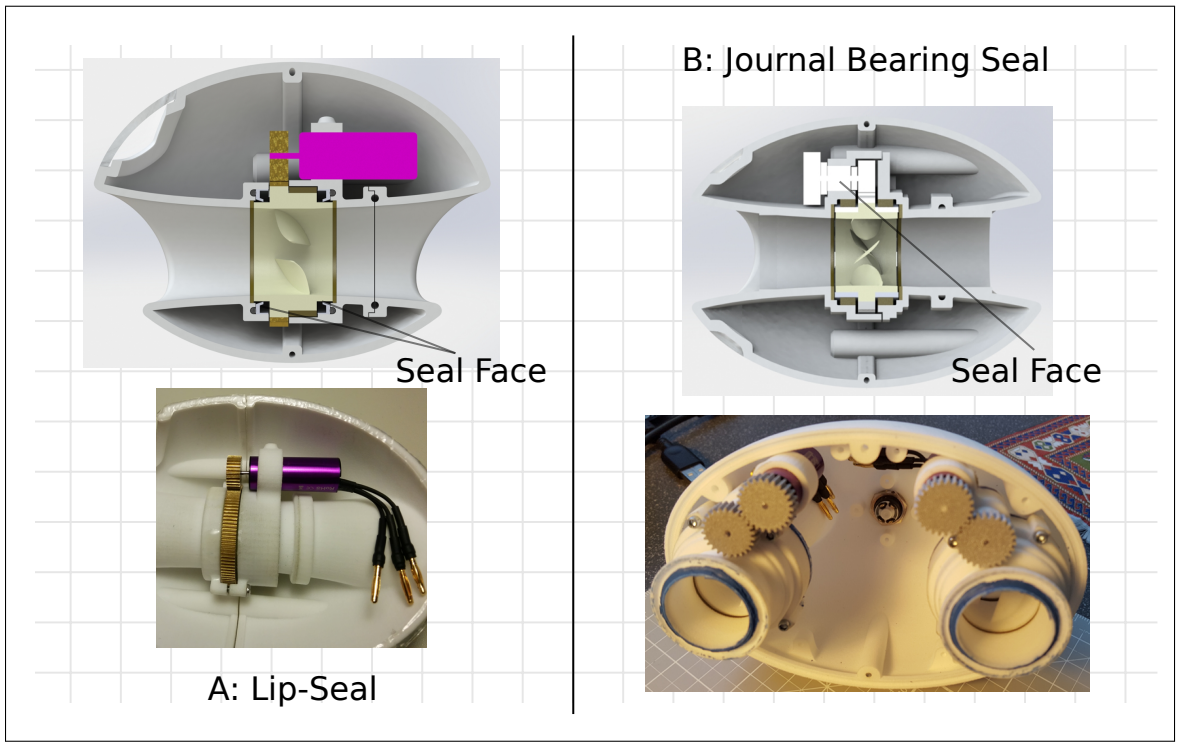

Figure 4.3: Exploratory Design Realizations - Internal View

This design architecture proved to be inefficient for a number of reasons.

1. A significant portion of the motor power is lost due to the in-efficiencies in the gearbox setup
2. There are 5 temporary seal faces in this design, making the sealing solution challenging and highly sensitive to errors in the dimensions of the seals and

shell structure.

3. The cooling ability is limited for internally installed motors.
4. The design included internally moving parts
5. The internal drive system significantly constrains the shape of the shell and μAUV in general.

The experience and insights gained from experimenting with this design concept have been invaluable toward further design and development.

4.2 μAUV Design Architecture

The primary μAUV design architecture adopted in this work, presents a simplified structure compared to the exploratory design concept. The architecture focused on ease of fabrication and assembly, allowing for rapid design variations and optimizations. The design architecture is composed of two modular components, a shell and a propulsion system.

The shell can be separately optimized in its shape and volume, without significantly affecting the propulsion system design and vice versa. In the following sections, the concept layout for this architecture will be illustrated and each of the major subsystems will be discussed. A design realization based on this architecture is produced and termed a nominal design. It is nominal in the sense that it forms a basis for further design analysis and optimization.

4.2.1 Design Variables

In the set of design variables presented in table 3.1 subject to the design constraints listed in table 3.4, we will focus only on a subset of design variables, namely the surface geometry $\bar{L}$, volume V, thruster impeller profile $\langle \alpha, N, D \rangle$, thruster allocation $\vec{r}_T$, center of buoyancy placement $\vec{r}_{B/G}$ and battery capacity C_{bat}.

The primary relationship between this subset of design variables and model parameters is shown on Figure 4.4. Note that the figure only highlights the primary relationship, the design variables are coupled and have secondary influence on the model parameters.

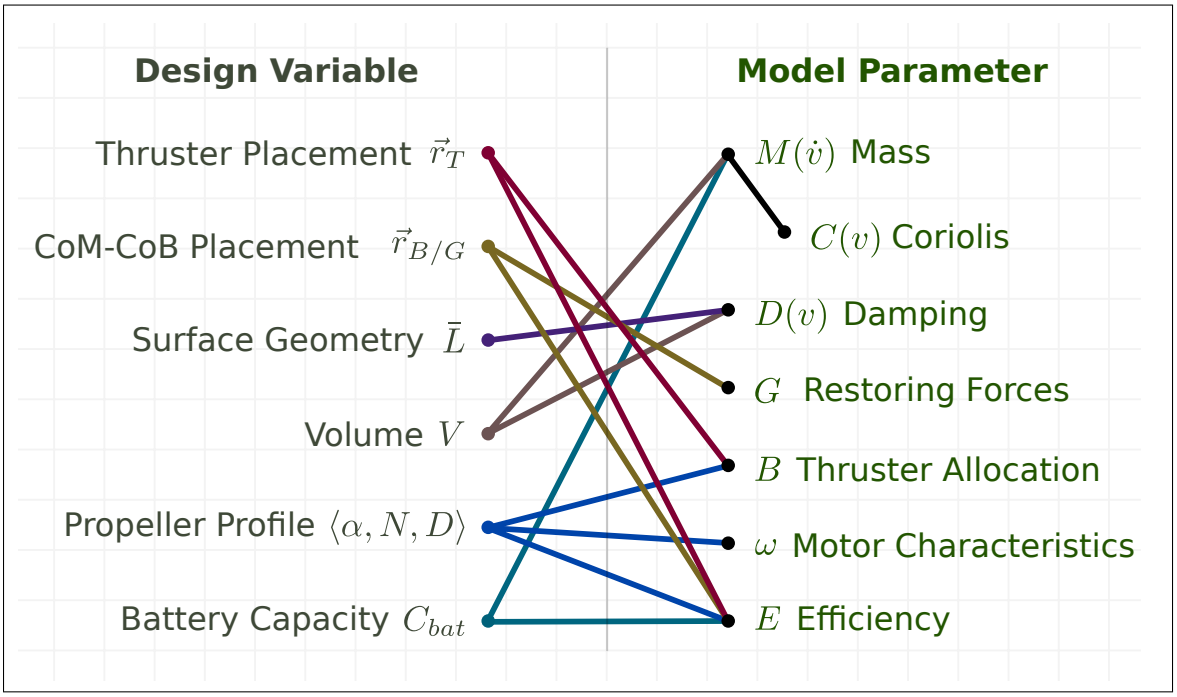

Figure 4.4: Design Variables to Model Parameter Direct Relationship: Subset Investigated

4.2.2 Concept Layout

The μAUV drive system is based on that of an aerial multi-rotor vehicle where the thrusters are placed normal to a common plane and distributed evenly with a distance $\vec{r}_T$ from a center. The thruster attachment is connected to a shell which houses the battery, electronics, optics and counterweight, or ballasts. The drive system is rigidly connected to the shell via a single fastner in addition to the motor wirings. Placing the motors outside the shell and exposed to the water allows them to be passively cooled in water, significantly increasing their continuous power output limits [33][34] [35]. Figure 4.5 outlines the concept generation process for the

system architecture.

In step A, selected electromechanical components are placed within a sphere defining the geometric constraint of the vehicle's maximum volume, this volume corresponds to the internal diameter of the target pipe, then the shell and drive system areas are outlined then defined.

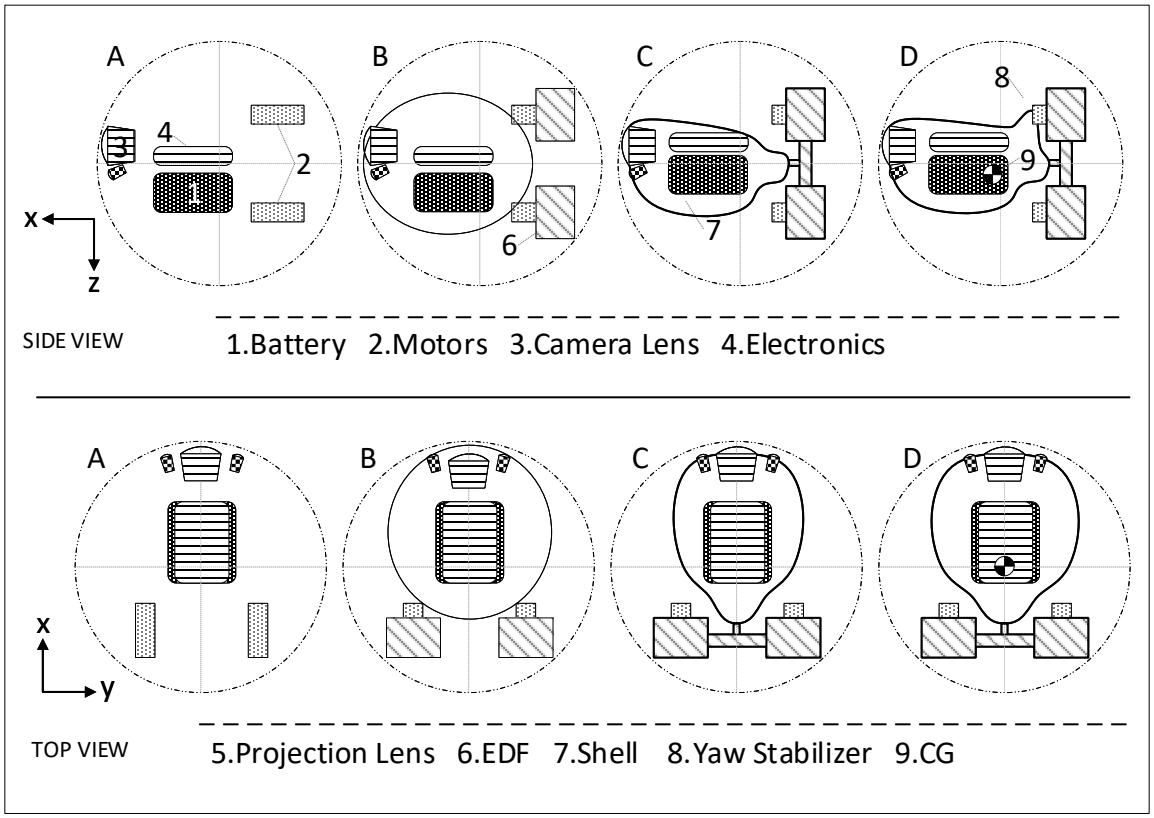

Figure 4.5: Nominal Design Architecture - Conceptualization

4.2.3 Shell Design

If it is desired to have a neutrally buoyant vehicle, which is required in this arrangement, otherwise it would require continuous control action to control the depth and static positioning will not be possible in the absence of sway and heave action, then the volume of the vehicle will directly define the mass of the vehicle. The minimum theoretical shell volume is the sum of the volume of the internal components

in addition the ballast, or air, volume required to attain neutral buoyancy. If the CoM and the CoB are desired to be in a specific location and relation to one another, then that would introduce another constraint on the geometry, and the same follows for the placement of internal components such as the optics and vision system, or the placement of the propulsion system.

Figure 4.6 conceptualizes the relationship between the volume, mass and hydrodynamic drag when designing the shell. Starting out at the theoretically minimal shell volume, the surface geometry will exhibit a high level of complexity, which introduces increased hydrodynamic drag that is magnified exponentially at higher motion velocities. As the volume increases relative to the internal components, there is more freedom to shape the surface to attain efficient hydrodynamic profiles; however, the increase in the nominal cross sectional area will continue to increase the hydrodynamic damping effect.

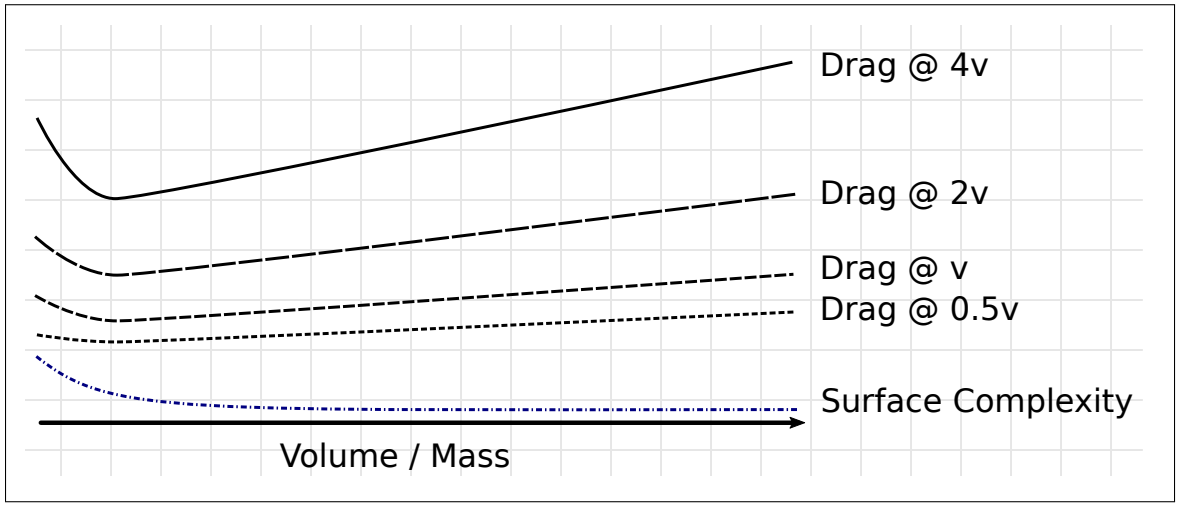

Figure 4.6: Shell Design Variables Conceptual Relationships

It is desired to minimize drag in the surge direction primarily; however, the vehicle will also experience motion in other directions and the proportion of different trajectory types performed by the vehicle, is influenced by the piping network structure, the controller and environmental disturbances. Ideally, the shape should be

optimized based on the expected motion trajectories. For now, and for the nominal design, the shell is made spheroidal with the longest axis along the surge direction. The highest hydrodynamic drag is expected to be in the heave direction, while the highest rotational drag in the roll direction, the roll position is not important in following a motion trajectory, unless it is required to orient perception sensors for instance. Later analysis in Chapter 5 will explore the differences in the hydrodynamic drag for each motion direction, both in open water and inside the pipe.

Agility is also required for navigating sharp corners and performing trajectory tracking corrections, the rotational drag is expected to be significantly lower than translational drag, but the propulsion system will also have reduced ability to generate torque, since the moment arm for pitch and yaw is small and the torque generated by the propellers for roll is also small. A yaw and roll stabilizer is added to our nominal design to evaluate its benefit. The vehicle is designed to be symmetric across the xz-plane.

4.2.4 Propulsion System Design

The propulsion potential significantly governs the realizability of the design intent. The choice of motors available for the scale of the μAUV are extremely limited, and there is room for a larger, and hence more powerful and even efficient motor within the geometrical constraint, if such one exists or is manufactured; however, we are still able to produce a realizable design with choice at hand.

A ducted propeller powered thruster was selected as the choice of thruster type. There are other possible choices, including jet propulsion [36], bio-inspired propulsion [23], or even an air propulsion [37]. The latter two do not offer an efficient form of energy conversion, but a jet propulsion system may be a viable candidate; however, it would require a larger longitudinal space to accommodate and it would

require a complex duct system to provide bidirectional thrust. We chose a direct drive ducted thruster as it offers a more compact and more efficient energy conversion, it also allows for maintaining the modularity of the drive system from the shell, and unlike a jet propulsion system, it would allow for bidirectional propulsion with the right propeller design only.

The propeller ducts provide an augmented thrust component, specifically at lower vehicle speeds [36]. More importantly, the ducts serve to protect the propellers when operating in a confined space.

Figure ?? illustrates the placement of the thrusters. Ideally, the thrusters' center axis should pass through the vehicles CoM , along the surge principal axis, achieving passive stability at full throttle forward surge motion and requiring symmetric thrust action for attitude control.

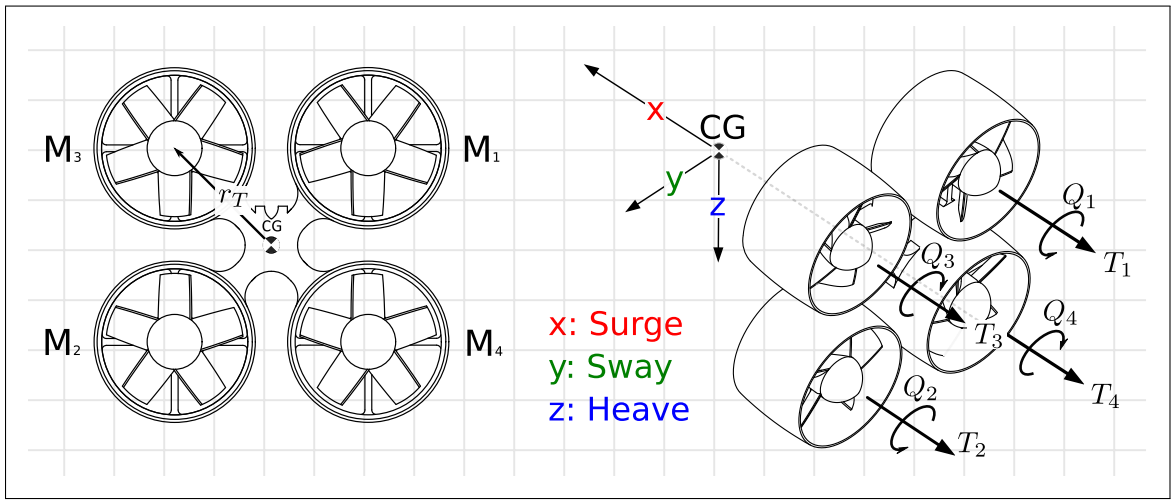

Figure 4.7: Thruster Assembly

With this configuration, the thruster allocation matrix from 2.24 reduces to

$$\boldsymbol{\tau} \in \mathbb{R}^6 = \begin{bmatrix} 1 & 1 & 1 & 1 & 0 & 0 & 0 & 0 \\ 0 & 0 & 0 & 0 & 0 & 0 & 0 & 0 \\ 0 & 0 & 0 & 0 & 0 & 0 & 0 & 0 \\ 0 & 0 & 0 & 0 & 1 & 1 & -1 & -1 \\ -r_T & r_T & -r_T & r_T & 0 & 0 & 0 & 0 \\ -r_T & r_T & r_T & -r_T & 0 & 0 & 0 & 0 \end{bmatrix} \begin{bmatrix} \boldsymbol{f_T}(\boldsymbol{\omega}) \\ \boldsymbol{f_Q}(\boldsymbol{\omega}) \end{bmatrix}, \; f(\omega)_{T,Q}\,\omega \geq 0 \quad (4.1)$$

With the design setup given, the drive system can be scaled to within the geometric constraint, as illustrated on Figure 4.8, without modifying the shell, except for the ballast mass and CoM and CoB locations which will have to be adjusted.

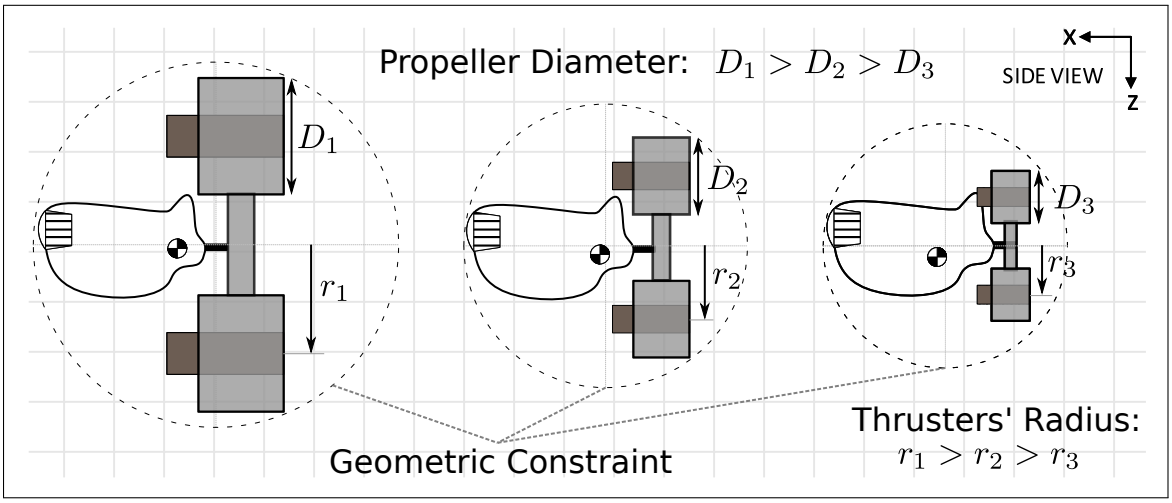

Figure 4.8: Scaling of Modular Thruster Drive Subassembly

With regards to the impeller design, a bi-directional impeller with a symmetric profile was conceptualized. A symmetric bi-directional impeller allows for bidirectional surge motion, as well as symmetric torque at zero translation velocity, for the full range of throttle. The symmetric thrust action is an assumption made under unobstructed open water conditions, more specifically under the assumption of symmetric water intake, around the thruster. In reality, the shell and motor placements will invalidate this assumption, and cause asymmetric thrust. This asymmetry can be identified and accounted for in the controller to produce symmetric bidirectional thrust mappings. Alternatively, the impeller profile will have to be made asymmetric to compensate for the flow obstruction effect, if it is necessary to maintain symmetric bi-directional thrust. Later analysis and optimization goals may suggest a highly asymmetric propeller, if for instance, higher forward thrust is required.

The bidirectional impeller blade profile is presented on Figure 4.9. In Chapter 5 we will investigate the affect of different propeller geometries given this blade profile,

specifically the blade pitch angle α, blade diameter D and duct geometry, and characterize their performance both through a Computation Fluid Dynamic analysis and experimentation.

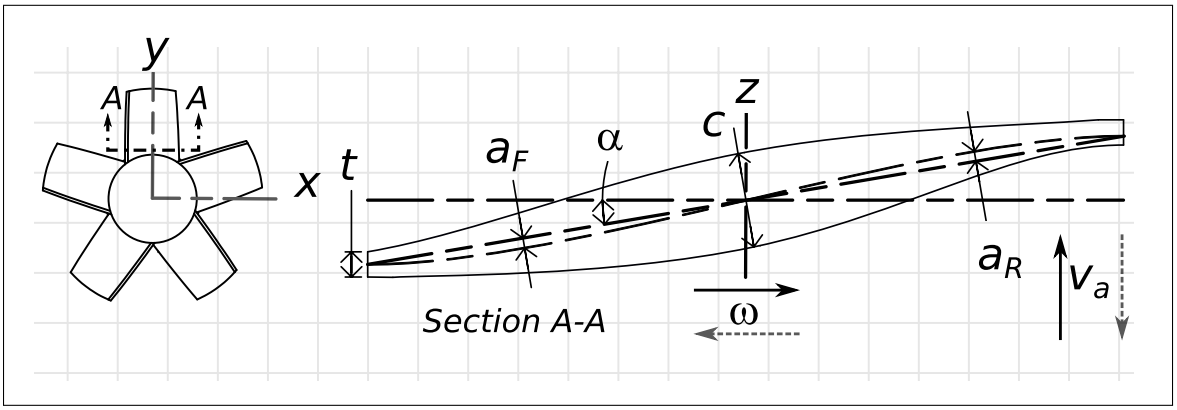

Figure 4.9: Impeller Blade Profile
With pitch angle α, tip width t, center width c, and forward and reverse angle of attacks a_F and a_R respectively

4.2.5 Center of Buoyancy

The μAUV is intended to be neutrally buoyant, this means the mass of the vehicle is equal to the mass of the water displaced by the μAUV. Recall equation 2.18 from Chapter 2, describing the restoring forces vector $\boldsymbol{G}({}^{I}\boldsymbol{R}_{B})$ for a neutrally buoyant vehicle. The CoB location with respect to the CoM affects the angular motion of the vehicle, and defines an explicit static equilibrium attitude in $SO(3)$. One option is to make both centers coincident, reducing the restoring forces vector to zero, another is to place them such that a controlled behavior is produced. For instance, placing the centers in the $xz - plane$ and apart by a distance $\vec{r}_{B/G}$ to introduce a controlled resistance to pitch and roll while the vehicle is moving horizontally. Alternatively, angular motion stability can also be achieved through control surfaces as well, such as a fixed rudder.

4.3 Perception & Optics

In order to navigate its enclosed surrounding the μAUV must have a capable perception system. The choice of systems include vision based, ultrasonic based perception or proximity sensing systems. Infrared sensors are not suitable for underwater use as they do not penetrate far enough. Ultraviolet proximity sensor can in theory perform much better than Infrared but they are not manufactured, the same would extend to LIDAR type sensors. Figure 4.10 shows the degree at which different light waves are absorbed underwater. Note how the $400 - 500nm$ wavelength range is the least absorbed wavelength. This corresponds to the range of blue to violet light.

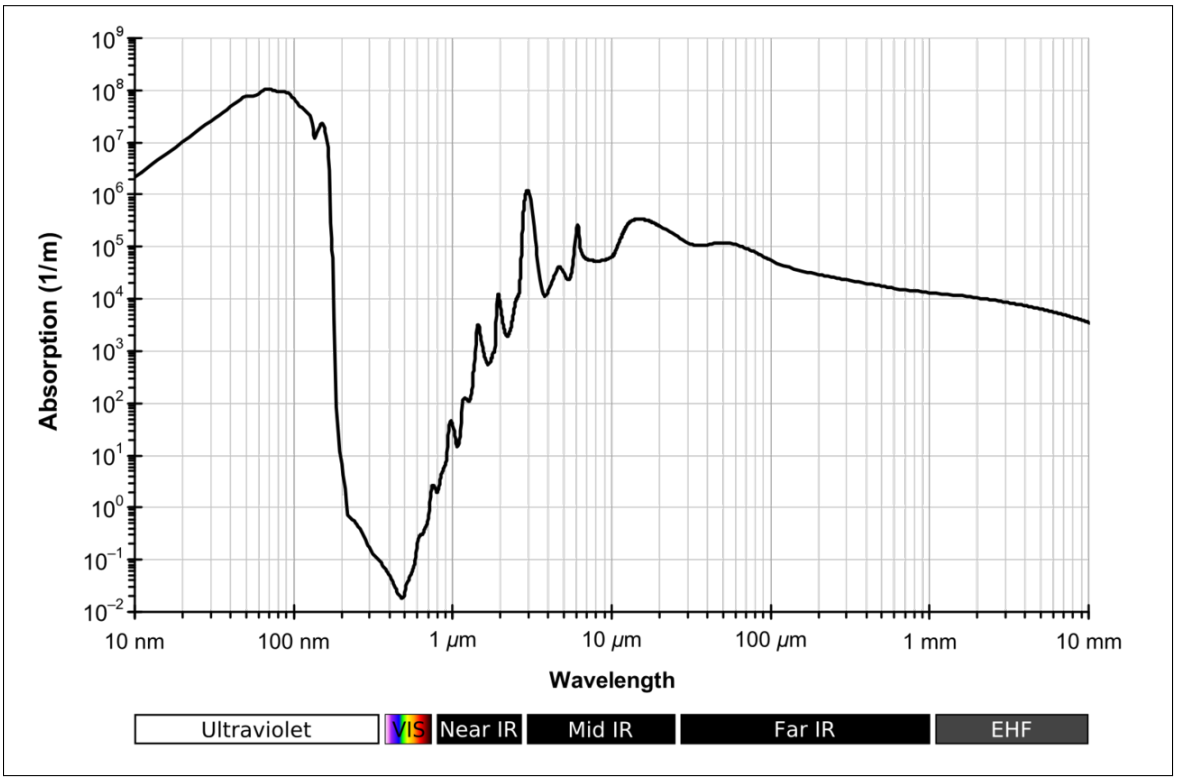

Figure 4.10: Liquid Water Absorption Spectrum [38]

Ultrasonics are a viable option for proximity sensing as well, and are an option worth evaluating for our application given the recent availability of surface mounted

ultrasonic transducers, allowing for ultrasonic sensing at the form factor and scale of our μAUV, and would also allow for placement of multiple ultrasonic sensors around the vehicle for a high degree of percept-ability.

Vision based perception methods on the other hand are, through computer-vision algorithms, a flexible option for navigating in confined spaces. The absence of light however, in underwater environments and in confined spaces particularly, renders vision-based methods useless unless the system is equipped with a projected light source. The form of the light source can be also designed to take a specific pattern. Knowledge of the form and projection geometry can not only help the vision system detect obstacles but can also perform pose estimation, where the position and attitude with respect to fixed objects can be estimated. In Chapter 8 we propose a method for pose estimation within confined spaces using structured light projection.

To design a projected light system for the scale of our μAUV, a basic understanding of optics and light collimation may be required. This is outside the scope of this work, but suffice to say that with the an appropriate collimation setup, a simple conic or even perfect cylindrical projection, where the target light is focused at infinity, can be produced from a small single LED light source, in a compact package as shown on Figure 4.11.

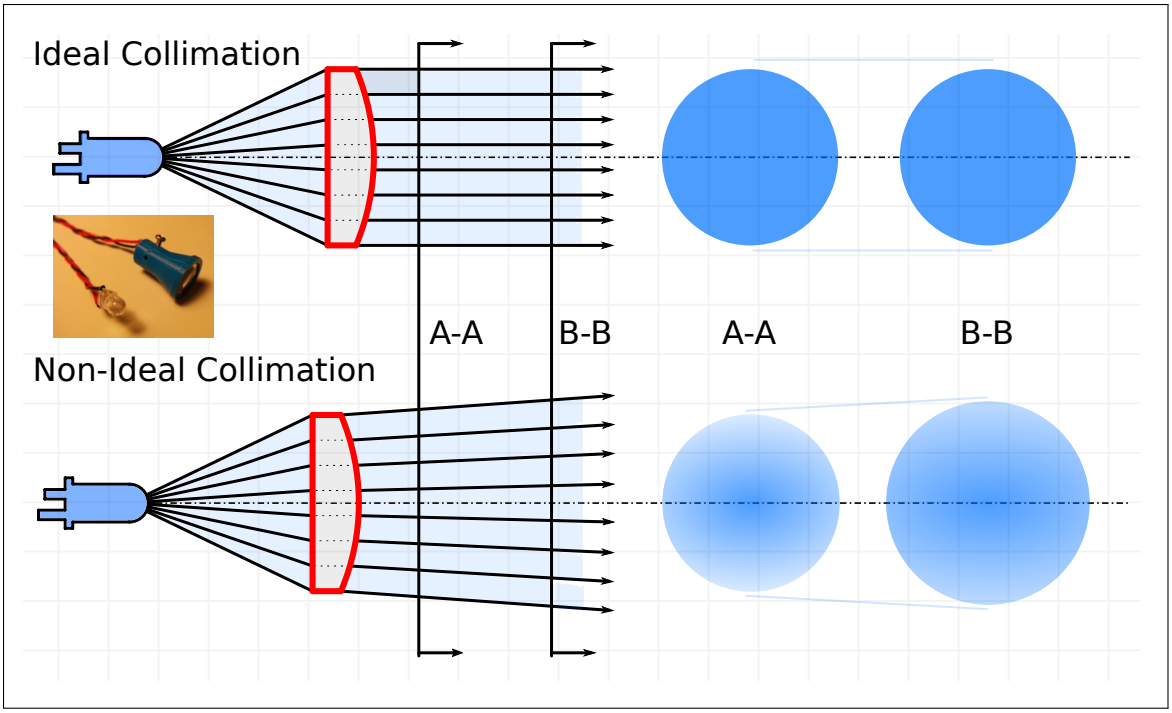

Figure 4.11: Ideal vs Non-Ideal Light Collimation

Ideal Collimation, where the focal point of the light source is coincident with the focal point of a bi-convex lens and is perpendicular to it, results in a cylindrical light projection pattern. With a non-Ideal Collimation where the focal points of the source and lens don't coincide, the resulting projection is a cone shaped light pattern. In both cases, a pattern with a crisp boundary and even brightness can be produced. A comparison between a collimated and uncollimated light is shown on Figure 4.12. From a collimated light additional optical layers can be added to form specific light patterns as shown on Figure 4.13.

Structured light projection is a robust technique used in object tracking [39] , 3D scanning of objects [40], as well as navigation [41]. Patterned light projections, while they can allow for robust and faster perception algorithms, have the disadvantage of obstructing much of the light source compared to simple conic or cylindrical light forms [42].

The vision system camera can be equipped with a filter to match the projected

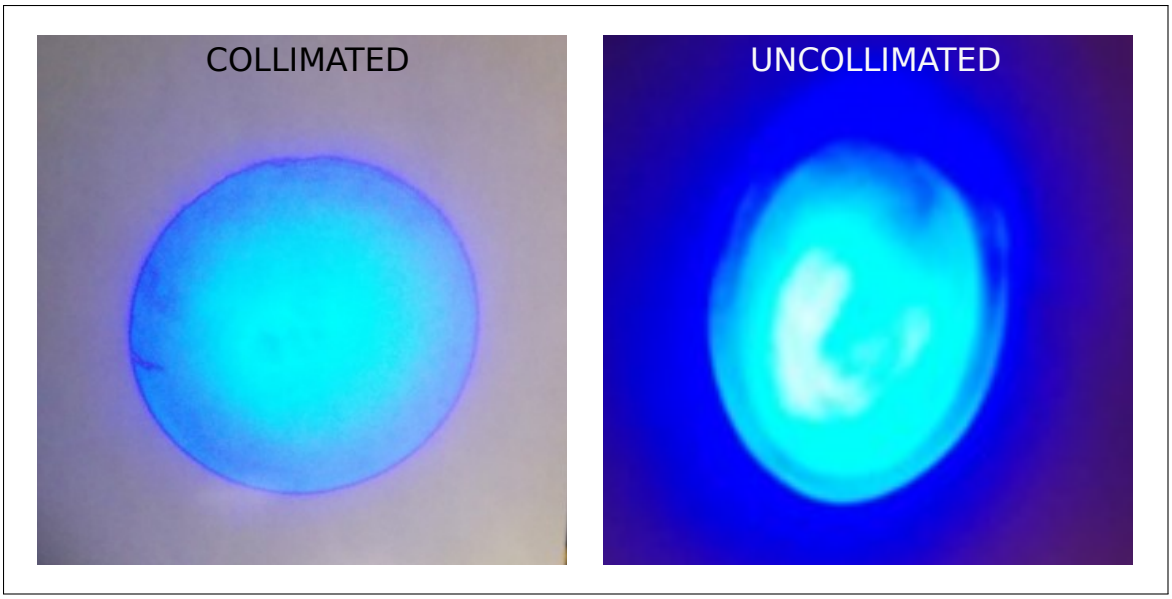

Figure 4.12: Collimated vs. Uncollimated Light

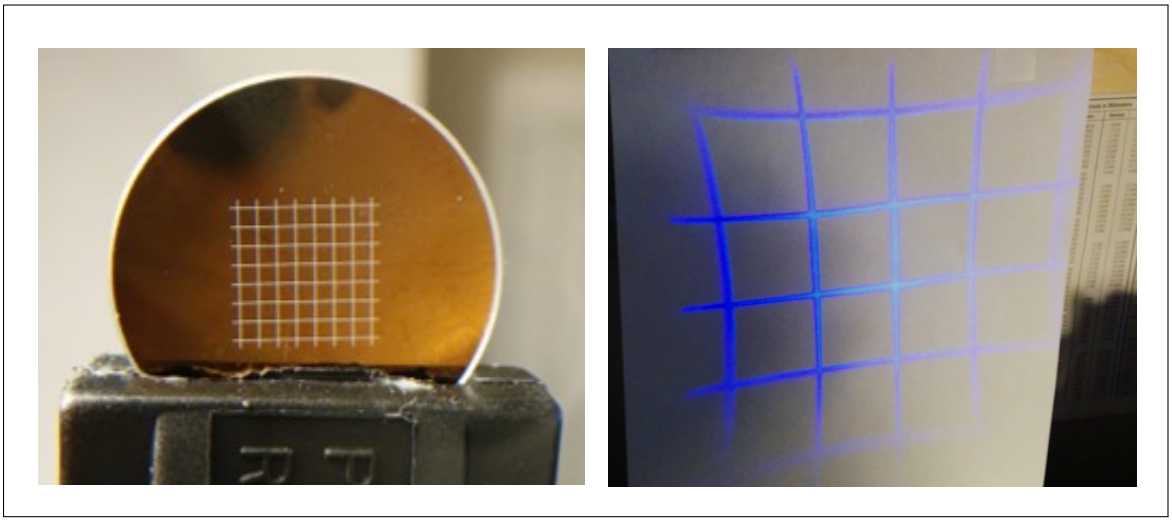

Figure 4.13: Structured Light Grid Pattern

light wavelength, this will reduce any noise generated by other light sources of different wavelengths. It would also allow for the camera to binarize the image faster, reducing the steps necessary to perform the vision algorithms. The fish-eye lens is advantageous in confined spaces as it can capture a large portion of the immediate surrounding. Figure 4.14 below illustrates a suggested perception system configuration for the μAUV. The figure shows a camera equipped with a light filter and a

fisheye lens, and a structured light projection system composed at a minimum from a diffuser, a collimating lens and a light source.

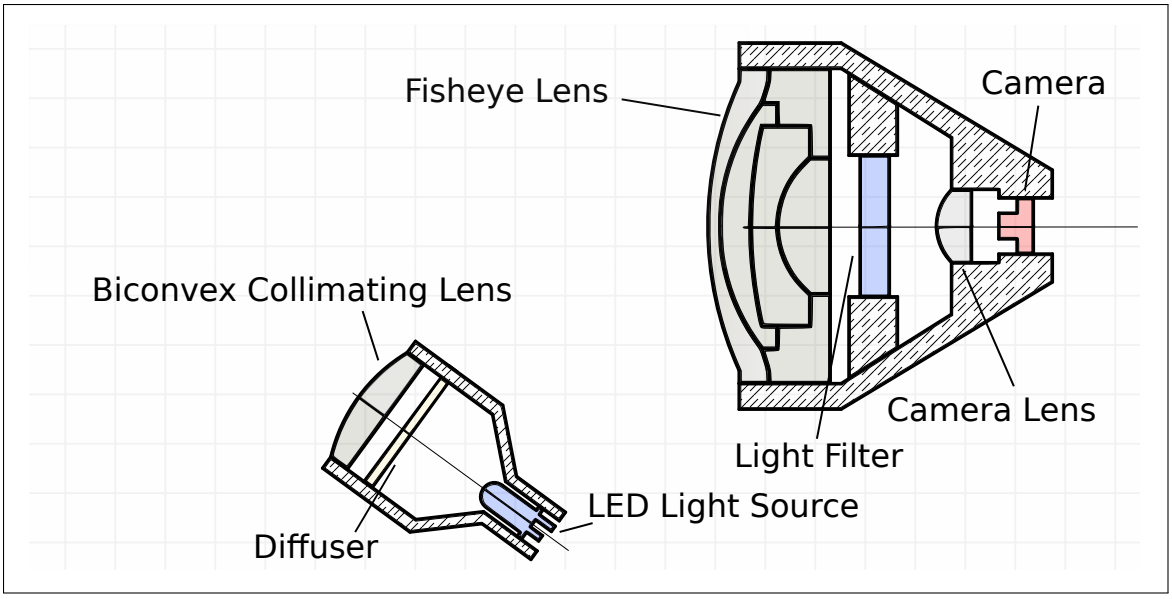

Figure 4.14: Perception System Components

View ports are used to provide an optically clear window for underwater optics; however, they introduce additional light refraction that distorts the projected light as well as the observed camera images. Refraction of light passing from the source through the optical lenses is magnified underwater [43], due to the the varying medium densities through which light passes. This problem is evident when using flat view ports. But it can be mitigated by instead using dome shaped viewports, where only perpendicular rays pass through the camera pinhole.

The dome would, however, introduce additional geometrical constraints in the design. Instead, a fisheye lens can be placed directly in contact with water, taking the function of the water sealing viewport, the function of reducing refraction and the function of a fisheye lens. The same is true for the collimating lens in the case of the projected light setup; the projected light lens can be placed in contact with water. This configuration will eliminate the need for dome ports. The disadvantages are that their design must be water tight and they will be prone to damage from

impact. These issues can be mitigated by design.

Pose estimation based on structured light will be discussed in Chapter 8.

4.4 Controllers and Electronics Architecture

The electronics and controllers that operate the μAUV are divided into several subsystems: Power, Propulsion, Autopilot, Perception and Communication. In this section we will review some design considerations that relate to each subsystem. These subsystems are highlighted on Figure 4.15.

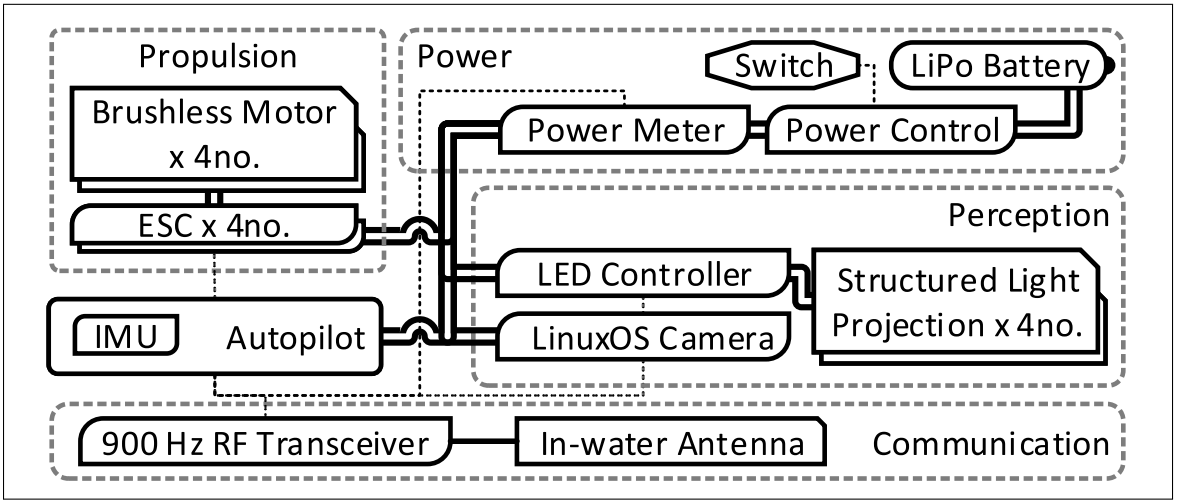

Figure 4.15: Mechatronic Architecture

4.4.1 Power

The vehicle can be powered via a rechargeable Lithium-Polymer, LiPo, battery. Other applicable types of batteries include Nickel based batteries such as Nickel Metal Hydride (NiMH), or other Lithium based batteries such as Lithium Iron Phosphate (LiFe) or Lithium-Ion (Li-ion). Lithium is the lightest metal, and provides the largest specific energy by weight. Lithium metal batteries are not manufactured due to their high instability, instead different mixes of Lithium ions based batteries are produced. They vary primarily in their cycle life, discharge rate, charge

rate and stability characteristics. LiPo batteries are less stable than some other batteries like LiFe batteries but they offer a higher specific energy and higher discharge rate. Proper sealing on the μAUV and connectors is critical in preventing severe damage by the battery [44].

Waterproof charging connectors or wireless charging can be added to reduce the need to break the vehicle's seal. While off-the-shelf LiPo batteries can be used, custom shaped batteries can also be acquired. And more promising, results have been reported success in the use of additive manufacturing to produce Lithium-Ion batteries [45], such advancements can help eliminate a major geometric constraint, which is the battery form, allowing for much more optimized μAUV design for the same power capacity.

4.4.2 Propulsion

The propulsion system requires dedicated programmable electronic speed controllers for each motor. For thruster applications, a sensorless BLDC motor is adequate for high speed motor control, since position control is not required. Sensorless BLDC motor control relies on measuring the zero-crossing of the phase currents of each of the three motor phases, to estimate the motor speed and direction, this method is reliable at high speeds only. With the μAUV propellers are expected to rotate at high speeds to produce effective thrust. Further discussion on motor and thruster characteristics will be presented in Chapter 5.

4.4.3 Autopilot

Miniature embedded controller with accurate inertial measurement sensors have become widely available. Their development was spurred primarily by the developments in micro aerial vehicles, including multi-rotor racing platforms. It is a standard expectation to have a small form autopilot equipped with an accelerometer,

gyroscope and a magnetometer, forming the sensor suite required to attain 6 degree of freedom (DOF) attitude and heading with tilt compensation, provided that appropriate attitude estimation algorithms are implemented. Such controller can also be equipped with barometers, this can be used to measure the vehicle's depth in water if they are exposed to the water surface. It is more practical, however, to use a stand-alone pressure sensor that can be practically integrated on the μAUV.

4.4.4 Perception

Embedded camera technologies are evolving rapidly. A small form factor camera running on top of a Linux operating system with GPU capabilities can be acquired at low cost. This field is expected to develop further, expanding the possible vision capabilities for μAUV at the intended scale, or even smaller. The structured light projection system would require a dedicated driver.

4.4.5 Communication

The communication system at a minimum should allow for manual control and command of the vehicle at near field, and for tracking the state as well as allow for basic tuning of controller parameters of the μAUV. The key design consideration of underwater communication systems is the signal range, especially when using radio wave frequencies as the signal carrier. Ultrasonic, or acoustic transmission, is the favored signal medium in underwater applications, since sound waves can travel much further in water than EM waves; however, they require a sizable setup to deliver signals of meaningful strength and are limited in their communication bandwidth [46].

Standard radio frequencies at the lower frequency end, such as UHF frequencies, can be applied for short range underwater communication ($< 2m$), provided the signal doesn't transverse across different mediums, meaning the air-water surface,

as this is where a significant amount of signal strength is lost. This condition can mitigated slightly by exposing both ends of the communication bridge antennas to the water directly [47]. The conductivity of water is a primary factor in the absorption rate of EM waves as well [48]. Embedded communication devices for standard radio frequencies are readily available. A combined acoustic and standard radio frequency communication system, if devised, can provide an ideal mix of short range high bandwidth communication through standard radio frequencies and far range critical communication through an acoustic bridge.

4.5 Design Realization

The first revision of the μAUVdesigned based on the proposed architecture is shown on Figure 4.16. The engineering details of the design are highlighted in B, as well as fabrication details. Further parameter estimation analysis, simulation and control were based on this design.

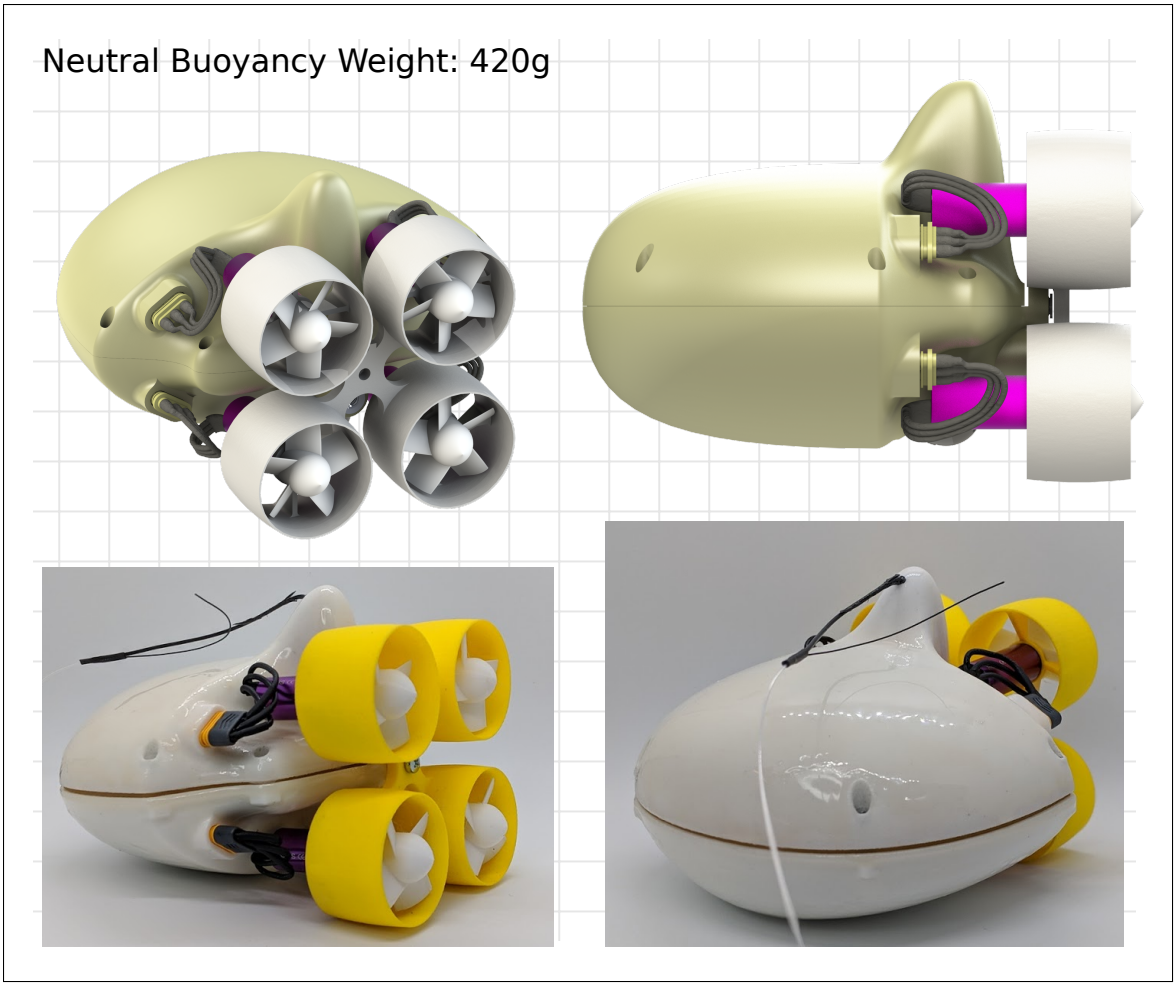

Figure 4.16: Realized Design - Revision 1

A revision of the prototype with a revised shell design is shown on Figure 4.17. Engineering details of this design are highlighted in Appendix C. We will discover that relaxing the assumption regarding the smoothness of the surface geometry with the intention to reduce drag, actually produces more efficient design, especially for attaining higher levels of agility in the confined space. We will also present a method for controlling buoyancy and $\vec{r}_{B/G}$, and even surface geometry with an external Urethane based rubber sleeve.

In Chapter 5 we will analysis the model parameters and in Chapter 7 we will analyze the performance of the design and justify the changes made in revision 2.

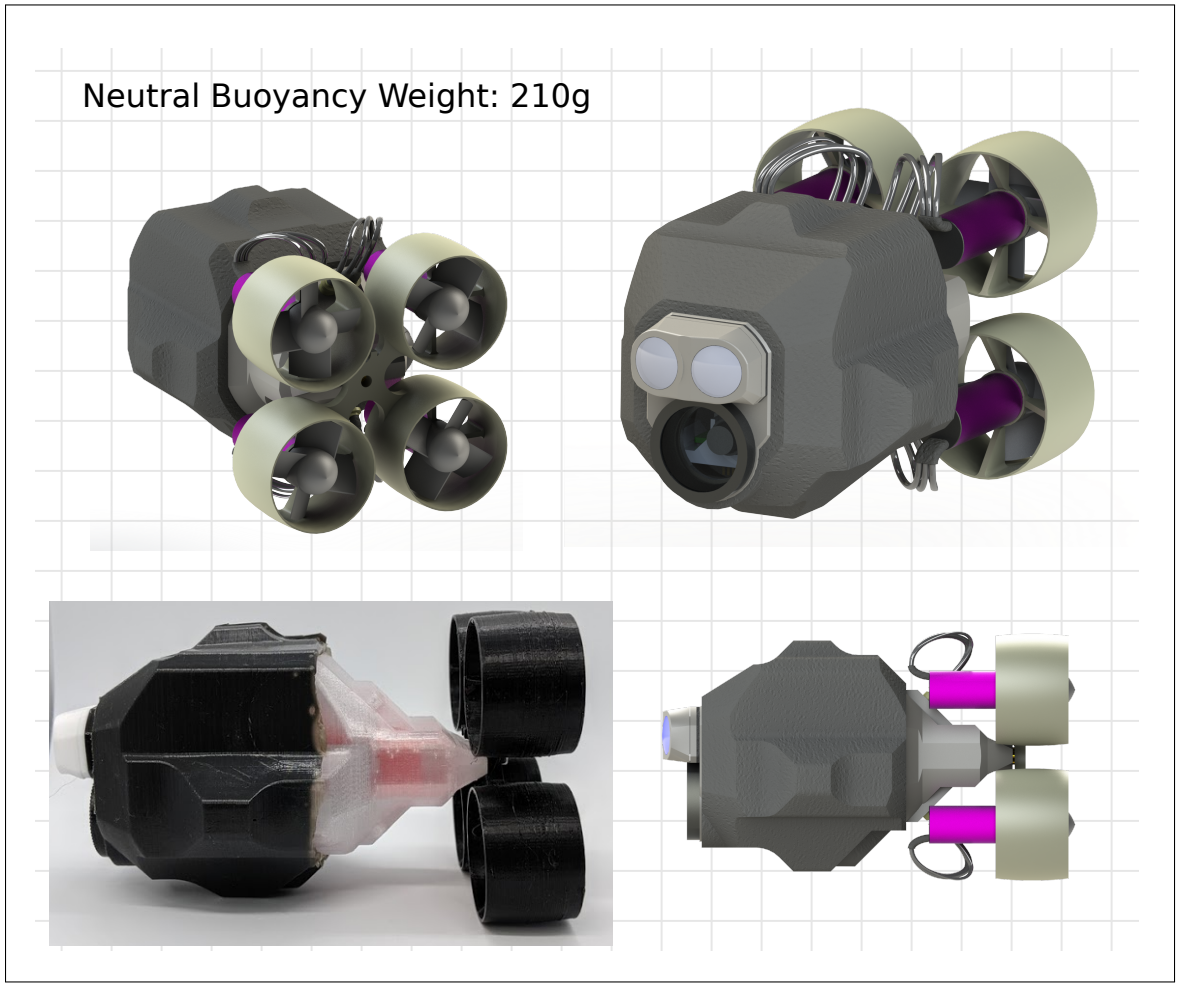

Figure 4.17: Realized Design - Revision 2

CHAPTER 5

PARAMETER IDENTIFICATION

This chapter investigates vehicle model parameters. The parameter identification will be based on the design presented in Chapter 4. However, the parameter identification methods utilized here can be applied to other μAUV designs.

The inertia and coriolis-centripetal terms will be briefly discussed then a detailed analysis of the hydrodynamic forces will be presented along with experimental validation results, followed by a detailed analysis of the thruster dynamics in addition to experimental validation results as well.

Recall that the underwater vehicle's dynamic model is

$$\tilde{\boldsymbol{M}}(\dot{\boldsymbol{v}}) + \tilde{\boldsymbol{C}}(\boldsymbol{v}) + \boldsymbol{D}(\boldsymbol{v}) + \boldsymbol{G}({}^{I}\boldsymbol{R}_{B}) = \boldsymbol{\tau} \in \mathbb{R}^{6\times 6}, \quad \forall \boldsymbol{v} \in \mathbb{R}^{6} \tag{5.1}$$

Achieving accurate parameters for the above model is critical for simulating the vehicle motion, to both assess its performance and develop suitable and realistic controllers, specifically for model-based control algorithms, as will be discussed in Chapter 9. As such, a thorough examination of the model parameters and how we can estimate them, is warranted.

5.1 Inertia and Added Mass

The added mass term is composed of a rigid body term M_{RB} and an added mass term M_A. The rigid body mass matrix elements, the mass and tensor matrix, are computed directly from the detailed CAD model. Computing the value of the added mass matrix elements, however, is not trivial. Brennan [49] describes the added mass phenomenon as that which "determines the necessary work done to change

the kinetic energy associated with the motion of the fluid". The added mass matrix is symmetric if the system is to be conservative. The number of distinct coefficients of the added mass matrix are 21, and any further reductions in the number of added mass matrix coefficients will be based on geometrical symmetry of the vehicle. A typical analytical method to derive the added mass terms is by applying the concept of fluid kinetic energy [29]. The kinetic energy can be presented as

$$T = \frac{1}{2}\boldsymbol{v}^T \boldsymbol{M}_A \boldsymbol{v}, \;\; \boldsymbol{v}^T = [v_x \, v_y \, v_z \, v_\phi \, v_\theta \, v_\psi], \;\; \boldsymbol{M}_A \in \mathbb{R}^{6\times 6} = \boldsymbol{M}_A^T > \boldsymbol{0} \tag{5.2}$$

The added mass coefficients can be derived using Kirchoff's equations to relate the force/moment elements $\boldsymbol{\tau}$ to acceleration $\dot{\boldsymbol{v}}$. For this work it is assumed that the vehicle exhibits an ideal spheroidal shape in open water. With this assumption, the added mass matrix can be assumed diagonal. Fossen [29], provides an expression for the added mass term for a spheroidal shape. For a diagonal added mass matrix

$$\boldsymbol{M}_A = -diag(X_{\dot{v}_x}, Y_{\dot{v}_y}, Z_{\dot{v}_z}, K_{\dot{v}_\phi}, M_{\dot{v}_\theta}, N_{\dot{v}_\psi}) \tag{5.3}$$

and an ellipsoid shaped, fully submerged vehicle with its center coincident with the ellipsoid center described by quadratic relationship, highlighted on Figure 5.1.

$$\frac{x^2}{a^2} + \frac{y^2}{b^2} + \frac{z^2}{c^2} = 1 \tag{5.4}$$

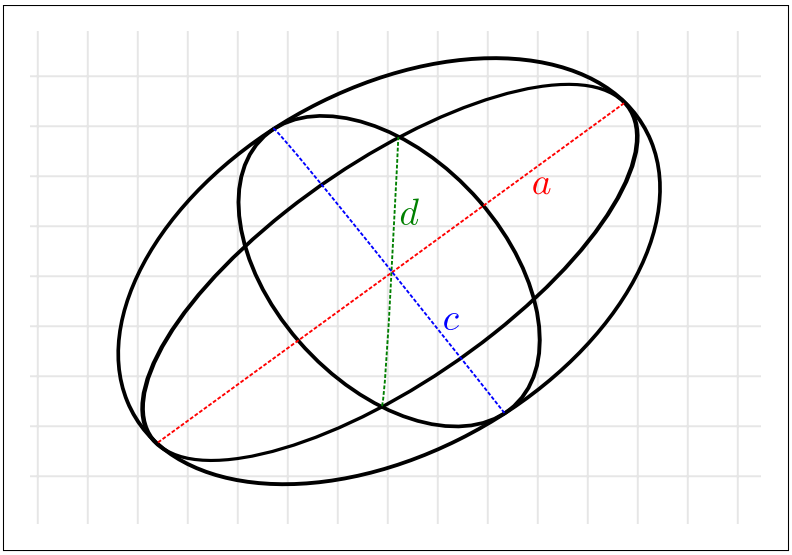

Figure 5.1: Simple Spheroid

The coefficients for a prolate spheroid, where $a = b$, are given as

$$X_{\dot{v}_x} = -\frac{\alpha_0}{2-\alpha_0}$$
$$Y_{\dot{v}_y} = Z_{\dot{v}_z} = -\frac{\beta_0}{2-\beta_0} m$$
$$K_{\dot{v}_\phi} = 0$$
$$M_{\dot{v}_\theta} = N_{\dot{v}_\psi} = -\frac{1}{5}\frac{(b^2-a^2)(\alpha_0-\beta_0)}{2(b^2-a^2)+(b^2+a^2)(\beta_0-\alpha_0)} m$$

With

$$\alpha_0 = -\frac{2(1-e^2)}{e^3}(\frac{1}{2} ln \frac{1+e}{1-e} - e),\ \beta_0 = \frac{1}{e^2} - \frac{1-e^2}{2e^3} ln \frac{1+e}{1-e},\ e = 1-(\frac{b}{a})^2 \quad (5.5)$$

To compute the spheroidal radii for the μAUV we can encapsulate it in a spheroid and use the resulting radii values. This results in a conservative estimate for the added mass matrix $\boldsymbol{M}_A$

For this project we will not focus on investigating further the added mass term,

albeit it is an important component of the model. [50][51][52]

5.2 Coriolis

The rigid body component of the coriolis term derives from the rigid body component of the inertia term, and likewise between the added mass component of the coriolis term and the added mass component of the inertia term, as given in equation 2.12

$$\boldsymbol{C}(\boldsymbol{v}) = \begin{bmatrix} \mathbf{0} & -[\boldsymbol{M}_{11}\boldsymbol{v}_1 + \boldsymbol{M}_{12}\boldsymbol{v}_2]_\times \\ -[\boldsymbol{M}_{11}\boldsymbol{v}_1 + \boldsymbol{M}_{12}\boldsymbol{v}_2]_\times & -[\boldsymbol{M}_{21}\boldsymbol{v}_1 + \boldsymbol{M}_{22}\boldsymbol{v}_2]_\times \end{bmatrix} \tag{5.6}$$

5.3 Hydrodynamic Forces and Moments

There is no explicit model available for calculating the dissipative forces' drag and lift coefficients, as this would require solving a set of Navier-Stokes equations. The tools available for estimating the hydrodynamic forces are confined to Computational Fluid Dynamic analysis, CFD, or scaled motion tests of which there are a number of methods and the planar motion mechanism being the more common one [52].

In this section, CFD analysis is used to estimate the hydrodynamic parameters of the designed μAUV in both open water and within a pipe segment. In addition to the CFD analysis, a decayed motion experiment is devised to validate the data from the CFD analysis.

The purpose of the hydrodynamic analyses conducted in this chapter is to measure the general steady state effects of hydrodynamic forces acting on the vehicle. This would aid in assessing the performance of the vehicle in terms of range and agility, in aiding the design process of the vehicle and selecting an optimal shell and thruster profile, and in simulating the environment inside the pipe, in order to de-

sign and test suitable control algorithms.

The experimental hydrodynamic analysis performed in section 5.3.2 later, will attempt to validate the CFD results. A combination of CFD analysis and experimentation will provide a reliable design tool for evaluating the hydrodynamic forces.

5.3.1 Hydrodynamic Forces and Moments CFD Analysis

For the CFD analysis, ANSYS-CFX is used, which employs a hybrid finite-volume/finite-element approach to discretize Navier-Stokes equations. This approach is extensively used in marine applications [53]. There are a number of assumptions that are used in the CFD setup summarized as follows:

1. Continuous and homogeneous flow
2. Steady-state flow
3. Steady-state turbulent flow
4. Complex but small geometries are ignored/reduced
5. Low velocity flow

We assume that the vehicle will operate in a fully filled enclosed volume, and that the fluid is a homogeneous and continuous body of water at a constant temperature, and is assumed to be incompressible.

In the context of mechatronic design, we are primarily interested in evaluating the steady-state performance of the vehicle. Transient effects are expected to influence the actual dynamic behavior, and consequently the controller performance, and so transient effects, including fluid fluctuations inside the pipe, should ultimately be taken into consideration for further design analysis and optimization; however, this is outside the context of our work.

Under the assumption of steady-state flow and steady-state turbulence, external transient forces are ignored, transient boundary conditions are ignored, and vortex stretching is also ignored [53]. A low order temporal discretization of the flow equations provides reliable convergence under the steady-state assumption.

The vehicle is expected to operate at low surge velocities, reaching a maximum of $2m/s$ and at an average nominal velocity of less than $1m/s$. There are subtle settings that are required in the analysis, to come up with arguably reasonable results, which we will highlight next.

5.3.1.1 CFD Setup

The steps to setup the CFD analysis include, in brief, starting with a model geometry with minimal surface complexities. This surface simplification helps to discard mesh errors and convergence errors, and reduces significantly the computational expense.

The mesh size and surface inflation layers must be chosen to balance between computational cost, accuracy, and sensitivity of solutions. This is performed by running a sensitivity analysis first and studying the simulation results against increasing mesh resolutions and across varying flow velocities. The results stabilize and converge at a certain mesh resolution. At this point the mesh settings are used to carryout the complete analysis.

Figure 5.2 illustrates the mesh configuration used in the simulation. The figure shows a section view of the mesh generated by ANSYS-CFX with the velocity streamline in surge motion shown as well. A body of influence is used to grow the mesh resolution near the vehicle body. Table 5.1 captures the key settings used.

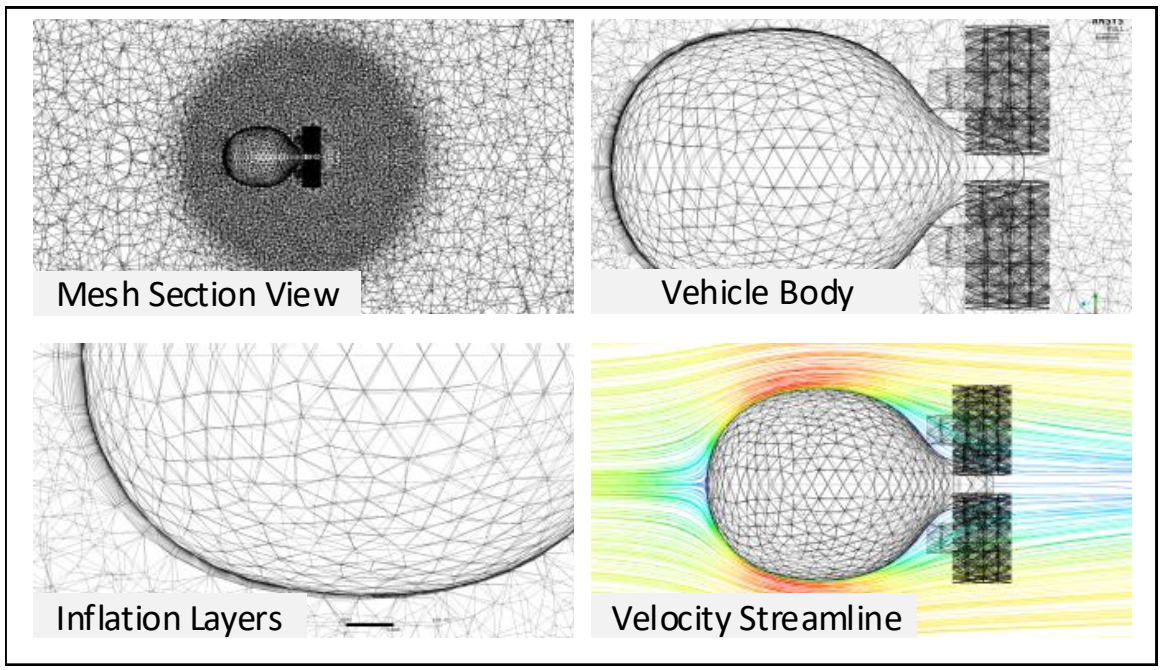

Figure 5.2: Ansys-CFX Mesh Setup

Table 5.1: CFD-CFX Shell Hydrodynamic Analysis Setup Parameters

Setting	**Value**
Outer Fluid Mesh Size	$18mm$
Body of Influence Mesh Size	$6mm$
Maximum Inflation Layers	35
First Inflation Layer Height	Function of Stream Velocity
Average y^+ value at vehicle surface	< 1
Linear Stream Velocity	0.125 - $4m/s$
Rotational Stream Velocity	0.75 - $25rad/s$
Turbulence Model	SST

Note that the geometric model used here is a simplified version of the actual design, but captures the general geometric form.

A turbulence model must also be chosen with specific initial conditions. For the choice of turbulence model there are specific methods to verify the validity of the mesh settings and solution, namely what is termed the y^+ value. The y^+ which is

a function of the friction velocity, the distance to the wall (vehicle surface) and the local kinematic viscosity of the fluid, for a Menter's Shear Stress Transport (SST) turbulence model, the y^+ should have an average value within 1. The y^+ value can be checked and verified with ANSYS-CFX [54].

With the assumption that the vehicle is geometrically symmetric and that its motion is uncoupled, we can investigate motion in each of the 6 directions independently, and then together build the parameters of the diagonal damping term. First, we simulate the vehicle in an open water environment. Figures 5.3 and 5.4 show the translational motion and rotational motion results for the open water hydrodynamic forces and moments, respectively.

As expected, the hydrodynamic force in the surge direction is lowest, followed by the sway direction then heave. The relationship is quadratic at higher stream velocities but a mixture of linear and quadratic at lower velocities. The rotational dissipative moments are much lower in comparison to the translational dissipative forces. Meaning, the vehicle's potential agility in attitude control is higher than the translational agility. Rotation is centered around the vehicle's volumetric center, or center of buoyancy, for each of the roll, pitch and yaw motions independently.

The solution is iterated over multiple velocity set points for each of the 6 directions. The CFD settings are kept uniform across the trials, except that the inflation layers' first layer height is changed to achieve a y^+ in the desired, and consistent range. The inflation layer height is tuned for each different stream velocity.
The coefficients are summarized in table 5.2. They represent the 3 translational hydrodynamic coefficients and the 3 rotational hydrodynamic coefficients respectively.

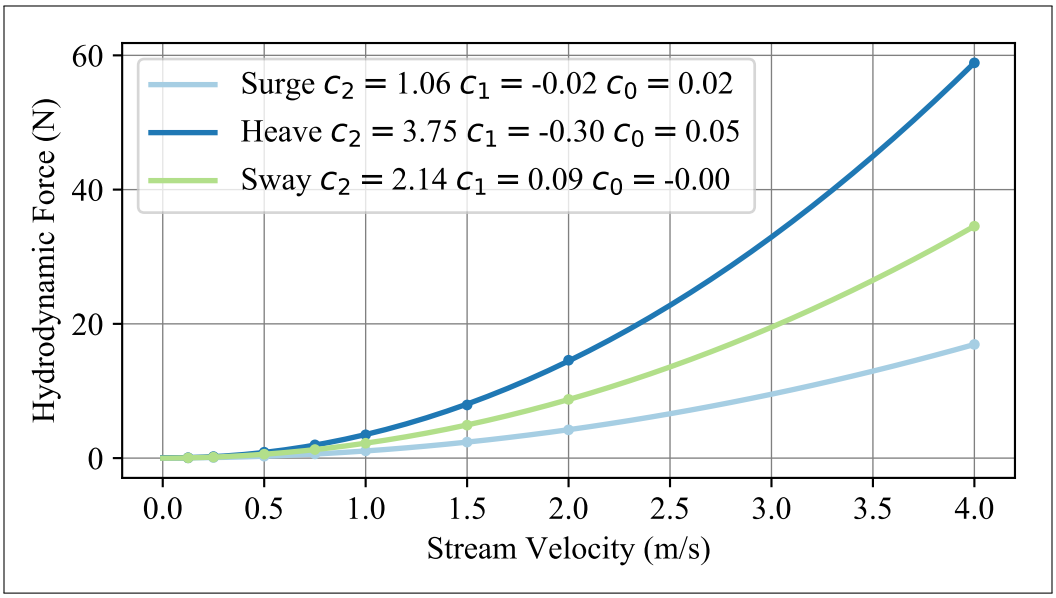

Figure 5.3: Hydrodynamic Forces for the μAUV in open water vs. translational stream velocity.

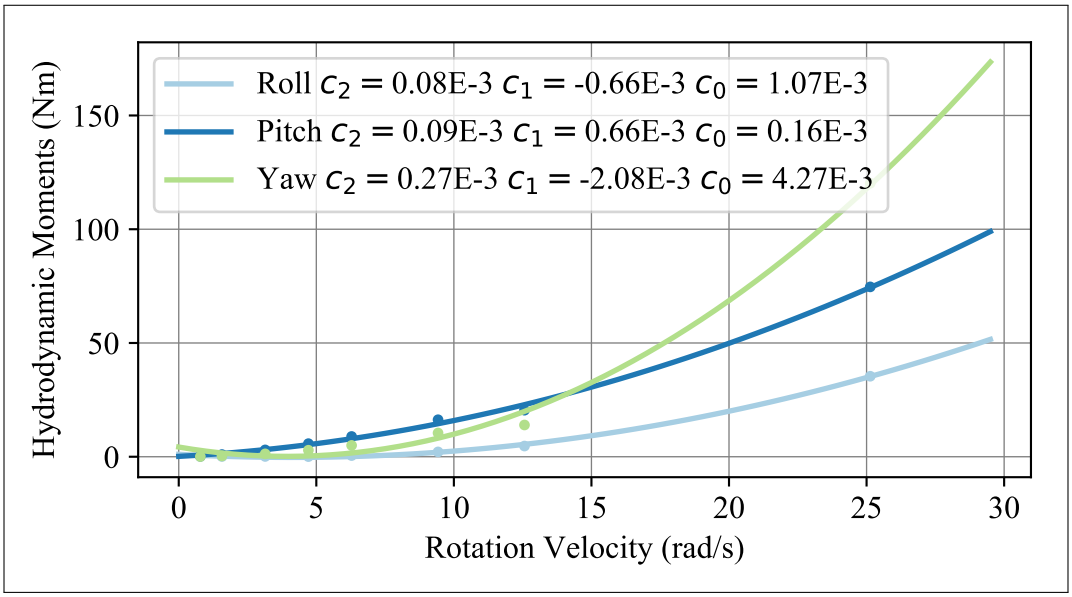

Figure 5.4: The hydrodynamic moments for the μAUV in open water vs. rotational stream velocity

Table 5.2: Hydrodynamic Coefficients Computed from CFD Analysis using ANSYS-CFX. The rotational hydrodynamic moments are scaled to Nmm

Direction	$-D(v)$ (N)	Direction	$-D(\omega)$ (Nmm)
Surge	$1.06v^2 - 0.02v + 0.02$	Roll	$0.08\omega^2 - 0.66\omega + 1.07$
Sway	$2.14v^2 + 0.09v$	Pitch	$0.09\omega^2 - 0.66\omega + 0.16$
Heave	$3.75v^2 - 0.30v + 0.05$	Yaw	$0.27\omega^2 - 2.08\omega + 4.27$

The above results may not be sufficiently representative of the environment where we desire to operate the μAUV namely the confined space of a pipe. Therefore, we examine the affect of constraining the flow through a pipe with the robot at its center, moving concentrically with the pipe. First, we look at varying the internal diameter of the pipe, and then look at the affect of varying the pitch angle up to its expected maximum drag affect.

Figure 5.5 shows the simulation results for hydrodynamic forces in the surge direction at varying internal pipe diameters and at different stream velocity setpoints. And Figure 5.6 shows the correlation between the increase in the cross-sectional area ratio normal to the surge direction, between the vehicle and the pipe, against the percentage increase in the hydrodynamic force.

Note that for the pipe diameter where the μAUV is intended to operate, which is in a pipe with 160mm internal diameter, the increase in surge hydrodynamic force compared to the open-water case ranges between 70% and 130%, for the range of stream velocities tested, and increases with decreasing stream velocity. This is explained by the increase in the hydrodynamic force due solely to the increase in flow compared to the augmented fluid velocity increase and, consequently, hydrodynamic force increase due to the Venturi Effect.

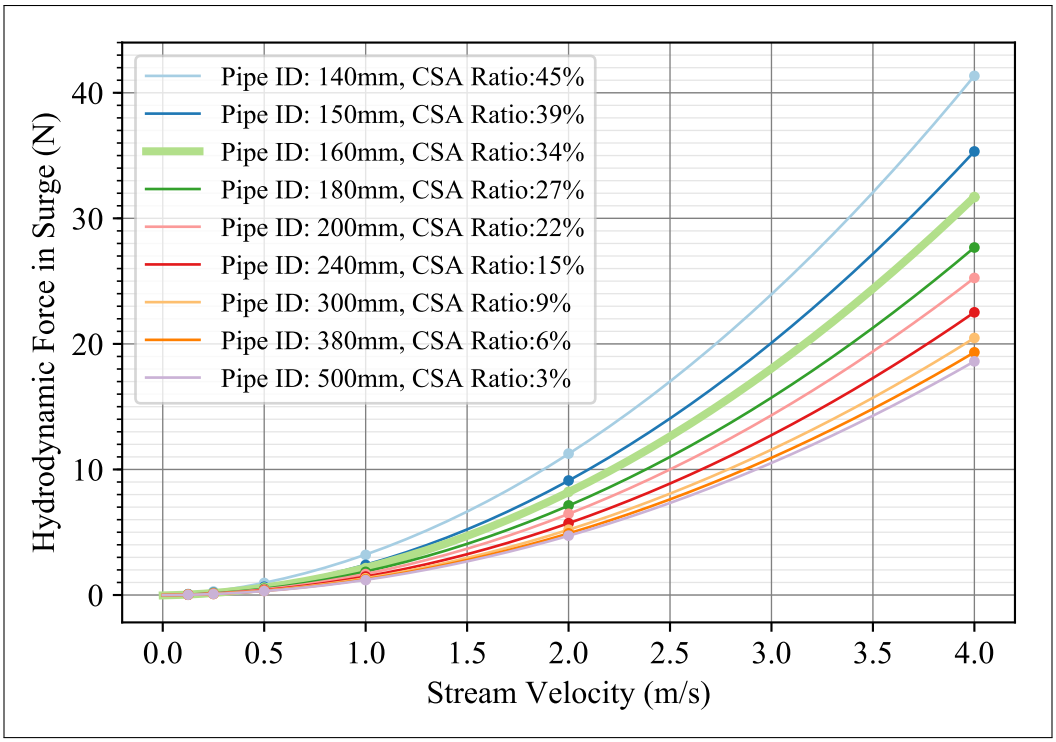

Figure 5.5: Hydrodynamics Force in Pipe With Varying Diameter

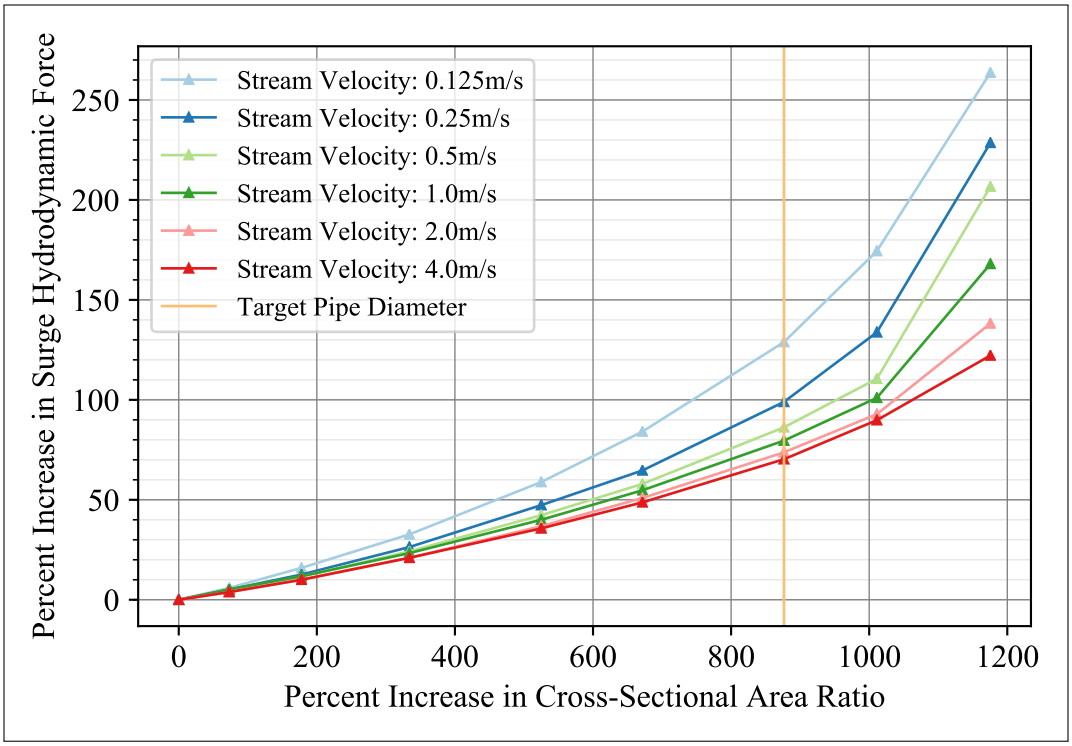

Figure 5.6: Correlation Between Cross Sectional Area Ratio and Increase in Hydrodynamic Force

If we look at the effect of the hydrodynamic force as the vehicle pitches relative to the pipe axis, we notice a significant increase in the experienced axial drag, as illustrated on figure 5.7. The axial drag is defined as the drag along the pipe axis. The passing fluid faces a larger drag coefficient due to the increased equivalent cross sectional area, as well as to the increase in the cross sectional area ratio between the vehicle and the pipe normal to the axial direction. The body surge direction changes as the vehicle surges, and becomes positive, forcing the vehicle forward onto the pipe, at higher pitch angles.

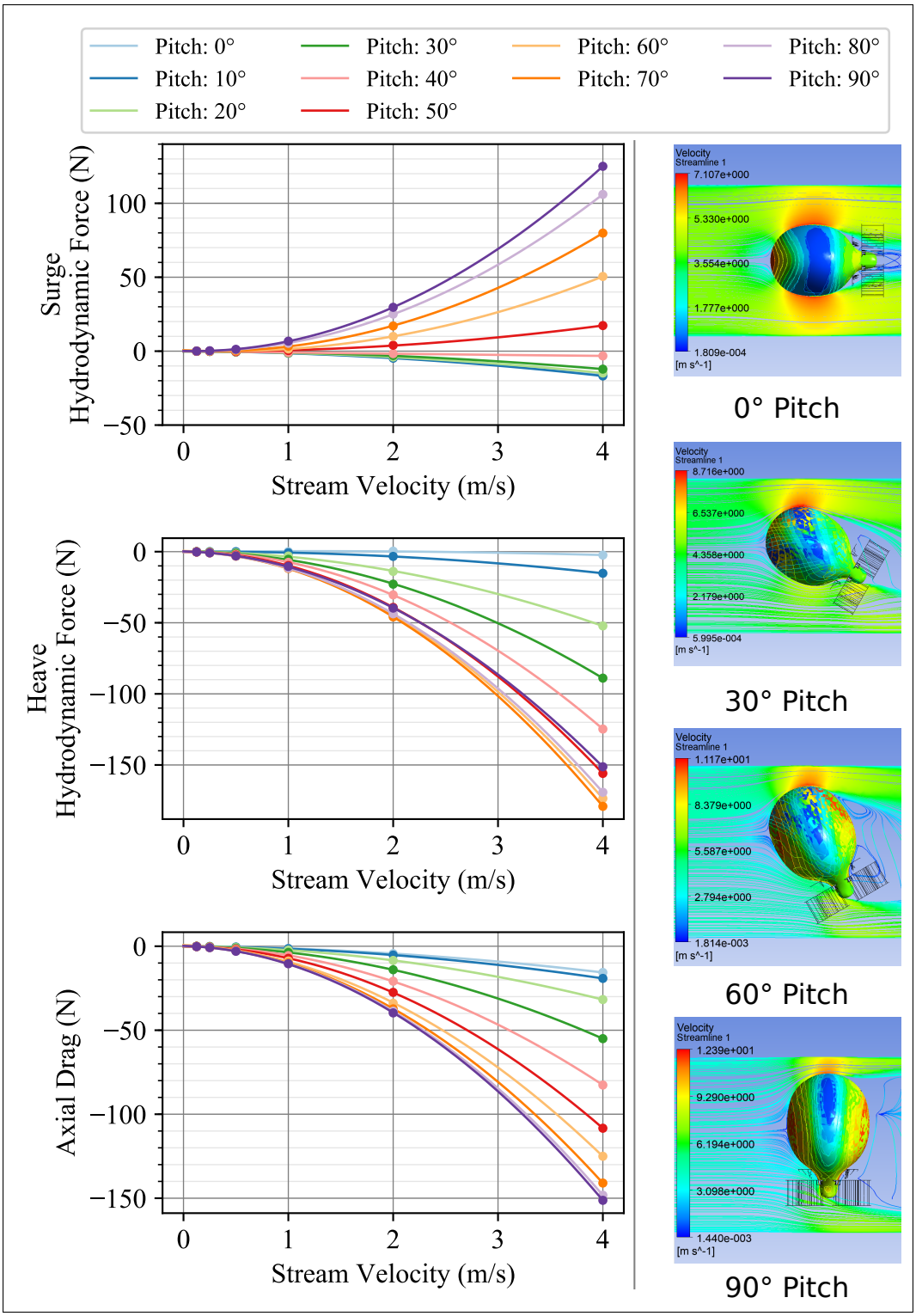

Figure 5.7: Hydrodynamic Forces in Pipe at Varying Vehicle Pitch Angles

Figures 5.8 and 5.9 show the velocity and pressure countours respectively, at the xz plane and for a $1m/s$ stream velocity. The velocity legend range is 0.0 to $4m/s$ and the pressure's legend range is -3.0 to $2.0kPa$.

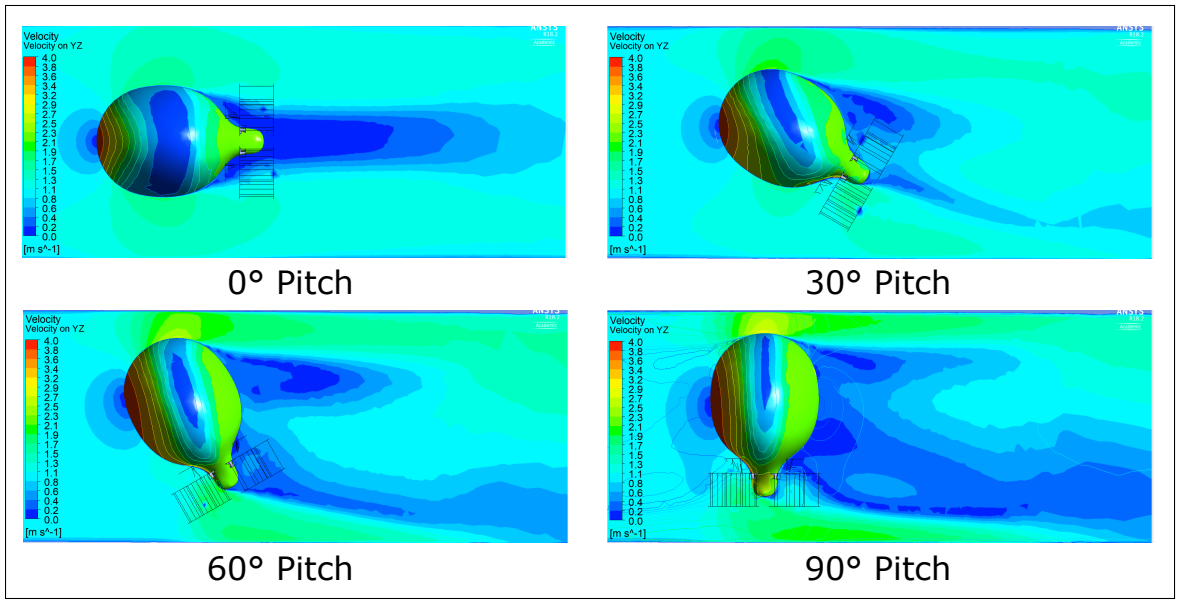

Figure 5.8: Velocity Contour at Varying Vehicle Pitch Angles - $1m/s$ Stream Velocity

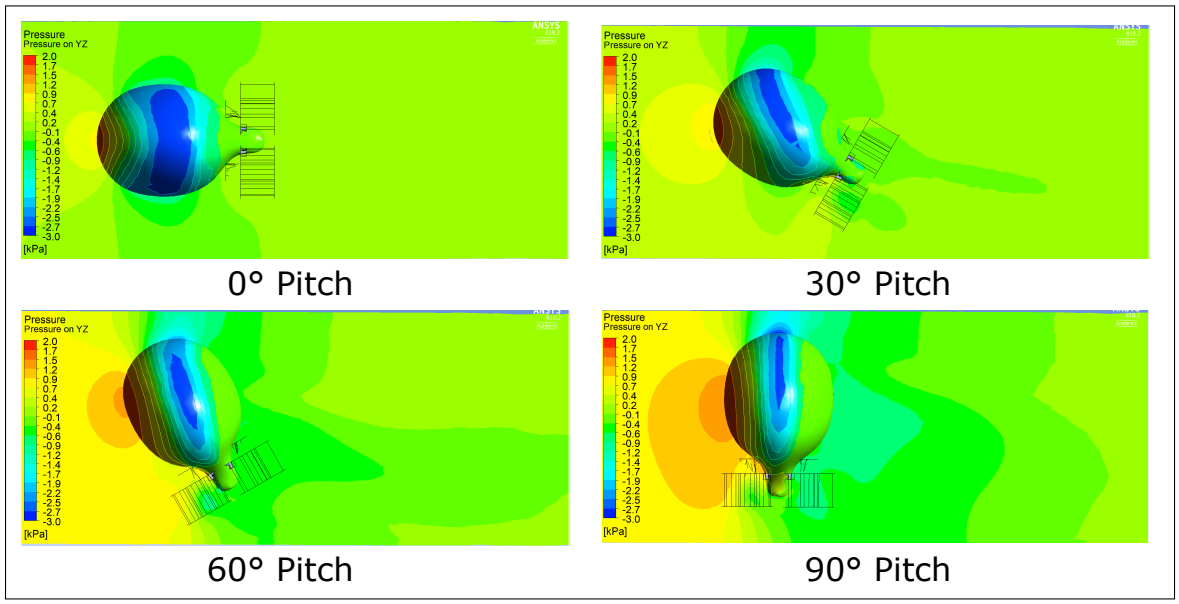

Figure 5.9: Pressure Contour at Varying Vehicle Pitch Angles - $1m/s$ Stream Velocity

The varying pitch angle analysis illustrates a key difficulty in controlling the μAUV

inside the pipe. The eccentricity and alignment of the μAUV along the pipe becomes exponentially harder to achieve as the vehicle deviates away from the concentric alignment, where the radial hydrodynamic force becomes larger and expels the vehicle toward the pipe wall in at least one configuration as shown above.

But since the attitude of the vehicle can be controlled at near-zero translation velocity, one way to overcome the radial hydrodynamic force problem is by prioritizing the μAUV trajectory on a concentrically aligned path and penalize surge motion when it becomes out of alignment. From a controller point of view, this translates into motion speed reduction as the vehicle deviates away from the concentric center.

The in-pipe hydrodynamic analyses do not take into account the effects of secondary flow generated by the thrusters and reflected back from the pipe wall. It is expected that such effects are significant and worth of further extended analysis.

Next we will validate some of the results attained in this section through experimentation.

5.3.2 Hydrodynamic Forces and Moments Experimental Test

There are several methods available to compute the hydrodynamic parameters experimentally. A traditional method would employ a planar motion mechanism (PMM) device, that generates an oscillatory motion and from the response derive the hydrodynamic parameters [52] [31]. Other methods attempt to perform the parameter estimation on-line, buy using an estimation method like a Kalman Filter [55]. Rather than use a PMM device, and since we have the benefit of working with a small vehicle, we will induce the oscillation by way of a damped pendulum motion, extending the work done by [56], by accounting for hinge friction, as well as CoB and CoM offsets.

Figure 5.10 illustrates the vehicle is setup for both an open-water environment and an in-pipe environment. A water tank is used to perform the damped oscillation experiment. The vehicle is lifted manually and released to oscillate while the high resolution encoder outputs the reading to a connected PC for post processing. A plastic PETG 3D printed pipe segment with a slot opening is added as shown on the top right. The pipe's curvature matches the radius of the μAUV on the pendulum, to simulate a concentric pipe motion.

The same setup is used to measure the sway and heave hydrodynamic forces as well by rotating the vehicle into the respective orientation. A torsional damping setup similar to this one can be used to measure the angular hydrodynamic moments coefficients, the challenge is in devising a torsional spring setup that allows for multiple periodic oscillations and with minimal spring damping, since the angular damping effects are significantly lower relative to the damping effects in the test structure itself.

The governing relationship between the pendulum angle and the vehicle parameters

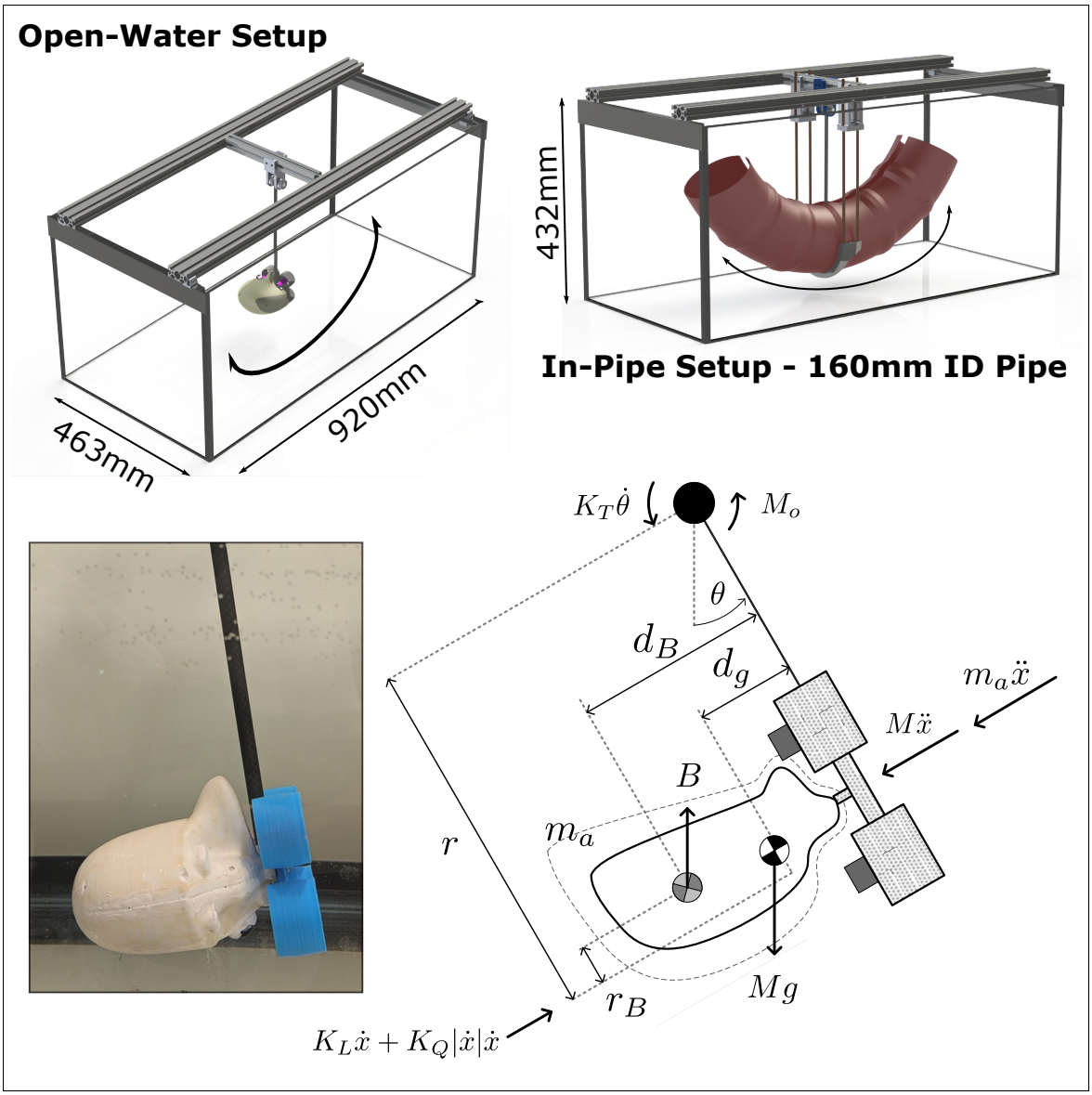

Figure 5.10: Damped Oscillation Setup for Hydrodynamic Parameters Estimation

is given by

$$\ddot{\theta} = \alpha cos\theta + \beta sin\theta - \gamma\dot{\theta} - \delta\left|\dot{\theta}\right|\dot{\theta} \tag{5.7}$$

where the coefficients equate to

$$\alpha = \frac{Mgd_g - Bd_B}{(M+m_a)r^2} \qquad \beta = \frac{B(r-r_B) - Mgr}{(M+m_a)r^2}$$

$$\gamma = \frac{K_L r^2 + K_T}{(M+m_a)r^2} \qquad \delta = \frac{K_Q r}{(M+m_a)}$$

K_T, K_L, K_Q are the hinge friction, linear hydrodynamic damping, quadratic hydrodynamic damping coefficients respectively. m_a is the vehicle's added mass. The angle is measured using a high resolution optical encoder. Offline, the parameters can be computed using a least squares estimation given the following relationship:

$$\hat{\theta}_{LS} = (H^T H)^{-1} H^T y \tag{5.8}$$

where $y = H(x)\theta$, equivalently:

$$\begin{bmatrix} \ddot{\theta_1} \\ \ddot{\theta_2} \\ \vdots \end{bmatrix} = \begin{bmatrix} cos\theta_1 & sin\theta_1 & -\dot{\theta_1} & -|\dot{\theta_1}|\dot{\theta_1} \\ cos\theta_2 & sin\theta_2 & -\dot{\theta_2} & -|\dot{\theta_2}|\dot{\theta_2} \\ \vdots & \vdots & \vdots & \vdots \end{bmatrix} \begin{bmatrix} \alpha \\ \beta \\ \gamma \\ \delta \end{bmatrix} + error \tag{5.9}$$

A model-based parameter estimator like a Hybrid Extended Kalman Filter was tested as well, but it requires additional differentiation of the state to produce acceleration data. The Least-Squares method was sufficient. The CoB coordinates r_B and d_B, are calculated from the CAD model, and the CoM coordinates d_G are computed by comparing the in-air pendulum angle static offset versus the in-water pendulum angle static offset. The hinge friction coefficient is computed with an in-air damped oscillation test, then the test is performed in-water to retrieve the remaining parameters. Additional weight, beyond what is required for neutral buoyancy, is added inside the shell to produce higher kinetic energy in the motion.

5.3.2.1 Experimental Results

Figure 5.11 shows the measured response from the open-water surge motion test, compared to the simulated response using the hydrodynamic coefficients estimated by the CFD analysis. The figure also shows the measured hydrodynamic force compared to the simulated hydrodynamic force as expected from the CFD analysis.

The Least-Square estimation results are sensitive to changes in the offset parameters and hinge friction coefficient. A sensitivity analysis to these parameters shows the measured hydrodynamic force response varies 15%. In this particular case of surge motion in open-water, the estimated hydrodynamic force response from the measurement is higher than the response estimated from the CFD.

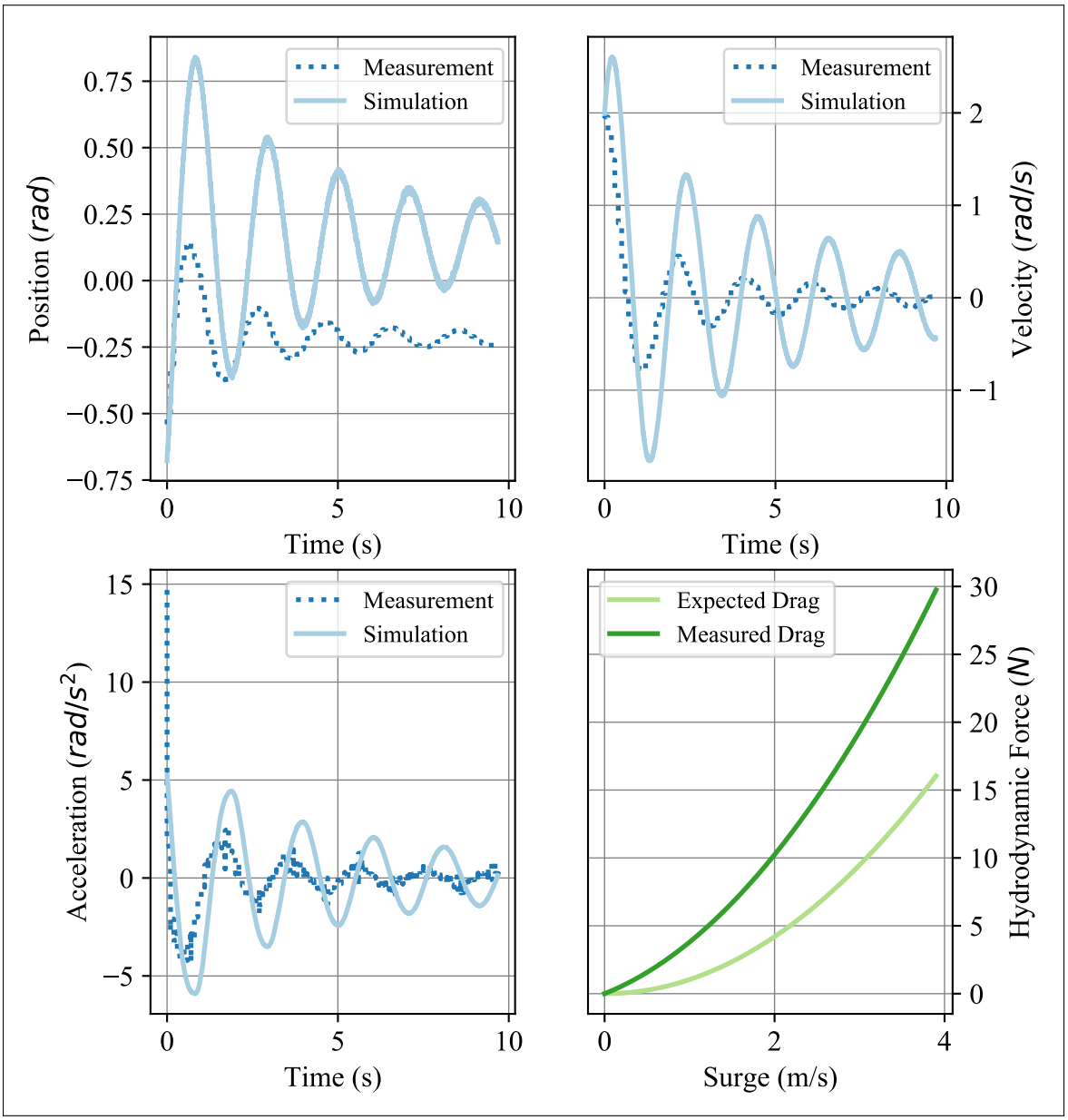

Figure 5.11: Open-Water Hydrodynamic Damping in Surge. CFD vs. Experiment

Figure 5.12 displays the hydrodynamic force response for the three translational motions as estimated by the experiment compared to the CFD analysis. Again, there is a significant deviation between the estimation methods; however, the relative response order between the three directions is consistent and is as expected.

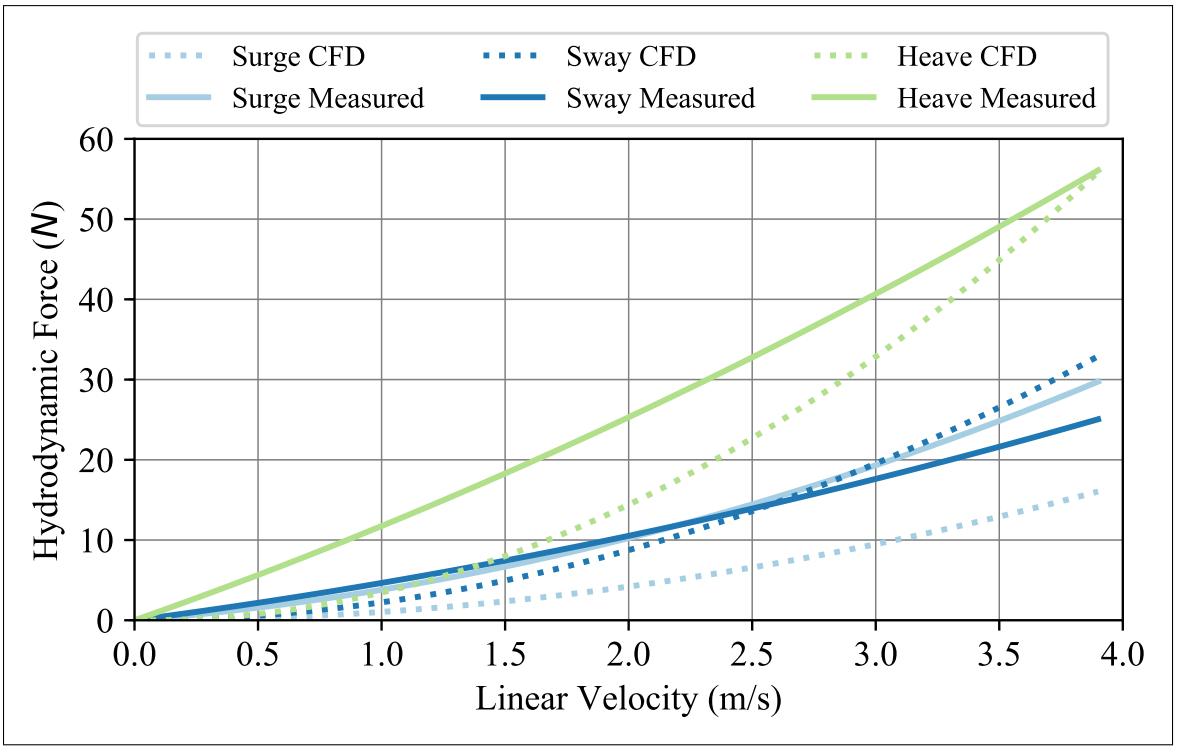

Figure 5.12: Open-Water Hydrodynamic Damping. CFD vs. Experiment

We now compare the result of open-water surge motion and in-pipe surge motion. On Figure 5.13, we can see the two responses as estimated by the two methods. The experimentally measured response is higher for both the open-water and in-pipe compared to the results from the CFD. In both cases there is a clear difference, and increase, between the in-pipe drag and open-water drag.

In this section we looked at modeling the dissipative hydrodynamic effects by way of a CFD analysis and an experimental pendulum decay test. The large sensitivity to other model parameters produces large deviations in the experimentally es-

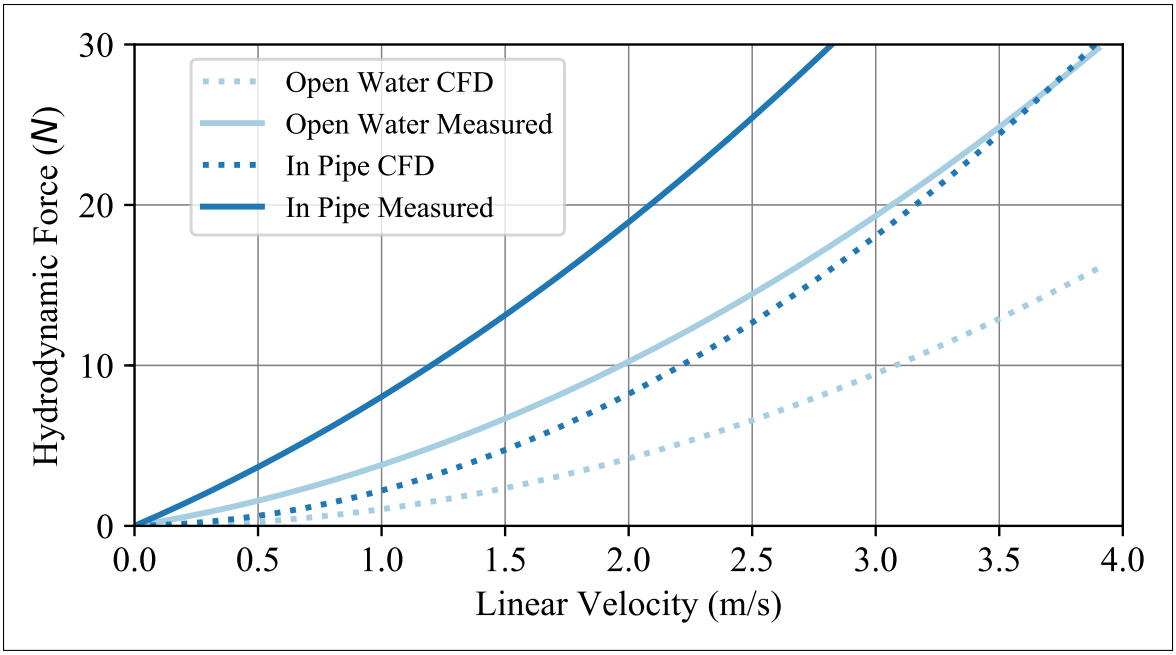

Figure 5.13: Open-Water Hydrodynamic Damping. CFD vs. Experiment

timated results. Further tuning of the model is required to achieve reliable results. In section 5.6 we will propose an on-line parameter estimation method that works with forced excitation behavior. For the purposes of simulating the behavior of the vehicle and assessing its performance for mechatronic and controller design purposes, we believe that the CFD analyses provide sufficiently reliable estimates.

The CFD setup can be expanded to capture hydrodynamic damping behaviour at more complex configurations in the pipe. It can be used to map the effects of near wall hydrodynamics, of reflected flow from the pipe and at curved pipe sections.

5.4 Thruster Dynamics

A critical component of the μAUV design and one that governs the realizability of the design goal is the performance of the thrusters. Understanding the behavior of the marine impellers, and thrusters in general allows for systematic design and optimization of the thrusters, allows for better performance modeling, for a realistic simulation, and for a robust thruster compensation model in the controller. The field of marine propellers is an established and comprehensive field of study, and it is certainly beyond the scope of this work to cover the theoretical foundation of propeller performance and theoretical propeller theory. But since the performance of a thruster is governed by both the performance of the motor and the propeller, we briefly outline the performance characteristics of motors first.

5.4.1 Motor Performance

The selected motor for this application is a Sensorless Brushless Electric Motor, BLDC. They have superior reliability compared to brushed motors, require no position sensors if positional control accuracy is not desired, and have a high power to size/weight ratio, especially with the use of Neodymium Magnets. And they are readily available at low cost. They do however require a dedicated controller, normally referred to as Electronic Speed Controllers, or ESCs.

A typical BLDC motor curve is illustrated on Figure 5.14. BLDC motors exhibit relatively constant torque behavior up to the field weakening region, as their operational theory suggests citeHughes2014. Their corresponding efficiency curves also show peaks at some operating speeds for a given supply voltage. The load line is governed by the inertia of the load, and for our thruster application, this equates to the impeller geometry and hydrodynamic condition. An appropriately designed propeller and duct will place the load line along our desired operating path with

respect to power, efficiency, thrust and torque characteristics.

Motor curves can either be provided by motor manufacturers or can be obtained through benchmarking with a Dynamometer. The thruster tests illustrated in the next subsections will show that we can operate the motor near the constant torque to field weakening region transition, given the appropriate propeller selection.

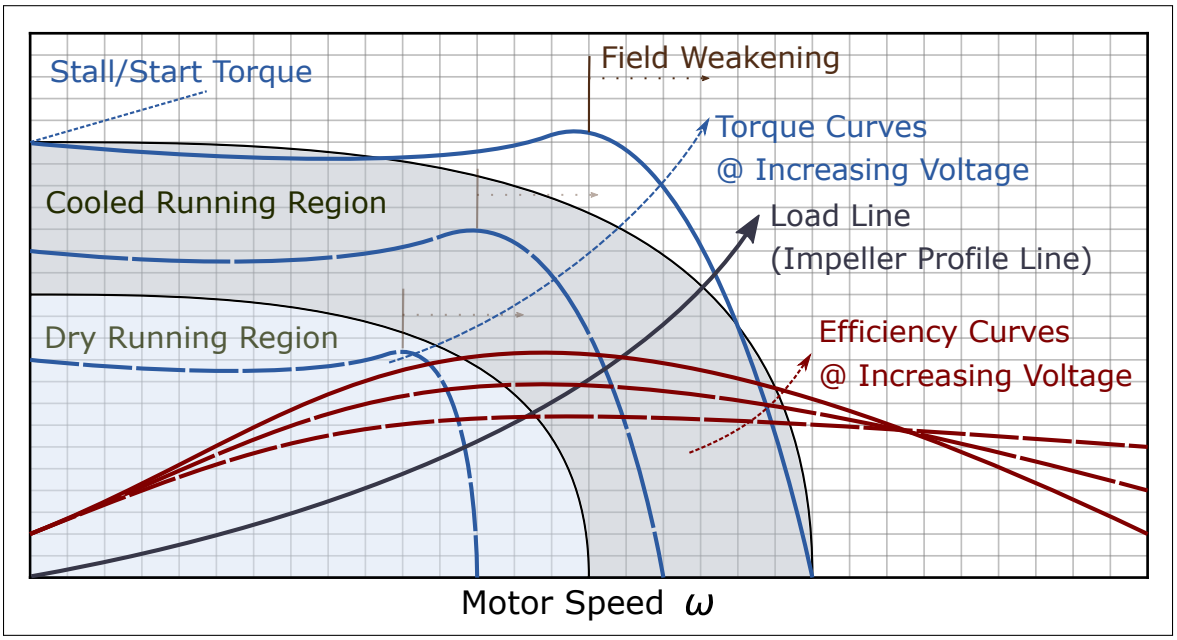

Figure 5.14: Typical BLDC Motor Performance Curve

A major impact on the performance of the motor is the fact that it operates underwater. The passive cooling of the motor allows it to continue to operate efficiently at significantly higher power output compared to in-air performance. The specific motor we use is rated for a burst power of 45Watt, but underwater tests showed that it continues to operate efficiently at over 90Watt of continuous output.

5.4.2 Propeller Performance Characterization

We are interested in utilizing a design approach for thrusters at the scale of the μAUV under investigation. Existing literature and design guides provide example profiles of propellers targeted toward large marine vehicles and often exhibit a dif-

ferent geometrical structure than the impeller profiles we seek. One approach is to exploit the property of similtude to scale and match the performance of our propellers to that of existing ones, using the set of dimensionless coefficients that relate the variables that influence propeller performance.

The factors that influence the performance of a propeller include the propeller diameter D, the speed of advance V_a, the rotational speed ω, the density of the fluid ρ, the viscosity of the fluid μ, and the static pressure of the fluid at the propeller p_s. A dimensionality relationship between thrust T and torque Q with the aforementioned variables gives, respectively, the thrust and torque coefficients K_T and K_Q [36].

$$K_T = \frac{T}{\rho\omega^2 D^4} \tag{5.10}$$

$$K_Q = \frac{Q}{\rho\omega^2 D^5} \tag{5.11}$$

The advance coefficient and Reynolds number are expressed as

$$J = \frac{V_a}{\omega D} \tag{5.12}$$

$$R_n = \frac{\rho\omega D^2}{\mu} = \frac{\rho V_a D}{\mu} \tag{5.13}$$

These coefficients form the basis of propeller performance characterization and design selection. The thrust loading T is also a function of the advance velocity V_a. And for a fixed motor rotation speed ω the effective thrust will tend to decline as the advance velocity increases. This is will become important when simulating the vehicle as it would not be sufficiently accurate to assume a thrust force independent of the μAUV translational velocity.

Defining the pitch ratio as the ratio between the pitch angle of the propeller blade to the diameter of the blade P/D, the characteristic curve for a specific propeller geometry would look similar to Figure 5.15. The figure shows the nondimensional torque and thrust coefficients as well as the efficiency curve. Ideally, we would like to have a validated characteristic diagram that matches our impeller's geometry. We are not aware of any that exist in the literature, so instead, we will produce ones for our nominal thruster design.

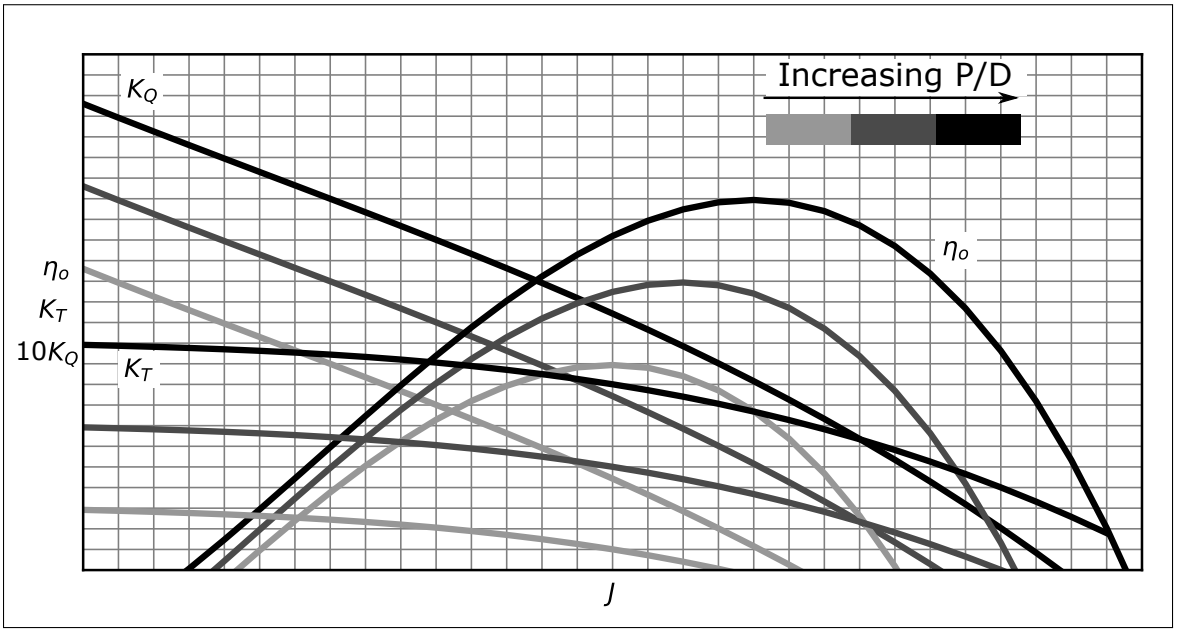

Figure 5.15: Generic Marine Propeller Performance Characteristic Diagram [36]

There are a number of theoretical methods for analyzing the performance of marine propellers. An early approach developed by Rankine and later improved by Froude,

is termed the Momentum Theory. The Momentum Theory assumes the propeller works in an ideal fluid with no losses and that it represents a disc that produces thrust without rotating the fluid [36]. The Momentum Theory may be useful in analyzing the behavior of the fluid upstream and downstream of the propellers, and in deriving a basic analytical model, but does not aid in the design of the propeller geometry.

The Blade Element Theory was later developed by Froude, where, as the name suggests, the propeller is sectioned into blade elements and a 2-dimensional aerofoil analysis is conducted, then the result is integrated over the full volume of the propeller blade. A number of other methods were developed over the years, including that of Burrill's Analysis, which is a strip theory method that combines the Momentum Theory and Blade Element Theory to analyze propeller performance.

All these methods require a deeper understanding of fluid mechanics and are after producing optimized results that satisfy the limits of propeller behavior. However, we are only concerned with the general behavior and performance of the thrusters. And that not only includes the propeller, but also the motor performance and motor controller thrust scaling. For this, we will rely on experimental analysis to profile a set of impeller profiles, and then revisit a systematic design approach for impellers using a CFD approach, equipped with the experimental results.

An additional complexity in analyzing thruster performance arises with the use of a ducted impeller. The duct acts as a thrust augmentation device at lower velocities. And its thickness, extension beyond the propeller rotation field and the propeller's tip clearance to the duct all influence the performance and efficiency of the thruster. Understanding these relationships can aide in optimizing the design of the μAUV as well.

5.4.3 Experimental Profiling

A thruster dynamometer was designed and constructed to test the thrust and torque performance of a number of ducted propeller profiles. The experimental setup is shown in Figure 5.16. The load cells are calibrated and linearized prior to tests. Each test is automated such that the throttle settings and sampling rates are consistent across the tests.

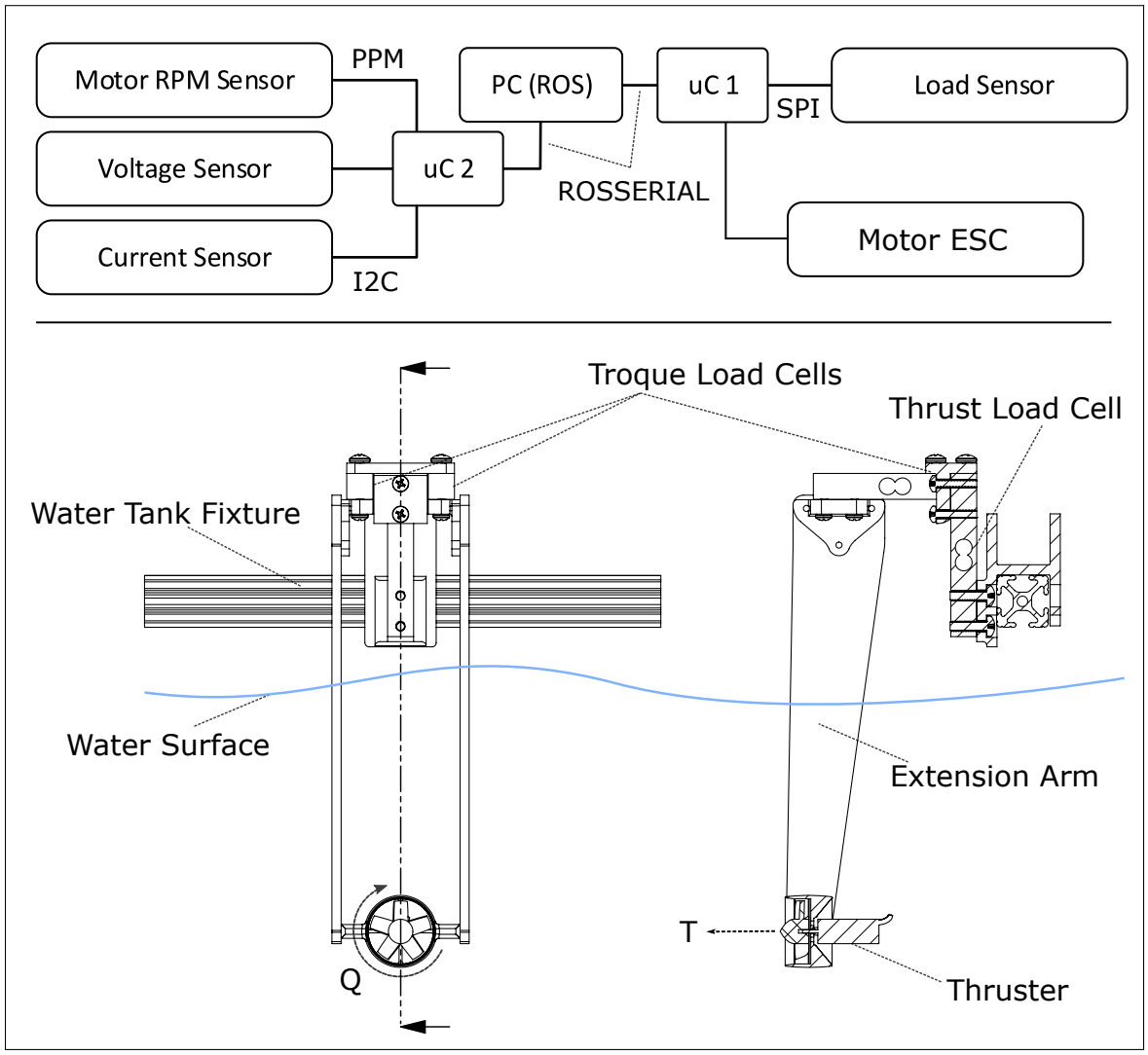

Figure 5.16: Thruster Dynamics Experimental Setup

The test rig is fixed on top of a water tank, similar to the one used for the damped oscillation in Section 5.3.2. A single load cell is used to measure thrust in forward

and reverse thrust direction, and two additional load cells are used to measure the torque produced by the thruster. Voltage and current sensors are attached to the load power supply, and a motor speed sensor is used as well.

Figure 5.17 shows the raw test data recorded for one propeller profile. The torque data produced from this test setup turned out to be somewhat unreliable, an independent torque measuring dyno design is required instead, with the placement of the load cells centerline close to the motor axis to avoid side loading of the cell under thrust. Alternatively, profiling the motor performance with an underwater motor dynamometer and matching the current profile with the electric current profile seen in the thruster tests, can estimate the torque produced by the thruster. For the generated torque, we will rely instead on the CFD results discussed in the next section.

Combining the results for a propeller profile at multiple blade pitch angles we can produce thrust to throttle and current to throttle curves for a thruster, as illustrated in Figure 5.18. The figure also shows the propeller profiles that were designed and fabricated for these tests. The propellers were fabricated with an FDM 3D printer using PLA plastic material. For the specific profiles nominal supply voltage tested, we can see that the motor operates in the "constant torque" region with 20° and 30° blade pitch angles. The motor can potentially produce more thrust with a higher supply voltage of 11.1V which is the maximum rated voltage for the motor, but it will either get into the "field weakening" region of operation and produce poor efficiency.

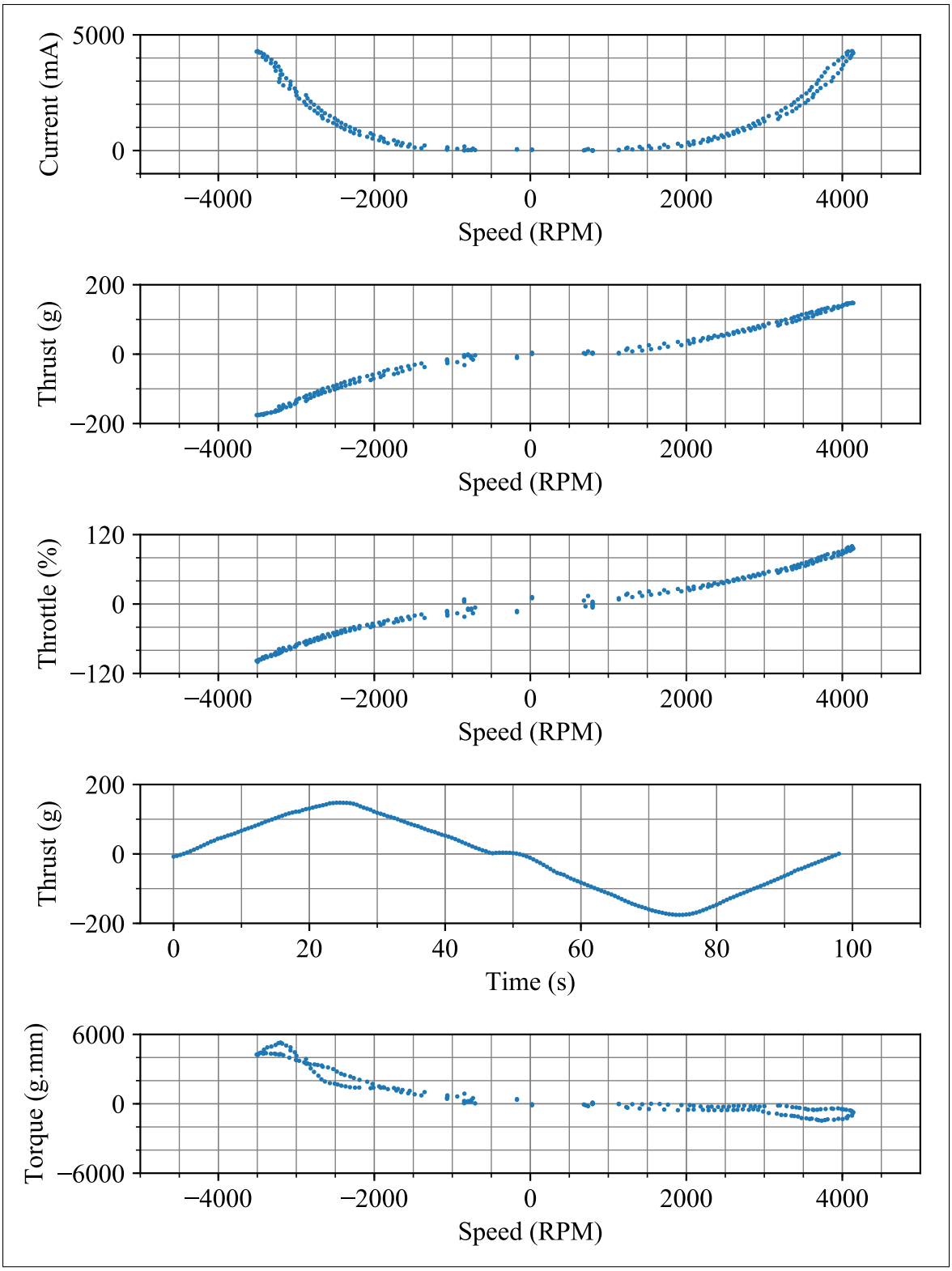

Figure 5.17: Thruster Dynamics Experimental Profiling Raw Test Data
Impeller Profile: 45^o pitch angle, No. Blades: 5, at 8Volt supply voltage

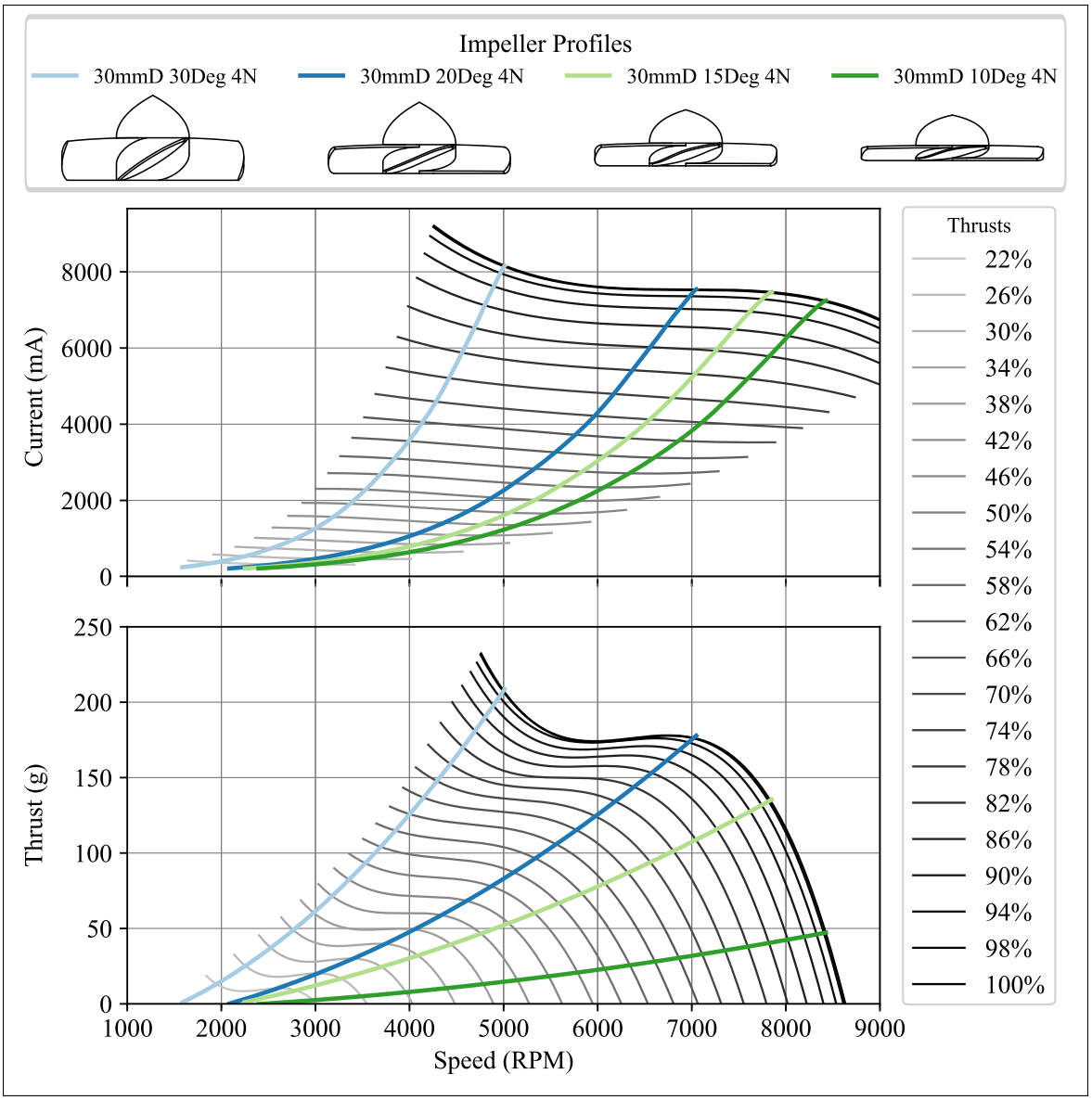

Figure 5.18: Thrust Characteristic Curves From Experiment
Impeller Profile: 30mm Diameter, No. blades: 4, varying blade pitch angle at 8Volt supply voltage

Looking at the electrical power delivery, the higher pitch angle profile produces a higher thrust to power ratio and at a lower motor speed, as shown on Figure 5.19. Similar tests, using the test rig, can be performed for varying propeller diameter, duct geometry, number of blades and blade to duct clearance, and of course different blade profiles. The blade pitch angles used in this work are radially fixed; however, ideally they should be a function of the radius in order to produce a uniform

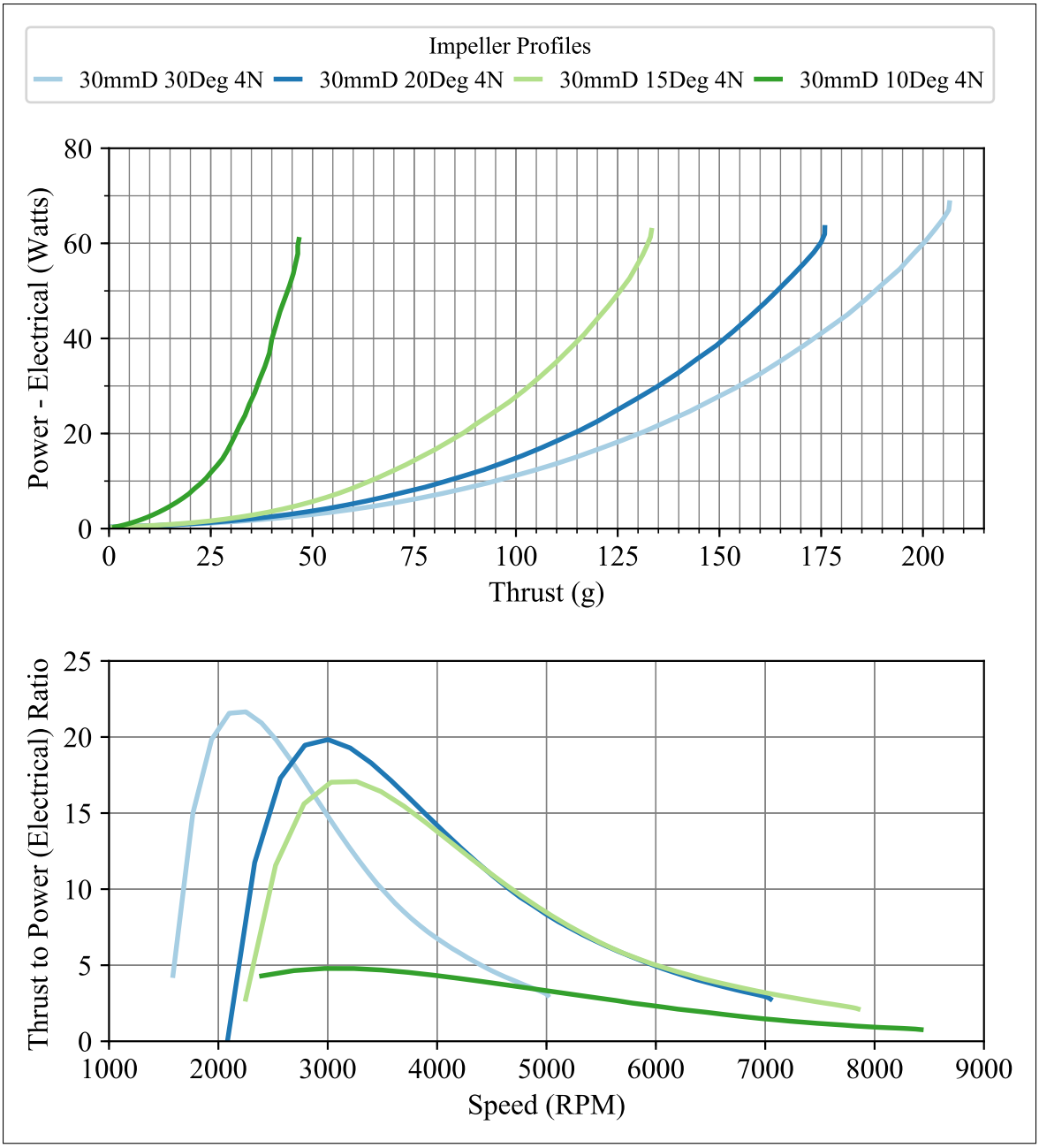

Figure 5.19: Thrust to Power Ratio Relationship
Impeller Profile: 30mm Diameter, No. blades: 4, varying blade pitch angle at 8Volt supply voltage

linear velocity over the blade. For a 30mm diameter propeller for instance, the linear blade velocity increases by a factor of 2.5 between the base of the blade at the hip and the blade tip. This increase is significant given the propeller rotates at very high speeds.

The above tests were conducted at zero stream velocity, resulting in what is termed the nominal thruster performance. The performance will vary as the stream velocity changes, to capture this effect the test rig can be modified and placed on a circular motion arm rotated at a set speed to produce the stream velocity affect, neglecting radial effects for a sufficiently long rotation arm. We will look at the affect of changing stream velocity by way of a CFD analysis in the next section.

5.4.4 Thruster CFD Analysis

Characterizing the thruster performance experimentally, can aid in performing a validated CFD analysis, since the operational characteristics of a propeller are intertwined with the motor performance characteristics, as seen on Figure 5.14.

We perform a parametric CFD analysis on the ducted thruster profiles that were fabricated and used in the experiment earlier, and this time we expand the analysis over more blade pitch angles, and with varying nonzero advance velocity, as well as with varying propeller diameters, in order to fully characterize the propeller as per the conceptual curve on Figure 5.15.

To automate the analysis, a parametric ducted propeller is designed in a CAD software (Solidworks), connected to ANSYS Mechanical. Design points are created in ANSYS for the combination of propeller geometry and flow conditions. The mesh size properties are fixed except that the inflation layer properties on the propeller blades are varied for different flow velocities. Figure 5.20 shows the CFD setup for a specific propeller geometry as well as an example flow behavior. The setup parameters are given in table 5.3.

Table 5.3: CFD-CFX Thruster Analysis Setup Parameters

Setting	**Value**
Frame Change Stationary-Rotating	Frozen Rotor: 360° pitch
Turbulence Model	SST
Fluid Timescale	Auto
Analysis Type	Steady State
Impeller First Layer Height	$0.001mm$
Impeller Maximum Inflation Layers	40
Impeller Inflation Algorithm	Post
Impeller Inflation Layers Growth Rate	1.025
Body of Influence Mesh Element Size	$0.75mm$
Equation Class	Continuity
Residual Type	RMS: 0.0001
Impeller Average y^+	< 1

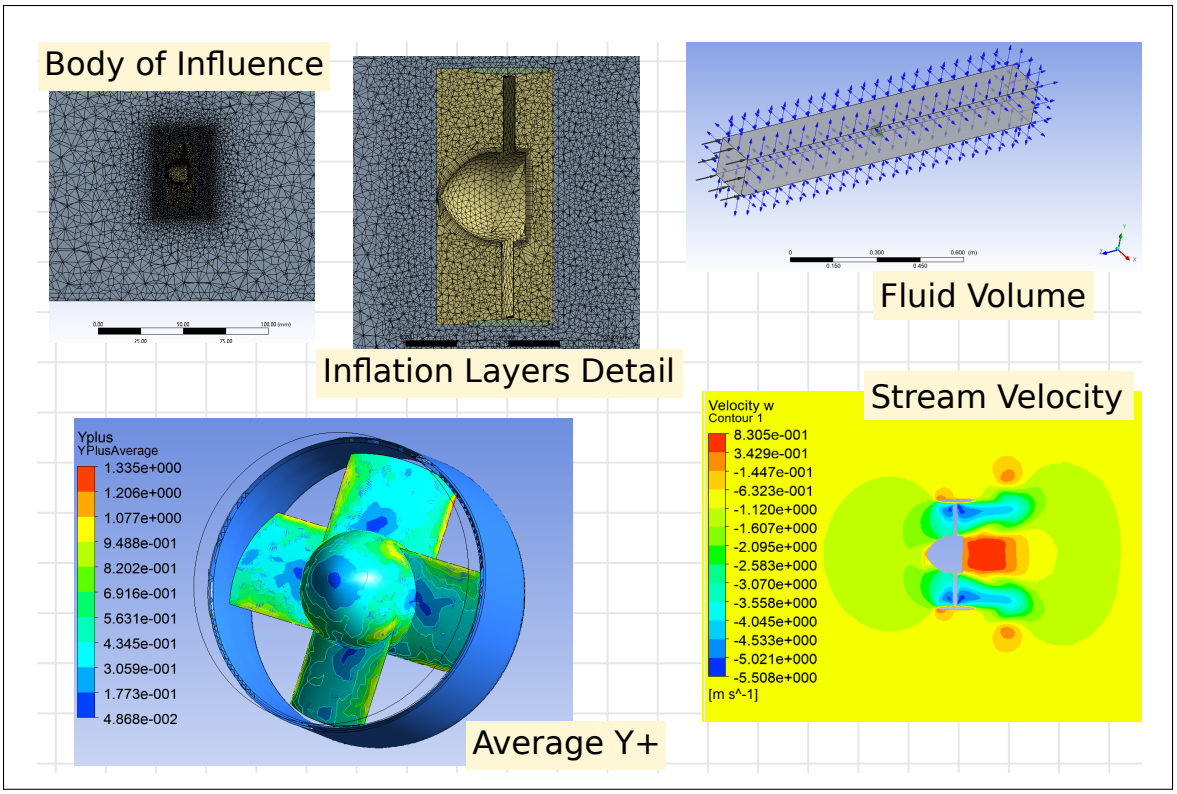

Figure 5.20: Thruster CFD Analysis: ANSYS Setup

The parametric analysis workflow is highlighted on the top of Figure 5.21. The figure also shows the propeller blade profile at lowest and highest pitch angle tested. The blade length, width and bidirectional angle of attacks are parametrically fixed and symmetric. The tip of the blade is given a fixed width and kept horizontal, primarily for the purpose of fabrication, namely 3D printing.

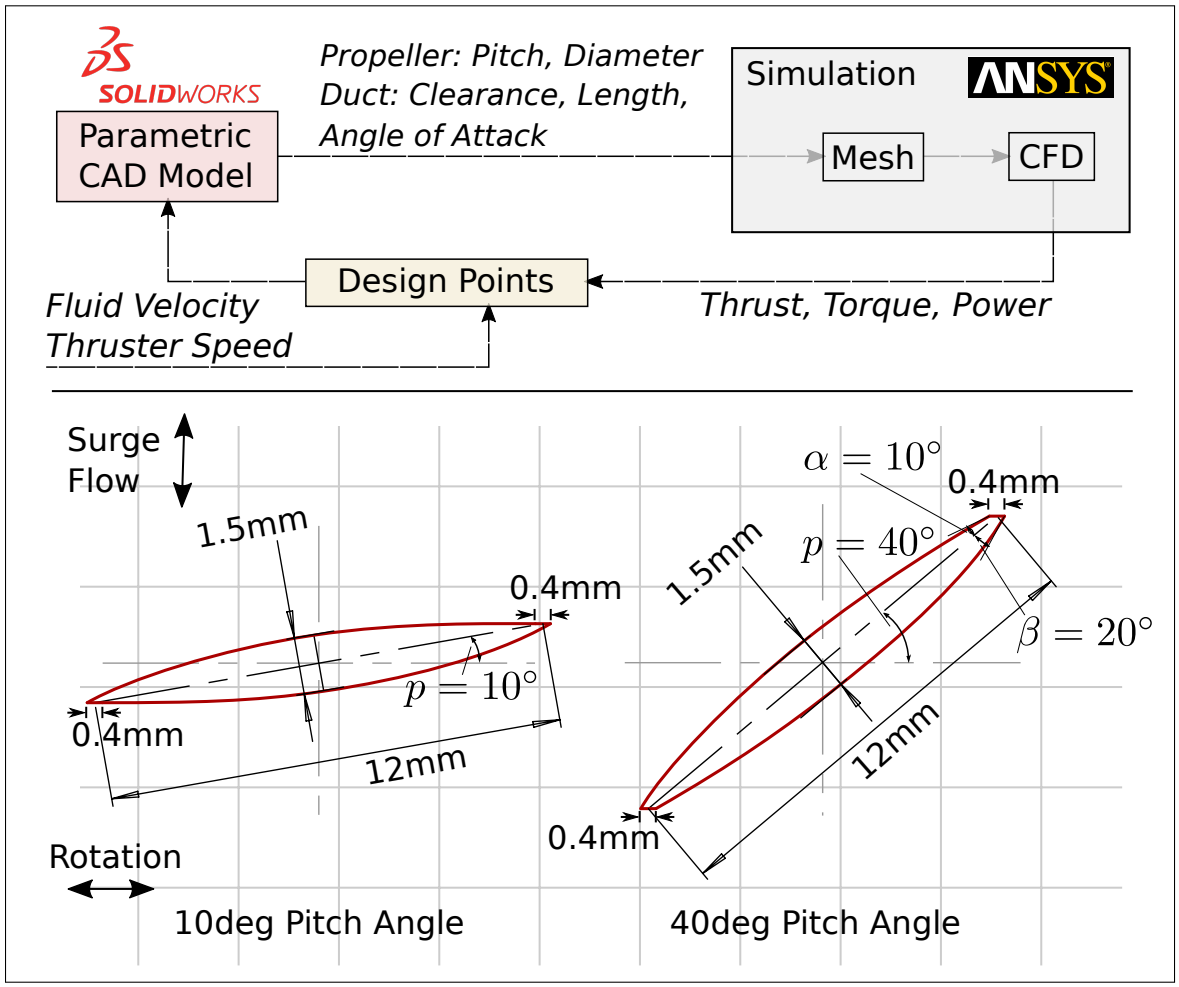

Figure 5.21: Paramteric CFD Thruster Analysis: Geometry and Workflow

Figure 5.22 shows the steady state thrust and torque CFD results for a number of ducted propeller profiles at varying pitch angles and at zero stream advance velocity, matching the same conditions used for the experiments. The results for the thrust match well with the earlier experiments. Fabrication tolerances, propeller imbalance or thrust load measurement accuracy may contribute to the variations

that exist between the CFD results and experiments. Note, for instance, the variation between the results for the 20° pitch propeller, compared to the closely matching results for the other three profiles. This validates the CFD analysis as an adequate method to design thrusters for the μAUV.

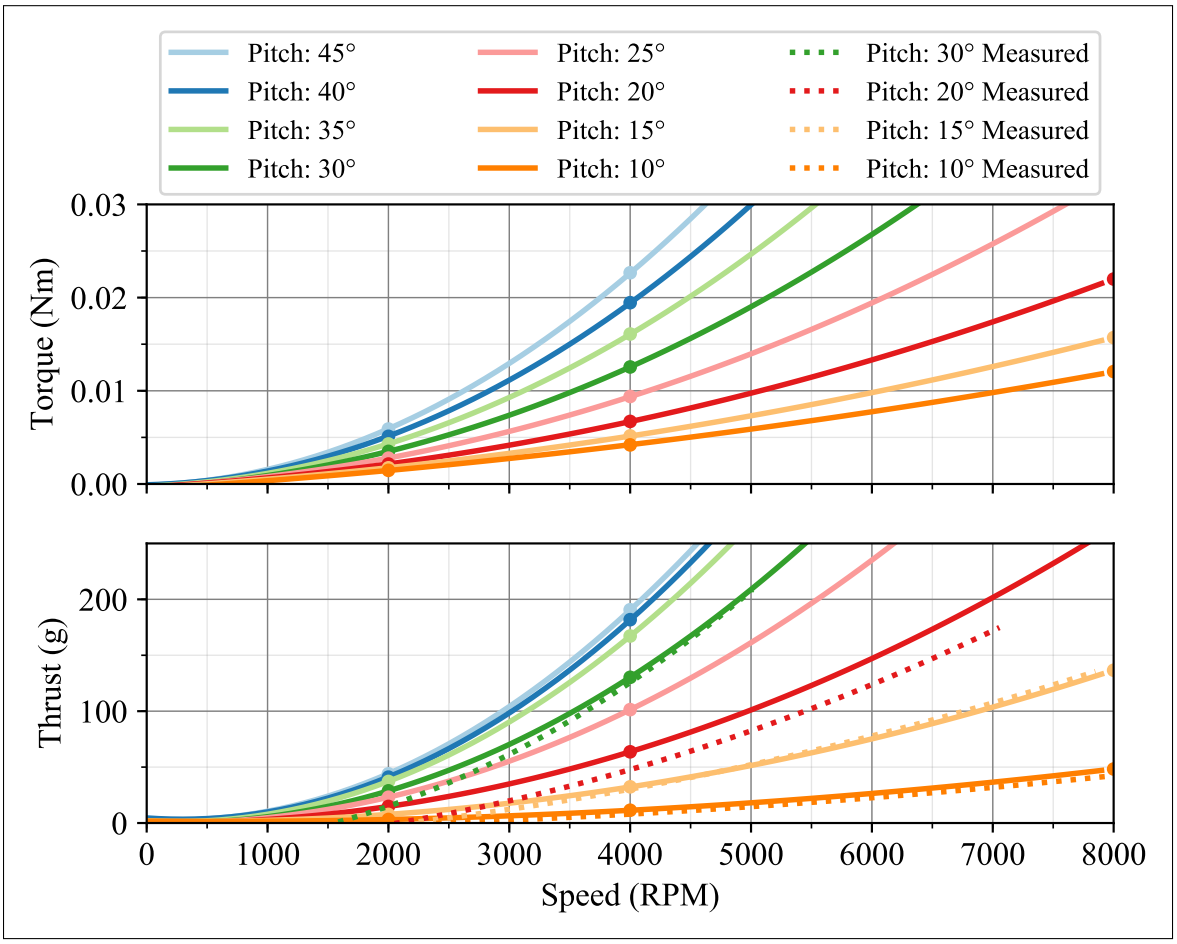

Figure 5.22: Thrust and Torque Performance by CFD Compared to Measurement Impeller Profile: Bidirectional, 30mm Diameter, No. blades: 4, $V_a = 0$, varying blade pitch angle.

While we do not have robust experimental measurements of torque, the torque results from the CFD do fall in the range of torque values measured, we will assume these values are sufficient for the purpose of analyzing the efficiency of the thrusters, and derive the thrust and torque coefficients, K_T and K_Q, as well as evaluate the efficiency of the thrusters using them.

The thruster efficiency is defined as the ratio of the mechanical power delivered over the electrical power supplied.

$$\eta_o = \frac{Q\omega}{VI} \tag{5.14}$$

Figure 5.23 shows the efficiency of the 4 profiles that were experimentally tested, using the torque values estimated by the CFD analysis. Peak propeller efficiencies are relatively similar, but lower pitch propellers provide wider efficiency curves.

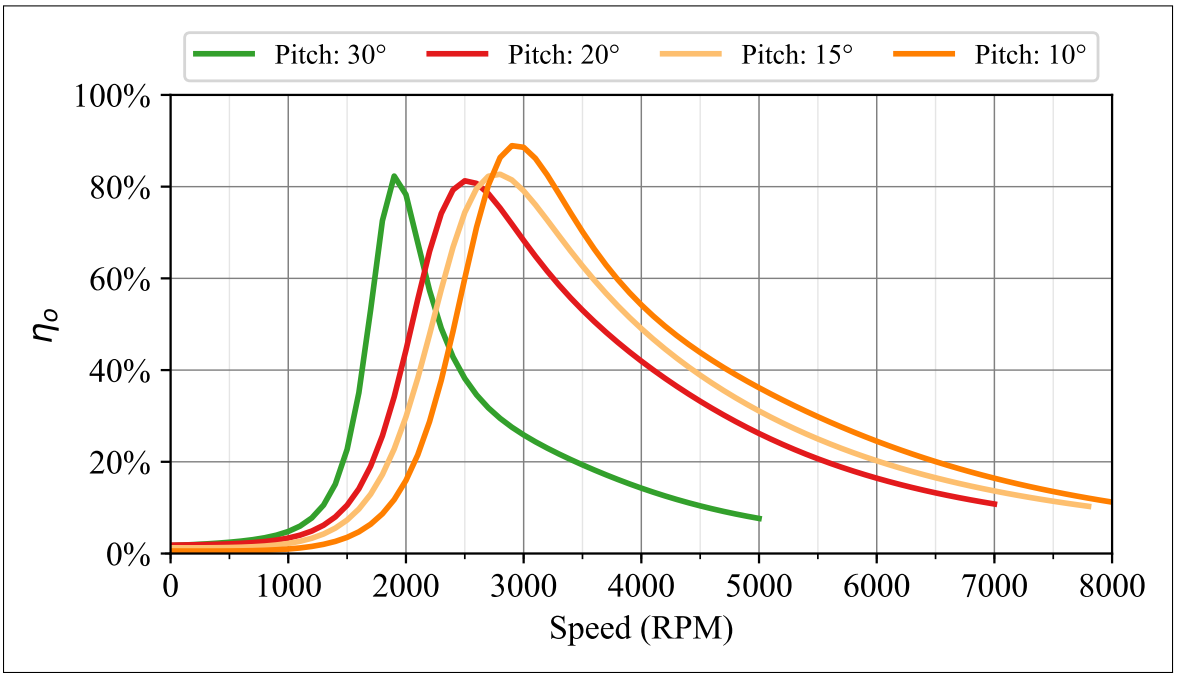

Figure 5.23: Power Efficiency of Propellers
Impeller Profile: Bidirectional, 30mm Diameter, No. blades: 4, $V_a = 0$, varying blade pitch angle.

Expanding the analysis to cover non-zero advance stream velocities V_a, we find the following performance characteristics of the ducted propeller, shown on Figure 5.24. This characteristic curve gives a dimensionless relationship between the advance coefficient J and the thrust and torque coefficients, K_T and K_Q respectively, for a given propeller profile. The analysis was performed with a fixed propeller diameter but varying pitch angle.

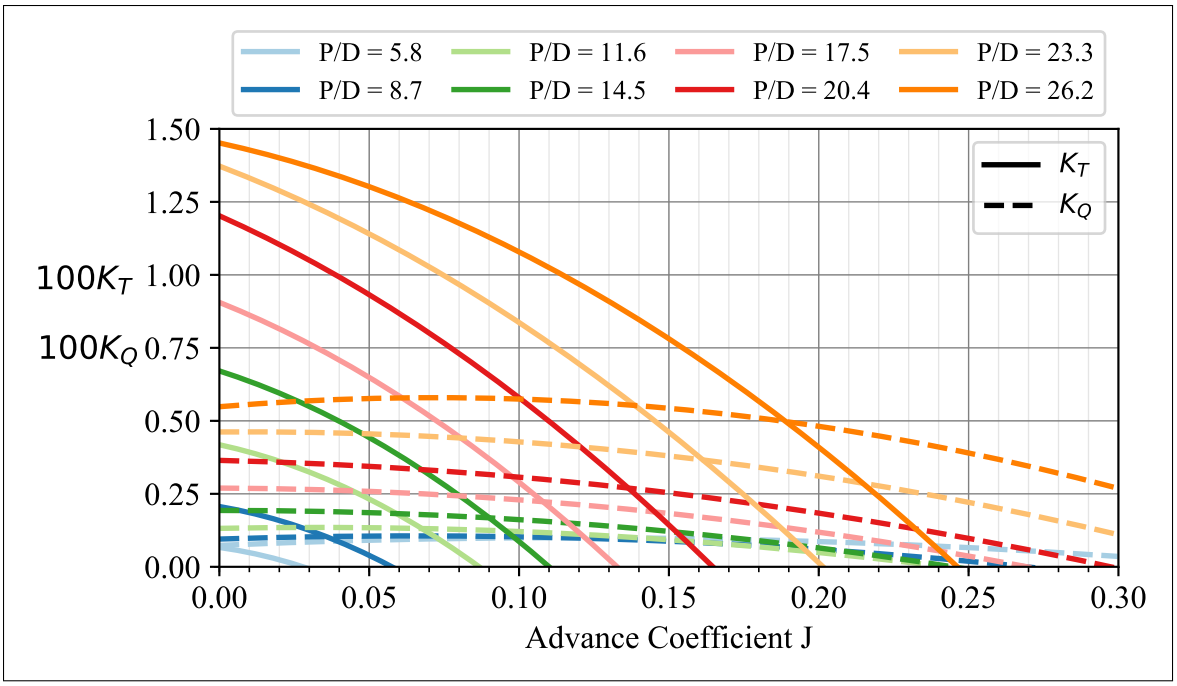

Figure 5.24: Propeller Characteristic Curve From CFD - Constant Propeller Diameter

Examining the effect of varying the duct parameters, we observe relatively less variations. The analysis of varying duct parameters is illustrated on Figure 5.25. The figure also highlights the geometrical profile of the duct. The main parameters are the duct length L, duct angle of attack α and duct clearance from the propeller blade tip t. From the results we notice that the length duct length increases the thrust but converges at a certain length. The thrust performance is more sensitive to tip clearance and even more so to the angle of attack of the duct.

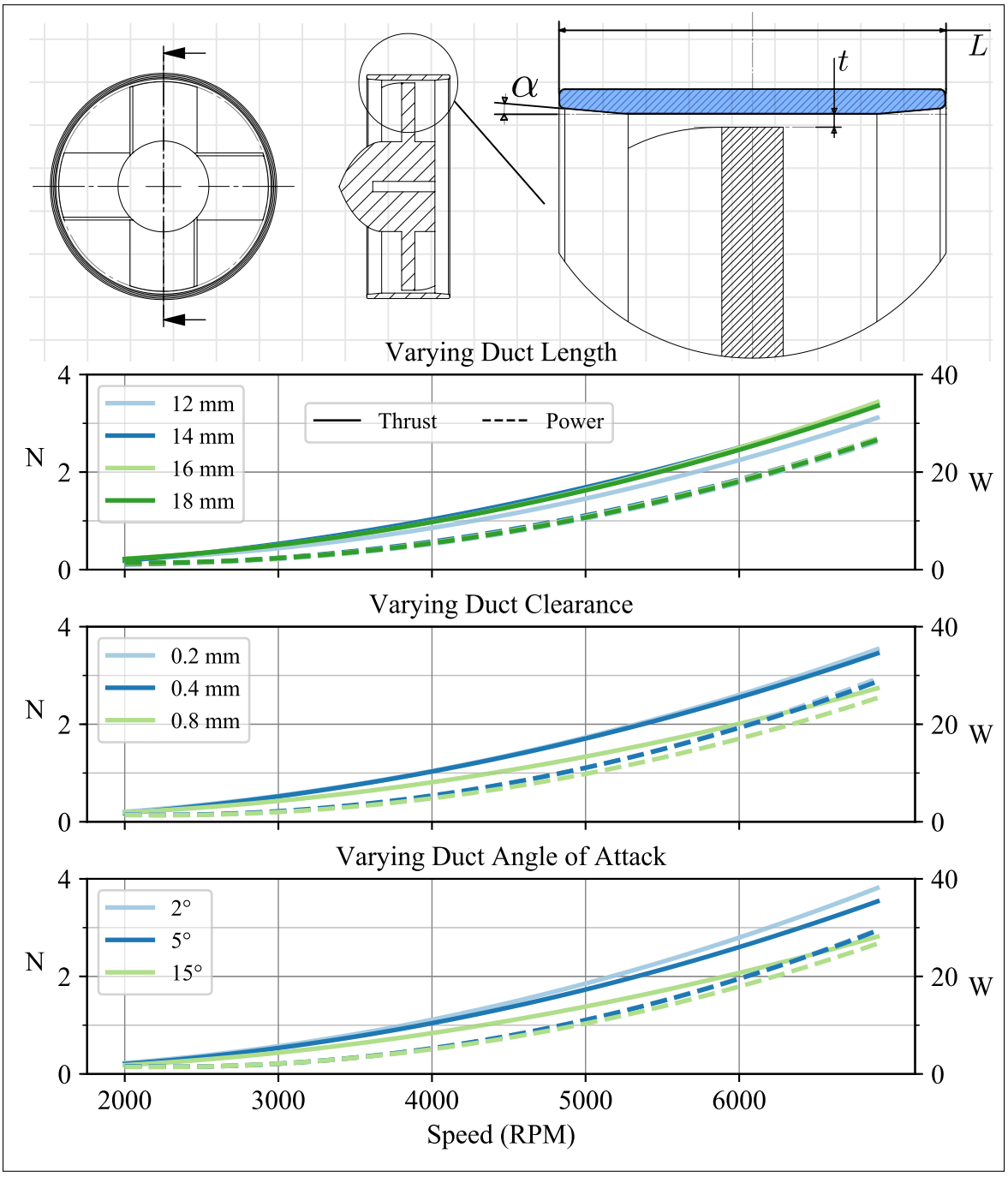

Figure 5.25: Effect of Varying Duct Geometry

5.4.5 Modeling Thruster Dynamics

With the propeller characteristic curve and the experimentally profiled thruster dynamics, we can model the thrusters for the purposes of both simulation and control. Thrust and torque control on the μAUV is achieved through voltage control, and specifically through throttle control by way of pulse width modulation (PWM), with the supply voltage from the battery varying itself, as will be discussed in the next section.

To achieve a desired thrust or torque, we first map the desired thrust or torque to the desired speed, then map the desired speed to a supply voltage setpoint, then map the voltage setpoint to a throttle setpoint, or PWM duty cycle.

We know from the propeller characteristic curve, that thrust and torque decrease with increasing stream velocity. The sensorless BLDC motor and controller are not tuned for low speed control. This produces a discontinuity at low speeds, and more specifically, during a change of direction with the bidirectional thruster as seen on Figure 5.17.

We wish to have a continuous mapping model between thrust/torque and speed of the forms:

$$\hat{\omega}_{T_d} = c_n T^n + c_{n-1} T^{n-1} + ... + c_1 T + c_0,\ c_n \in \mathbb{R} \tag{5.15}$$

$$\hat{\omega}_{Q_d} = c_n Q^n + c_{n-1} Q^{n-1} + ... + c_1 Q + c_0,\ c_n \in \mathbb{R} \tag{5.16}$$

To compensate for the discontinuity at near-zero speeds, we apply a piecewise sigmoid function, to connect the two ends of the curves for the desired model forms of

5.15 and 5.16, such that

$$\hat{\omega}_d \in C^2 = \begin{cases} c_2 T^2 + c_1 T + c_0, & \text{if } \|T\| > T_o \\ \frac{kT}{1+\|T\|}, & \text{if } \|T\| \leq T_o \end{cases}$$

The coefficients will be fixed for a selected thruster; a motor and impeller profile, and T_o can be selected as the smallest nonzero thrust value from the experiment. Note that, unlike the theoretical quadratic model of the thruster from Equation (5.10), we instead use a 2^{nd} order polynomial to model the thruster.

To account for the advance velocity effect on the thrust and torque, we compensate for the velocity set point by the thrust coefficient K_T or torque coefficient K_Q ratios. From the nominal thrust relationship in Equation (5.15), the compensated velocity setpoint, for a fixed propeller geometry is

$$\omega_d^2 = \omega_{sp}^2 \frac{K_{To}}{K_{Tn}} = \alpha_{K_T}(J)\omega_{sp}^2 \tag{5.17}$$

where K_{Tn} is the nominal thrust coefficient ($V_a = 0$), and the K_{To} is the advance-velocity adjusted thrust coefficient, and α_{K_T} is the square root of the ratio of the two. Similarly, for the torque coefficient we have

$$\omega_d^2 = \omega_{sp}^2 \frac{K_{Qo}}{K_{Qn}} = \alpha_{K_Q}(J)\omega_{sp}^2 \tag{5.18}$$

For a given thruster profile, the ratio α can be mapped directly to the advance velocity V_a:

$$\alpha_{K_T} = c_2 J^2 + c_1 J + 1,\ c_n \in \mathbb{R} \tag{5.19}$$

$$\alpha_{K_Q} = c_2 J^2 + c_1 J + 1,\ c_n \in \mathbb{R} \tag{5.20}$$

This gives the following mapping between the desired speed and speed setpoint

$$\omega_d^2 = c_2 \frac{V_a^2}{D} + c_1 \frac{V_a}{D} \omega_{sp} + \omega_{sp}^2 \approx c \frac{V_a^2}{D} + \omega_{sp}^2 \tag{5.21}$$

The coefficients an be calculated from the CFD computed propeller characteristics curve. Figure 5.26 shows the mapping behavior between thrust and speed, as the advance velocity increases, for a selected thruster profile. Note how significant the drop in effective thrust at higher stream velocities. The target μAUVsurge velocity, or cruise velocity, will influence the choice of optimal thruster profile. The effective thrust can be calculated directly by

$$T = N_{K_T}(J)\, T_{nom}\,, \quad N_{K_T}(J) \approx c_2 J^2 + 1 \tag{5.22}$$

And $N_{K_T}(J)$ is the normalized thrust coefficient function, its coefficients can be computed for a specific thruster profile as well.

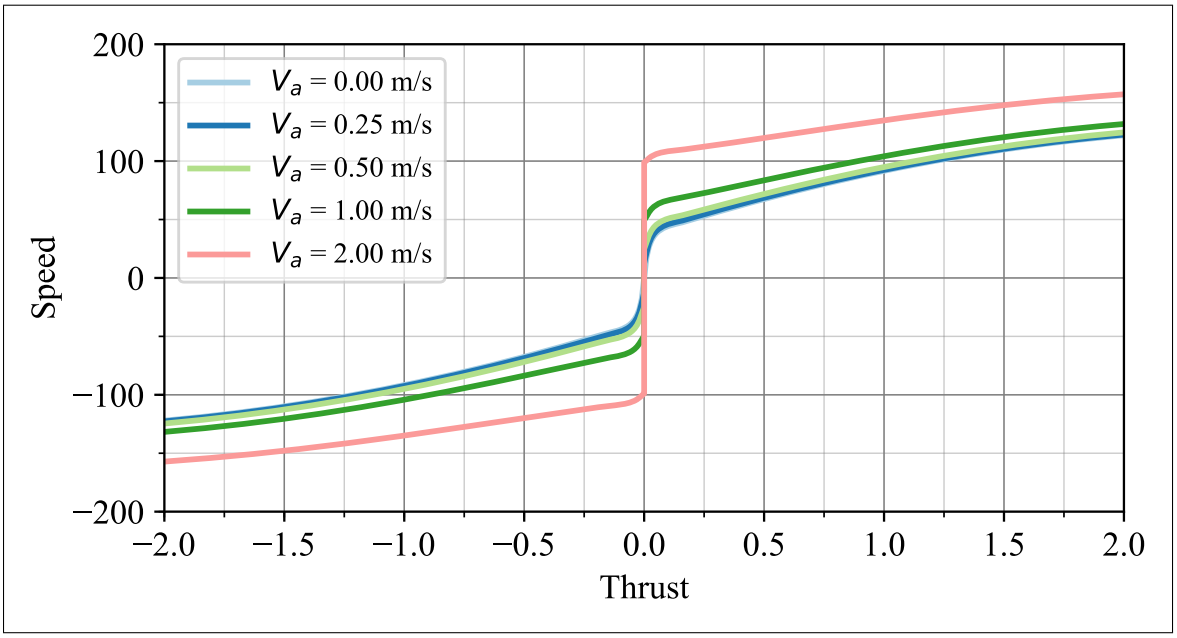

Figure 5.26: Motor Speed Set-Point Mapping from Desired Thrust With V_a Compensation
Impeller Profile: 30mmD, No. Blades: 4, 20^o Blade Pitch Angle

To account for the advance velocity when calculating thrust with the μAUV, we assume that only the axial advance flow affects the thrust performance. By a rigid body dynamic relationship, the thruster velocity becomes

$$\vec{v_T} \cdot \vec{x} = (\vec{v_{B_1}} + \vec{r}_{T/B} \times \vec{v_{B_2}}) \cdot \vec{x} \tag{5.23}$$

as shown on Figure 5.27

Where $\vec{v_{B_1}}$ is the μAUV CoM velocity in the body-frame, assuming static fluid conditions. Defining $\boldsymbol{B}_T$ as the bottom left submatrix of the thrust allocation matrix $\boldsymbol{B}$, the thruster's velocities can be computed as

$$\boldsymbol{v}_T = v_x + \boldsymbol{B}_T^T \begin{bmatrix} v_\theta \\ v_\psi \end{bmatrix} \text{ , } \boldsymbol{B}_T^T \in \mathbb{R}^{4x2} \tag{5.24}$$

v_x, v_θ, v_ψ are the surge, pitch and yaw velocities respectively. The thruster allocation matrix is defined by equation 2.24.

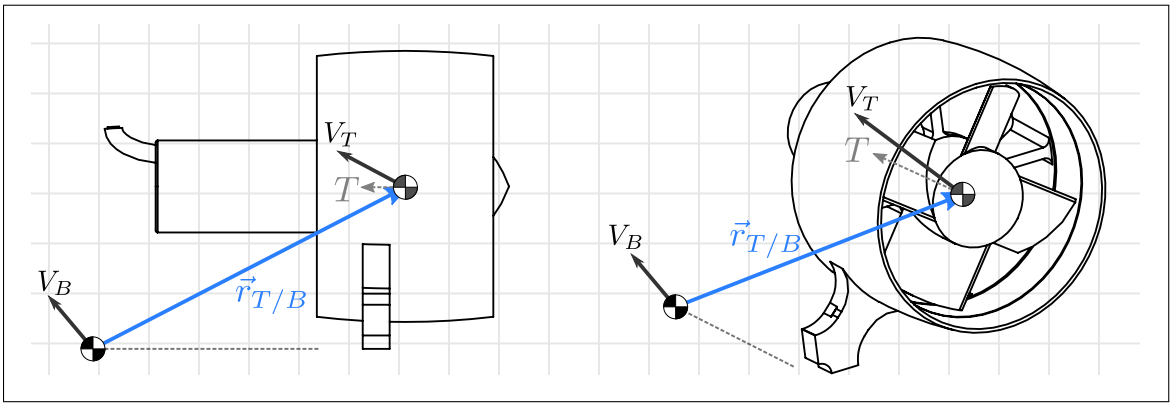

Figure 5.27: Thruster Dynamics - Velocity Relationship

Note that the advance speed effect is also exhibited when the flow is in the opposite direction to the thrust. Looking at the thrusters performance with bidirectional flow, we can see that the effect can be assumed to be symmetric around the $0m/s$ advance speed, as illustrated on Figure 5.28.

A 2^{nd} order polynomial model is also used to map the motor speed setpoint to a

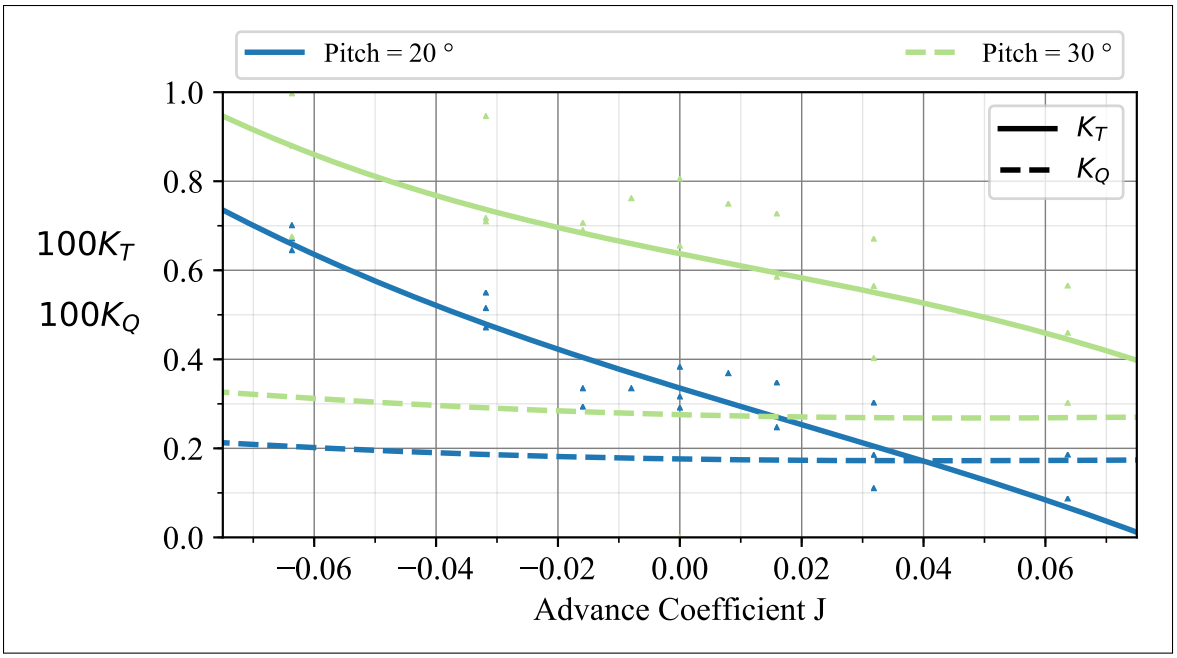

Figure 5.28: Thruster Characteristic Curves with Bidirectional Advance Velocity

voltage setpoint. We can use the experimental results to determine the coefficients, or if we have a model of the motors performance we can use the power and efficiency relationship to map the speed to the voltage.

$$V_{sp} = c_n w^n + c_{n-1} w^{n-1} + ... + c_1 w + c_0 \tag{5.25}$$

The throttle setpoint is then calculated based on the battery's nominal voltage. The throttle and voltage relationship is linear

$$Throttle = \frac{V_{sp}}{V_{bat}} \tag{5.26}$$

To simulate the thruster dynamic response, the reverse of the above process is carried out. The simulator will receive a throttle setpoint and output a thrust and torque value. An additional step in the simulation would include the addition of

a first order response to compute the actual motor velocity

$$\frac{d\omega}{dt} = \frac{1}{\tau}(\omega_{sp}(t) - \omega(t)) \tag{5.27}$$

The selection of the optimal thruster profile needs to be informed by the overall μAUV performance. We will look at the μAUV operational efficiency with the different parameters combined through simulation in Chapter 7.

5.4.6 Thruster Analytical Model

Going back to the conservation of mass momentum principle, the ideal thrust generated by the propeller can be define as

$$T_{ideal} = \dot{m}(v_t - v_s) = \rho A(v_t^2 - v_t v_s) \tag{5.28}$$

where ρ is the density of the fluid, v_t is the propelled fluid velocity downstream the propeller blade, v_s is the free or upstream fluid velocity, and A is the effective propeller area. The propelled fluid velocity is, ideally, a function of the propeller blade pitch and rotation speed.

$$v_t = P\,\omega \tag{5.29}$$

where P is the effective "screw pitch" of the propeller. This ideal model would result in an extreme over estimation of the real thrust force, since the effective stream and propelled fluid velocities are different than in the ideal model. We can, however, express the thrust with a correction factor that is a function of the pitch to diameter ratio.

$$T_{real} = \rho A(v_t^2 - v_t v_s)\,\delta(\frac{P}{D}) \tag{5.30}$$

And from 5.10

$$\delta(\frac{P}{D}) = \frac{K_T D^2}{\pi\omega(P\omega - v_s)} = \frac{cD}{(Pw - vs)} \approx c\frac{D}{P\omega} \tag{5.31}$$

which can be parametrized from the analysis of the propeller profiles to approximate thrust analytically without looking up the thrust coefficient. This form of approximation may be useful for performing design optimizations.

5.5 Battery Model

While not part of the dynamic model, understanding the behavior of the battery can help produce a realistic simulation of the vehicle's performance as well as allow for thrust power compensation via the controller.

The battery type used here is a Lithium-Polymer battery (LiPo). LiPo batteries, like all Lithium-based batteries, have a highly nonlinear discharge behavior due to their chemistry [44], specifically near the far ends of the charged states. A fully charged LiPo cell normally measures at 4.2 Volts, but they are specified as having 3.7 Volts nominal voltage, this reflects the fact that the fully charged voltage, or the Open-Circuit Voltage (OCV), is shortly lived, and that the median, or nominal voltage is more close to 3.7 Volts.

Figure 5.29 below illustrates a typical discharge curve for a LiPo battery. Note that, under load, the in-circuit battery voltage, is lower due to the battery's Equivalent Series Resistance (ESR). The battery's ESR reduces the delivered voltage to the system. The value of the ESR can be measured directly for the installed battery. The cut-off voltage per cell for a LiPo battery typically ranges between 2.9-3.3 Volts, depending on the manufacturer's recommendation.

A fifth order polynomial can be used to model the discharge behavior of the bat-

tery.

$$V_0 = c_5 I^5 + c_4 I^4 + c_3 I^3 + c_2 I^2 + c_1 I + c_0 \tag{5.32}$$

$$V_n = V_0 - I R_{ESR} \tag{5.33}$$

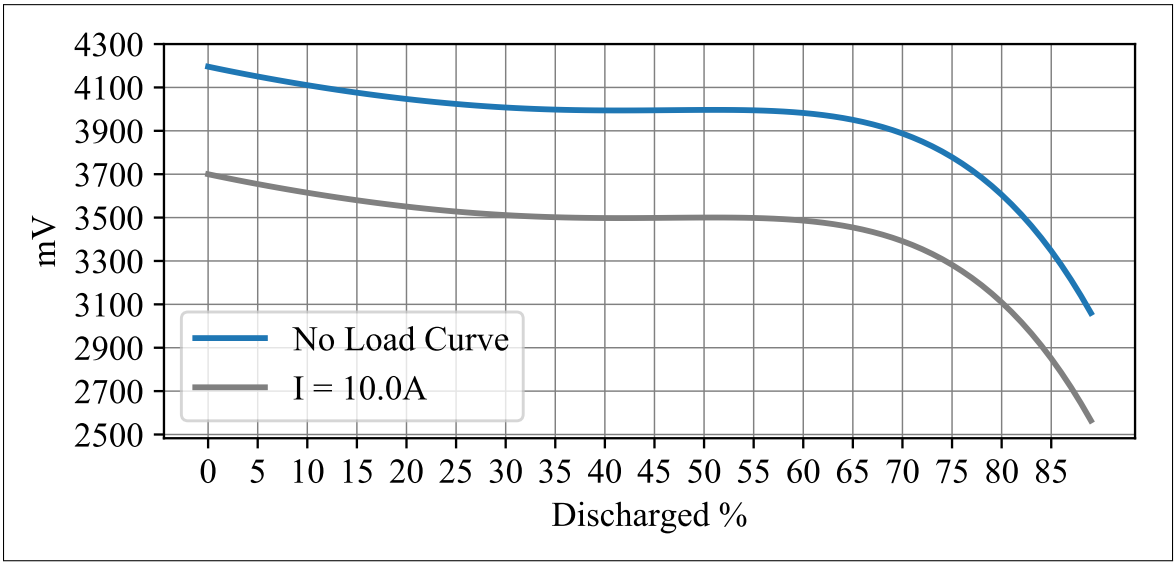

Figure 5.29: LiPo Battery Disharge Curve. ESR = $0.05 Ohms$

5.6 On-Line Parameter Estimation

With the set of parameters identified from the previous section, we can setup an on-line parameter estimation framework that utilizes the μAUV's on-board sensors to estimate the hydrodynamic damping coefficients, the added mass matrix coefficients, the thruster dynamics, as well as calibrate the geometrical offsets between the CoM and CoB $\vec{r}_{B/G}$.

In [55] an Extended Kalman Filter is proposed to perform on-line parameters estimations, the simulation results in the cited work showed positive outcomes for identifying the hydrodynamic damping coefficients for an underwater vehicle in

open-water. We will propose an approach here to perform on-online parameter estimation based on the parameters we are interested in the most, using a Hybrid Extended Kalman Filter EKF, and by using the dynamic model as proposed in Chapter 2.

Given the following Hydrid Extended Kalman Filter algorithm from [57], where we have the continuous nonlinear dynamic system and associated discrete measurement model.

$$\dot{x} = f(x, u, w, t) \tag{5.34}$$

$$y_k = h_k(x_k, m_k) \tag{5.35}$$

where x is the system state, u is the input to the system, w is the process noise and v_k is the measurement noise. The process and measurement noise are assumed to be white, Gaussian with zero-mean: $w(t) \sim N(0, Q)$, $m_k \sim N(0, R)$. Q is the process noise covariance matrix and R is the measurements noise covariance matrix. The goal of the Hybrid-EKF is to estimate the state $\hat{x}$ and its associated covariance matrix P. The continuous-time covariance matrix is modeled as

$$\dot{P} = \mathrm{AP} + PA^T + \mathrm{LQL}^T \tag{5.36}$$

$\boldsymbol{A}$ and $\boldsymbol{L}$ are the partial derivatives of the nonlinear dynamic function $f(x, u, w, t)$, with respect to the state and noise respectively, computed at the estimate $\hat{x}$.

$$A = \frac{\partial f}{\partial x}|_{\hat{x}},\ L = \frac{\partial f}{\partial w}|_{\hat{x}} \tag{5.37}$$

The algorithm follows a two-step update, a time-update step where the continuous nonlinear state and covariance matrix are integrated to produce aproiri estimates

$\hat{x}^-$ and $\hat{P}^-$, followed by a measurement update step to produce the aposterior estimates $\hat{x}^+$ and $\hat{P}^+$. The algorithm proceeds as summarized in Algorithm 1 below.

Algorithm 1 Hybrid EKF

Initialize $\hat{x}_0^+ = E(x_0)$ ▷ Time-Update

Initialize $P_0^+ = E\left[\left(x_0 - \hat{x}_0^+\right)\left(x_0 - \hat{x}_0^+\right)^T\right]$

while Estimator Running do

  Integrate: $\hat{x}^- \leftarrow \dot{x} = f(\hat{x}, u, 0, t)$

  Integrate: $\hat{P}^- \leftarrow \dot{P} = \mathrm{AP} + PA^T + \mathrm{LQL}^T$

  if New Measurement Received then ▷ Measurement Update

    Compute:

      $K_k = P_k^- H_k^T \left(H_k P_k^- H_k^T + M_k R_k M_k^T\right)^{-1}$

      $\hat{x}_k^+ = \hat{x}_k^- + K_k\left(y_k - h_k\left(\hat{x}_k, 0\right)\right)$

      $P_k^+ = \left(I - \mathrm{K}_k H_k\right) P_k^- \left(I - \mathrm{K}_k H_k\right)^T + K_k M_k R_k M_k^T K_k^T$

  end if

end while

H_k and M_k are the partial derivatives matrices of the discrete measurement model $h_k(x_k, m_k)$ with respect to x_k and v_k respectively, computed at the apriori estimate $\hat{x}^-$.

For our system, we can compose our state vector, $\boldsymbol{x}$, from the inertial pose and body-rates:

$$\boldsymbol{x} = \begin{bmatrix} \boldsymbol{p} \\ \boldsymbol{v} \end{bmatrix}, \ \boldsymbol{p} \in \mathbb{R}^7, \ \boldsymbol{v} \in \mathbb{R}^6 \tag{5.38}$$

The nonlinear dynamics can be defined as

$$\dot{\boldsymbol{x}} = \begin{bmatrix} \dot{\boldsymbol{p}} \\ \dot{\boldsymbol{v}} \end{bmatrix} = f(\boldsymbol{x}, \boldsymbol{\tau}, \boldsymbol{w}, t) \tag{5.39}$$

$\dot{\boldsymbol{v}}$, the body-rates vector derivative, can be calculated from the inverse dynamics

$$\dot{\boldsymbol{v}} = \tilde{\boldsymbol{M}}^{-1}(\boldsymbol{\tau}(\boldsymbol{\omega}) - \boldsymbol{C}(\boldsymbol{v}) - \boldsymbol{D}(\boldsymbol{v}) - \boldsymbol{G}({}^I\boldsymbol{R}_B)) \tag{5.40}$$

And the inertial pose vector derivate $\dot{\boldsymbol{p}}$ can be calculated from $\dot{\boldsymbol{v}}$, by the inverse

jacobian $\boldsymbol{J}^{-1}(q)$, described later in Chapter 6.

$$\dot{\boldsymbol{p}} = \boldsymbol{J}^{-1}(q)\dot{\boldsymbol{v}} \tag{5.41}$$

With regards to measurements, this depends on the available sensors. In the μAUV, we can at a minimum measure the angular body-rates by the gyroscope, the linear acceleration by the accelerometer. If we have a depth sensor we can measure position along the water depth, and attitude with the fused inertial measurement model. We can also measure the current draw and the speed of each of the thrusters. This gives the following measurement vector

$$\boldsymbol{y}[k] \in \mathbb{R}^{16} = \begin{bmatrix} \dot{\boldsymbol{v}}_1[k] & \boldsymbol{v}_2[k] & {}^{I}z_B[k] & \boldsymbol{q}[k] & I[k] & \boldsymbol{\omega}[k] \end{bmatrix}^T + \boldsymbol{m}_k[k] \tag{5.42}$$

The partial derivate matrices can be computed symbolically from the above given relationships and used in the Hybrid-EKF algorithm. We are interested however in using the above dynamic relationship and Hybrid-EKF to estimate the model parameters. We can augment the state vector with the parameters vector $\boldsymbol{\Phi}$ that includes the desired parameters to be estimated

$$\dot{\boldsymbol{x}}' = \begin{bmatrix} \dot{\boldsymbol{p}} \\ \dot{\boldsymbol{v}} \\ \boldsymbol{\Phi} \end{bmatrix} + \boldsymbol{w} \tag{5.43}$$

The parameter vector can be composed of the 12 diagonal elements of the hydrodynamic damping matrix, the 6 diagonal elements of the added mass. It can include the three elements of $\vec{r}_{B/G}$, and the thrust and torque coefficients K_T and K_Q, which can be divided to forward and reverse thrust, assuming a simple quadratic

relationship in the thruster model. This gives

$$\boldsymbol{\Phi}^T \in \mathbb{R}^{25} = \begin{bmatrix} dg[\boldsymbol{M}_A](\dot{\boldsymbol{v}}) & dg[\boldsymbol{D}_Q](\boldsymbol{v}) & dg[\boldsymbol{D}_L](\boldsymbol{v}) & \boldsymbol{r}_{B/G}(\boldsymbol{G}) & ... \\ K_{T_F}(\boldsymbol{\tau}, \boldsymbol{\omega}, I, v_x) & K_{Q_F}(\boldsymbol{\tau}, \boldsymbol{\omega}, I, v_x) & K_{T_R}(\boldsymbol{\tau}, \boldsymbol{\omega}, I, v_x) & K_{Q_R}(\boldsymbol{\tau}, \boldsymbol{\omega}, I, v_x) & \end{bmatrix} \quad (5.44)$$

Where $dg[]$ denotes the diagonal elements of the matrix. $\boldsymbol{D}_Q$ and $\boldsymbol{D}_L$ denote the quadratic and linear hydrodynamic elements respectively, assuming a 2^{nd} order polynomial model with no zero offset. And the F and R subscripts in the thrust and torque coefficients denote forward and reverse respectively.

We can also reduce the above on-line estimation algorithm to one dimension, and adapt it to the decay experiment presented in section 5.3.2, to improve the experimental method in estimating the hydrodynamic coefficients, as well as compute the added mass terms. With the experimental setup, measurements will also include direct full pose measurement from the encoder.

CHAPTER 6

UNDERWATER VISIO-DYNAMIC SITL SIMULATION

Now that the dynamic model corresponding to the realized μAUV has been defined, it will be used to develop a simulation environment to carry out further controller design and to assess the performance of the μAUV.

A dynamic simulation platform of the μAUV is a valuable tool for developing and testing perception and control algorithms, as the complexities involved in testing the μAUV underwater and applying changes are high compared to overground platforms. A reasonably photo-realistic simulation of the underwater environment is also highly valuable in generating virtual camera images to test the perception algorithms. We leverage an existing open-source underwater scenery rendering tool for underwater vehicles, from [58], along with an open-source software-in-the-loop (SITL) controller stack, targeted toward unmanned aerial vehicles, from [59].

We leverage these two tools, and integrate other components around them, to build a complete visual dynamic SITL simulation of the μAUV. The simulation setup is illustrated on Figure 6.1.

The modules, or nodes, of the simulation operate and intercommunicate over the ROS framework [60]. The visual modules group includes the visual rendering component UWSim [58], based on Open-Scene Graph [61], as well as the structure light projection model and the virtual camera model. The sensor modules add appropriate stochastic noise, biases or drift to generate realistic sensor data to the control and vision modules.

The vision modules emulate the on-board camera, where image processing, pose estimation from projected light and obstacle detection are performed. The dynamic

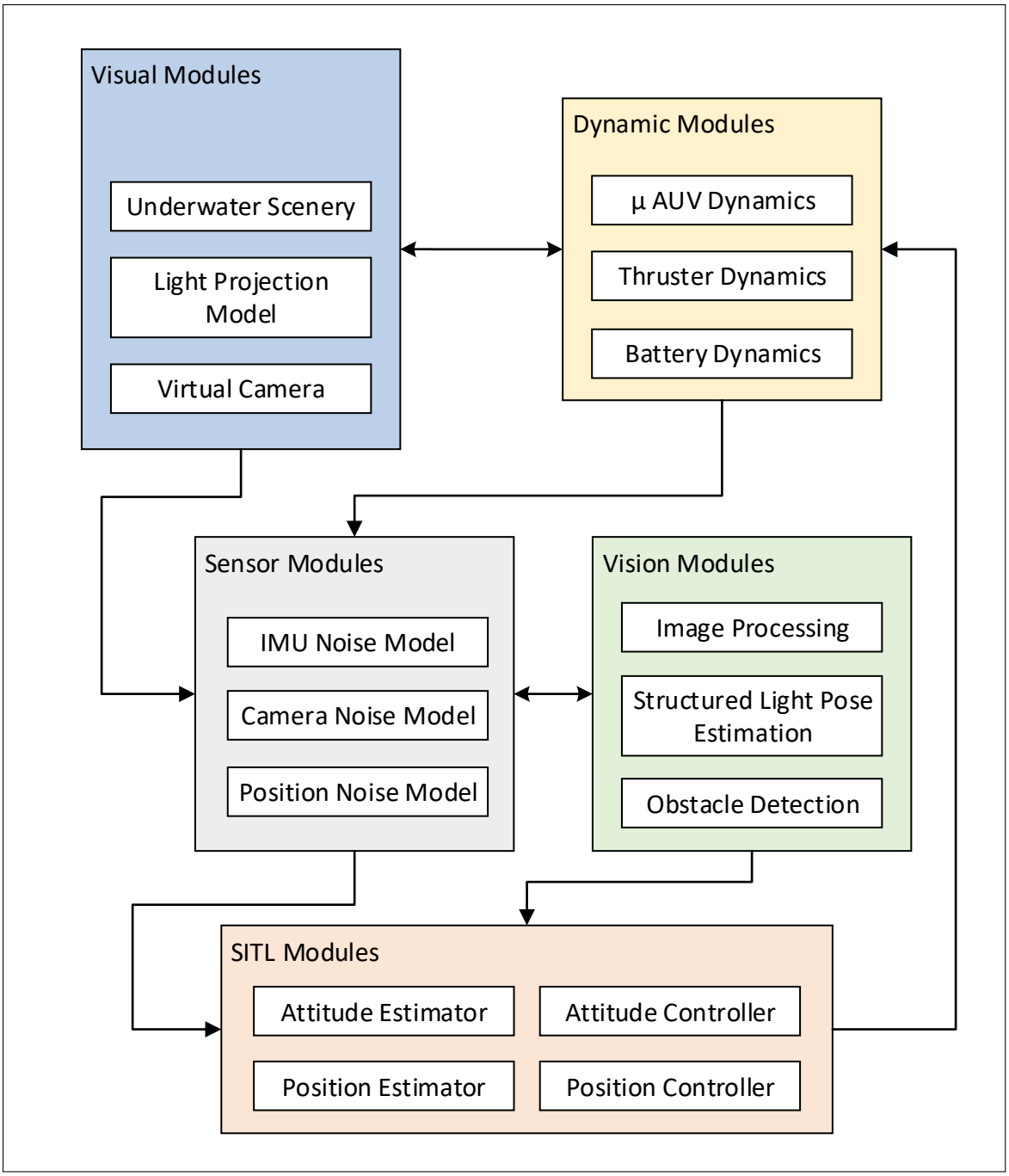

Figure 6.1: Visual Dynamic Simulation Setup

modules as the name suggests include all the dynamic components associated with the μAUV system. And finally, the SITL modules include the pose and attitude estimators, and the controllers which can be ported directly onto the on-board controller in the μAUV.

Details of some of the components of the simulation will be discussed in this chapter.

6.1 Quaternion Attitude Representation

In simulating and controlling the μAUV, quaternion operators will be used to represent attitude, perform attitude and rate frame transformations. The vehicle is expected to operated over all possible attitude angles and using quaternion rotations will prevent the occurrence of geometric singularities. This section is only intended to summarize the key quaternion notation and operation used in this work. For a more comprehensive review, the reader is advised to review [62]. The right handed convention, or Hamilton convention, of quaternion rotation will be used where the imaginary units are defined as $k = ij = -ji$. A quaternion is composed of real scalar part and an imaginary vector part.

$$\boldsymbol{q} = q_w + \boldsymbol{q}_v = q_r + q_i i + q_j j + q_k k \tag{6.1}$$

A unit quaternion is a normalized quaternion such that

$$\boldsymbol{q}_{unit} = \frac{\boldsymbol{q}}{||\boldsymbol{q}||} \tag{6.2}$$

A quaternion product is defined as

$$\boldsymbol{q} \otimes \boldsymbol{p} = \begin{bmatrix} p_r q_r - p_i q_i - p_j q_j - p_k q_k \\ p_r q_i + p_i q_r + p_j q_k - p_k q_j \\ p_r q_j - p_i q_k + p_j q_r + p_k q_i \\ p_r q_k + p_i q_j - p_j q_i + p_k q_r \end{bmatrix} \tag{6.3}$$

A quaternion's conjugate $\boldsymbol{q}^*$ has the imaginary part's sign inverted.

$$\boldsymbol{q}^* = \begin{bmatrix} q_w \\ -\boldsymbol{q}_v \end{bmatrix} \tag{6.4}$$

A quaternion's inverse is defined as giving the identity quaternion when a quaternion is multiplied by its inverse, and for a unit quaternion the inverse of a quaternion is equal to its conjugate

$$\boldsymbol{q} \otimes \boldsymbol{q}^{-1} = \boldsymbol{q}_{identity} \tag{6.5}$$

$$\boldsymbol{q}_{unit}^{-1} = \boldsymbol{q}_{unit}^* \tag{6.6}$$

From here on, references to a quaternion will mean a unit quaternion unless otherwise noted. Given a unit rotation vector $\boldsymbol{u}$ and associated rotation angle ϕ, $\langle \boldsymbol{u}, \phi \rangle$, a unit quaternion can be composed as

$$\boldsymbol{q} = \begin{bmatrix} cos(\phi/2) \\ \boldsymbol{u} sin(\phi/2) \end{bmatrix} \tag{6.7}$$

Given the vector $\boldsymbol{x} \in \mathbb{R}^3$, the rotation operation of a vector in $\mathrm{SO}(3)$, from say frame B to frame A, using quaternions, with its equivalent rotation operation using Euler angles $\mathrm{SO}(3)$, is given as

$${}^A\boldsymbol{x} = \boldsymbol{q}_{BA} \otimes {}^B\boldsymbol{x} \otimes \boldsymbol{q}_{BA}^* \Leftrightarrow {}^A\boldsymbol{x} = {}^A\boldsymbol{R}_B \, {}^B\boldsymbol{x} \tag{6.8}$$

$\boldsymbol{q}_{BA}$ is the quaternion that represents a unit vector along frame B's origin, in frame A

The rotation matrix $\boldsymbol{R} \in \mathrm{SO}(3)$ can be defined from the unit rotation vector and

angle $\langle \mathrm{u}, \phi \rangle$ by Rodrdigues Rotation Formula

$$\mathrm{R} = \mathrm{I} + sin\phi[\mathrm{u}]_x + (1 - cos\phi)[\mathrm{u}]_x^2 \tag{6.9}$$

The operator $[\,]_x$ is denotes the skew symmetric matrix $[\mathrm{v}]_x \in \mathbb{R}^{3\times3}$ of a vector in $\mathrm{v} \in \mathbb{R}^3$, such that

$$[\mathrm{v}]_x = \begin{bmatrix} 0 & -v_x & v_y \\ v_z & 0 & -v_x \\ -v_y & v_x & 0 \end{bmatrix} \tag{6.10}$$

The rotation matrix $\mathrm{R} \in \mathrm{SO}(3)$ can also be defined, in a more useful format, using the unit quaternion

$$\mathrm{R} = \begin{bmatrix} -2q_j^2 - 2q_k^2 + 1 & 2q_iq_j + 2q_kq_r & 2q_iq_k - 2q_jq_r \\ 2q_iq_j - 2q_kq_r & -2q_i^2 - 2q_k^2 + 1 & 2q_iq_r + 2q_jq_k \\ 2q_iq_k + 2q_jq_r & -2q_iq_r + 2q_jq_k & -2q_i^2 - 2q_j^2 + 1 \end{bmatrix} \tag{6.11}$$

, and its inverse

$$\mathrm{R}^{-1} = \begin{bmatrix} -2q_j^2 - 2q_k^2 + 1 & 2q_iq_j - 2q_kq_r & 2q_iq_k + 2q_jq_r \\ 2q_iq_j + 2q_kq_r & -2q_i^2 - 2q_k^2 + 1 & -2q_iq_r + 2q_jq_k \\ 2q_iq_k - 2q_jq_r & 2q_iq_r + 2q_jq_k & -2q_i^2 - 2q_j^2 + 1 \end{bmatrix} \tag{6.12}$$

The mapping between quaternion and Euler rotation matrices is a single mapping, while the reverse, mapping from quaternion space to Euler angles, is not, and produces a double mapping. This can be directly observed by looking at equation 6.7, where solving for $\phi/2$, the angle between a quaternion vector and the origin unit vector, from $cos(\phi/2)$, in the range $0 < \phi < 4\pi$ we get two possible solutions.

The μAUV attitude can be represented in $SO(3)$ using unit quaternions as presented above. The double mapping from quaternions to Euler angles becomes an issue only when performing attitude control, but it can be mitigated by carrying the sign of the real parts, this will be discussed in Chapter 9.

To represent attitude rates with quaternions, quaternion derivatives and integrals are used. The time derivative of a quaternion given its angular rate vector $\Omega(t) \in \mathbb{R}^3$, is given as

$$\dot{\boldsymbol{q}} = \boldsymbol{q} \otimes \Omega(t) \tag{6.13}$$

And its integral, for a constant Ω can be expressed as

$$\boldsymbol{q}(t) = \boldsymbol{q}(0) \otimes e^{\Omega t} \tag{6.14}$$

In discrete-form, assuming constant Ω_c in the interval δt, the integral using Zeroth order integration can be expressed as

$$\boldsymbol{q}[k+1] = \boldsymbol{q}[k] \otimes \boldsymbol{q}\{\Omega_c \Delta t\} \tag{6.15}$$

$$\boldsymbol{q}\{\Omega_c \Delta t\} = \begin{bmatrix} cos(||\Omega_c|| \frac{\Delta t}{2}) \\ \frac{\Omega_c}{||\Omega_c||} sin(||\Omega_c|| \frac{\Delta t}{2}) \end{bmatrix} \tag{6.16}$$

Equation 6.15 can be used to express and integrate attitude rates in the inertial frame, without the need to handle Euler angles ranges, as will be shown in the next section on the μAUV dynamics simulation.

While visual interpretations are not easily deduced from quaternion values, key rotations configurations are represented on Figure 6.2, and they can aid in providing a sanity check on the quaternion operations.

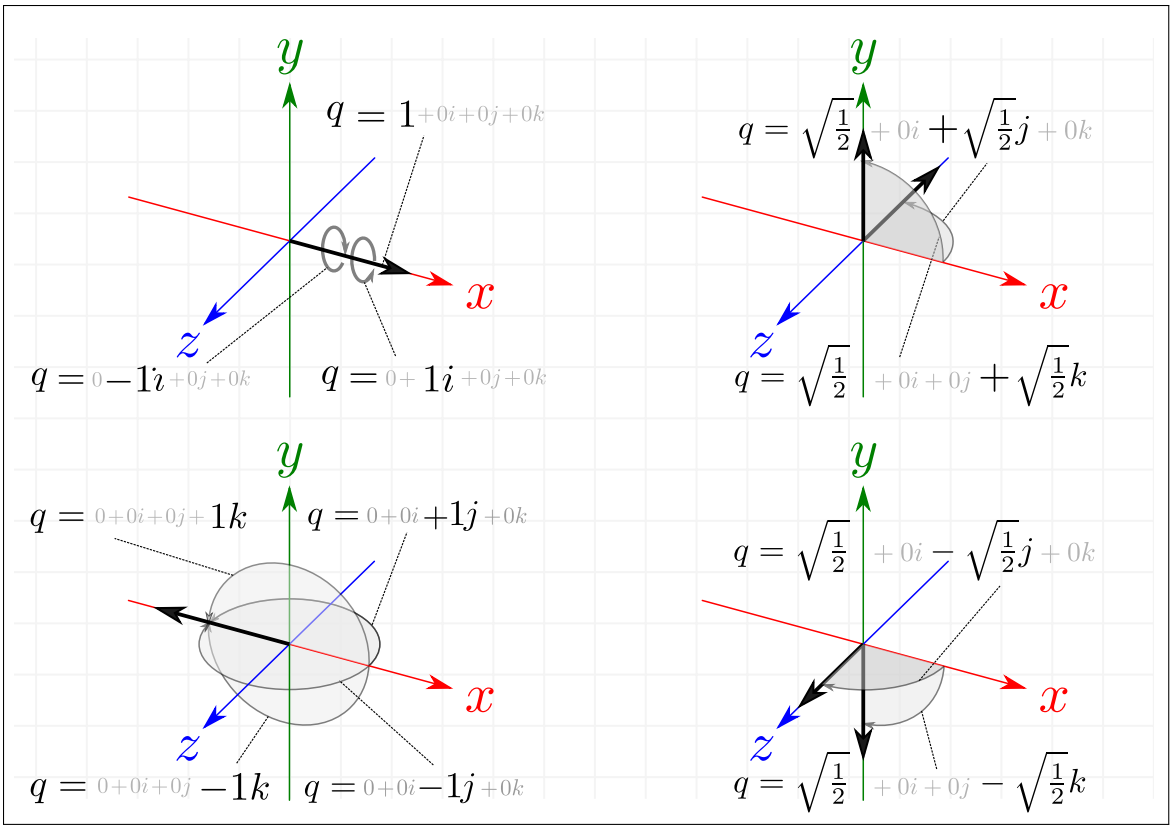

Figure 6.2: Visualizing Simple Quaternion Representations

To transform frame rates from frame A to frame B, the Jacobian operator $\boldsymbol{J}(\boldsymbol{q})$ can be used such that

$$^{B}\dot{\boldsymbol{x}} \in \mathbb{R}^3 = \boldsymbol{J}(\boldsymbol{q}_{BA})^{A}\dot{\boldsymbol{x}},\ \boldsymbol{J}(\boldsymbol{q}) = \begin{bmatrix} 0.5qr & -0.5qk & 0.5qj \\ 0.5qk & 0.5qr & -0.5qi \\ -0.5qj & 0.5qi & 0.5qr \\ -0.5qi & -0.5qj & -0.5qk \end{bmatrix} \tag{6.17}$$

To convert between Euler angles and Quaternions, we first have to define the Euler rotation sequence used. Out of the 12 possible sequences, a common sequence is the Tait-Bryan ZYX, or 3-2-1, sequence, in which the full rotation expression is composed of a yaw ψ, pitch θ and then followed by roll ϕ: $\boldsymbol{R}(\phi,\theta,\psi) \in \mathbb{R}^{3\times3} = \boldsymbol{R}(\phi)\boldsymbol{R}(\theta)\boldsymbol{R}(\psi)$.

Given the rotation matrix $\boldsymbol{R}(q)$ 6.11 the Euler angles can be obtained by

$$\begin{bmatrix} \phi \\ \theta \\ \psi \end{bmatrix} = \begin{bmatrix} tan^{-1}\frac{R_{23}(q)}{R_{33}(q)} \\ -sin^{-1}R_{13}(q) \\ tan^{-1}\frac{R_{12}(q)}{R_{11}(q)} \end{bmatrix} \tag{6.18}$$

To convert from Euler angles to Quaternion representation the ZYX Tait-Bryan sequence can be applied in with unit vector rotations as given by equation (6.7)

6.2 μAUV Dynamics

The μAUV dynamics stack is summarized in Algorithm 2. Throttle setpoints, external forces and an in-pipe mapping function are updated into the dynamics loop. The throttle setpoints are mapped into speed setpoints using the mapping model discussed in Chapter 5.

From the speed setpoint, the thruster dynamics and output forces are calculated. The motor speeds are used to update the battery charge level. Then, the inverse dynamics is performed where the model parameters are computed based on the model presented in Chapter 2 and the parameters derived in Chapter 5. And finally, the inverse kinematics step updates the pose of the vehicle, and the states are published to simulator network.

The step response of the μAUV is summarized on Figure 6.3. The figure compares the response between implementing ideal nominal thrust forces compared to the advance-velocity-adjusted case. The figure also shows the surge response when in-pipe drag effects are added.

There are two opposing actions observed here. As the vehicle increases in its velocity, the effective thrust decreases due to the advance velocity effect, but in the pipe,

Algorithm 2 μAUVDynamics

procedure Dynamics(Th, τ_{ext}, $\hat{f}_D$)
    Initialize $\boldsymbol{M}$, $\boldsymbol{B}$ ▷ Initialize Mass Matrix & Thruster Allocation Matrix
    Callback Interrupt: Th ▷ Throttle Setpoint Update
    Callback Interrupt: τ_{ext} ▷ Environment Forces Update
    Callback Interrupt: $\hat{f}_D$ ▷ In-Pipe Mapping Update
    while Simulation Running do
        $\boldsymbol{\omega}_{sp} = f(Th)$ ▷ Throttle to Speed Setpoint
        τ_m, $\boldsymbol{\omega} = f(\boldsymbol{\omega}_{sp}, \boldsymbol{B}, \boldsymbol{v})$ ▷ Thruster Dynamics
        $V_{nom} = f(\boldsymbol{\omega})$ ▷ Battery Dynamics
        $\boldsymbol{v} = \int Dynamics(\boldsymbol{q}, \boldsymbol{v}, \tau)dt$ ▷ Inverse Dynamics
        $\boldsymbol{q} = Kinematics(\boldsymbol{q}, \boldsymbol{v})$ ▷ Inverse Kinematics
    end while
end procedure

function $Dynamics(\boldsymbol{q}, \boldsymbol{v}, \tau)$
    $D = Damping(\boldsymbol{v})$
    $C = Coriolis(\boldsymbol{v})$
    $g = gravity(\boldsymbol{q})$
    $\dot{\boldsymbol{v}} = \boldsymbol{M}^{-1}(\tau - D - C - g)$ ▷ Inverse Dynamics Model
    return $\int \dot{\boldsymbol{v}}dt$
end function

function $Kinematics(\boldsymbol{q}, \boldsymbol{v})$
    $\dot{\boldsymbol{q}}_1 = R_q^{-1}(\boldsymbol{q}_2)\boldsymbol{v}_1$ ▷ From Body-Frame to Inertial-Frame
    $\boldsymbol{q}_1 = \int \dot{\boldsymbol{q}}_1 dt$
    $\boldsymbol{q}_2 = \boldsymbol{q}_2\, EXP_q(v_2, dt)$ ▷ Quaternion Attitude Propagation
    return $\boldsymbol{q} = \begin{bmatrix} \boldsymbol{q}_1 \\ \boldsymbol{q}_2 \end{bmatrix}$
end function

and due to the higher drag forces, the steady state velocity is lower, so for the same throttle setpoint, the steady state thrust achieved is effectively higher in the pipe, this results in the reduction in the gap between the maximum surge velocity of the μAUV in open water compared to concentric surge motion in the pipe.

The simulation also keeps track of the estimated current drawn, the remaining battery capacity, and the effective nominal battery voltage, as modeled in Section 5.5.

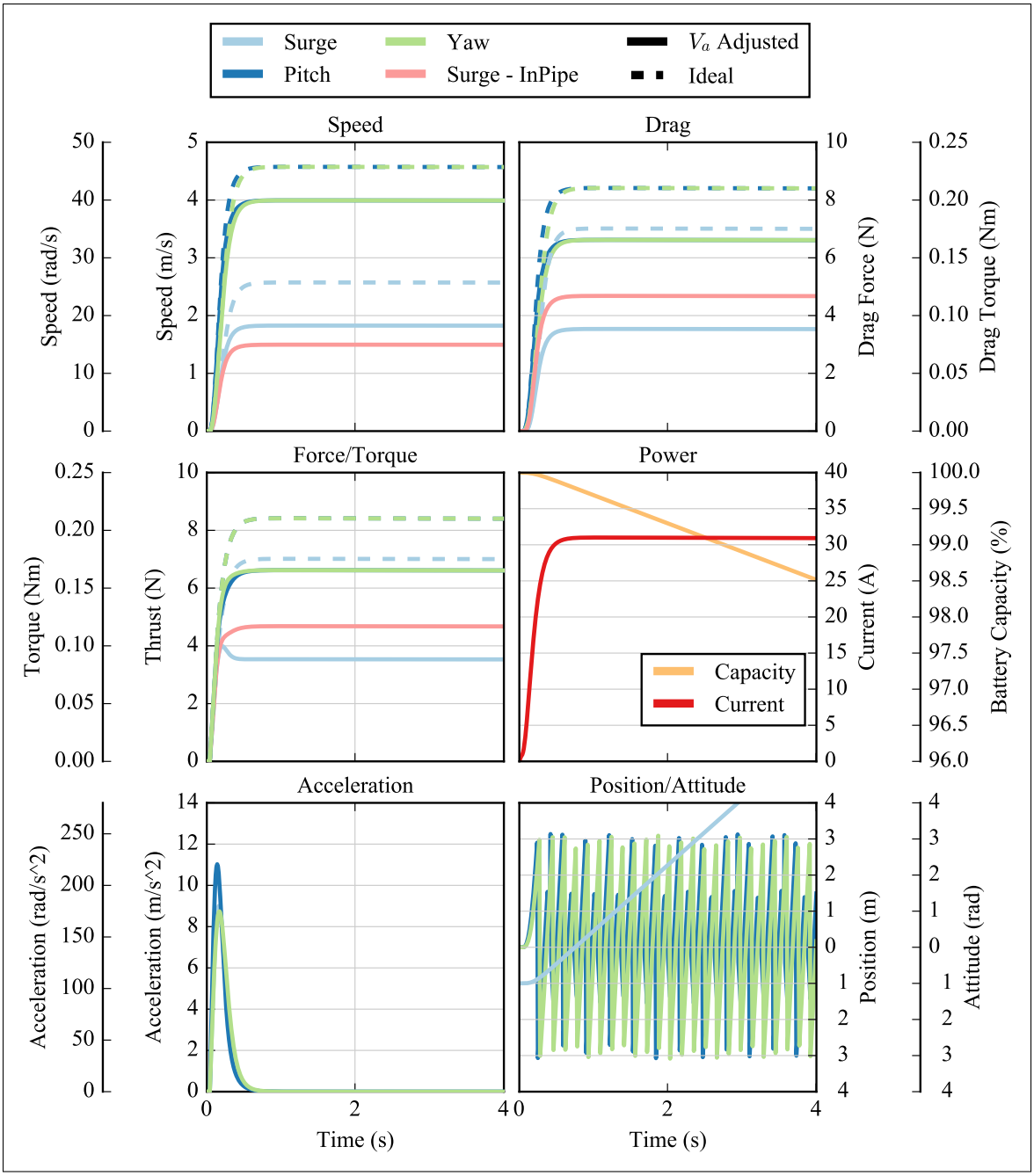

Figure 6.3: Dynamic Simulation Step Response

6.3 Sensor Models

The attitude of the μAUVis estimated by using an on-board 9DOF Inertial Measurement Unit (IMU), which is composed of a gyroscope, accelerometer and a magnetometer. Sensor data are fused through an Extended Kalman Filter to estimate

the attitude as part of the SITL controller. Here, we are interested in simulating the three IMU sensors from the real dynamic output.

The Gyroscope and Accelerometer are mounted with an orientation as shown on Figure 6.4, in which the IMU frame is rotated 180° around the x_B axis from the body-frame. The simulated gyroscope sensor data are derived from the angular velocity state, inverted about the x_B axis then noise is added.

The simulated accelerometer data is derived from the linear acceleration state in the body frame, added to the gravity element transformed into the body frame, then inverted to match the sensor orientation, and noise is added to the data. The noise model used for the gyroscope and the accelerometer is composed of a white noise element and a bias, or drift, element, as proposed in [63].

The discrete form of the gyroscope and accelerometer models are given as:

$$G_{sen}[k] = \mathbf{q}_{dm}\, {}^{q}\vec{\boldsymbol{v}}_{B_2}[k]\, \mathbf{q}_{dm}^{-1} + \boldsymbol{b}_d[k] + \boldsymbol{n}[k] \tag{6.19}$$

$$\boldsymbol{A}_{sen}[k] = \mathbf{q}_{dm}\, {}^{q}\vec{\boldsymbol{v}}_{B_1}[k]\, \mathbf{q}_{dm}^{-1} + \mathbf{q}_{dm}\, \mathbf{q}_{ud}\, {}^{q}\vec{\mathbf{g}}\, \mathbf{q}_{ud}^{-1}\, \mathbf{q}_{dm}^{-1} + b_d[k] + n[k] \tag{6.20}$$

q_{dm} represents the quaternion operator that performs the transformation between the body-frame to the sensor-frame. $\boldsymbol{q}_{ud}$ is the quaternion operator that transforms from the inertial frame to the body frame. ${}^{q}\vec{\_}$ denotes a quaternion vector. $\boldsymbol{b}_d[k]$ is the bias error term, it is a Brownian "Colored" Noise defined in discrete-form as:

$$\boldsymbol{b}_d[k] = \boldsymbol{b}_d[k-1] + \sigma_g \sqrt{dt}\, \boldsymbol{w}[k] \tag{6.21}$$

where σ_g is the random walk constant in $\frac{rad}{s^2}\frac{1}{\sqrt{Hz}}$ for the gyroscope and $\frac{m}{s^3}\frac{1}{\sqrt{Hz}}$ for the accelerometer. The random walk coefficients are often supplied by the sensor

manufacturers. $w[k]$ is a unity normal-distribution zero-mean white-noise, and $n[k]$ is the white noise term defined as:

$$n[k] = \sigma_w \frac{1}{\sqrt{dt}} w[k] \tag{6.22}$$

σ_w is the white noise density constant, in $\frac{rad}{s\sqrt{Hz}}$ for the gyroscope and $\frac{\mu m}{s^2\sqrt{Hz}}$ for the accelerometer. It is assumed that the noise characteristic is uniform across the three axes for both the gyroscope and the accelerometer.

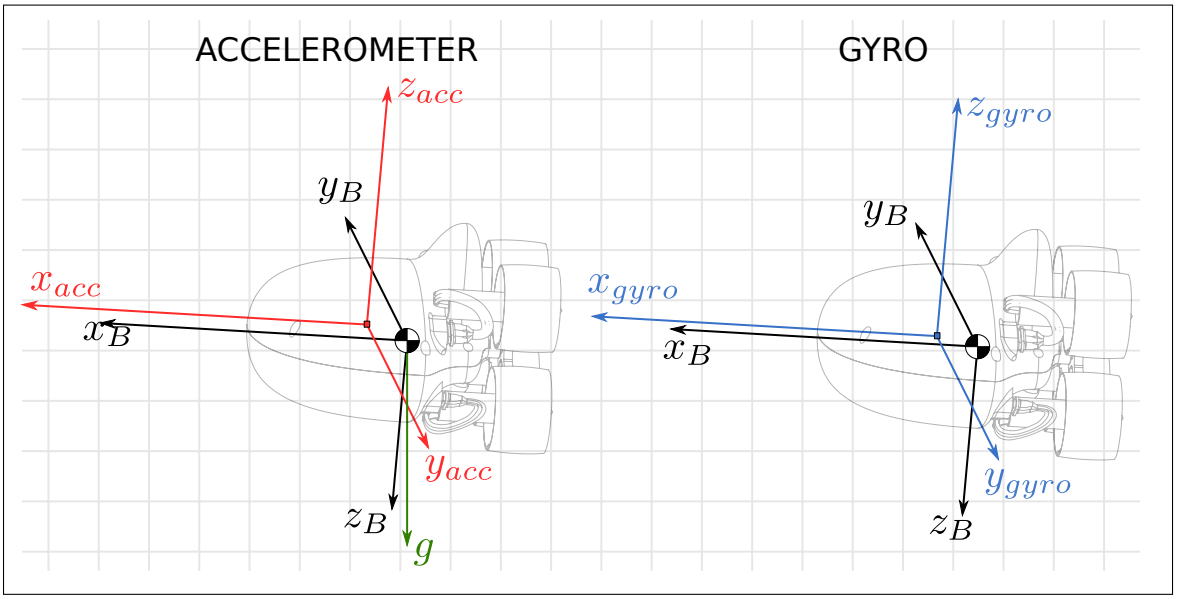

Figure 6.4: Gyroscope and Accelerometer Sensors Coordinate Frames

The magnetometer is simulated by first assuming that true north is coincident with the inertial frame's x axis. Magnetic Inclination δ_i and Declination δ_d offsets, as shown on Figure 6.5, are added to the true north direction vector to simulate a magnetometer sensor in the inertial-frame, this resultant vector is then rotated into the body-frame, and then white noise is added onto the data. The simulated magnetometer is expressed in discrete-form as:

$$\boldsymbol{M}_{sen}[k] = \mathbf{q}_{ud}\, \mathbf{q}_{fu}\, {}^{q}\mathbf{q}_{north}\, \mathbf{q}_{fu}^{-1}\, \mathbf{q}_{ud}^{-1} + \boldsymbol{w}_m[k] \tag{6.23}$$

${}^{q}\mathbf{q}_{north}$ is the magnetic north quaternion vector, a unity k direction vector. $\mathbf{q}_{fu}$ is the quaternion operator that transforms the coordinates from the magnetic north to the true north frame. $\mathbf{q}_{ud}$ is the quaternion operator that transforms the coordinates from the inertial-frame to body-frame. Finally, $\boldsymbol{w}_m[k]$ is a normally distributed zero-mean white noise term.

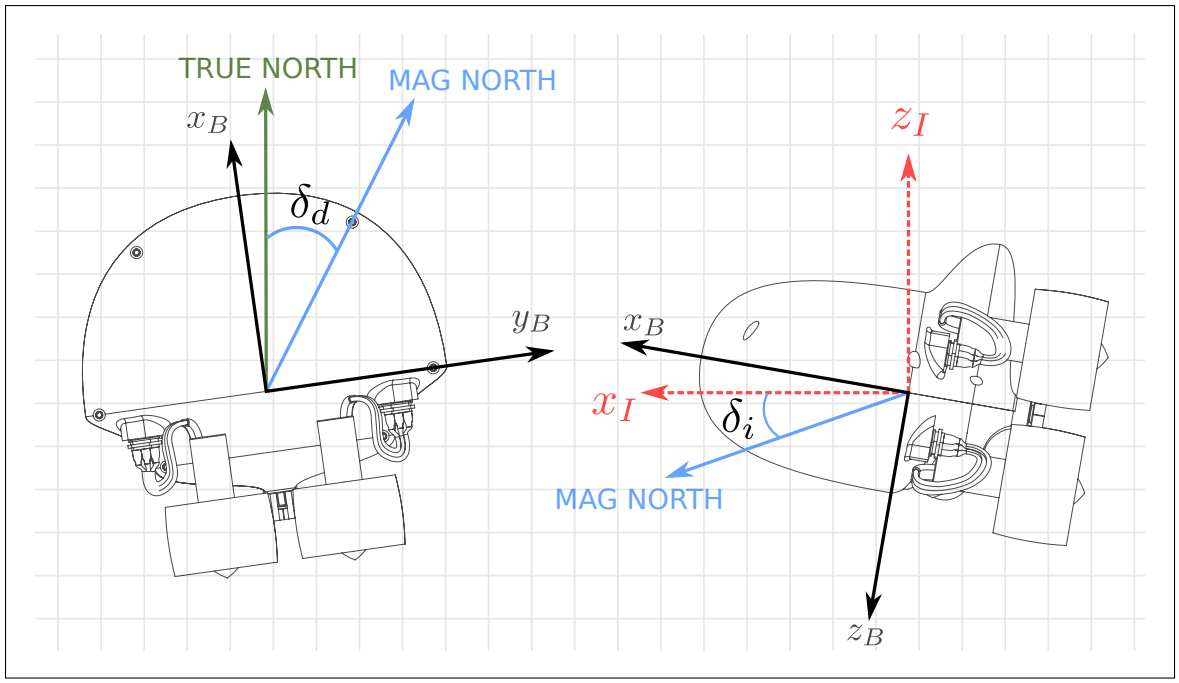

Figure 6.5: Magnetometer Coordinate Frame

The outputs of the dynamic simulation in addition to the simulated sensors are shown on Figure 6.6. The response is simulated using a bang-bang command in each of the four surge, roll, pitch, yaw directions respectively. The sensor data are generated at 50Hz, the $\sqrt{dt}$ scaling assumes an ideal low-pass filter applied to the sensor measurements. Otherwise the "white noise" exhibited by the gryo and accelerometer sensor data would be more noticeable.

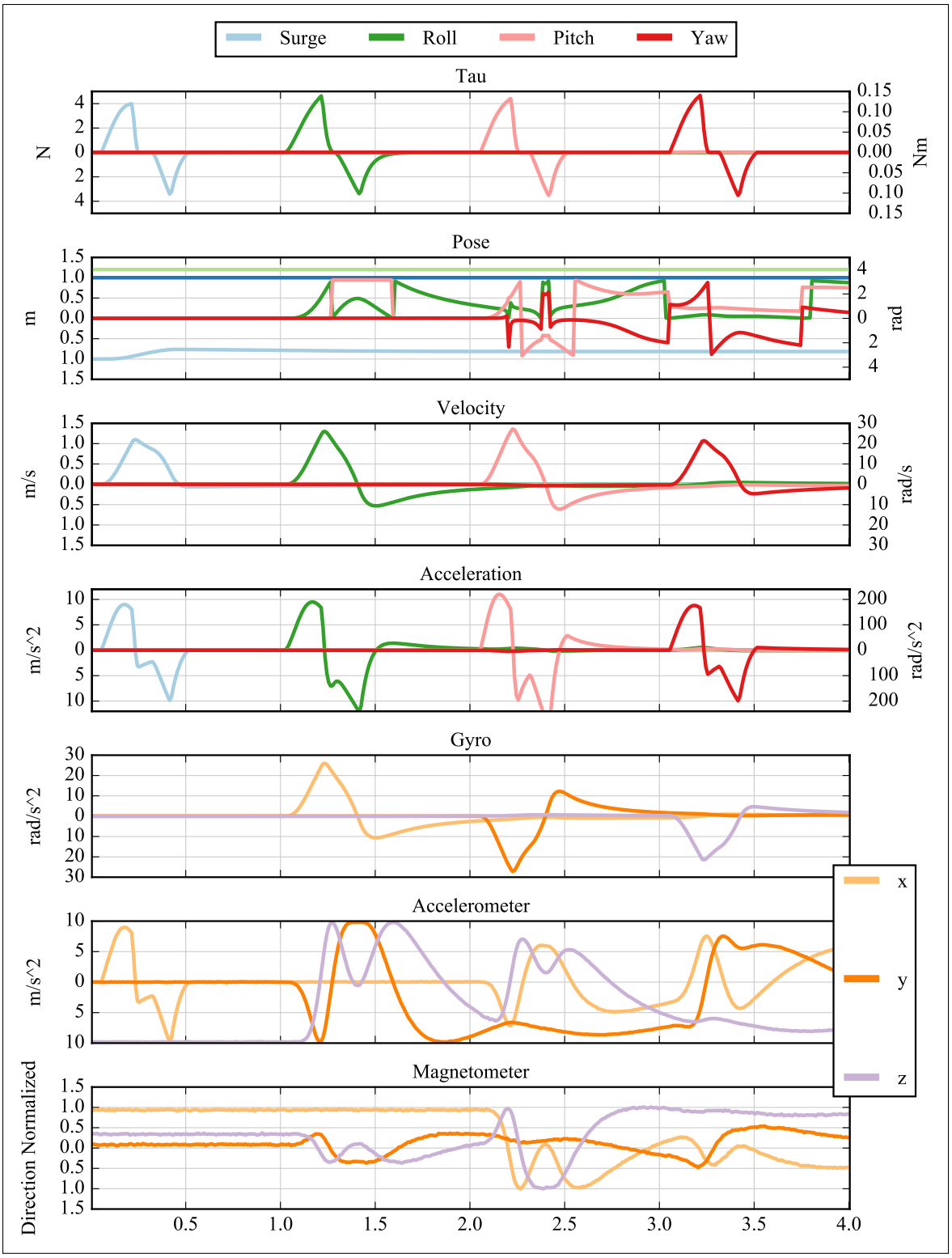

Figure 6.6: Mixed Bang-Bang Response with IMU Simulated Sensor

A barometer, as a water depth sensor, is also simulated with added white noise. A generic position estimator is provided too with an option to set the noise characteristics. Both would use the μAUV position state to simulate the sensor readings.

6.4 SITL Controller

The overall control architecture of the μAUV is illustrated on Figure 6.7. The controller is divided into a attitude rate controller, on top of it an attitude controller and then a position controller. Details of the control algorithms will be discussed in Chapter 9.

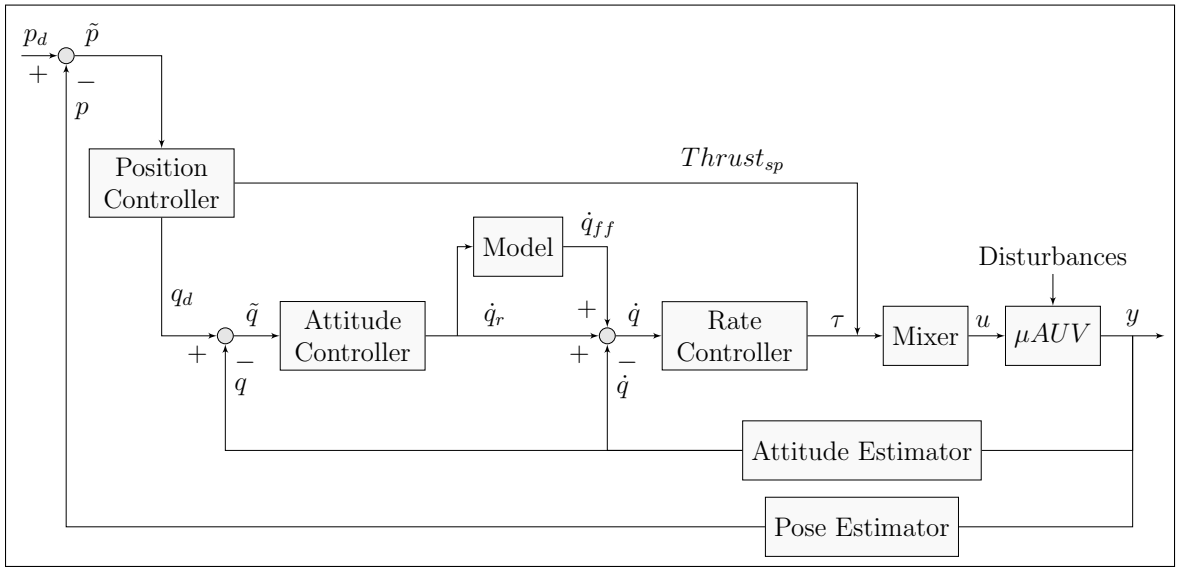

Figure 6.7: Overall μAUVControl System Architecture

The attitude estimation algorithms as well as the vehicle control algorithms are programmed on the PX4 [59] platform. The platform provides a software in the loop, SITL, framework for executing the same code as part of a software simulation or on the μAUV's autopilot microcontroller. A MAVROS [64] bridge is used to relay the Visual-Dynamic simulator data and emulate them as real sensor data to the autopilot and to receive output commands back into the dynamic model. And manual control input is relayed to the SITL controller via QGroundControl [65].

Depending on the attitude control mode, the manual input may map into thrust plus angular rates command, or to thrust plus attitude setpoint commands, or if a full attiude-pose controller is used the attitude controller would output all the rate commands.

The nodes for the different components of the simulation, such as the dynamics, sensor or SITL controllers, are built in a service-node control-block fashion. The service-node serve to execute and communicate with other nodes while the control blocks are abstracted and made modular. Algorithm 3 highlights the basic program flow structure. This also allows for rapidly restructuring the components for different simulation purposes, since the blocks have a well defined and consistent functional interface.

Algorithm 3 Service-Node Control-Block Generic Structure

```
1: procedure Simulation Node
2:     Get Initial State, Constants and Other Configuration
3:     Block → setInitialState()
4:     Block → setConstants()
5:     while Node Running do
6:         Receive Input for Block
7:         Block → setInputs()
8:         Block → iterate(dt)
9:         Block → getOutput()
10:        Send Output from Block
11:        Service Node
12:    end while
13: end procedure
```

CHAPTER 7

DESIGN PERFORMANCE AND DESIGN IMPROVEMENT

We can now assess the performance of the nominal μAUV design based on the identified parameters and using the simulation environment developed. The goal is to produce a performance benchmark that can be used as a step into improving the various design parameters based on the desired performance and response characteristics.

7.1 μAUVPerformance - Nominal Design

A key performance measure is the range and speed the μAUV is capable of. If we assume the μAUV is traversing a $160mm$ internal diameter pipe, maintaining concentric motion with the pipe at all times. We observe the following: for a choice of 30° pitch angle thruster profile, the peak efficiency speed is approximately $0.6m/s$, and with the installed battery capacity of $1500mAh$, the range is approximately 1800 meters, as shown on Figure 7.1

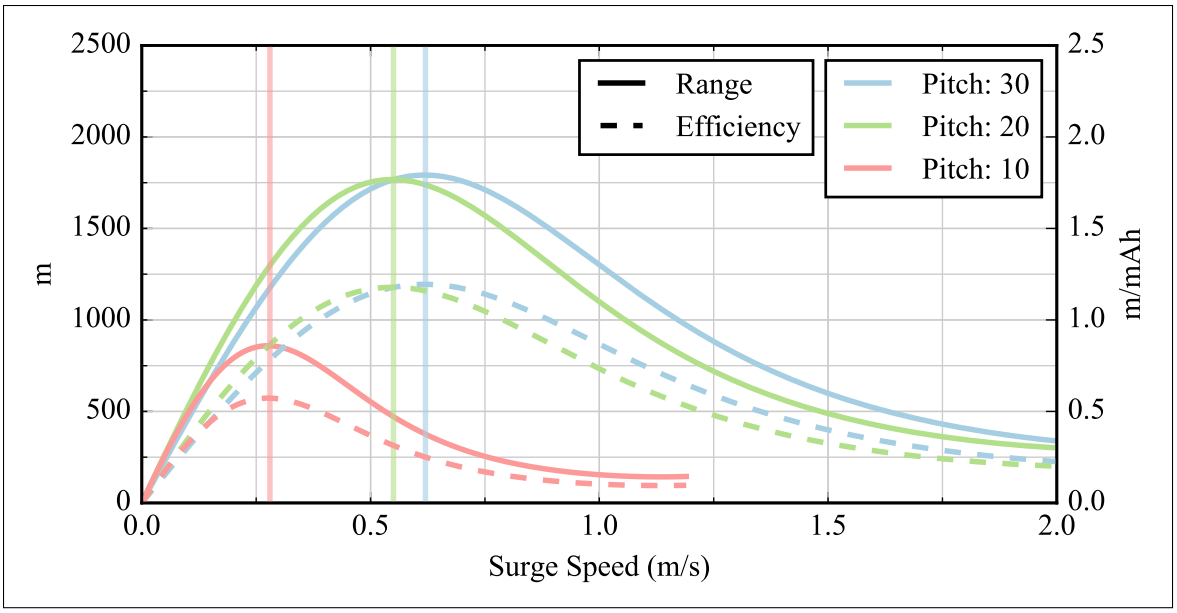

Figure 7.1: Range and Efficiency of Nominal μAUVDesign
Varying Propeller Pitch Angle, 30mmD profile. Battery capacity of 1500mAh

Assessing the agility of the vehicle, the maximum speed, brake times and reverse accelerations for surge and the three angular motions are illustrated on Figure 7.2.

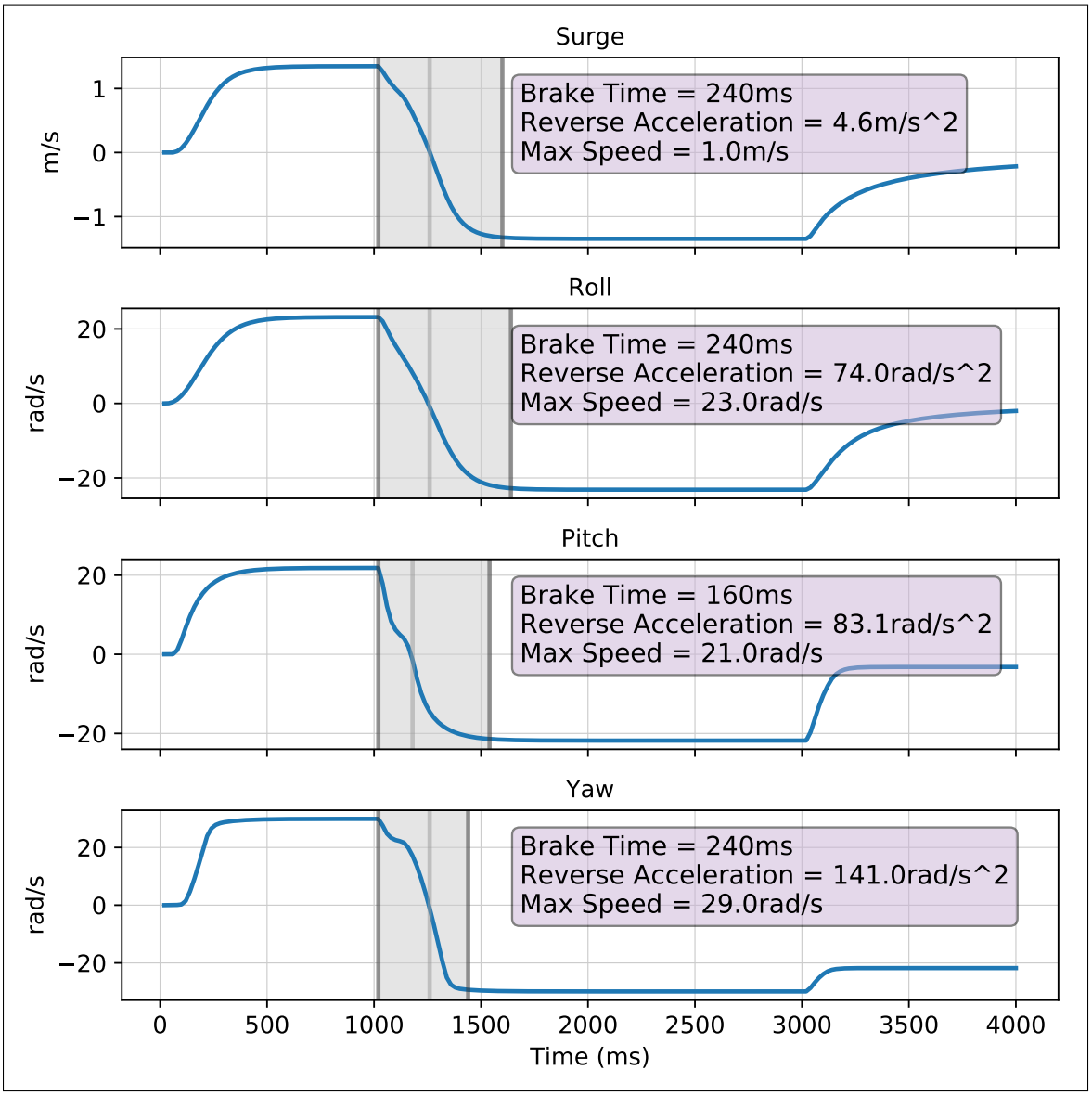

Figure 7.2: Agility of Nominal μAUVDesign
Thruster Profile: $30mmD$, $30°Pitch$

7.2 Shell Design Improvement

We can see from the previous performance results that the volume of the μAUV shell significantly impacts the performance of the μAUV in the pipe, much more so than in the open water. In other words, the cost of attaining a smooth surface geometry (by generally, increasing the volume of the shell) is high due to the Venturi Effects in the pipe.

Given this insight, we now attempt to relax our constraint for a smooth surface geometry and shrink the shell to fit around the internal components of the μAUV. The resulting neutrally buoyant shell has a mass reduction of 50% and only requires 10 grams of ballast weight on top of the functional internals, compared to 200 grams of ballast weight for the nominal design.

The resulting shell design is smaller in volume but has a complex and "non-smooth" surface geometry. The resulting shell design (R2) is illustrated on Figure 7.3.

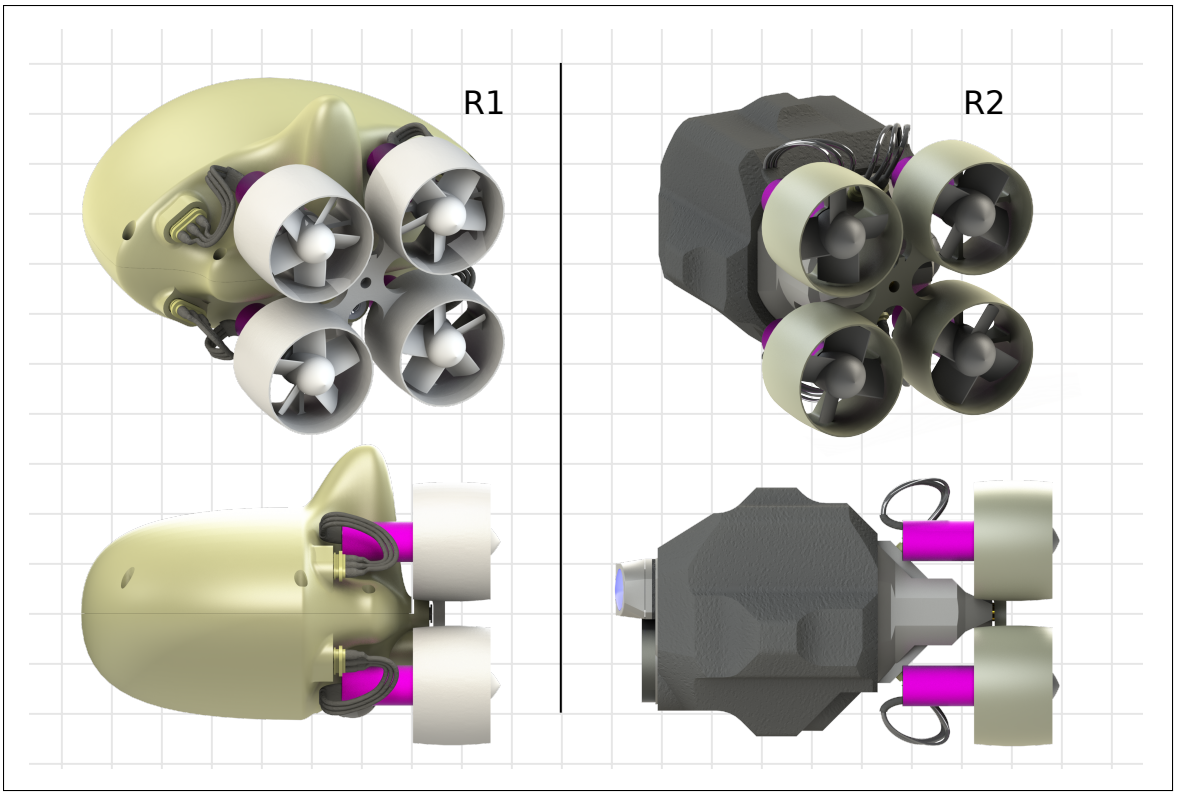

Figure 7.3: Realized Design - Revision 2 vs. Revision 1

Comparing the surge drag between the two shells, there is little difference between them, for both open-water or in-pipe. Figure 7.4 compares the surge drag between the nominal design R1 and the revised shell R2. A complex surface geometry is compensated for by an overall smaller cross-sectional area.

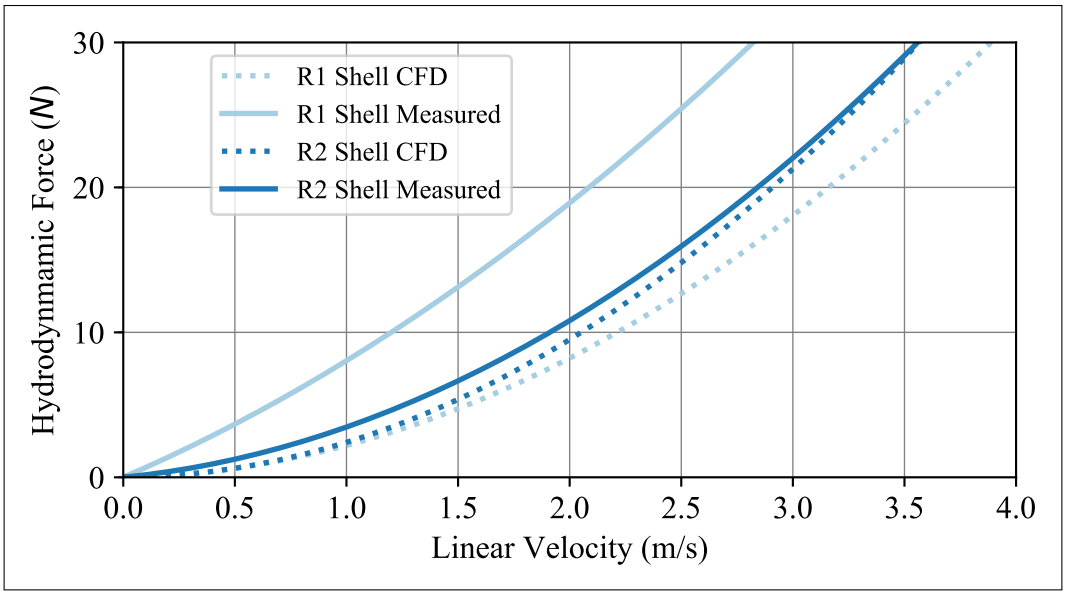

Figure 7.4: Surge Hydrodynamic Force In-Pipe. Shell Revision 1 vs Revision 2

The range and peak-range efficiency speed is not expected to change between the two shell designs, since this is a property of the thrusters at steady state, as compared on Figure 7.5. However, realistically the μAUV will continuously be varying its speed and a lower mass will clearly expend less energy. The shell can now be expanded again to house a larger capacity battery with only an incremental cost associated with the battery's mass and not necessary the expanded volume to maintain a smooth surface geometry.

7.3 Neutral Buoyancy & Surface Geometry Control

While the volume and mass of the vehicle can be controlled by design, it is not always convenient to precisely attain neutral buoyancy due to a number of reasons, and it is even more complex to control the location of center of buoyancy with respect to the center of mass. On the other hand, the fitted shape of the shell devised in the previous section, while it reduces the mass and volume, it does not generate an optimal surface geometry from the perspective of hydrodynamic drag.

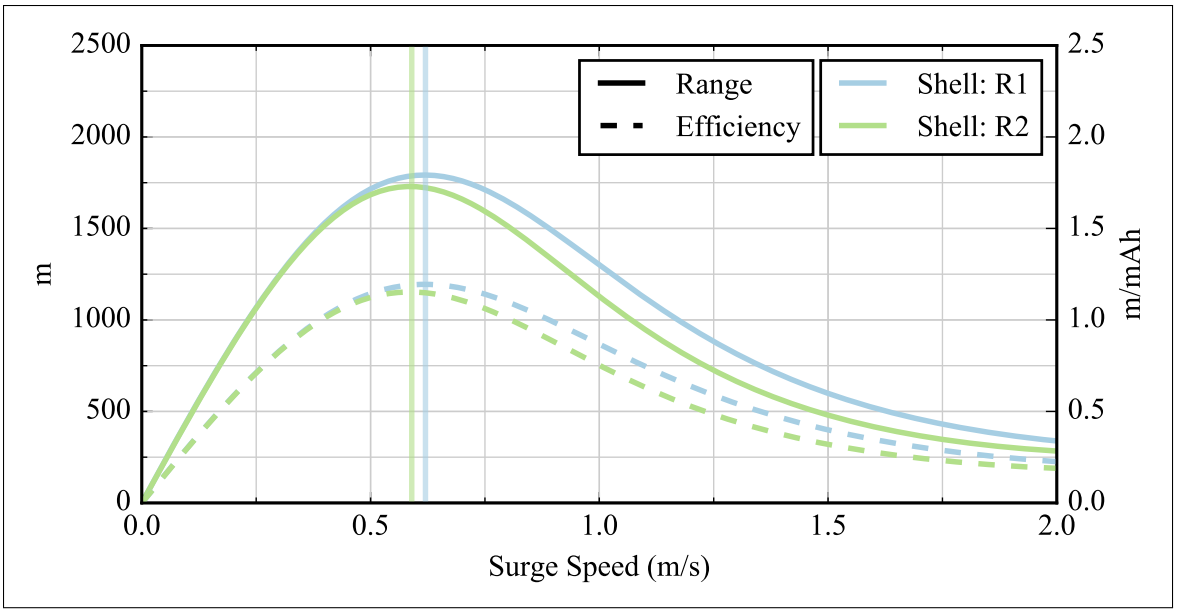

Figure 7.5: Range and Efficiency. Nominal μAUVDesign vs With Revised Shell Design

Using the same thruster profile of: $30mmD$, 30° blade pitch angle. Battery capacity of $1500mAh$

We therefore devise a simple rapid prototyping method to create a sleeve that serves multiple design functions. The design method would produce a sleeve that form-fits around the shell, and has controllable density, thickness, mass and volume distribution. Independent from the shell design but fabricated around it. The flexibility in selecting the form and density of the sleeve provides a way to fine tune the μAUV's mass and CoM to CoB relationship.

A 3-piece sleeve mold created from the shape of the μAUV's shell with a specified form and thickness is designed and printed. The cast material can be that of silicon or urethane rubber. The specific density of the cast materials would be measured, and as required, brass powder is added to the mix to increase the specific density of the cast. The setup and an example output result is shown on Figure 7.6.
The density of the cast can also be layered by selectively adding a different density mix, within the resin work-time window to ensure bonding between the segments, as shown on Figure 7.7.

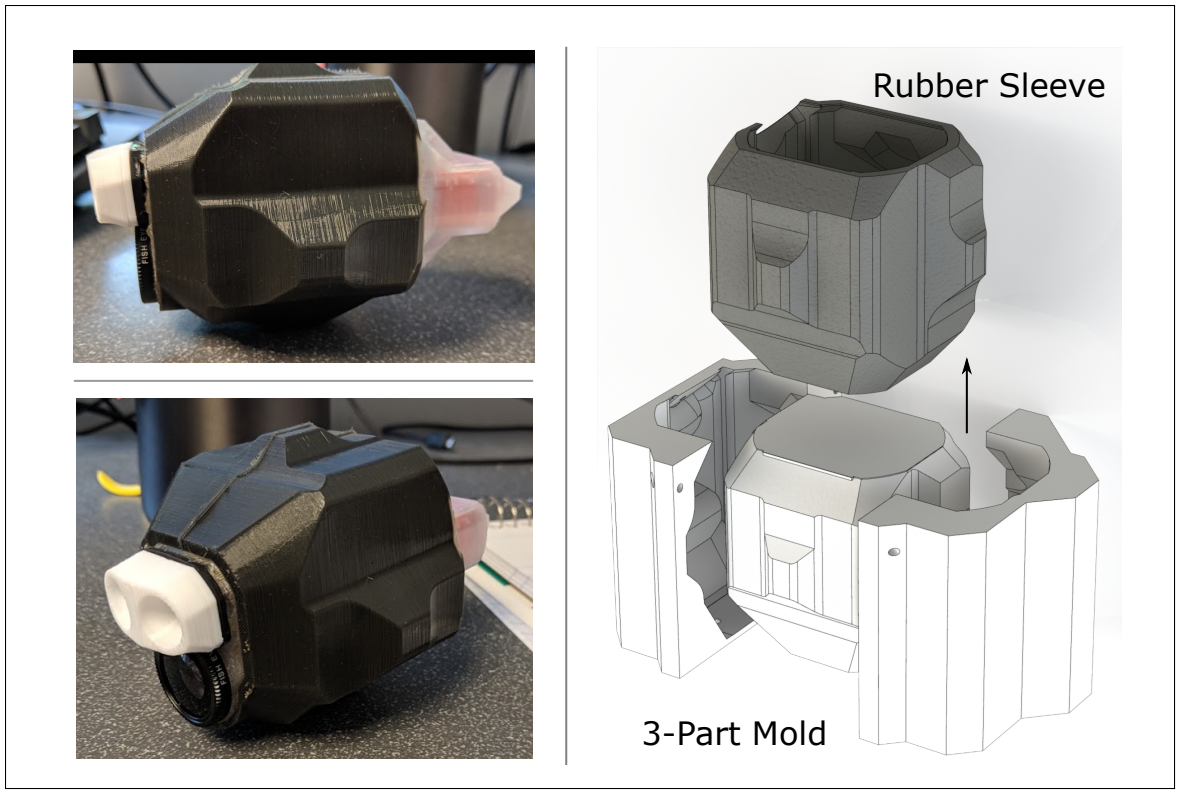

Figure 7.6: μAUV Sleeve Mold

With the sleeve added to the shell, the shell surface geometry shape optimization can now move on to the sleeve outer shape rather than the hard shell itself. This allows for rapid testing and replacement of the sleeve to account for changes in the mass of the core μAUV minimizing the risk of breaking the water tight seal of the shell and complex design changes. Control surfaces can now be added as well with the flexible material without risking damage to μAUV when it collides with the enclosed space structure.

Performing the CFD analysis and experimentation presented earlier on the modified shell and sleeve design. We get the following results. The hydrodynamic drag from the CFD analysis in-pipe is shown on figure ??. A key improvement in the new shell is seen by the reduced heave drag, and overall heave cross-sectional area.

This is beneficial in reducing the large variation in axial drag when the μAUV experiences a pitching motion within the pipe. As noted early, the increase in axial

drag in the pipe is exponential with the increase in the cross sectional area ratio between the vehicle and the pipe's cross section. Figure 7.8 compares the translational drag in open water between the two design revisions.

This concludes the design part of the thesis. Next, the attitude control and trajectory control of the μAUV will be treated.

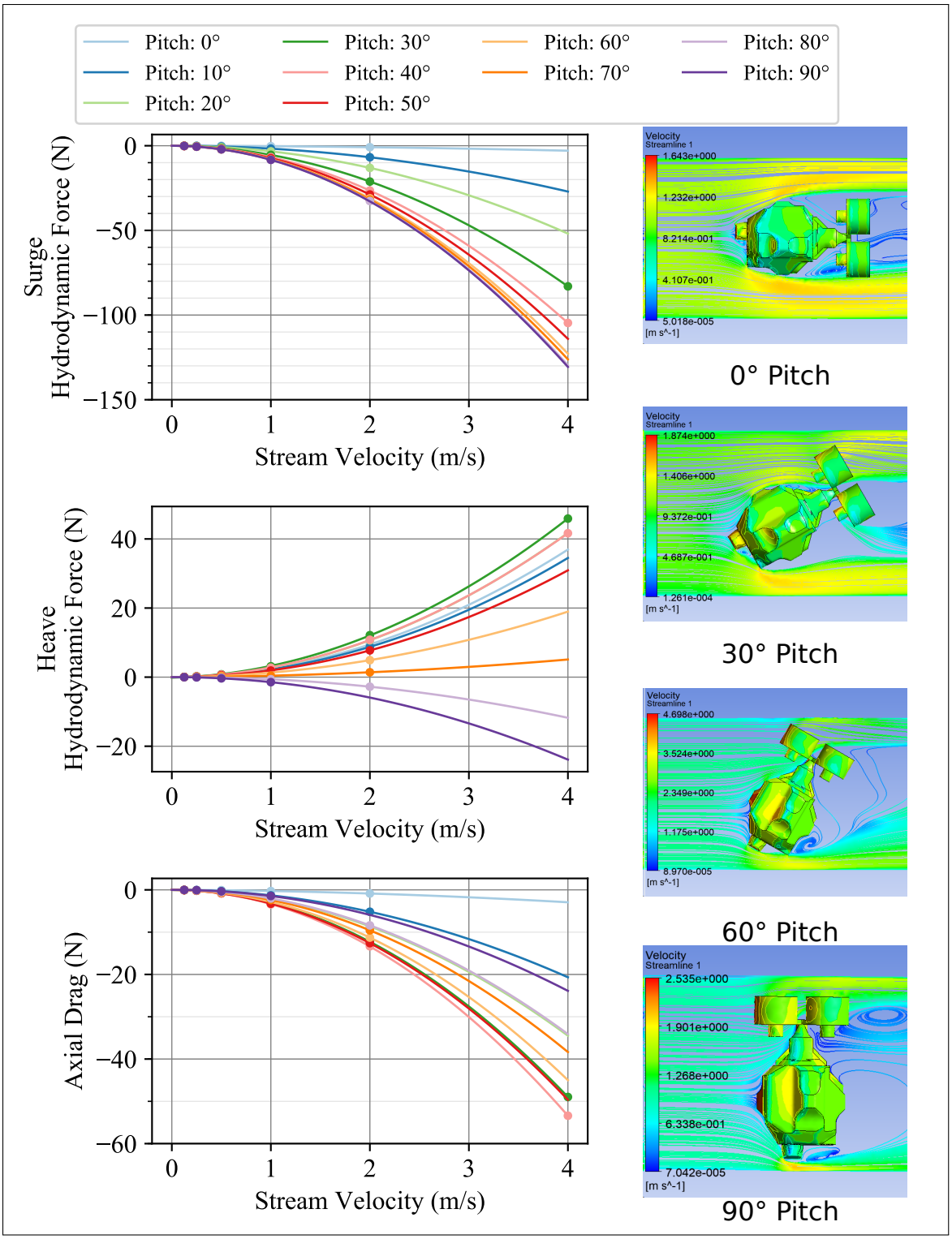

Figure 7.7: Hydrodynamic Force with Varying Vehicle Pitch in a 160mm ID Pipe with the Redesigned Shell

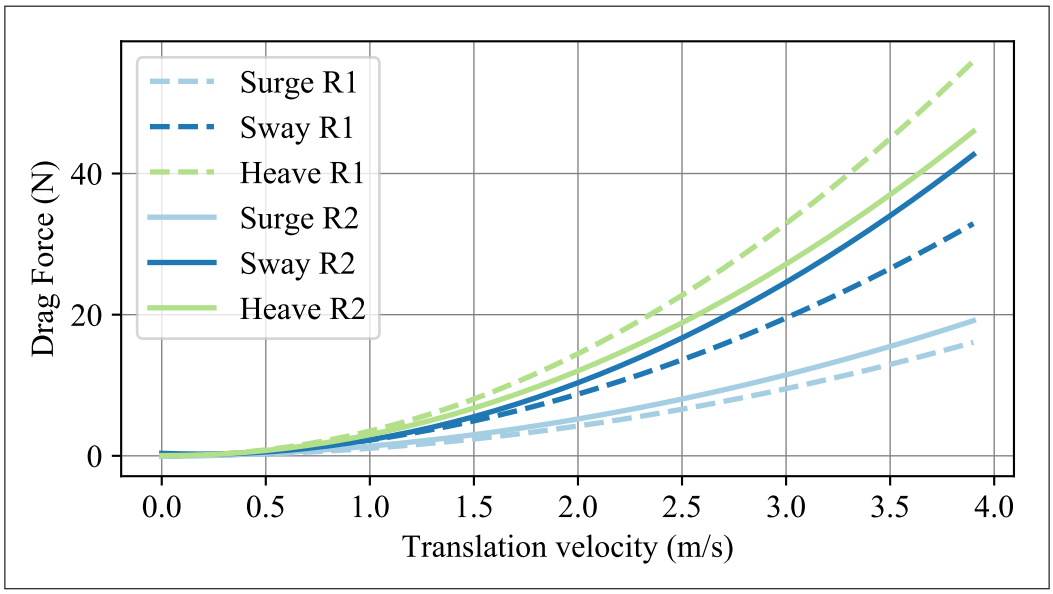

Figure 7.8: Open Water Translation Drag: R2 vs R1

CHAPTER 8

POSE ESTIMATION

A core component of the robot design is giving it the ability to perceive its environment. In order for the vehicle to navigate within a confined space it needs to estimate its position with respect to its surrounding and determine an obstacle free path to follow. We propose a method here to perform pose estimation and consequently localization using structured light.

8.1 Pose Estimation

In this work we propose using a monocular vision camera coupled with an IMU to tackle the pose estimation problem. Other methods using a stereovision camera have also proven to be effective in autonomous navigation and environmental scanning. Stereovision; however, requires a set of calibrated cameras and a larger processing power. The robot is intended for use in confined spaces, and naturally, such spaces have poor illumination, if any, and lack distinguishable features that allow existing feature based visual servoing techniques to be applied. We propose instead the use of structured light, projecting known patterns on the surrounding surfaces of the robot environment, taking advantage of the fact that in confined spaces and in near proximity to surfaces, the projected patterns are limitedly scaled and can remain in full view of the camera. Such known projected features will be used to aid in estimating the robots attitude with respect to its surrounding.

There are two main approaches to performing visual servoing, image based visual servoing (IBVS) and feature based visual servoing (FBVS). The latter requires a well calibrated camera and the control law lies in the Cartesian space, the former

is considered more robust to camera calibration and would be more suitable in systems with limited image quality and processing power [39].

Many confined space environments have well-structured shapes, such as cylindrical in the case of pipes and pipelines for instance, or rectangular in the case of venting ducts or subsea risers. These shapes provide either a curved cylindrical surface or a plane onto which the projected light patter will intersect and form a distinguishable feature, which can be used in visual servoing.

A perspective camera model is used for the monocular vision camera. A simple projected light pattern would be a collimated light that forms a cone, a member of natural quadric surfaces as shown in Figure 8.1. The other light pattern would be a collimated set of orthogonal lines forming a grid pattern. We will discuss how each pattern forms a feature when projected onto both a flat plane and a cylindrical curved surface and how it can be used to estimate the attitude of the vehicle.

In this chapter, the following specific notations listed in table 8.1 will used. Adopted primarily from [66]

8.1.1 Cone Plane Intersection

Let us take the case where the robot navigates through a rectangular channel as shown in Figure 8.2. A collimated LED light projected onto one of the planes of the rectangular channel will represent a cone intersecting a plane, resulting in a conic section, and for our case, where the apex of the cone is constrained to within a certain distance and angle from the plane, the result would be an ellipse (or a circle if the projection axis is normal to the plane). Before we discuss the particulars of our pose analysis lets review some basic geometric properties.

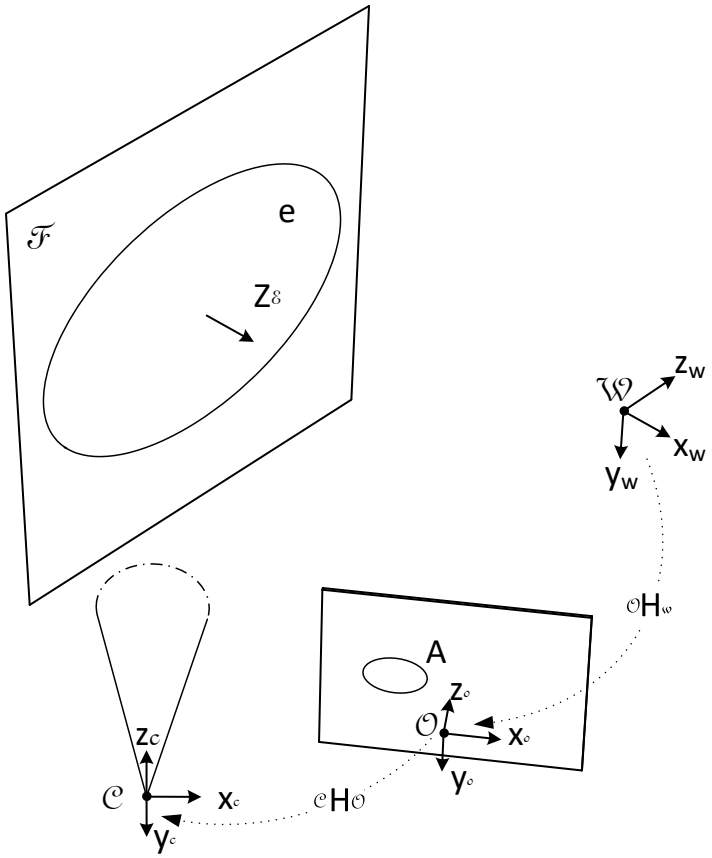

Figure 8.1: Single Ellipse Projection on Plane

Table 8.1: Notations

	Inhomogeneous		Homogeneous	
Element	2D	3D	2D	3D
Points	x, y, ...	X, Y, ...	x, y, ...	X, Y, ...
Lines	l, m, ...	L, M, ...	l, m, ...	L, M, ...
Planes / Surfaces		A, B,C, ...		A, B,C, ...
Reference Frames	$\mathcal{O}$, $\mathcal{P}$,Q,$\mathcal{V}$,$\mathcal{W}$			
Transformation (from $\mathcal{O}$ to $\mathcal{W}$)	${}^{\mathcal{W}}\mathbf{R}_{\mathcal{O}}x + {}^{\mathcal{W}}\mathbf{T}_{\mathcal{O}}$		${}^{\mathcal{W}}\mathbf{H}_{\mathcal{O}}x$, ${}^{\mathcal{W}}\mathbf{H}_{\mathcal{O}} = \begin{bmatrix} {}^{\mathcal{W}}\mathbf{R}_{\mathcal{O}} & {}^{\mathcal{W}}\mathbf{T}_{\mathcal{O}} \\ \mathbf{0} & 1 \end{bmatrix}$	
Vectors / Matrices	$\mathbf{x}$, $\mathbf{y}$, $\mathbf{z}$, $\mathbf{R}$, $\mathbf{H}$,...			
Sub/Superscripts	Vector of object C expressed in $\mathcal{O}$ frame: ${}^{\mathcal{O}}\mathbf{z}_{\mathcal{C}}$			

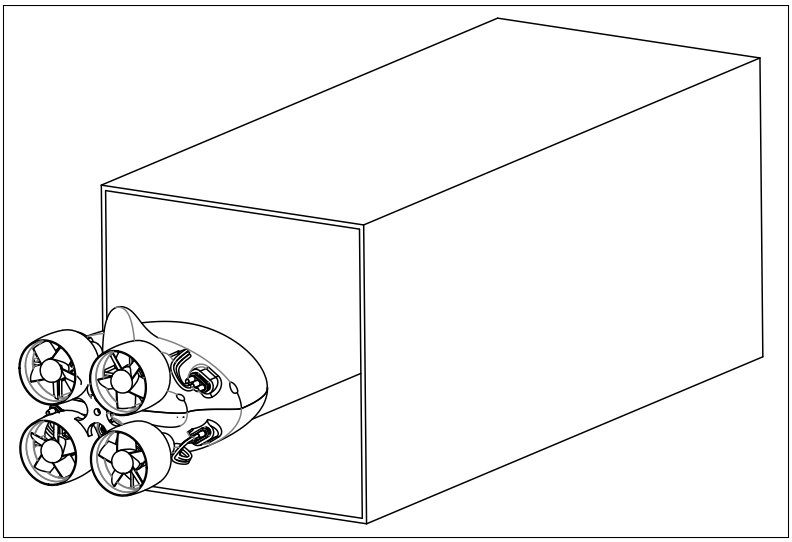

Figure 8.2: Robot Entering a Rectangular Channel

A general quadric surface $\mathcal{E}$ has the implicit polynomial form

$$f(x,y,z) = ax^2 + by^2 + cz^2 + 2hxy + 2fyz + 2gxz + 2px + 2qy + 2rz + d = 0 \quad (8.1)$$

With the following homogeneous form

$$\mathcal{E} : \mathbf{E} = \begin{bmatrix} a & h & g & p \\ h & b & f & q \\ g & f & c & r \\ p & q & r & d \end{bmatrix} \quad , \quad \mathrm{X}^T \mathbf{E} \mathrm{X} = 0 \quad , \quad \mathrm{X} = \begin{bmatrix} x \\ y \\ z \\ 1 \end{bmatrix} \quad (8.2)$$

A cone $\mathcal{C}$ with its apex at the origin and its axis aligned with the z-axis and cone angle α, reduces the general quadratic form to the following implicit and homogeneous form.

$$x^2 + y^2 - C^2 z^2 = 0 \quad , \; Cone\,Height \geq \; z \geq 0 \quad , \quad \alpha = 2\tan^{-1}(C) \quad (8.3)$$

$$\mathcal{C} : \mathbf{C} = \begin{bmatrix} 1 & 0 & 0 & 0 \\ 0 & 1 & 0 & 0 \\ 0 & 0 & -C^2 & 0 \\ 0 & 0 & 0 & 0 \end{bmatrix} \quad , \quad \mathrm{X}^T \mathbf{C} \mathrm{X} = 0 \quad , \quad \mathrm{X} = \begin{bmatrix} x \\ y \\ z \\ 1 \end{bmatrix} \tag{8.4}$$

A plane with a normal vector N and distance s from the origin has the following implicit and homogeneous form

$$ax + by + cz - d = 0 \quad , \quad \mathrm{X}^T \mathbf{N} = 0 \quad , \quad \mathbf{N} = \sqrt{a^2 + b^2 + c^2} \begin{bmatrix} n_1 \\ n_2 \\ n_3 \\ -\mathrm{s} \end{bmatrix} \tag{8.5}$$

An intersection between a cone and plane in the configuration shown in Figure 8.1, results in a conic section. A conic section is a planar curve and has the following implicit and homogeneous form. The conic section can take different geometrical forms including an ellipse or a circle.

$$f(x, y) = ax^2 + 2hxy + by^2 + 2gx + 2fy + c = 0 \tag{8.6}$$

$$e : \mathbf{e} = \begin{bmatrix} a & h & g \\ h & b & f \\ g & f & c \end{bmatrix} \quad , \quad \mathrm{x}^T \mathbf{e} \mathrm{x} = 0 \quad , \quad \mathrm{x} = \begin{bmatrix} x \\ y \\ 1 \end{bmatrix} \tag{8.7}$$

Lets consider one of the 4 planes in the rectangular channel in our analysis. As shown in Figure 8.1

We have the quasi-inertial frame $\mathcal{W}$ with its $y - axis$ along the gravity vector and the $z - axis$ parallel to plane $\mathcal{F}$ and collinear with the channel center axis. Our

robot is represented by the camera frame $\mathcal{O}$ for simplicity. The cone representing the collimated light is positioned at $\mathcal{C}$ and is rigidly attached to the robot with a determined homogeneous transformation matrix from the camera origin ${}^{\mathcal{C}}\mathbf{H}_{\mathcal{O}}$. The cone axis is $\mathbf{z}_{\mathcal{C}}$.

The q-inertial global frame $\mathcal{W}$ moves along its $z - axis$ such that the robot coordinate $\mathcal{O}$ is always coincident with the $xy - plane$ of $\mathcal{W}$. The plane $\mathcal{F}$ has the normal $\mathbf{z}_{\mathcal{F}}$ and lies distance s from $\mathcal{W}$ in the normal direction. The ellipse formed by the intersection of the cone and the plane, has the object centered coordinate $\mathcal{E}$ with its $x - axis$, $\mathbf{x}_{\mathcal{E}}$ along the major axis of the ellipse and the $y - axis$, $\mathbf{y}_{\mathcal{E}}$ along the ellipse minor axis. The ellipse projects into another ellipse A on the image plane.

Using a calibrated perspective camera model, with the image plane a distance $z = 1$ from the camera origin, objects expressed in camera coordinates can be scaled into the image plane using the ray projection assumption $\mathrm{X} = \lambda \mathrm{x}$. Transforming the ellipse e gives

$$\mathbf{G}^T\mathbf{E}\mathbf{G} = \lambda\mathbf{A} \tag{8.8}$$

where $\mathbf{G} \in {}^{3x3}$ is the first to columns of ${}^{\mathcal{O}}\mathbf{R}_{\mathcal{E}} \in \mathrm{SO}(3)$ and ${}^{\mathcal{O}}\mathbf{T}_{\mathcal{E}} \in {}^{3x1}$, and for an ellipse or circle $\mathbf{E} = \begin{bmatrix} {}^{1}/_{a^2} & 0 & 0 \\ 0 & {}^{1}/_{b^2} & 0 \\ 0 & 0 & -1 \end{bmatrix}$ where a is the major ellipse axis and b is the minor axis.

We are interested in finding, from our knowledge of the light source location with respect to the camera, its projection angle, and find from the ellipse parameters in the image, the transformation matrix from the camera $\mathcal{O}$ to the global coordinate $\mathcal{W}$, our absolute pose.

Algebraic Approach

To solve for the pose parameters, we can find the implicit equation that describes the intersection of the cone (8.3) and plane (8.5) and describe the elliptical conic section (8.6) in $\mathbb{R}^3$ with respect to the camera frame. This method is cumbersome and results in a numerically unstable set of equations that are sensitive to measurement errors. A better and more intuitive approach would be to employ a hybrid mix of geometrical and algebraic analysis.

Hybrid Approach

We know that the ellipse major axis $\mathbf{x}_{\mathcal{E}}$ lies in the same plane formed by the cone axis $\mathbf{z}_{\mathcal{C}}$ and the ellipse normal $\mathbf{z}_{\mathcal{E}}$ (in the same direction as the plane normal $\mathbf{z}_{\mathcal{F}}$) and since we are always projecting light toward the forward sphere in relation to the camera coordinate we also know their relative sign. This gives 8.9, and consequently 8.10

$$\mathbf{y}_{\mathcal{E}} = \frac{-\mathbf{z}_{\mathcal{C}} \times \mathbf{z}_{\mathcal{E}}}{\|-\mathbf{z}_{\mathcal{C}} \times \mathbf{z}_{\mathcal{E}}\|} \tag{8.9}$$

$$\mathbf{x}_{\mathcal{E}} = \frac{\mathbf{y}_{\mathcal{E}} \times \mathbf{z}_{\mathcal{E}}}{\|\mathbf{y}_{\mathcal{E}} \times \mathbf{z}_{\mathcal{E}}\|} \tag{8.10}$$

The cone projection angle α is a known property of the calibrated and collimated light system. The distance between the cone apex and the ellipse center $\left\|{}^{\mathcal{C}}\mathbf{T}_{\mathcal{E}}\right\|$ and α determine the ellipse's minor diameter as seen in Figure 8.3.

$$b^2 = \tan(\alpha/2) \left\|{}^{\mathcal{C}}\mathbf{T}_{\mathcal{E}}\right\|^2 \tag{8.11}$$

The first two columns of the ellipse to image transformation matrix $\mathbf{G}$ from (8.8) can be defined as the normalized major and minor axis vectors of the ellipse expressed in camera coordinates, thus $\mathbf{G} = \begin{bmatrix} \mathcal{O}_{\mathbf{x}_{\mathcal{E}}} & \mathcal{O}_{\mathbf{y}_{\mathcal{E}}} & \mathcal{O}_{\mathbf{T}_{\mathcal{E}}} \end{bmatrix}$. From (8.8) we have 6

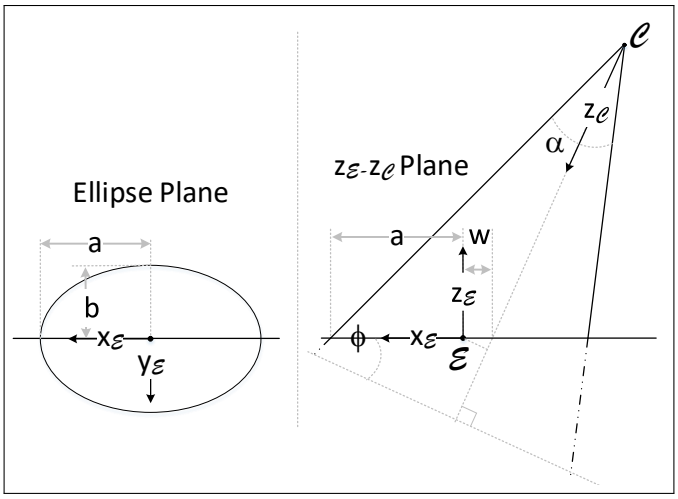

Figure 8.3: Ellipse Formed by Cone and Plane Intersection

constraints

$$
\begin{aligned}
{}^{\mathcal{O}}\mathbf{x}_{\mathcal{E}}^{T}\mathbf{E}^{\mathcal{O}}\mathbf{x}_{\mathcal{E}} = \lambda a_{11},\ {}^{\mathcal{O}}\mathbf{x}_{\mathcal{E}}^{T}\mathbf{E}^{\mathcal{O}}\mathbf{y}_{\mathcal{E}} = \lambda a_{12},\ {}^{\mathcal{O}}\mathbf{x}_{\mathcal{E}}^{T}\mathbf{E}^{\mathcal{O}}\mathbf{T}_{\mathcal{E}} = \lambda a_{13} \\
{}^{\mathcal{O}}\mathbf{y}_{\mathcal{E}}^{T}\mathbf{E}^{\mathcal{O}}\mathbf{y}_{\mathcal{E}} = \lambda a_{22},\ {}^{\mathcal{O}}\mathbf{y}_{\mathcal{E}}^{T}\mathbf{E}^{\mathcal{O}}\mathbf{T}_{\mathcal{E}} = \lambda a_{23},\ {}^{\mathcal{O}}\mathbf{T}_{\mathcal{E}}^{T}\mathbf{E}^{\mathcal{O}}\mathbf{T}_{\mathcal{E}} = \lambda a_{33}
\end{aligned}
\tag{8.12}
$$

We have 9 independent unknowns, 6 in $\mathbf{G}$ plus λ, and the ellipse major and miner axes a and b. We have 8 constraints so far in (8.12), (8.11) and (8.9). The 9th constraint can be derived by knowing that the angle between the cone axis $\mathbf{z}_{\mathcal{C}}$ and the ellipse (plane) normal $\mathbf{z}_{\mathcal{E}}$ determine the ratio of the major to minor ellipse axis.

$$
{}^{a}/_{b} \sim \ \cos^{-1}\left(\frac{\mathbf{z}_{\mathcal{E}} \cdot \mathbf{z}_{\mathcal{C}}}{\|\mathbf{z}_{\mathcal{E}}\|\ \|\mathbf{z}_{\mathcal{C}}\|}\right) \tag{8.13}
$$

We still want to resolve the absolute pose of our robot with respect to the q-inertial frame. We can compute the gravity vector $\mathbf{g}_{\mathcal{O}}$ in the camera frame using the on-board IMU, which is aligned to the $\mathbf{y}_{\mathcal{W}} \approx \mathbf{g}_{\mathcal{O}}$ axis. $\mathbf{z}_{\mathcal{W}}$ can be found by $\mathbf{z}_{\mathcal{W}} = \frac{\mathbf{z}_{\mathcal{E}} \times \mathbf{y}_{\mathcal{W}}}{\|\mathbf{z}_{\mathcal{E}} \times \mathbf{y}_{\mathcal{W}}\|}$ and consequently $\mathbf{x}_{\mathcal{W}} = \frac{\mathbf{y}_{\mathcal{W}} \times \mathbf{z}_{\mathcal{W}}}{\|\mathbf{y}_{\mathcal{W}} \times \mathbf{z}_{\mathcal{W}}\|}$

The absolute pose to the q-inertial frame would then be

$$ {}^{\mathcal{O}}\mathbf{H}_{\mathcal{W}} = \begin{bmatrix} {}^{\mathcal{O}}\mathbf{x}_{\mathcal{W}} & {}^{\mathcal{O}}\mathbf{y}_{\mathcal{W}} & {}^{\mathcal{O}}\mathbf{z}_{\mathcal{W}} & {}^{\mathcal{O}}\mathbf{T}_{\mathcal{W}} \\ & \mathbf{0} & & 1 \end{bmatrix} \tag{8.14} $$

where ${}^{\mathcal{O}}\mathbf{T}_{\mathcal{W}} = {}^{\mathcal{O}}\mathbf{T}_{\mathcal{E}} + {}^{\mathcal{E}}\mathbf{T}_{\mathcal{W}}$, ${}^{\mathcal{E}}\mathbf{T}_{\mathcal{W}} \cdot \mathbf{z}_{\mathcal{E}} = -S$, ${}^{\mathcal{E}}\mathbf{T}_{\mathcal{W}} \cdot (\mathbf{z}_{\mathcal{E}} \times \mathbf{z}_{\mathcal{W}}) = 0$ and ${}^{\mathcal{O}}\mathbf{T}_{\mathcal{W}}(3) = 0$

Multiple Projections

So far weve discussed a single light projection on a single surface. But we can employ the symmetry in a square channel or a narrow corridor and project a second light onto another parallel and opposing surface, or a surface normal to the first. The new ellipse will introduce the same set of constrains and equations as above, but in addition to that, we know the relationship between the plane normal and our inertial frame, which is fixed to the center of the channel. We can project 4 different lights on the four surfaces of the square channel as well as seen in Figure 8.4

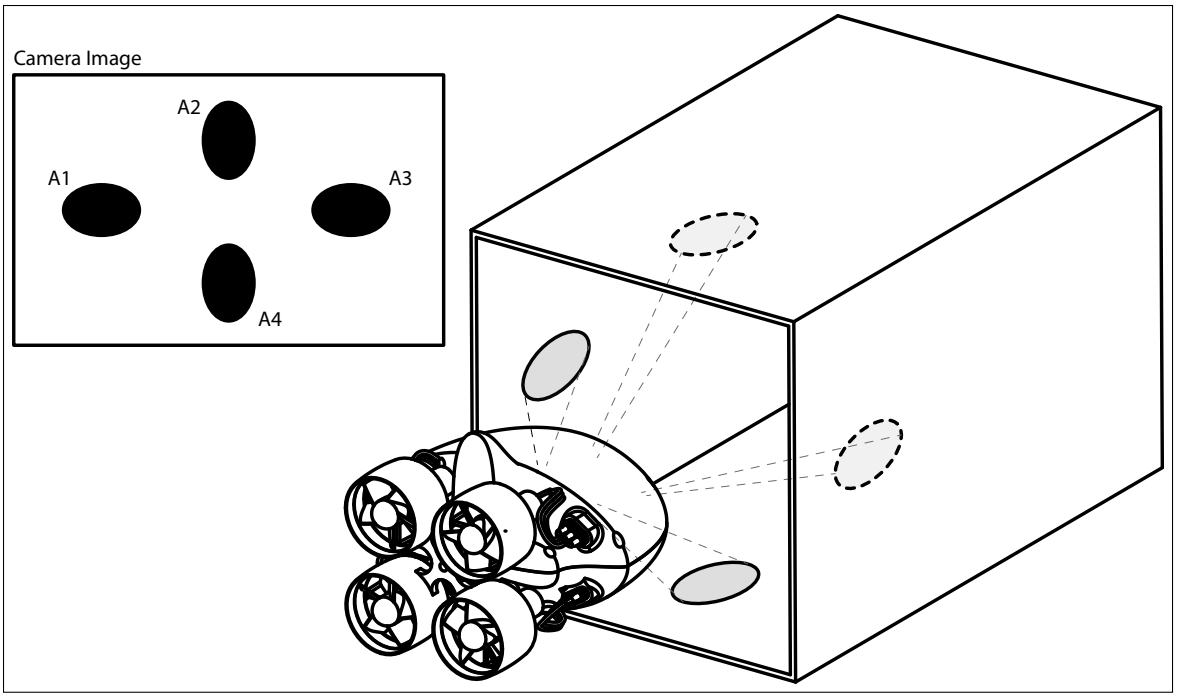

Figure 8.4: Robot Navigating a Rectangular Channel with 4 Light Projections

8.1.2 Cone Cylinder Intersection

One specific application targeted by this research is navigation within a water pipe. Unlike with a flat plane, the intersection of a cone with a quadric surface, such as a cylindrical pipe as shown in Figure 8.5, forms a non-planer quartic curve; a polynomial with degree 4. There is no simple implicit representation of the resultant curve. There are number of methods to tackle this problem.

Ruled Surface Assumption and Planar Equivalence Approach

The intersection of any two natural quadrics, results in at least one ruled surface along an axis [67]. For our specific application, the ruled surface would be along the pipe axis. This can be used to decouple the curve effect on the light projection. We can assume the projected ellipse is curved along the pipe's tangential axis and, if we know apriori the pipe diameter, then we can determine the curvature. We can also add the curvature effect as a variable. The pipe naturally has an infinite num-

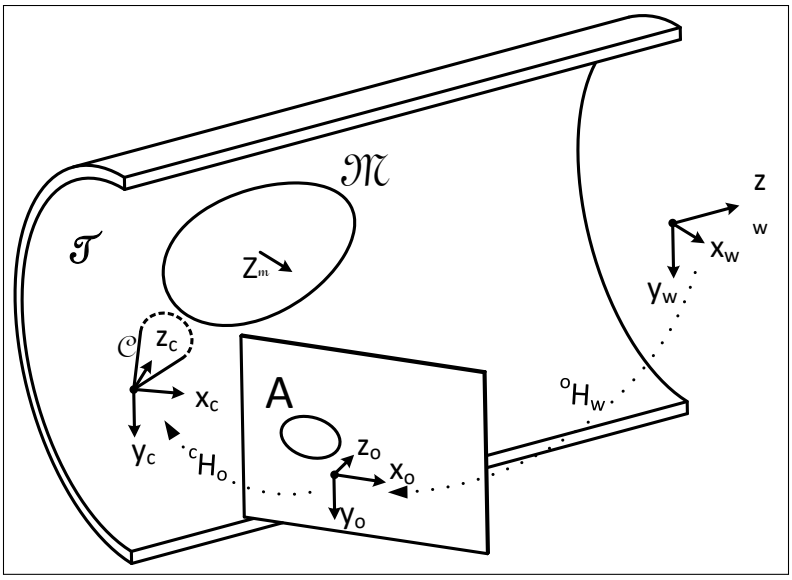

Figure 8.5: Single Light Projection on a Cylindrical Surface

ber of symmetric surfaces radially, and this can be used to estimate the pose with multiple light projections along any plane coincident with the camera's $z - axis$.

Image Based Visual Servoing

In a pipe, we are interested in maintaining the robot's position in the center of the pipe radially. If we project 3 or 4 lights radially-forward, then we will get 3 or 4 ellipses in our image plane. We can derive a control law in the image plane to position the ellipses in the image to a specific location corresponding to the attitude with respect to the pipe. This method can be particularly useful in our application since we will be using a fish-eye lens in an underwater environment, and distortion in this situation is large and requires us to have a reliable camera calibration. A calibrated camera may not be required to the same degree of accuracy, if we use Image Based Visual Servoiing (IBVS).

8.1.3 Projected Patterns

We can use a light pattern other than a simple cone. For example, we can project a grid pattern onto the surrounding surfaces. This results in a set of lines that can be used to estimate our absolute pose, as shown in Figure 8.6 . This method is computationally more efficient in theory, but suffers from several application-specific limitations. One limitation is that we are restricted within the robots physical space and the grid pattern projection may require a larger lens than the regular cone projection. The other limitation is that projecting a pattern would naturally mean most of the light is blocked and refracted at the pattern plate. This effect greatly reduces the intensity of the light being projected.

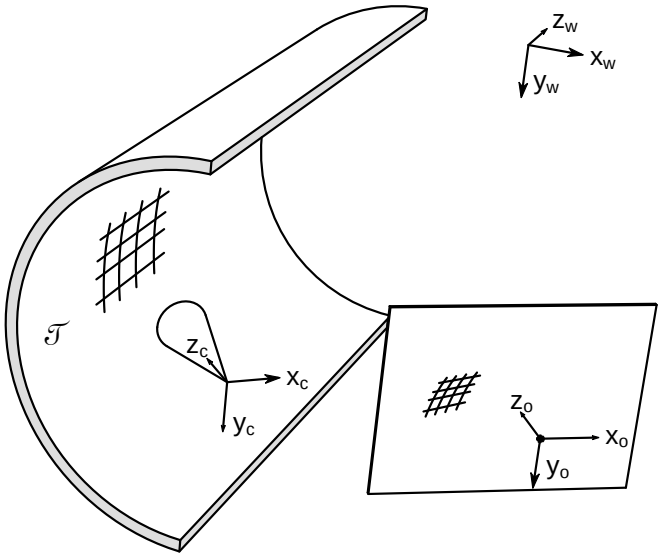

Figure 8.6: Single Grid Projection on a Cylindrical Surface

8.1.4 Attitude Estimation

The previous discussion focused on estimating the absolute pose of the robot with respect to a defined global reference frame, using projected features. However, the robot will be moving constantly. Therefore, an estimate of the pose will require taking into account the motion of the robot between each frame, defined as the rel-

ative pose ${}^{k}\mathbf{P}_{k-1}$.

$$ {}^{k}\mathbf{P}_{k-1} = \begin{bmatrix} {}^{k}\mathbf{R}_{k-1} & {}^{k}\mathbf{T}_{k-1} \\ \mathbf{0} & 1 \end{bmatrix} \tag{8.15} $$

The global pose estimate is computationally burdensome. Relying on it only to estimate the global pose, will result in a low sample rate that leads to drift in the position estimate. Faster methods can be used to estimate the relative motion. However, these methods generally require a fixed scenery in space. They boil down to tracking the position of pixels in the image and matching their correspondence from frame to frame.

In [68], optical flow is used via a monocular vision system pointed down, to estimate the relative horizontal position of a multi-rotor in a GPS-denied environment. And in [69], the global pose estimate is initially used to initialize a tracking EKF prediction filter, employed to track the position of a pole while flying in close proximity to it with a multirotor.

With relative pose estimation algorithms, the global pose can then be calculated by concatenating the relative pose with the previous global pose estimate ${}^{k}\mathbf{H}_{0} = {}^{k}\mathbf{P}_{k-1}{}^{k-1}\mathbf{H}_{0}$. The relative pose estimation can occur in parallel to estimating the global pose as shown in Figure 8.7.

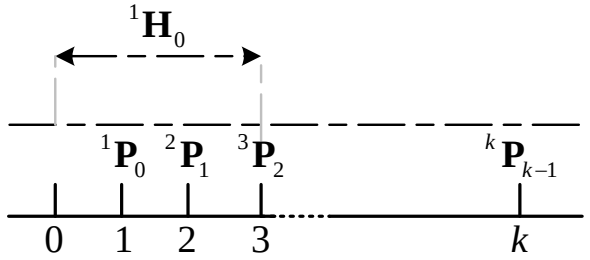

Figure 8.7: Parallel Global Pose Estimation with Relative Pose from Motion

CHAPTER 9

ATTITUDE CONTROL

In this chapter we will present a nonlinear attitude control method for the μAUV based on quaternion error kinematics. Given that the vehicle is expected to maneuver over the complete attitude space $SO(3)$, a globally stable attitude controller is required, and using an Euler Angles based attitude representation results in mathematical singularities at some kinematic configurations.

It is also the case with computing attitude rates in the inertial frame that using Euler angles limits the numerical computation of the Jacobian transformation as seen in Chapter 6. Quaternion error representations are also numerically stable under the condition of unity of magnitude, compared to rotations matrices.

In the full pose $\mathbb{R}^6$ space, the μAUVis under-actuated, but for a neutrally buoyant underwater vehicle and zero restoring forces; where the CoM and CoB are coincident, the unforced underwater vehicle is globally asymptotically stable.

$$\dot{p}(t) \in \mathbb{R}^6 \leq 0\,,\, \forall\, \tau \in \mathbb{R}^6 = 0\,,\, t > 0 \tag{9.1}$$

For sufficiently small rotational restoring forces $\boldsymbol{G}_2({}^{I}R_{B}) \leq \mathrm{C} \in \mathbb{R}^3$, the unforced μAUVis locally asymptotically stable around the equilibrium point and is fully actuated in the attitude space $\mathbb{R}^3$. The μAUVis controllable in the surge + attitude space $\mathbb{R}^4$.

First, an attitude rates controller and an output mixer algorithm as are presented. The attitude rates controller composes the inner loop of the attitude controller. Next, quaternion based segmented attitude controller will be presented, followed by a full model-based controller will be presented.

9.1 Attitude Rates Control

The rates controller implemented is a proportional-integrate-derivative controller with a feed-forward compensation term. The feed-forward term is useful for responding to the first order dynamics of the attitude rates, particularly to the slower dynamic response of roll motion, since roll motion is induced by the reaction torque of the thrusters, and for low torque thrusters relative to the roll hydrodynamic drag and the magnitude of the restoring forces term in roll, the first order response time constant τ_{roll} may be large.

There are two saturation limit conditions applied to the integral term, for each rotation axis respectively. The first condition is that there is a non-zero torque setpoints and that the torque setpoints are not saturated for the specific axis. The second condition is a hard limit imposed on the maximum integral term value.

The output of the PID + Feedforward controller is a torque setpoint. A saturation limit is applied to the torque setpoints based on the the estimated maximum achievable torques by the thrusters. An inverse thruster dynamics model is then used to map the thrust setpoint along with the torque setpoints to voltage setpoints as illustrated in algorithm 4, which are finally mixed into scaled voltage setpoints as the output for each thruster motor.

The output mixer maps the individual rates into actuator specific set-points. Ideally the rates are superimposed algebraically and divided over the actuators, but it is often that after mixing the compensated torque rates, one or more thruster setpoint becomes saturated. The mixer scales and shifts the output accordingly, to achieve the desired rates. The mixer can also be used to prioritize the rates by assigning specific relative scaling to each rate element. For instance, the thrust setpoint can be lowered to accommodate the desired attitude rates setpoints. Note

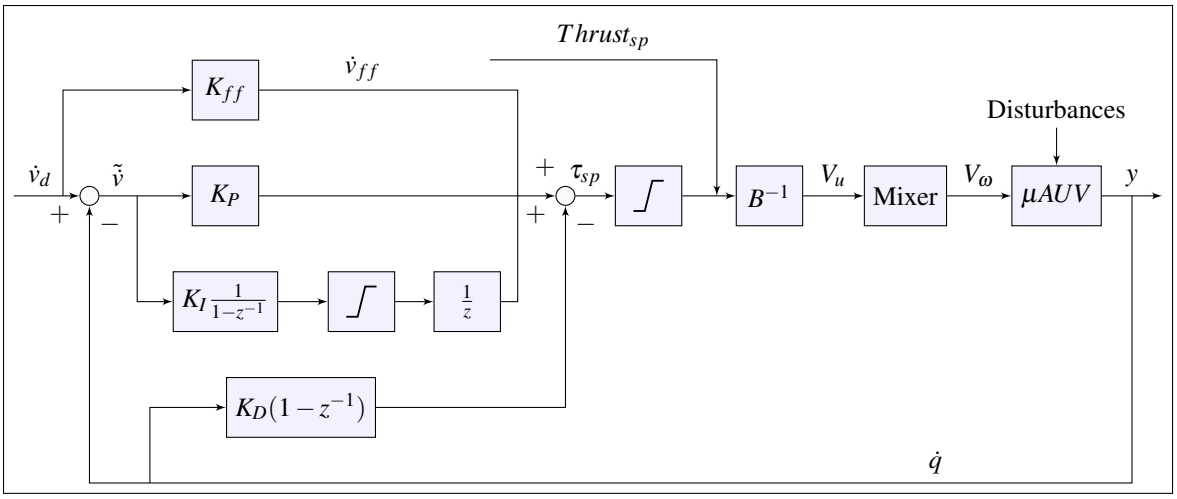

Figure 9.1: Attitude Rates Controller

The desired attitude rates and thrust are calculated upstream, the actual rates are estimated directly from the gyro sensor. The integral term is updated only when rate set-points for the specific axis of rotation are non-zero. The torque setpoint saturation limits may not be in effect since the rate limits are based on the maximum modeled thruster forces and torques.

that when the mixer scales and shifts the output in the case of saturation, the actuator commands no longer map accurately to the desired torque set-points, this may result in an unmapped behavior when implementing a trajectory controller. The rate controller gains and limits can be balanced and tuned to minimize the occurrence of mixer output inaccuracies.

The simulation output of the rate controller is illustrated in Figure 9.2. A yaw rate

Algorithm 4 Thruster Dynamics Compensation

1: function B^{-1}(u, $Thrust_{sp}$, $V_{battery}$)
2: $T_{roll} \leftarrow \frac{u_1}{N_{rotors}}$ ▷ Torque per thruster
3: F_{roll}, $F_{roll} \leftarrow \frac{u_2}{N_{rotors}R}$, $\frac{u_3}{N_{rotors}R}$ ▷ Thrust force per thruster
4: V_{roll}, V_{pitch}, $V_{yaw} \leftarrow f_T(T_{roll})$, $f_F(F_{pitch})$, $f_F(F_{roll})$ ▷ Map forces/torques to voltages
5: $V_{thrust} \leftarrow f_N(Thrust_{sp})$ ▷ Linearize thrust and map to voltage
6: return V_{roll}, V_{pitch}, V_{yaw}, V_{thrust} ▷ Return voltages scaled by battery voltage
7: end function

command through a joystick is given, there imperfect command also produces a noticeable pitch command as well. The output is not of a well tuned rate controller, but it illustrates the potential response rate of the controller.

A major concern with the control behavior seen here is the rapid reversal of motor commands, inducing jitter, energy loss in the system and degrading the high speed motor bearings. The rate input is scaled by a maximum rate gain as well, for yaw in this example it is scaled up to $2\pi(rad/s)$

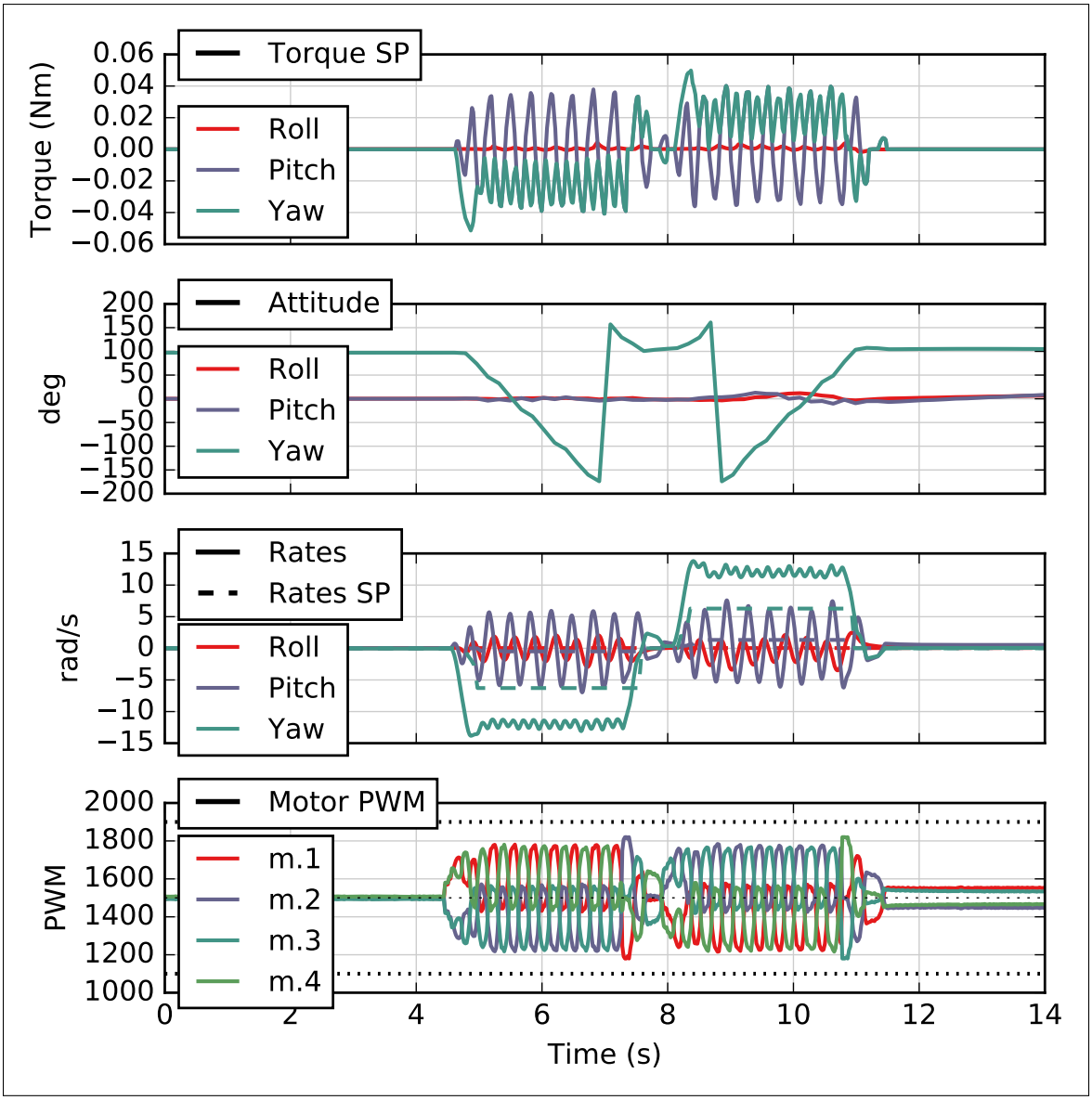

Figure 9.2: Rate Control Output - Simulation

9.2 Model-Based Quaternion Attitude Control

We can exploit the parameterized and validated dynamic system model of the μAUVto implement a model-based attitude controller. A model-based attitude controller for underwater vehicles is proposed by [70]. We would like to implement a controller that is potentially adaptive to dynamic changes in the model parameters, primarily that of the hydrodynamic damping effects inside the pipe. A case where an adaptive model-based controller is arguably more robust in performance compared to a tuned PID controller.

Given the 6DOF pose error $\tilde{\mathrm{p}}$, where $\mathrm{p} = \begin{bmatrix} x \\ y \\ z \\ \boldsymbol{q} \end{bmatrix}$, let's define the rates control tracking error $\boldsymbol{s}$

$$\boldsymbol{s} \in \mathbb{R}^7 = K_P \tilde{\boldsymbol{p}} + K_I \int \tilde{\boldsymbol{p}}(t)dt + K_D \dot{\tilde{\boldsymbol{p}}} \tag{9.2}$$

Let's consider the quadratic Lyapunov candidate function

$$\boldsymbol{V} \in \mathbb{R}^7 = \frac{1}{2} \boldsymbol{s}^T {}^I\boldsymbol{M}_B \, \boldsymbol{s}^T > 0 \tag{9.3}$$

Where ${}^I\boldsymbol{M}_B \in \mathbb{R}^7$ is the body μAUVmass matrix expressed in the inertial frame by the Jacobian rotation operator $\boldsymbol{J}^+(\boldsymbol{q}) \in \mathbb{R}^{6\times7}$ given in section 6.1. [70] proofs that the candidate function $\boldsymbol{V}$ has a derivative $\dot{\boldsymbol{V}}$ that is strictly negative and $\ddot{\boldsymbol{V}}$ is bounded. Resulting in the following model-based rate control law expressed in the inertial frame.

$${}^I\boldsymbol{\tau}_B = {}^I\boldsymbol{M}_B \ddot{\boldsymbol{p}}_r + {}^I\boldsymbol{C}_B(\dot{\boldsymbol{p}}_r) + {}^I\boldsymbol{D}_B(\dot{\boldsymbol{p}}_r) + {}^I\boldsymbol{G} - \boldsymbol{K}_s \boldsymbol{s} \tag{9.4}$$

The strictly negative condition of $\dot{\boldsymbol{V}}$ is held with a choice of $\boldsymbol{K}_s \in \mathbb{R}^{7\times7}$ that is

strictly positive, such that

$$\boldsymbol{K}_s \boldsymbol{s} \neq 0 \tag{9.5}$$

And using Barbalat's Lemma, the tracking error is shown to globally converge to zero.

The condition 9.5 is not valid with our controller for the full 6DOF tracking error. For a reduced 4DOF attitude + surge tracking error $\hat{\boldsymbol{s}} \in \mathbb{R}^4$, the condition is satisfied. In an ideal environment and non-coupled motion the sway and heave can be assumed stable, but as these assumptions break down, especially in confined spaces when lift forces and coupled hydrodynamic drag affects the sway and heave motion. For that, a trajectory planner would have to be developed to take into account minimizing these effects. Reducing 9.4 gives the model based control law expressed in the body frame and the associated tracking error

$$\hat{\boldsymbol{\tau}} \in \mathbb{R}^4 = \hat{\boldsymbol{M}}_B(\dot{\hat{\boldsymbol{v}}}_r) + \hat{\boldsymbol{C}}_B(\hat{\boldsymbol{v}}_r) + \hat{\boldsymbol{D}}_B(\hat{\boldsymbol{v}}_r) + {}^B\hat{\boldsymbol{G}} - \hat{\boldsymbol{J}}(\boldsymbol{q})\hat{\boldsymbol{K}}_s\hat{\boldsymbol{s}} \tag{9.6}$$

$$\hat{\boldsymbol{s}} \in \mathbb{R}^4 = K_P\tilde{\hat{\boldsymbol{p}}} + K_I \int \tilde{\hat{\boldsymbol{p}}}(t)dt + K_D\dot{\tilde{\hat{\boldsymbol{p}}}} \tag{9.7}$$

Where $\hat{\boldsymbol{v}}_r \in \mathbb{R}^4 = \begin{bmatrix} v_{1_r} \\ v_{4_r} \\ v_{5_r} \\ v_{6_r} \end{bmatrix}$ is the reduced desired body velocity rates. The controller block diagram is illustrated on Figure 9.3.

Note, that to implement the controller in this form, the estimated μAUVattitude has to be provided as quaternion rates, or calculated as such, by the following relationship

$$\dot{\boldsymbol{q}} = \frac{1}{2}\boldsymbol{q} \otimes \boldsymbol{v}_2 \tag{9.8}$$

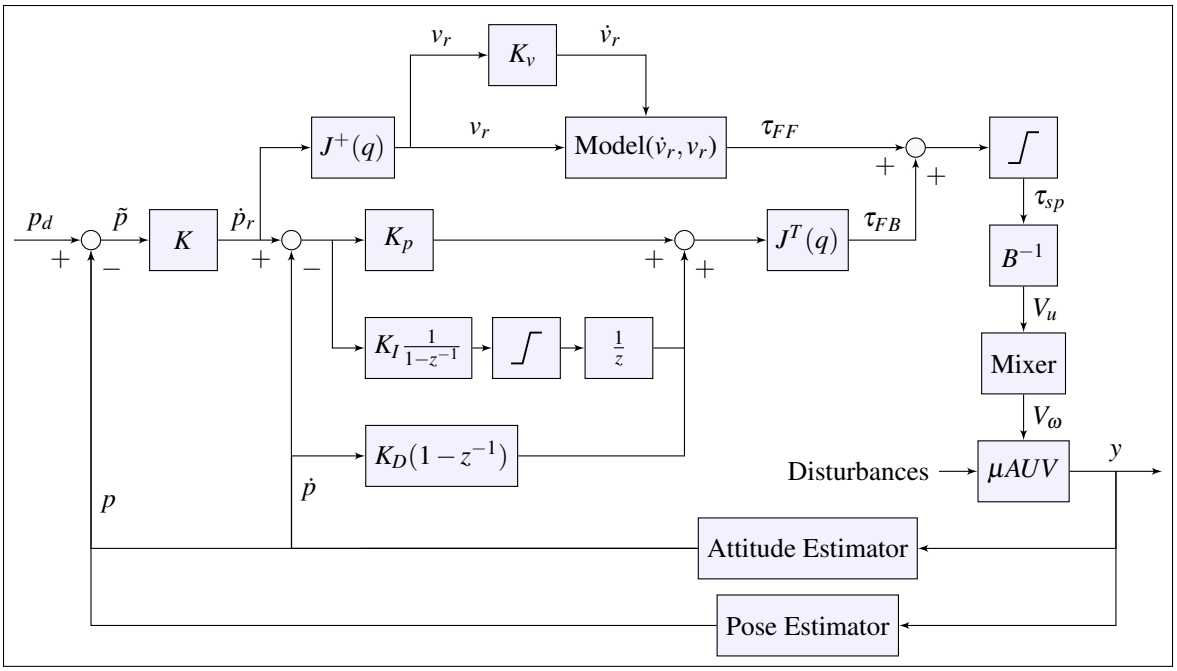

Figure 9.3: Model-Based Controller with Quaternion Rates

The linear position error can be calculated by subtraction between the desired and measured positions, and the quaternion attitude error can be calculated by the following quaternion product rule

$$\tilde{\boldsymbol{q}} = \boldsymbol{q}^* \otimes \boldsymbol{q}_d \tag{9.9}$$

The quaternion rate can be calculated from the quaternion error by the following product rule

$$\dot{q}_r = \frac{1}{2}\tilde{\boldsymbol{q}} \otimes \boldsymbol{K}\,,\, \boldsymbol{K} \in \mathbb{R}^4 = \begin{bmatrix} 0 \\ \boldsymbol{K}_r \\ \boldsymbol{K}_p \\ \boldsymbol{K}_y \end{bmatrix}_{\textit{Proportional Gain}} \tag{9.10}$$

The choice of a P controller for the attitude assumes a well tuned inner loop rate control and the attitude response exhibits a first-order response behavior, and the gains can be chosen to correspond to the rate controlled closed loop system's time constant. The inner rate control loop is assumed to run at a higher sample rate

than the attitude control loop. Similarly, the torque set-points from the quaternion rates error, can be calculated with a quaternion product rule for each of the proportional, integral and derivative gains and the following quaternion product rule can be applied to transform the quaternion rates to torque set-points.

$$\boldsymbol{\tau} = \frac{1}{2}\tilde{\boldsymbol{q}} \otimes \boldsymbol{K}\,,\, \boldsymbol{K} \in \mathbb{R}^4 = \begin{bmatrix} 0 \\ \boldsymbol{K}_{roll} \\ \boldsymbol{K}_{pitch} \\ \boldsymbol{K}_{yaw} \end{bmatrix}_{P,I\,Gains} \tag{9.11}$$

$$\boldsymbol{\tau} = \frac{1}{2}\dot{\boldsymbol{q}} \otimes \boldsymbol{K}\,,\, \boldsymbol{K} \in \mathbb{R}^4 = \begin{bmatrix} 0 \\ \boldsymbol{K}_{roll} \\ \boldsymbol{K}_{pitch} \\ \boldsymbol{K}_{yaw} \end{bmatrix}_{D\,Gain} \tag{9.12}$$

In the case of the μAUVthe angular rates are calculated directory by the onboard sensors, so while the quaternion rate reference can be computed as above, the rate controller can conveniently be implemented as in the previous section, where the angular rate references are expressed in Euler angles. This can be implemented easily by applying the left inverse Jacobian $J^{+}(q)$ upstream of the rate controller as shown on Figure 9.4.

The resulting rate controller is similar to the one applied earlier in section 9.1, except that a model based feed-forward controller implemented and the thrust setpoint is now a surge velocity setpoint. The latter assumes a linear velocity estimator is running on the controller.

The quaternion attitude error can be calculated directly as $\tilde{\boldsymbol{q}} = \boldsymbol{q}^* \otimes \boldsymbol{q}_d$, but this can correspond to two quaternions in $\mathbb{H}$. We are interested in the shortest path to the desired attitude, this can be ensured by taking carrying the sign of the real part, $\tilde{q}_r$ so that unit rotation angle is always less than or equal to 180°

$$\tilde{\boldsymbol{q}} \in \mathbb{H} = sign(\tilde{q}_r)(\boldsymbol{q}^* \otimes \boldsymbol{q}_d) \tag{9.13}$$

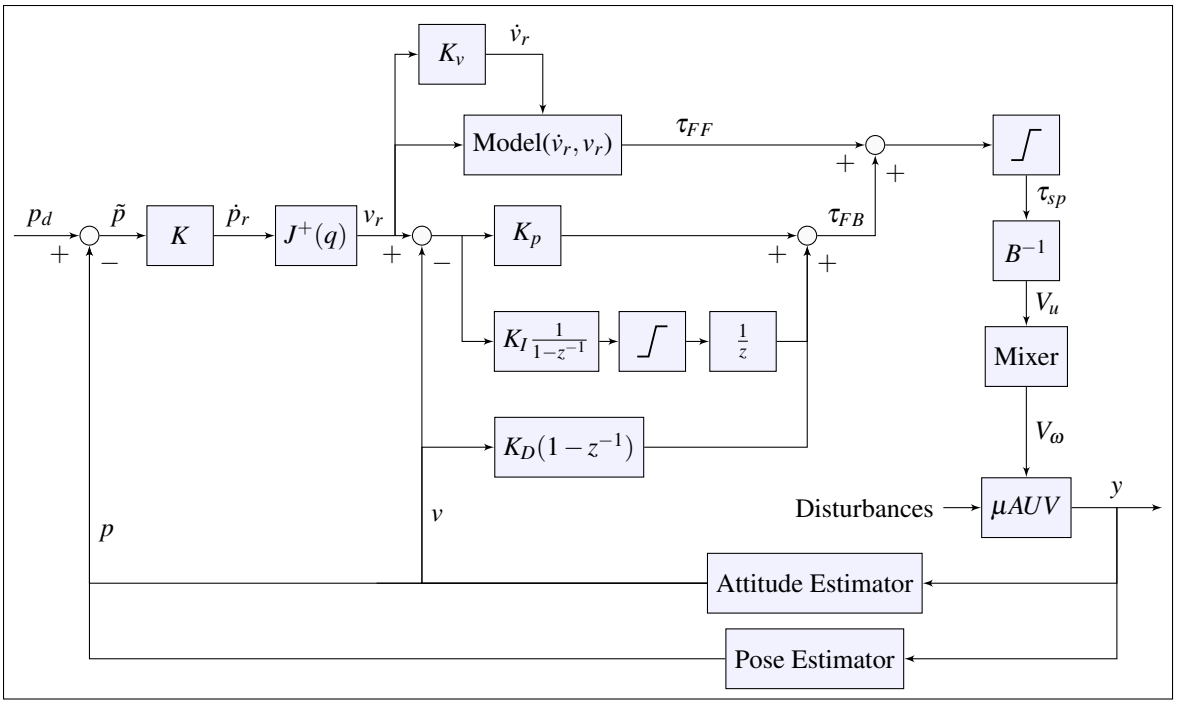

Figure 9.4: Model-Based Controller with Euler Rates

This sign carrying operation results in discontinuities when the desired attitude is

180° from the μAUV's attitude, producing a singularity and a non-converging controller near that point as shown by [71], specifically in the presence of measurement noise. As an example, consider the case where the vehicle is desired to pitch 180° as shown on Figure 9.5.

Ideally, both rotation directions would result in the same command, but in the presence of measurement noise, the resulting error direction can oscillate. This is only a momentary situation in the controller and one way to handle it is by commanding the rotation to follow the angular velocity sign if the quaternion error angle is close to 180°, since this is the minimum energy path, in the case of open water motion or with no trajectory constraints.

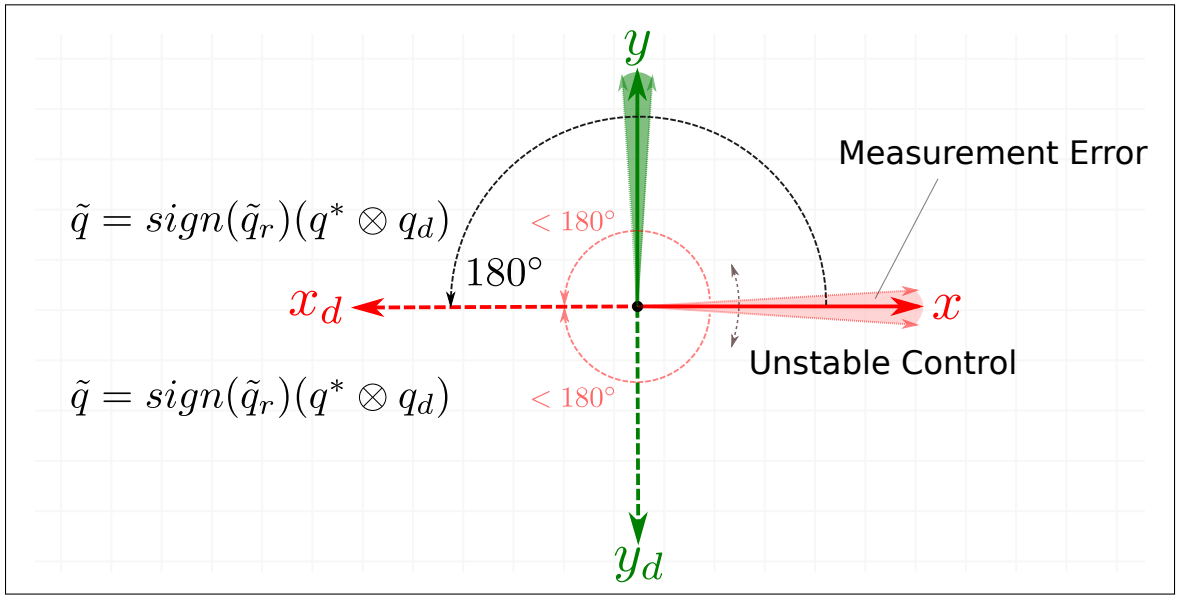

Figure 9.5: Quaternion Error Discontinuity

9.3 Geometric Quaternion Attitude Error

We can also exploit the geometry of the μAUVthrusters to compute the attitude error. Observe that thrust is always aligned with the surge direction $\vec{\boldsymbol{x}}$, and that the roll angle is inconsequential in tracking a trajectory for the μAUV, but it may be required to orient the perception sensors with a full attitude setpoint. The pitch and yaw rotation between the current and desired attitude can be expressed as the rotation of the surge vector $\vec{\boldsymbol{x}}$ by angle $\boldsymbol{\alpha}$ around $\vec{\boldsymbol{e}}_r$ as shown on Figure 9.6.

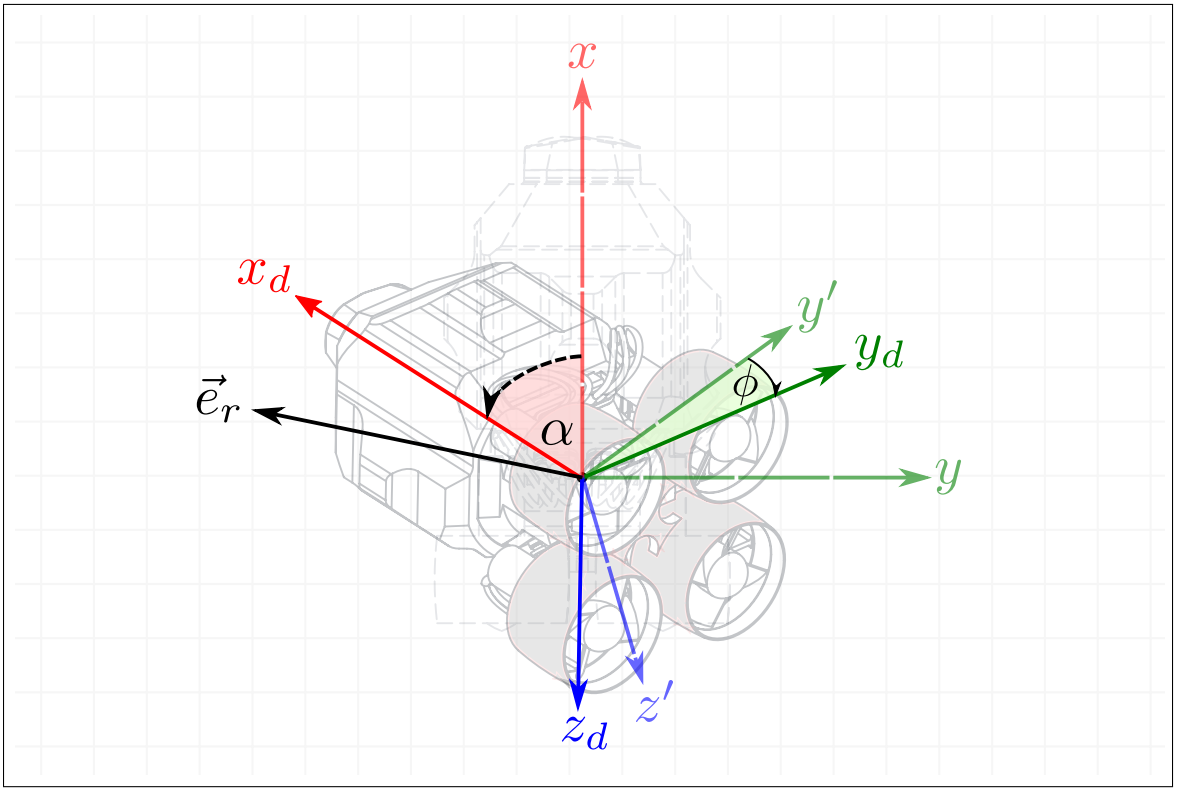

Figure 9.6: Attitude Error Representation

The roll rotation can then be performed over the rotated thrust vector $\vec{\boldsymbol{x}}_d$ by angle $\boldsymbol{\phi}$. Segmenting the controller into these two steps is useful in prioritizing pitch and yaw over roll, since the actuation effort is limited and it is useful to be able to achieve minimal pitch and yaw error tracking by not running into the risk of scaling

down the thrust effort by the mixer.

$$\tilde{\boldsymbol{q}} \in \mathbb{H} = \tilde{\boldsymbol{q}}_{roll} \otimes \tilde{\boldsymbol{q}}_{p,y} \tag{9.14}$$

$$\tilde{\boldsymbol{q}}_{p,y} = \langle \vec{\boldsymbol{e}}_r, \boldsymbol{\alpha} \rangle, \quad \vec{\boldsymbol{e}}_r = \frac{\vec{\mathrm{x}} \times \vec{\mathrm{x}}_d}{||\vec{\mathrm{x}} \times \vec{\mathrm{x}}_d||}, \quad \boldsymbol{\alpha} = cos^{-1} \frac{\vec{\mathrm{x}} \cdot \vec{\mathrm{x}}_d}{||\vec{\mathrm{x}}|| \cdot ||\vec{\mathrm{x}}_d||}, \quad 0^\circ \leq \boldsymbol{\alpha} \leq 180^\circ \tag{9.15}$$

$$\tilde{\boldsymbol{q}}_r = \langle \vec{\boldsymbol{x}}_d, \boldsymbol{\phi} \rangle \tag{9.16}$$

A summary of the attitude control algorithm is presented in algorithm 5. The discontinuity experienced when the thrust set-point is completely opposite the current thrust vector, can be handled by assigning the pitch-yaw error, or thrust vector error the full desired attitude vector, in the direction of the thrust vector rotation velocity. This will reduce the chance the μAUV jerks in the opposite direction, even if the motion is not path-optimal. It will be time-optimal and energy-optimal.
A useful attitude controller design tool is to treat the μAUVwith the the tuned rate controller as a closed loop system with a first-order response as shown on Figure 9.7. This allows for rapid development and testing of attitude controller algorithms and higher level algorithms. The closed-loop first-order time response characteristics of the real system can be calculated experimentally and used in the simulation.

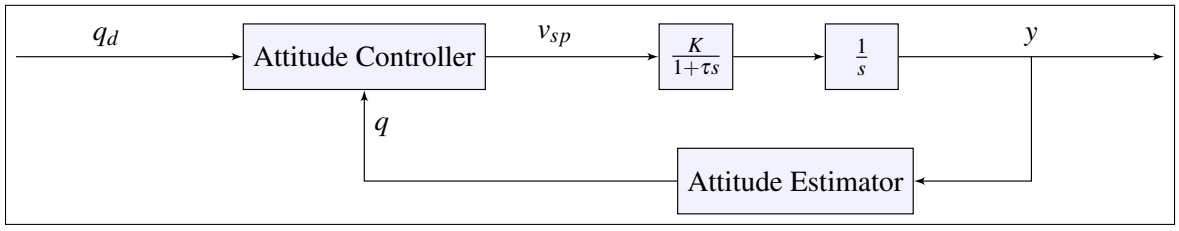

Figure 9.7: Attitude Controller with a First-Order Closed-Loop Rate Controller
The μAUVwith a well tuned rate controller behaves like a first-order closed loop system, allowing for a simplified attitude controller design process.

Algorithm 5 Attitude Controller

procedure Att Control($\boldsymbol{q}_d$, $\boldsymbol{q}$)
    if Full Attitude Control then
        $\boldsymbol{q}_d \leftarrow \boldsymbol{q}_d$
    else if Segmented Attitude Control then
        ${}^{B}\boldsymbol{q}_{py} \leftarrow \langle \vec{\boldsymbol{e}}, \alpha \rangle$
        if $\alpha \approx 180^\circ$ then
            ${}^{I}\boldsymbol{q}_{py} \leftarrow sign(\dot{\alpha})\boldsymbol{q}_d$ ▷ Handle discontinuity
        else
            ${}^{I}\boldsymbol{q}_{py} \leftarrow {}^{B}\boldsymbol{q}_{py} \otimes \boldsymbol{q}$ ▷ Rotate to I frame
        end if
        ${}^{B'}\boldsymbol{q}_{roll} \leftarrow \langle \vec{\boldsymbol{x}}_d, k\phi \rangle$ ▷ Scale roll error
        $\boldsymbol{q}_d \leftarrow {}^{I}\boldsymbol{q}_{py} \otimes {}^{B'}\boldsymbol{q}_{roll}$
    end if
    $\tilde{\boldsymbol{q}} \leftarrow \boldsymbol{q}^* \otimes \boldsymbol{q}_d$ ▷ Attitude error
    $\dot{\boldsymbol{q}}_{sp} \leftarrow \frac{1}{2} sign(\tilde{q}_r)\tilde{\boldsymbol{q}} \otimes \boldsymbol{K}$ ▷ Rates set-point to rate controller
    $\boldsymbol{v}_{sp} \leftarrow \boldsymbol{J}^{+}(\boldsymbol{q})\dot{\boldsymbol{q}}_{sp}$ ▷ Euler rates set-point in B frame
end procedure

Looking at one example where the vehicle is commanded by ramp-step command, to move 180° in the yaw direction and 45° in the pitch direction, we can see the response of the attitude controller shown on Figure 9.8. The figure displays key maneuver frames undertaken by the vehicle to reach the desired pose in an optimal-path.

The response to the SITL simulation with the above controller is illustrated in the following figures. Figure 9.9 shows the response to a yaw control command through a joystick and Figure 9.10 show the response to another command with mixed attitude set-points.

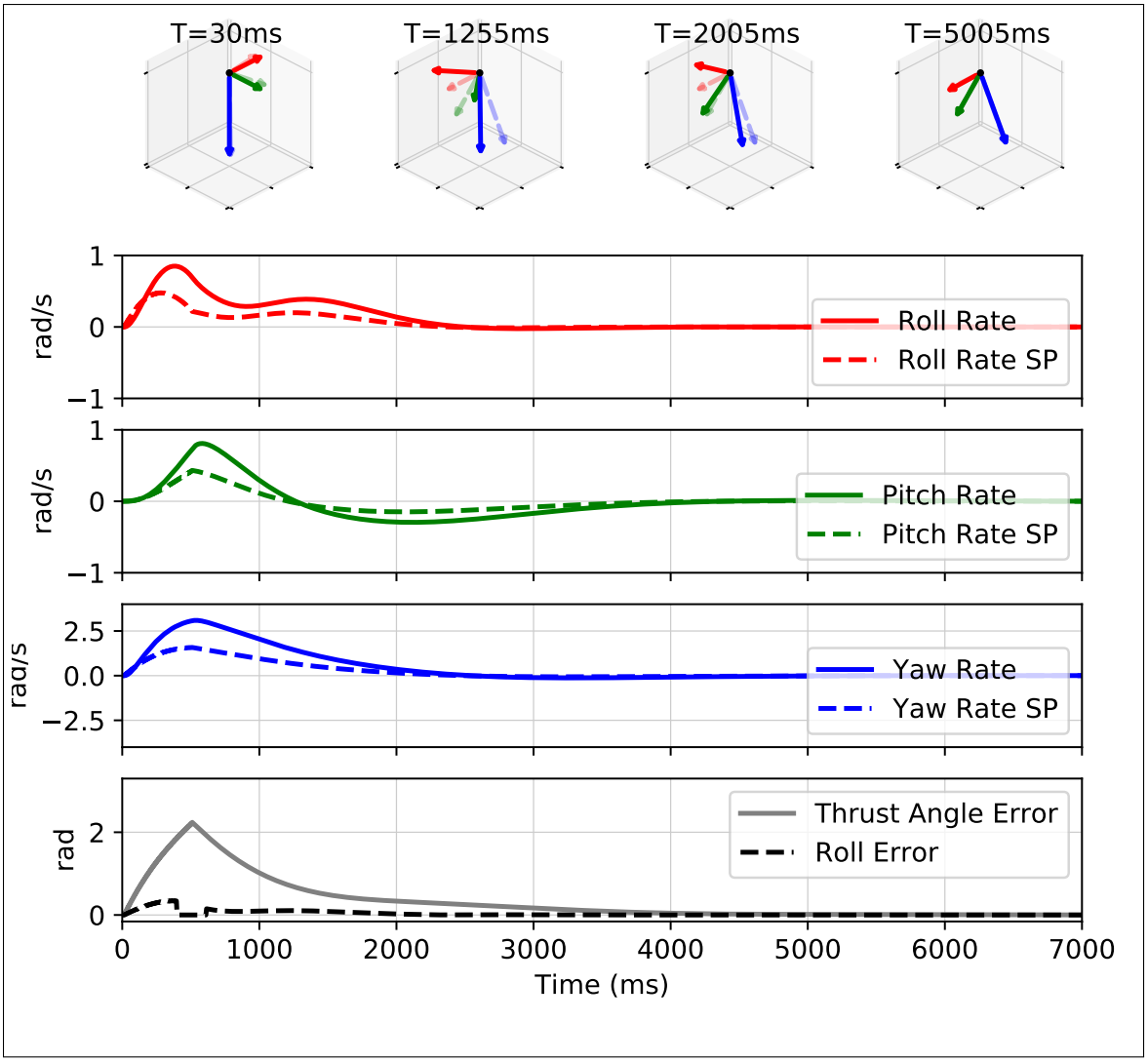

Figure 9.8: Geometric Attitude Control Simulated Response - Closed-Loop Rate Controlled System

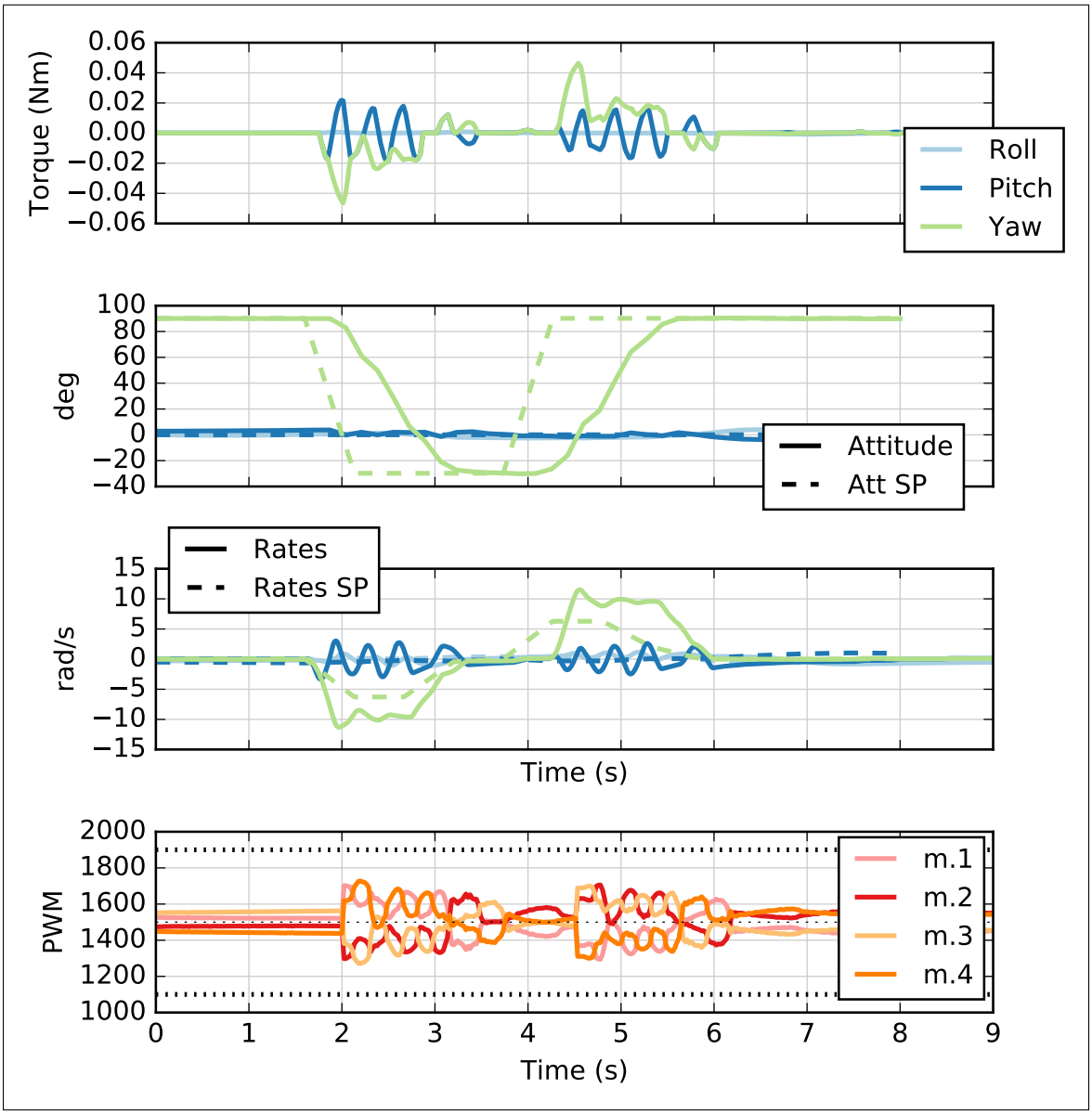

Figure 9.9: Attitude Control Output - Simulation. Yaw Command

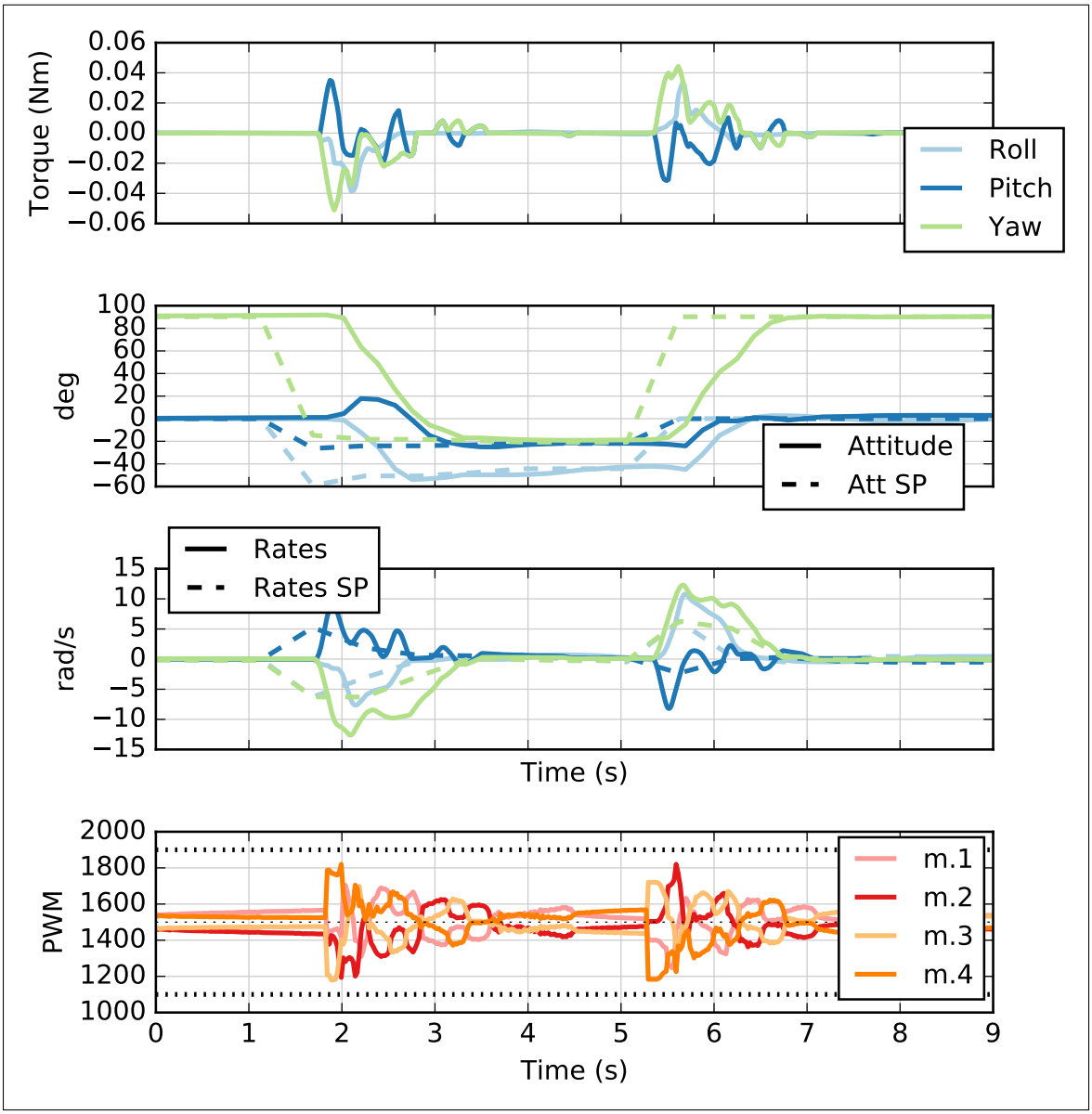

Figure 9.10: Attitude Control Output - Simulation. Mixed Command

CHAPTER 10

CONCLUSION AND FUTURE WORK

In this work we developed a mechatronic design methodology for design a micro autonomous underwater vehicle μAUV, targeted specifically to the confined space of a water pipe network. We derived a parameterized set of model parameters with respect to design variables and devised a design architecture for the μAUV. A fully functioning design realization was produced and termed a nominal design. This nominal design was then used to devise tools for estimating key model parameters, mainly the hydrodynamic drag coefficients and the thrust dynamics. The methods were validated experimentally.

The dynamic model and validated model parameters were used to develop a visual dynamic software-in-the-loop simulation platform. The simulation platform integrated a visual underwater simulation tool, together with an image processing module, a controller, and sensor dynamics around the dynamic model of the μAUV. This platform allows for further development of control algorithms, and expansion of the μAUV dynamics as well as for developing perception based pose estimation and obstacle detection algorithms.

A structured light projection based approach was proposed as a method to perform pose estimation in confined spaces with well defined structures, such as rectangular channels. The method can be extended to cylindrical sections such as pipes.

Finally a quaternion based attitude controller was implemented, on top a model-based attitude rate controller. This research opens the opportunity to a number of tangential developments in each of the areas investigated. We will summarize possible future work in the following sections

10.1 Design Architecture

Different design architecture with alternative thruster allocations can be explored as well, to tackle the problem of in-pipe navigation. For instance, thrusters with a radial component that compensate for heave and sway error may be beneficial in centering the vehicle in the pipe and minimizing the drag effects cause by deviating away from the center.

10.2 Electromechanical Design

Using UHF communication still offers a limited operational range. Investigating the use of ultrasonic communication on the scale of the μAUV is an active research area and is worth exploring for intended application of this work. With regards to design realizations, a method to wirelessly charge the onboard battery can be highly beneficial, it can allow for flexibility in designing the seals as they don't have to be temporary.

10.3 Parameter Estimation

The added mass matrix elements highly affect the accuracy of the dynamic model, especially with agile type motion. It is worth investigating methods for identifying those parameters for the μAUV beyond the use of basic spheroidal shape assumptions. It will be even more useful to study the effect of motion near other rigid bodies on the added mass.

A Hybrid Extended Kalman Filter approach was proposed for identifying the model parameters online. Performing experimentations to validate the proposed approach and improve it would be useful. The method can be extended by using particle filters and implementing the particle filter on GPU capable microprocessors, which

can be acquire and installed on similar scale μAUVs.

With regards to the thruster dynamics, the experimental profiling can be expanded to test propellers of varying blade geometries and diameters. A dynamometer can be devised to accurately measure torque underwater to result in more robust experimentation. It is useful to look at the effects of proximity of the pipe wall to the thruster, and its performance gets affected.

10.4 Simulation

The collision dynamics applied in the simulation can be improved to capture the elasticity of the shell material as well is a more accurate geometric representation of the vehicle. Since it is likely that the vehicle will collide with the pipe wall, it would be useful to simulate and test the controller under this scenario.

The hydrodynamic in-pipe model can also be investigated in more depth, including the affect of near wall motion and at bends and tees in the pipe.

The visual simulation platform can be replaced with a more realistic environment, such as with using the Unity3D gaming environment [72].

10.5 Perception

Alternative to the conic light projection, a different pattern, such as a grid pattern can be investigated as a method for visualizing the internal of the pipe and performing pose estimation as well. It is also worth investigating the use of surface mounted ultrasonic sensors as a method to perform pose estimation and obstacle detection.

10.6 Control

Trajectory generation has not been discussed in this work. Trajectory generation techniques such as differential flatness can be investigated to produce agile trajectories in the pipe. The model-based rate controller can be tested further against highly varying hydrodynamic drag in the environment.

Appendices

APPENDIX A

EXPLORATORY DESIGNS

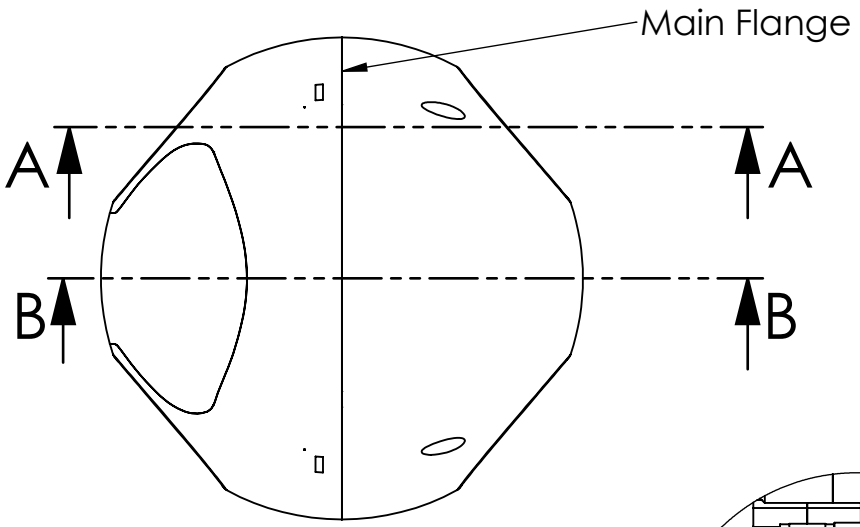

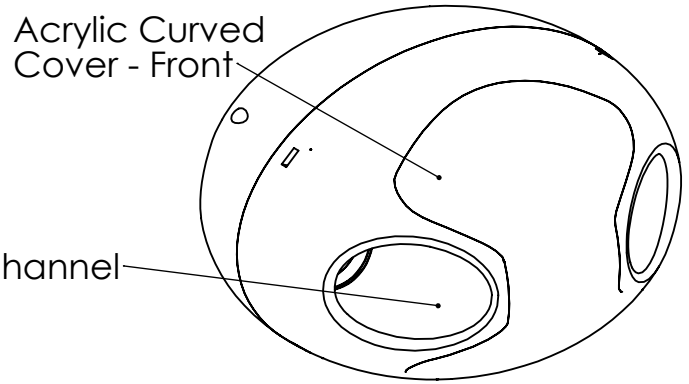

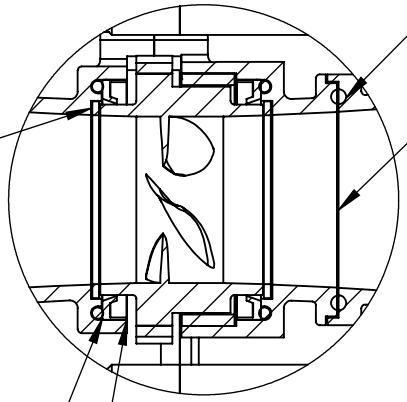

DETAIL D

SCALE 1 : 1

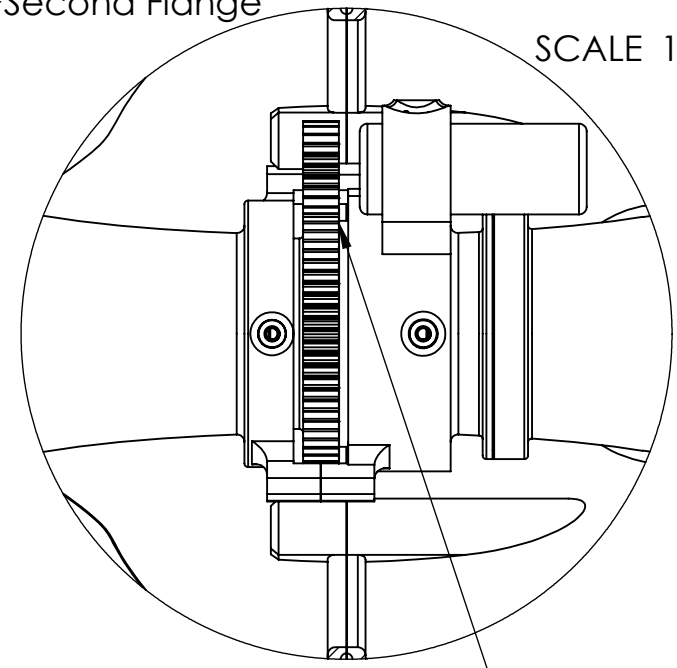

DETAIL C

SCALE 1 : 1

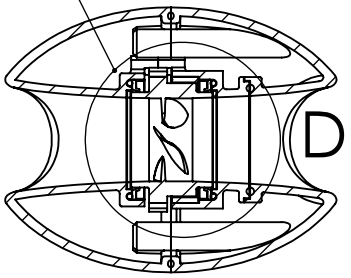

SECTION A-A

SECTION B-B

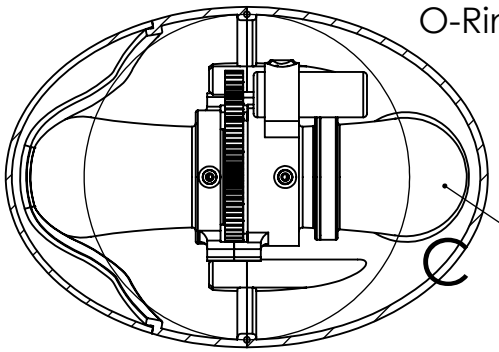

	DESIGNED AND DRAWN	TITLE: Ellipsoidal mAUV	
NAME	Ali AlSaibie		
DATE	03/15/2015	SIZE A	PROPRIETARY AND CONFIDENTIAL
		REV 1	SCALE: 1:2 / SHEET 1 OF 1

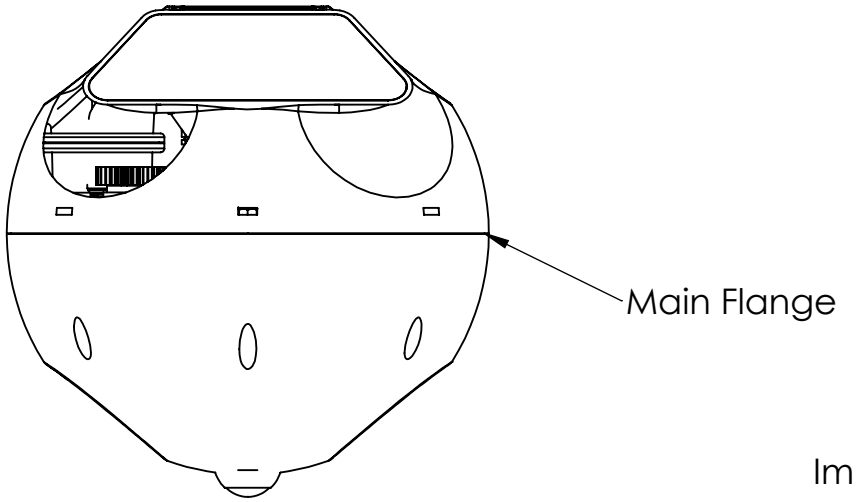

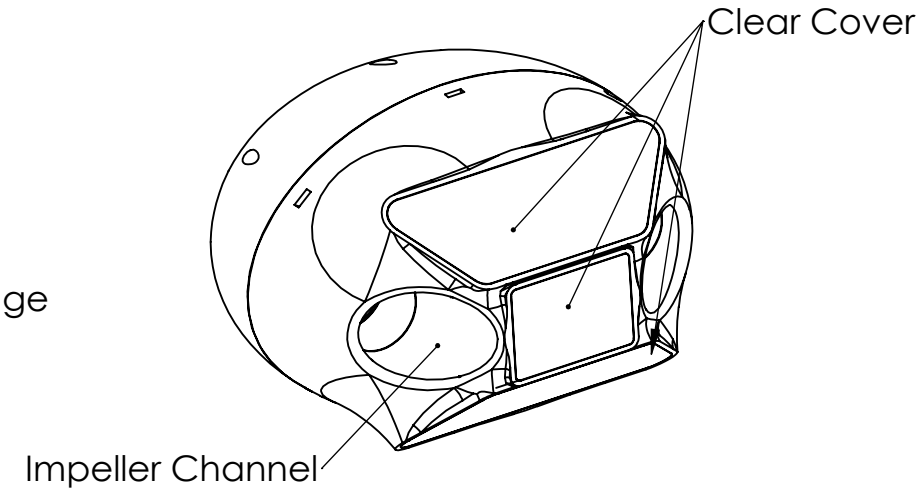

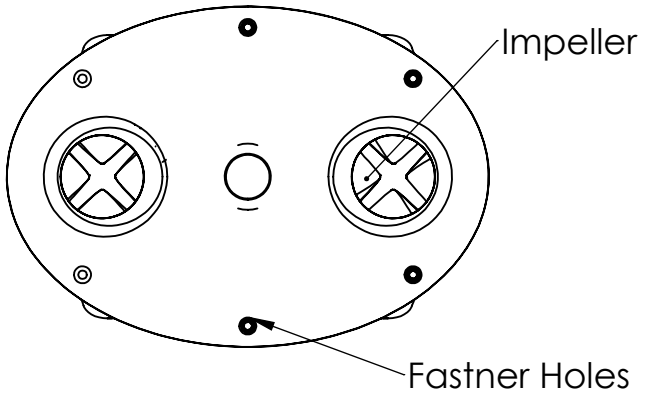

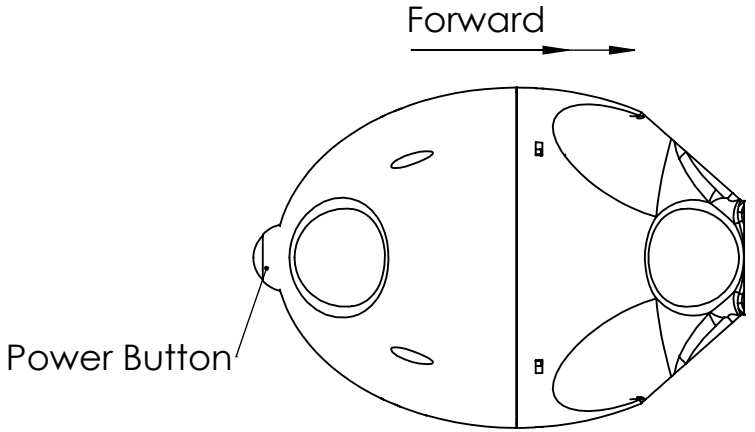

	DESIGNED AND DRAWN	TITLE: Ellipsiodal mAUV
NAME	Ali AlSaibie	
DATE	05/15/2015	SIZE A — PROPRIETARY AND CONFIDENTIAL
		REV 2 — SCALE: 1:2 — SHEET 1 OF 2

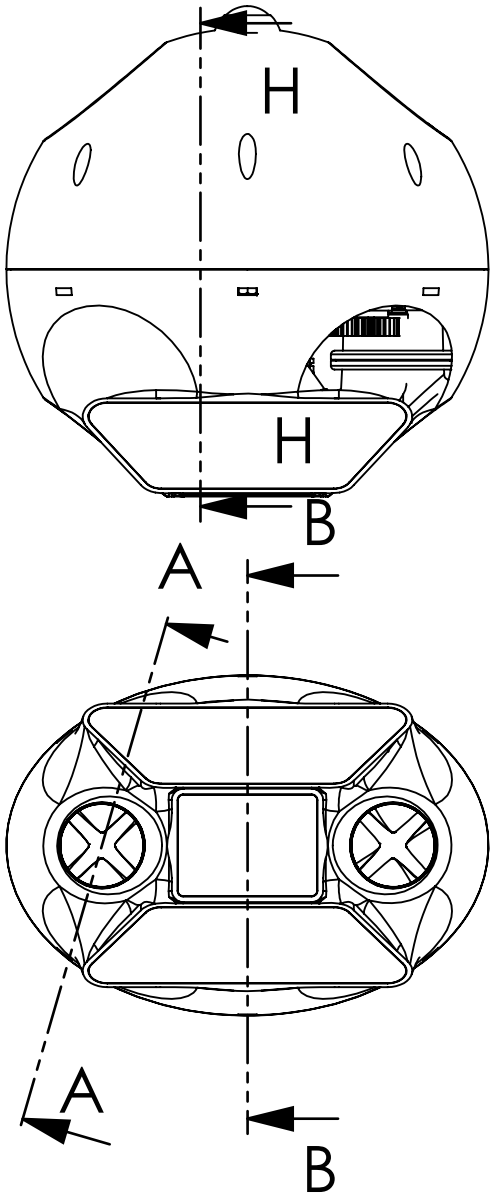

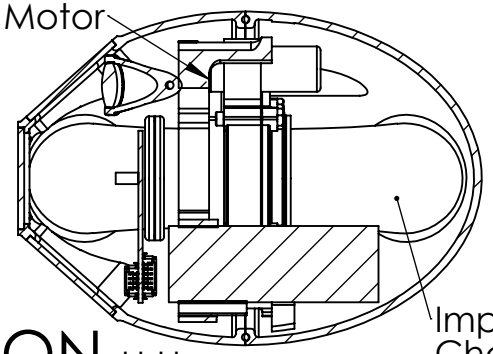

SECTION H-H

SCALE 1 : 2

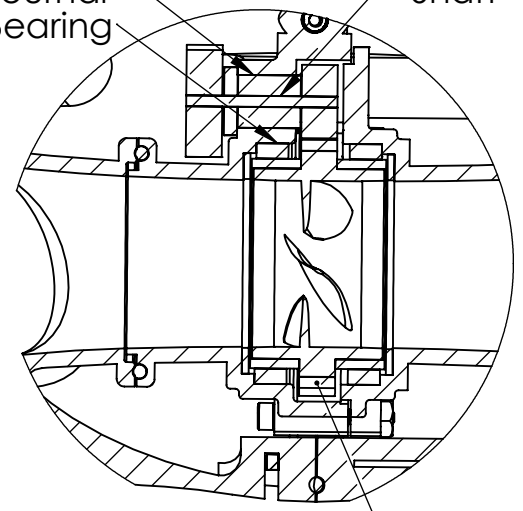

DETAIL G

SCALE 1 : 1

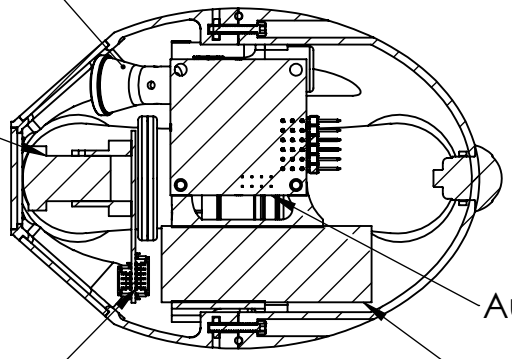

SECTION B-B

SCALE 1 : 2

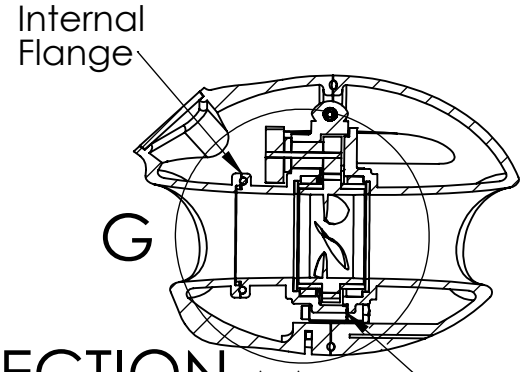

SECTION A-A

SCALE 1 : 2

	DESIGNED AND DRAWN	TITLE: Ellipsoidal mAUV
NAME	Ali AlSaibie	
DATE	05/15/2015	SIZE A / PROPRIETARY AND CONFIDENTIAL
		REV 2 / SCALE: 1:5 / SHEET 2 OF 2

APPENDIX B

μAUV DESIGN R1

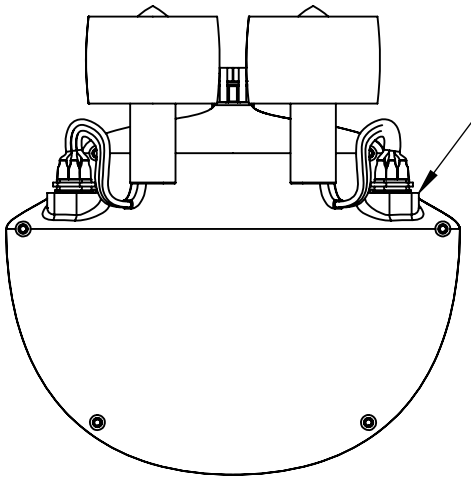

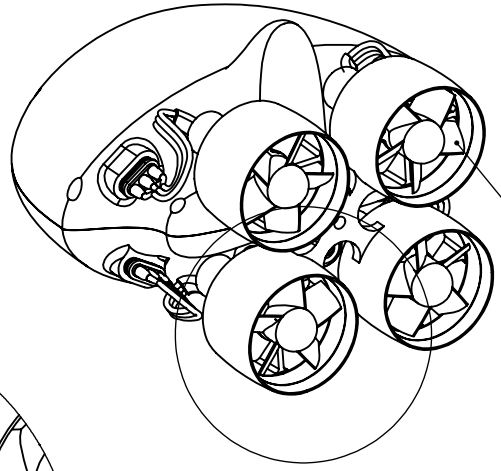

E

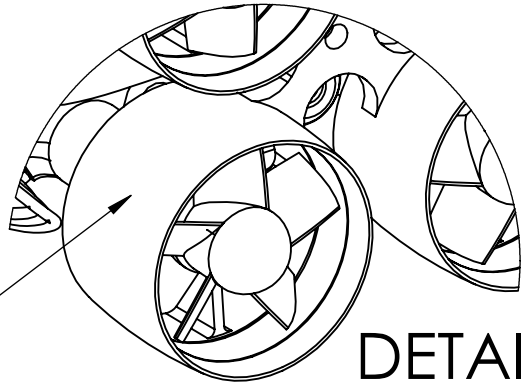

DETAIL E

SCALE 1 : 1

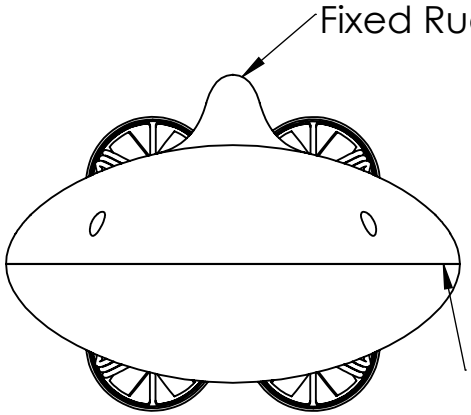

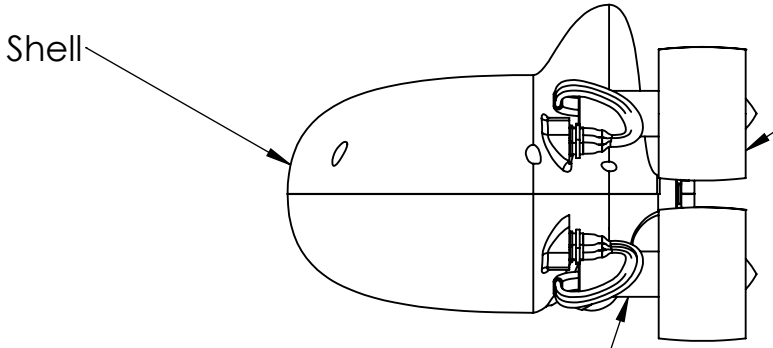

	DESIGNED AND DRAWN	TITLE: Multirotor Inspired mAUV	
NAME	Ali AlSaibie		
DATE	03/15/2017	SIZE A	PROPRIETARY AND CONFIDENTIAL
		REV 1	SCALE: 1:2 / SHEET 1 OF 2

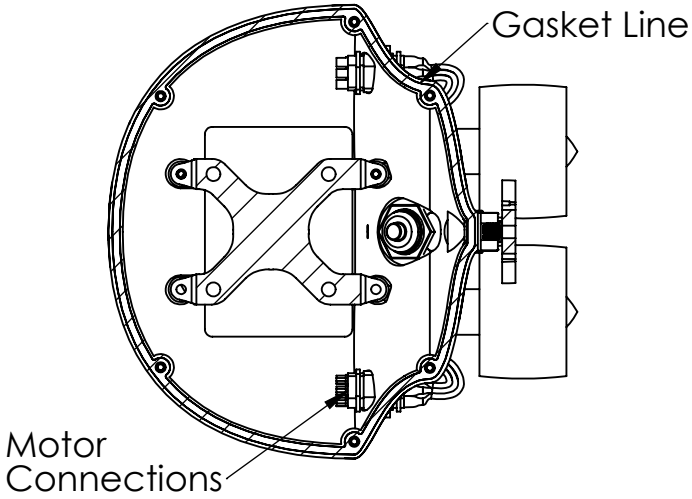

SECTION A-A

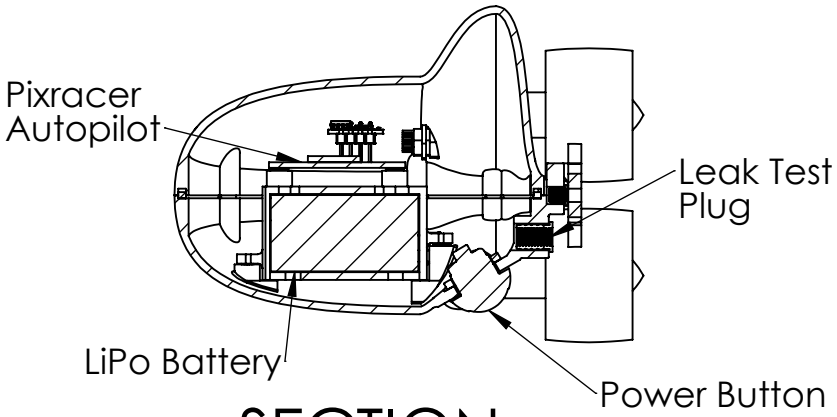

SECTION B-B

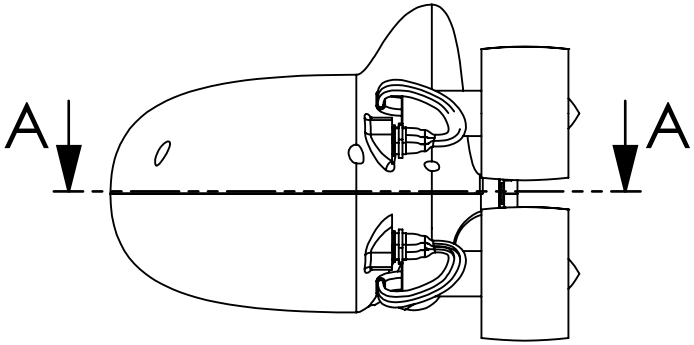

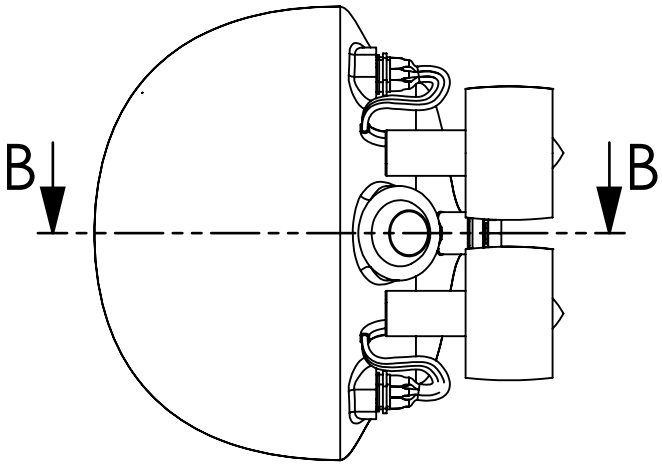

	DESIGNED AND DRAWN	TITLE: Multirotor Inspired mAUV	
NAME	Ali AlSaibie		
DATE	03/15/2017	SIZE A	PROPRIETARY AND CONFIDENTIAL
		REV 1	SCALE: 1:2 / SHEET 2 OF 2

APPENDIX C

μAUV DESIGN R2

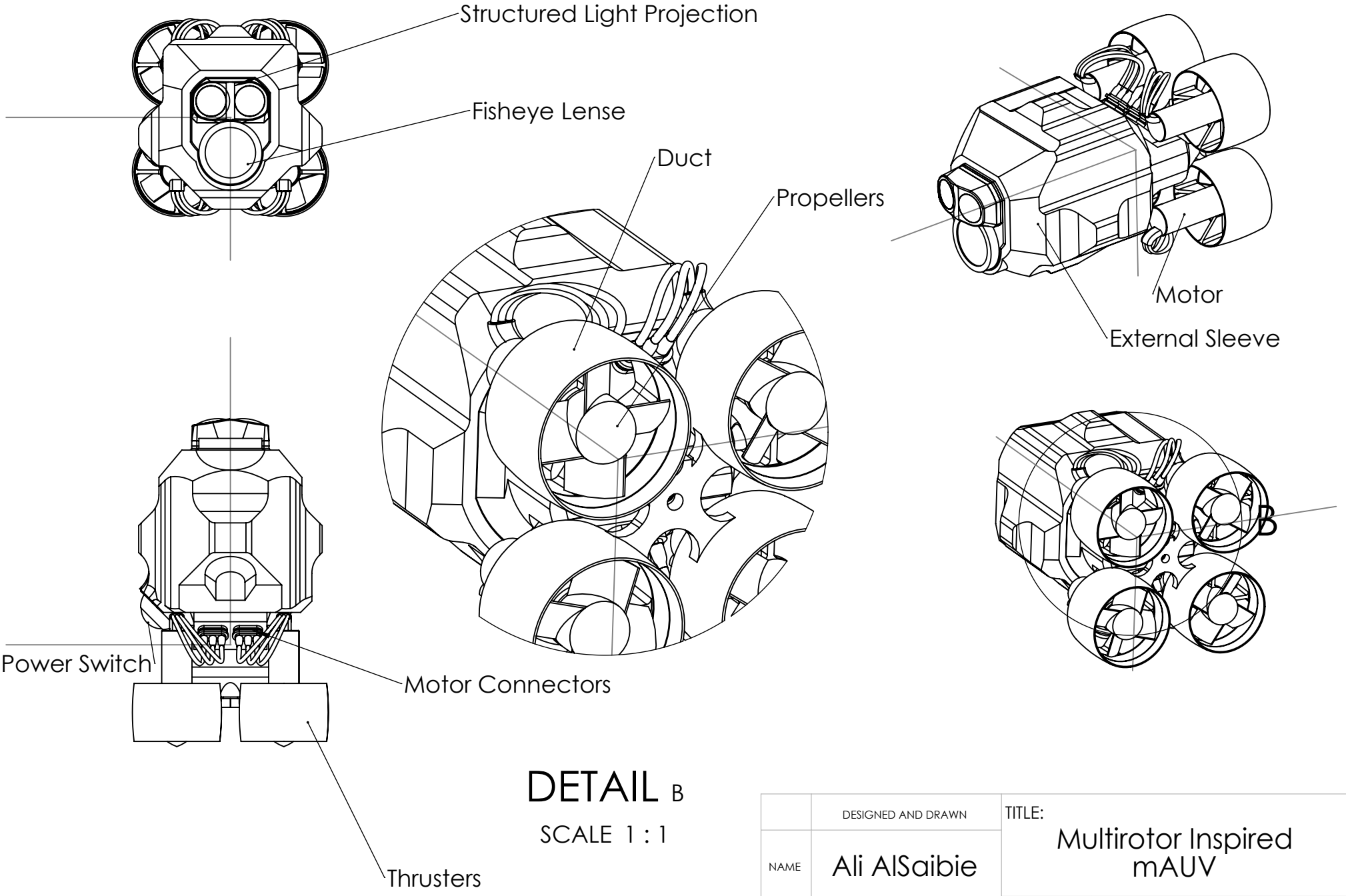

DETAIL B

SCALE 1 : 1

	DESIGNED AND DRAWN	TITLE: Multirotor Inspired mAUV	
NAME	Ali AlSaibie		
DATE	05/15/2018	SIZE A	PROPRIETARY AND CONFIDENTIAL
		REV 1	SCALE: 1:2 / SHEET 1 OF 2

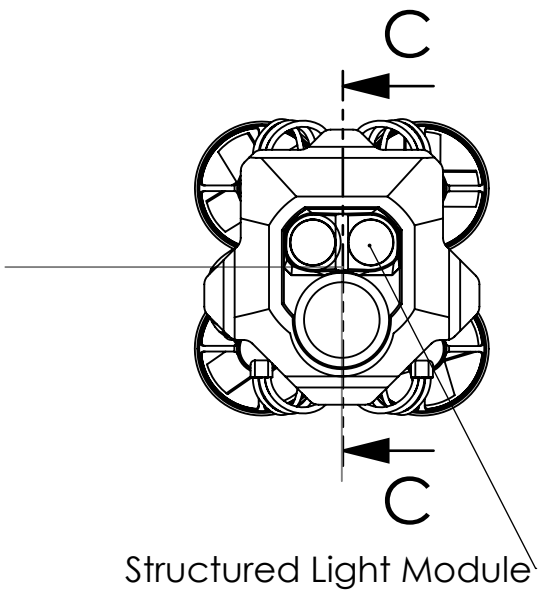

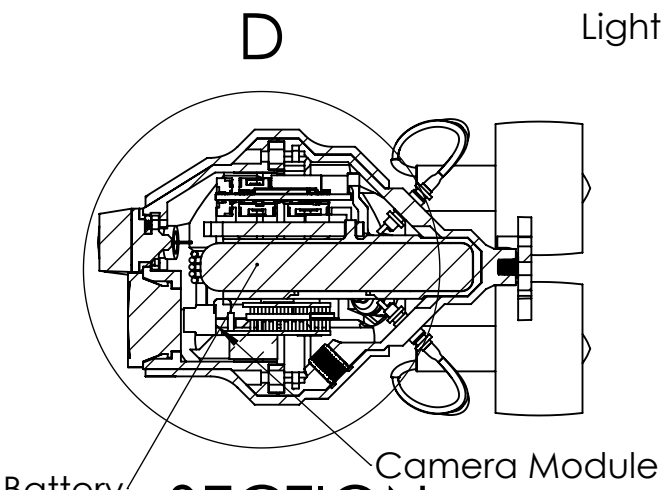

SECTION C-C

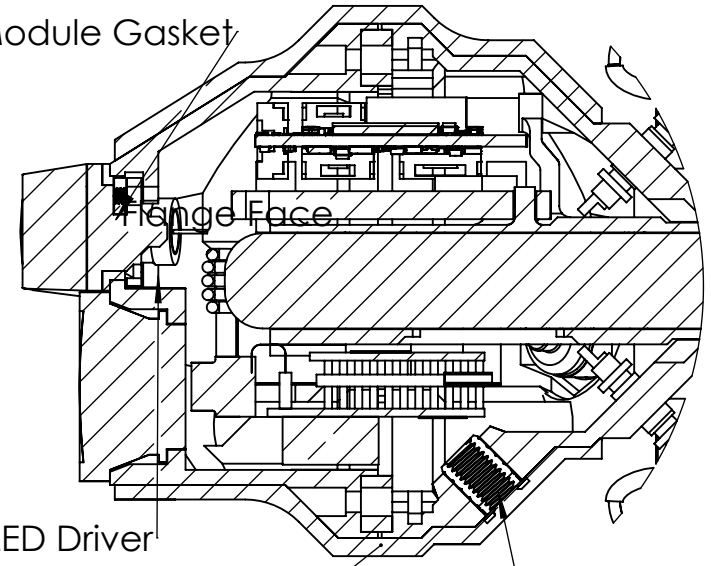

DETAIL D

SCALE 1 : 1

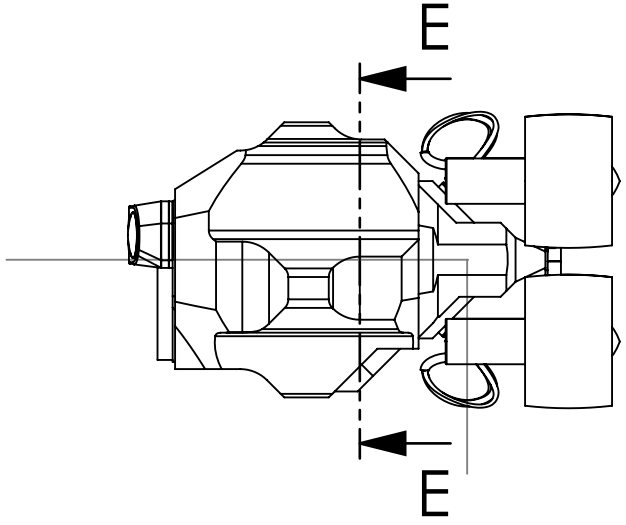

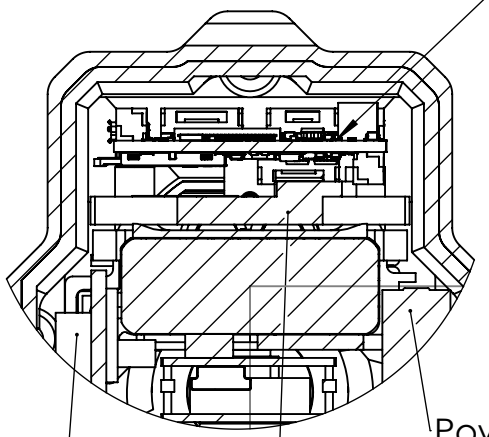

DETAIL F

SCALE 1 : 1

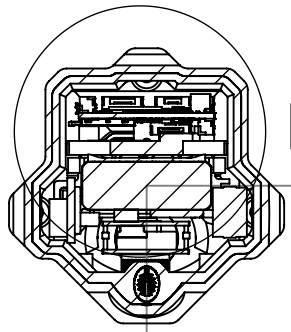

SECTION E-E

	DESIGNED AND DRAWN	TITLE: Multirotor Inspired mAUV	
NAME	Ali AlSaibie		
DATE	05/15/2018	SIZE A	PROPRIETARY AND CONFIDENTIAL
		REV 1	SCALE: 1:2 SHEET 2 OF 2

REFERENCES

[1] C. Choi, B. Park, and S. Jung, "The design and analysis of a feeder pipe inspection robot with an automatic pipe tracking system", IEEE/ASME Trans. Mechatronics, vol. 15, no. 5, pp. 736–745, 2010.

[2] R. Aracil, R. Saltarén, and O. Reinoso, "Parallel robots for autonomous climbing along tubular structures", Rob. Auton. Syst., vol. 42, no. 2, pp. 125–134, 2003.

[3] T. Fukuda, H. Hosokai, and M. Otsuka, "Autonomous pipeline inspection and maintenance robot with inch worm mobile mechanism", Proceedings. 1987 IEEE Int. Conf. Robot. Autom., vol. 4, 1987.

[4] K. Reber, S. Hartmann, and A. Boensich, "Inspection of Subsea Pipelines with the MEC COMBI Crawler", Pipeline Technol. J., vol. June, 2016.

[5] S. H. Lee, "Design of the out-pipe type pipe climbing robot", Int. J. Precis. Eng. Manuf., vol. 14, no. 9, pp. 1559–1563, 2013.

[6] J. Okamoto, J. C. Adamowski, M. S. Tsuzuki, F. Buiochi, and C. S. Camerini, "Autonomous system for oil pipelines inspection", Mechatronics, vol. 9, no. 7, pp. 731–743, 1999.

[7] A. Industries and Rosen, "The Ultimate Guide to Unpiggable Pipelines", Pipelines Int., 2013.

[8] Z. Hu and E. Appleton, "Dynamic characteristics of a novel self-drive pipeline pig", IEEE Trans. Robot., vol. 21, no. 5, pp. 781–789, 2005.

[9] K. H. Yoon and Y. W. Park, "Design, fabrication, and characterization of in-pipe robot with controllable magnetic force", 2012 IEEE Int. Conf. Autom. Sci. Eng., pp. 786–789, 2012.

[10] S.-g. Roh and H. R. Choi, "Differential-drive in-pipe robot for moving inside urban gas pipelines", IEEE Trans. Robot., vol. 21, no. 1, pp. 1–17, 2005.

[11] C. Choi, D. M. Chatzigeorgiou, R. Ben-mansour, and K. Youcef-toumi, "Design and Analysis of Novel Friction Controlling Mechanism with Minimal Energy for In-Pipe Robot Applications", in IEEE Int. Conf. Robot. Autom., 2012, pp. 4118–4123, isbn: 9781467314053.

[12] J. Qiao, J. Shang, and A. Goldenberg, "Development of Inchworm In-Pipe Robot Based on Self-Locking Mechanism", IEEE/ASME Trans. Mechatronics, vol. 18, no. 2, pp. 799–806, 2013.

[13] M. Takahashi, I. Hayashi, N. Iwatsuki, K. Suzumori, and N. Ohki, "The development of an in-pipe microrobot applying the motion of an\nearthworm", 1994 5th Int. Symp. Micro Mach. Hum. Sci. Proc., pp. 35–40, 1994.

[14] F. Trebu, I. Virgala, M. Pástor, T. Lipták, and U. Miková, "An inspection of pipe by snake robot", Int. J. Adv. Robot. Syst., no. 1-12, 2016.

[15] A. Kuwada, S. Wakimoto, K. Suzumori, and Y. Adomi, "Automatic Pipe Negotiation Control for snake-like robot *", no. 438, pp. 558–563, 2008.

[16] K. Suzumori, S. Wakimoto, and M. Takata, "A miniature inspection robot negotiating pipes of widely varying diameter", 2003 IEEE Int. Conf. Robot. Autom. (Cat. No.03CH37422), vol. 2, pp. 2735–2740, 2003.

[17] You Wu, "Design and fabrication of a maneuverable robot for in-pipe leak detection", PhD thesis, Massachusetts Institute of Technology, 2014.

[18] RovMarine Technologies, The history of ROVs - RovMarine Technologies. [Online]. Available: `http://www.rovmarine.it/en/home-eng/14-not-categorized/16-the-history-of-rovs` (visited on 01/24/2017).

[19] G. Antonelli, Underwater Robots. 2014, vol. 96, isbn: 9783540317524.

[20] Wikipedia, Il ROV Pluto Plus, 2009. [Online]. Available: `https://commons.wikimedia.org/wiki/File:ROV{\_}Pluto.jpg` (visited on 01/25/2017).

[21] G. A. Ribeiro, A. Pinar, E. Wilkening, S. Ziaeefard, and N. Mahmoudian, "A Multi-level Motion Controller for Low-Cost Underwater Gliders", pp. 1131–1136, 2015.

[22] Underwater robot for port security — MIT News. [Online]. Available: `http://news.mit.edu/2014/underwater-robot-for-port-security-0926` (visited on 03/14/2017).

[23] R. Du, Z. Li, K. Youcef-Toumi, and P. Valdivia y Alvarado, Robot Fish; Bio-inspired Fishlike Underwater Robots. 2015, p. 377, isbn: 9783662468692.

[24] S. Ghosh, R. Ray, S. R. K. Vadali, S. N. Shome, and S. Nandy, "Reliable pose estimation of underwater dock using single camera: a scene invariant approach", Mach. Vis. Appl., vol. 27, no. 2, pp. 221–236, 2016.

[25] J. Lu, M. Xia, W. Li, W. P. Guo, and K. C. Yang, "3-D location estimation of underwater circular features bymonocular vision", Optik (Stuttg)., vol. 124, no. 23, pp. 6444–6449, 2013.

[26] A. Yamashita, Y. Shirane, and T. Kaneko, "Monocular underwater stereo - 3D measurement using difference of appearance depending on optical paths", IEEE/RSJ 2010 Int. Conf. Intell. Robot. Syst. IROS 2010 - Conf. Proc., pp. 3652–3657, 2010.

[27] J.-S. Lee, S.-g. Roh, D. W. Kim, H. Moon, and H. R. Choi, "In-pipe robot navigation based on the landmark recognition system using shadow images", 2009 IEEE Int. Conf. Robot. Autom., pp. 1857–1862, 2009.

[28] Z. Zeng, L. Lian, K. Sammut, F. He, Y. Tang, and A. Lammas, "A survey on path planning for persistent autonomy of autonomous underwater vehicles", Ocean Eng., vol. 110, pp. 303–313, 2015.

[29] Thor I. Fossen, Guidance and Control of Ocean Vehicles, 1. Wiley, 1994, p. 494, isbn: 978-0471941132.

[30] J. N. Newman and J. Grue, Marine hydrodynamics. 1977, p. 426, isbn: 9780262534826.

[31] T. I. Fossen, Handbook of Marine Craft Hydrodynamics and Marine Craft Hydrodynamics and. 2011, isbn: 9781119991496.

[32] S. M.I.o. T. Wu, You, "Design and fabrication of a maneuverable robot for in-pipe leak detection", 2014.

[33] N. Paine and L. Sentis, "Design and Comparative Analysis of a Retrofitted Liquid Cooling System for High-Power Actuators", Actuators, vol. 4, no. 3, pp. 182–202, 2015.

[34] K. Bennion, "Electric Motor Thermal Management", U.S. Dep. Energy Veh. Technol. Progr. Annu. Merit Rev., 2011.

[35] P. Torque and C. Torque, "Examining How Cooling Impacts the Torque & Power of PMAC Motors", Tech. Rep.

[36] J. CARLTON, Marine Propelllers and Propulsion, 2nd. Butterworth-Heinemann, 2007, p. 560, isbn: 9780750681506.

[37] S Bhattacharyya, A. Reyes, and H. Asada,
"Dynamical modeling of a micro AUV in hydrodynamic ground effect",
in Ocean. 2016 MTS/IEEE Monterey, IEEE, 2016, pp. 1–5, isbn: 978-1-5090-1537-5.

[38] Kebes English Wikipedia, CC BY-SA 3.0. [Online]. Available:
`https://commons.wikimedia.org/w/index.php?curid=23793083`.

[39] S. Hutchinson, G. Hager, and P. Corke, "A Tutorial on Visual Servo Control",
IEEE Trans. Robot. Autom., vol. 12, no. 5, pp. 651–670, 1996.

[40] L Guisser, R Payrissat, and S Castan, "An Accurate 3D Vision System Using a
Projected Grid for Surface Geometrical Study",
Proc. MVA'92 IAPR Work. Mach. Vis. Appl. Tokyo, vol. 18, pp. 449–452, 1992.

[41] B. Ouyang, F. Dalgleish, S. Negahdaripour, and A. Vuorenkoski, "Experimental
study of underwater stereo via pattern projection",
Ocean. 2012 MTS/IEEE Harnessing Power Ocean, 2012.

[42] M. Rückwardt, A. Göpfert, M. Rosenberger, G. Linß, and S. Kienast, "Investigation,
Design and Practical Testing of LED Linear Light as an Alternative to a Laser Line
Generator", tm - Tech. Mess., vol. 78, no. 11, pp. 496–502, 2011.

[43] D. Slater, "Afocal viewport optics for underwater imaging",
vol. 9192, no. September 2014, 91920P–91920P–13, 2014.

[44] I. Buchmann and Cadex Electronics Inc.,
Batteries in a portable world : a handbook on rechargeable batteries for non-engineers.
Cadex Electronics, 2001, p. 292, isbn: 0968211828.

[45] M. S. Saleh, J. Li, J. Park, and R. Panat, "3D printed hierarchically-porous
microlattice electrode materials for exceptionally high specific capacity and areal
capacity lithium ion batteries", Addit. Manuf., vol. 23, no. July, pp. 70–78, 2018.

[46] F Nickols, D Ho, S. O. Harrold, R. T. Bradbeer, and L Yeung, "An Ultrasonically
Controlled Robot Submari for Pipe Inspection City University of Hong Kong",
Proc. Fourth Annu. Conf. Mechatronics Mach. Vis. Pract. 1997, pp. 142–147, 1997.

[47] J. Palmer, N. Yuen, J.-p. Ore, C. Detweiler, and E. Basha, "On Air-to-Water Radio
Communication between UAVs and Water Sensor Networks", pp. 5311–5317, 2015.

[48] U. M. Qureshi, Z. Aziz, U. M. Qureshi, F. K. Shaikh, Z. Aziz, S. M. S. Shah,
S. M. S. Shah, A. A. Sheikh, E. Felemban, and S. B. Qaisar, "RF path and
absorption loss estimation for underwaterwireless sensor networks in differentwater
environments", Sensors (Switzerland), vol. 16, no. 6, 2016.

[49] C. E. Brennen, "A review of added mass and fluid inertial forces", Ocean Eng., no. January, p. 50, 1982.

[50] X. Ai, "Added mass of ellipse and ellipsoid moving in ideal fluid", Tech. Rep.

[51] C.-C. Lin, R.-C. Chen, and T.-L. Li, "Experimental determination of the hydrodynamic coefficients of an underwater manipulator", J. Robot. Syst., vol. 16, pp. 329–338, 1999.

[52] B. J. Anderson, "Analysis of Pmm Data for Underwater Vehicles", PhD thesis, University of Tasmania, 1999.

[53] G. Lloyd and a Espanoles, "Best practice guidelines for marine applications of computational fluid dynamics", ... Consult. Members NSC, MARNET-CFD ..., 2002.

[54] C. S. Chin, Computer-Aided Control Systems Design, 1st. Boca Raton: CRC Press, 2012, pp. 2–209, isbn: 9781466568525.

[55] M. T. Sabet, P. Sarhadi, and M. Zarini, "Extended and Unscented Kalman filters for parameter estimation of an autonomous underwater vehicle", Ocean Eng., vol. 91, pp. 329–339, 2014.

[56] Y. Eng, W. Lau, E. Low, G. Seet, and C. Chin, "Identification of the Hydrodynamics Coefficients of an Underwater Vehicle using Free Decay Pendulum Motion", Eng. Lett., vol. 16, no. 3, pp. 326–331, 2008.

[57] D. Simon, Optimal State Estimation. Hoboken, NJ, USA: John Wiley & Sons, Inc., 2006, isbn: 9780470045343.

[58] M. Prats, J. Perez, J. J. Fernandez, and P. J. Sanz, "An open source tool for simulation and supervision of underwater intervention missions", IEEE Int. Conf. Intell. Robot. Syst., pp. 2577–2582, 2012.

[59] L. Meier, D. Honegger, and M. Pollefeys, "PX4: A node-based multithreaded open source robotics framework for deeply embedded platforms", Proc. - IEEE Int. Conf. Robot. Autom., 2015.

[60] M. Quigley, K. Conley, B. Gerkey, J. Faust, T. Foote, J. Leibs, E. Berger, R. Wheeler, and A. Mg, "ROS: an open-source Robot Operating System", Icra, vol. 3, no. Figure 1, p. 5, 2009. arXiv: 1106.4561.

[61] R. S. engineer) Wang and X. Qian, Openscenegraph 3.0 : Beginner's Guide. Wang2010: Gardners Books, 2010, p. 385, isbn: 9781849512824.

[62] J. Solà and J. Sol, "Quaternion kinematics for the error-state Kalman filter", 2017. arXiv: 1711.02508.

[63] J. Rehder, J. Nikolic, T. Schneider, T. Hinzmann, and R. Siegwart, "Extending kalibr: Calibrating the extrinsics of multiple IMUs and of individual axes", Proc. - IEEE Int. Conf. Robot. Autom., vol. 2016-June, pp. 4304–4311, 2016.

[64] MAVROS. [Online]. Available: https://github.com/mavlink/mavros.

[65] QGroundControl. [Online]. Available: http://www.qgroundcontrol.com/.

[66] R. Hänsch, W. Förstner, and B. P. Wrobel, Photogrammetric Computer Vision, ser. Geometry and Computing. Cham: Springer International Publishing, 2016, vol. 11, pp. 2–2, isbn: 978-3-319-11549-8.

[67] J. R. Miller, "Geometric approaches to nonplanar quadric surface intersection curves", ACM Trans. Graph., vol. 6, no. 4, pp. 274–307, 1987.

[68] D. Honegger, L. Meier, P. Tanskanen, and M. Pollefeys, "An open source and open hardware embedded metric optical flow CMOS camera for indoor and outdoor applications", Proc. - IEEE Int. Conf. Robot. Autom., pp. 1736–1741, 2013.

[69] I. Sa, "Shared Autonomy for Close-Quarters Navigation and Control of a VTOL Platform", PhD thesis, Queensland University of Technology, 2014, p. 224.

[70] O. E. F. Fossen and T. I., "Quaternion Feedback Regulation of Underwater Vehicles", in 1994 Proc. IEEE Int. Conf. Control Appl., vol. 2, 1994, pp. 857–862, isbn: 0-7803-1872-2.

[71] R. Brescianini, Dario; Hehn, Markus; D'Andrea, "Nonlinear Quadrocopter Attitude Control Technical Report", vol. 44, no. 23, 2013.

[72] Y. Hu and W. Meng, "ROSUnitySim: Development and experimentation of a real-time simulator for multi-unmanned aerial vehicle local planning", Simulation, vol. 92, no. 10, pp. 931–944, 2016.